

**DOCTORAL THESIS**

# Fluid-Structure Interaction Analysis of Impact-Induced Loads and Hydroelastic Responses of Ship Structures

Saeed Hosseinzadeh

TALLINN UNIVERSITY OF TECHNOLOGY  
DOCTORAL THESIS  
59/2023

# **Fluid-Structure Interaction Analysis of Impact-Induced Loads and Hydroelastic Responses of Ship Structures**

SAEED HOSSEINZADEH



TALLINN UNIVERSITY OF TECHNOLOGY

School of Engineering

Department of Civil Engineering and Architecture

This dissertation was accepted for the defence of the degree of Doctor of Philosophy (Ph.D.)  
on 19/10/2023

**Supervisor:**

Professor Kristjan Tabri  
Department of Civil Engineering and Architecture  
Tallinn University of Technology  
Tallinn, Estonia

**Opponents:**

Professor Smiljko Rudan  
Faculty of Mechanical Engineering and Naval  
Architecture  
University of Zagreb  
Zagreb, Croatia

Professor Alessandro Iafrati  
Institute of Marine Engineering (CNR-INM)  
National Research Council of Italy  
Italy, Rome

**Defence of the thesis:** 01/12/2023, Tallinn

**Declaration:**

Hereby I declare that this doctoral thesis, my original investigation and achievement, submitted for the doctoral degree at Tallinn University of Technology has not been submitted for any academic degree elsewhere.

Saeed Hosseinzadeh

-----  
signature



European Union  
European Regional  
Development Fund



Investing  
in your future

Copyright: Saeed Hosseinzadeh, 2023

ISSN 2585-6898 (publication)

ISBN 978-9916-80-059-1 (publication)

ISSN 2585-6901 (PDF)

ISBN 978-9916-80-060-7 (PDF)

Printed by Koopia Niini & Rauam

TALLINNA TEHNIKAÜLIKOO  
DOKTORITÖÖ  
59/2023

**Vedeliku ja konstruktsiooni vastasmõju  
analüüs löökoormuste ja konstruktsiooni  
hüdroelastse vaste hindamiseks**

SAEED HOSSEINZADEH





# Contents

Contents.....	5
Abstract.....	7
Lühikokkuvõte.....	8
Acknowledgements.....	9
List of Abbreviations.....	10
List of Publications.....	11
Author’s Contribution to the Publications.....	12
Original Features.....	13
1 Introduction.....	15
1.1 Background.....	15
1.2 State of the Art.....	18
1.3 Objective of the Thesis.....	20
1.4 Scope of Work.....	21
1.5 Limitations.....	23
2 Experimental Study.....	25
2.1 Test Set-up.....	26
2.2 Test Section, Sensors and DAQ.....	26
2.3 Experiments Procedure.....	28
3 Numerical Simulations.....	30
3.1 MMALE Coupling Method.....	31
3.2 CFD-FEM Coupling Method.....	33
4 Results and Discussions.....	36
5 Conclusions.....	44
References.....	46
Appendix 1 (Publication I).....	55
Appendix 2 (Publication II).....	75
Appendix 3 (Publication II).....	97
Curriculum vitae.....	119
Elulookirjeldus.....	121



## **Abstract**

### **Fluid-Structure Interaction Analysis of Impact-Induced Loads and Hydroelastic Responses of Ship Structures**

Water entry impact, also known as slamming impact, is a phenomenon that occurs on ships and offshore structures over a short period of time in rough sea conditions. This highly non-linear fluid-structure interaction problem causes large hydrodynamic loads on the structure that can lead to significant structural damage. Although slamming impacts have been extensively studied, the elasticity contribution to structural behaviour has rarely been taken into consideration. Since the dynamics of slamming involve air-water-structure interactions, a severe impact can easily induce elastic deformations that affect the fluid flow and the pressure field, i.e., the response is hydroelastic. Therefore, it may not always be accurate to simplify the problem to a rigid body impact. To properly address this phenomenon, it is essential to comprehend the effect of the hydrodynamic loads and the simultaneous structural responses of the ship's hull.

This thesis studies impact-induced loads acting on a 3D non-prismatic wedge section and its dynamic responses, both experimentally and computationally. A series of systematic free-fall drop tests were conducted on a 3D complex V-shaped section at various drop heights. A drop test tower was constructed to allow experiments to be carried out at various heights ranging from 25 cm to 2 metres. Two wedges with different masses were tested to investigate the effects of wedge mass on slamming loads and responses. To study the effect of flexural rigidity on structural responses, the bottom plates of the wedge were designed with two different bending stiffnesses. The importance of hydroelastic analysis is explained based on experimental observations.

Experiments provide the insight into the hydroelastic phenomenon. The experimental findings are exploited in the development of a coupled fluid and structure simulation model. The findings indicate that a two-way coupling numerical model is needed to accurately simulate slamming loads and structural responses at high impact velocities. Consequently, the simultaneous interaction between the fluid and structural dynamics is considered in the proposed numerical simulations.

In this thesis, both 2D and 3D flexible structures are simulated to get a deeper insight into the dynamics of hydroelastic slamming. Firstly, the water entry problem is numerically analysed by implementing a two-way coupling approach on 2D steel and aluminium structures. A comparison of constant velocity and freefall impact is presented to examine the effect of freefall motions. It is found that hydroelasticity depends on the deadrise angle and impact velocity, and the elastic behaviour increases with smaller deadrise angles and higher drop heights. Secondly, a 3D aluminium wedge with varying deadrise angles is simulated using two different numerical models. The slamming problem is modelled using an explicit nonlinear finite element method (MMALE) and an implicit CFD-FEM coupling approach. The results of the two numerical methods are validated and compared with the experimental data. The numerical computations obtained from different methods are found to be in satisfactory agreement with the experimental measurements, indicating their reliability and accuracy. The importance of simulating the fluid-structure interaction problems is evaluated by considering a hydroelasticity factor that exhibits a noteworthy influence on the unstiffened bottom plate for all examined impact velocities. A detailed analysis is performed to compare different numerical approaches and thoroughly discuss the advantages and disadvantages associated with each method.



## Lühikokkuvõte

### Vedeliku ja konstruktsiooni vastasmõju analüüs löökoormuste ja konstruktsiooni hüdroelastse vaste hindamiseks

Laeva ja avamerekonstruktsioonid kogevad vette sisenemisel hüdrodünaamilisi löökoormusi, mida tuntakse slämming koormustena. Slämming koormused on lühiajalised löökoormused, mida esinevad peamiselt keeruliste mereolude korral. Tegemist on mitte-lineaarse ja väga dünaamilise nähtusega, millega kaasnevad märkimisväärsed vibratsioonid või lausa konstruktsioonide kahjustumine. Ehkki hüdrodünaamilisi koormusi on laialdaselt uuritud, oletatakse konstruktsioonid sageli lõpmatult jäigaks ja seeläbi ignoreeritakse konstruktsiooni elastsuse mõju koormuste ja konstruktsiooni vaste hindamisel. Slämming koormuste hindamine kätkeb endas õhu, vee ja konstruktsiooni vastasmõju hindamist. Hüdrodünaamiline löök võib põhjustada konstruktsiooni deformeerumist, mis omakorda mõjutab vedeliku voolamist ja rõhujaotust ehk tegemist on hüdroelastse protsessiga. Seega ei saa konstruktsioone alati oletada lõpmatult jäigaks. Löökoormuste täpseks kirjeldamiseks on oluline mõista seoseid hüdrodünaamilise koormuste ja samaaegselt asetleidva konstruktsiooni vaste vahel.

Käesolev töö uurib hüdrodünaamilisi löökoormusi ekperimentaalselt ja numbriliselt. Meretehnoloogia kompetentsikeskuse mudelkatsebasseinis viidi läbi katsed, kus kolmemõõtmelisel mitteprismaatilisel kiilul lasti erinevatelt kõrgustelt vette langeda. Kiilu kukkumiskõrgust varieeriti vahemikus 0.25–2 m. Lisaks varieeriti kiilu massi uurimaks massi mõju löögikoormustele. Kiilu põhjakonstruktsioonid on konstrueeritud selliselt, et kiilu erinevate parraste jäikused erinevad märkimisväärselt.

Ekperimentaalsete katsete käigus tehtud järeldusi kasutati numbrilise simulatsioonimudeli loomisel. Katsete tulemused näitasid, et hüdroelastse protsessi täpseks kirjeldamiseks on vajalik kahesuunaline numbriline mudel, mis samaaegselt hindab hüdrodünaamilist rõhku ja konstruktsiooni vastet.

Saamaks paremat arusaama hüdroelastse slämmingu olemusest, on käesolevas töös simuleeritud nii kahe- kui kolmemõõtmelisi konstruktsioone. Esmalt hinnati slämming koormusi ja konstruktsiooni vastet kahemõõtmelise deformeeruva konstruktsiooni korral nii konstantse kui ka aeglustuva sisenemiskiiruse puhul. Leiti, et hüdroelastsus sõltub kiilu kaldenurgast ja löökiirusest. Konstruktsiooni elastsuse tähtsus kasvab põhja tõusunurga kahanedes ja löögikiiruste suurenedes.

Hüdroelastse slämmingu kirjeldamiseks kolmemõõtmeliste elastsete konstruktsioonide puhul arendati kaks erinevat numbrilist mudelit. Esimeseks mudeliks oli nõ. ilmutatud kujul formuleeritud lõplike elementide meetod, kus vee käitumise kirjeldamiseks kasutati meelevaldset Lagrange-Euleri meetodit ehk MMALE meetodit, kus ühes arvutuslikus ruumielemendis saab samal ajahetkel olla mitu erinevat materjali ning elemendi mõõtmeid, kuju ja materjalide mahtu saab kohandada arvutuse stabiilsuse tagamiseks. Teises numbrilises mudelis ühendati omavahel arvutuslik vedelikdünaamika ja imlutamata kujul formuleeritud lõplike elementide meetod. Mõlema numerilise meetodi tulemusi võrreldi ja valideeriti basseinikatsetega. Mõlemad arvutuslikud meetodid suutsid rahuldava täpsusega kirjeldada nii löökoormusi kui ka konstruktsiooni vastes. Hüdroelastsuse tähtsust kirjeldati hüdroelastsusteguri kaudu ning määrati soovituslikud piirid, milliste konstruktsioonijäikuste ja löökoormuste korral on vajalik kasutada kahesuunalist vedeliku-konstruktsiooni vastasmõju analüüsi. Erinevate arvutuslike lähenemiste eeliseid ja puudused on põhjalikult analüüsitud.

## Acknowledgements

This thesis is a result of the research conducted in the Mechanics of Fluids and Structures Research Group, located in the Department of Civil Engineering and Architecture at Tallinn University of Technology. Financial support for this thesis was provided by the Estonian Research Council through grants PRG83 (Numerical simulation of the FSI for the dynamic loads and response of ships) and PRG1820 (Dynamic response of offshore structures). This financial support is greatly appreciated. Additionally, the author acknowledges the financial support received from the European Regional Development Fund through the Dora Plus Study Mobility for Doctoral Students program, which facilitated a long-term study visit to the Department of Mechanical Engineering at Aalto University.

I would like to express my heartfelt gratitude to my supervisor, Professor Kristjan Tabri, for his unwavering encouragement, guidance, and support throughout the doctoral process. His exceptional technical expertise played a pivotal role in the successful completion of this research. I would also like to extend my thanks to DSc. Hendrik Naar for providing guidance and advice on experimental work. Furthermore, I am grateful to Prof. Spyros Hirdaris from the Marine Technology Group at Aalto University for his valuable guidance and advice during the course of this research.

I would like to take this opportunity to thank the professors, colleagues, and staff members of the Mechanics of Fluids and Structures Research Group for their continuous support and helpfulness during my doctoral program. I am also grateful to the staff of the Marine Technology Competence Center at Kuressaare College of Tallinn University of Technology (TALTECH MARTE), specifically Prof. Mihkel Kõrgesaar, Tarmo Sahlk, Ruttar Teär, and Kaarel Koppel, for their invaluable support during the experimental study.

Lastly, I would like to express my deepest appreciation to my parents and siblings for their unwavering support and dedication throughout this journey. Their encouragement during challenging and exhausting times has been invaluable, and without them, the completion of this thesis would not have been possible. Finally, I would like to thank my friends in Iran for their constant encouragement and support during my research, as well as my friends in Estonia and Finland for the unforgettable moments we have shared together.

Tallinn, December 2023

Saeed Hosseinzadeh

## List of Abbreviations

FSI	Fluid-Structure Interaction
FFSI	Flexible Fluid-Structure Interaction
EFD	Experimental Fluid Dynamics
2D	Two-dimension
3D	Three-dimension
DAQ	Data Acquisition
ALE	Arbitrary Lagrangian-Eulerian
MMALE	Multi-Material Arbitrary Lagrangian-Eulerian
EOS	equation of state
SMP	Symmetric multiprocessing
MMP	Massively parallel processing
RANS	Reynolds-Averaged Navier-Stokes
CFD	Computational Fluid Dynamics
CSD	Computational Solid Dynamics
FVM	Finite Volume Method
FEM	Finite Element Method
FEA	Finite Element Analysis
VOF	Volume of Fluid
SIMPLE	Semi-Implicit Method for Pressure-Linking Equations
HIRC	High-Resolution Interface Capturing
URF	Under-Relaxation Factor
AMR	Adaptive Mesh Refinement
FFT	Fast-Fourier Transformation
DFBI	Dynamic Fluid Body Interaction
HPC	High-performance computing

## List of Publications

This thesis consists of publications in the following peer-reviewed journals:

- I Hosseinzadeh, S., & Tabri, K. (2021). Hydroelastic effects of slamming impact loads during free-fall water entry. *Ships and Offshore Structures*, 16(sup1), 68–84.  
<https://doi.org/10.1080/17445302.2021.1954320>
- II Hosseinzadeh, S., Tabri, K., Hirdaris, S., & Sakh, T. (2023). Slamming loads and responses on a non-prismatic stiffened aluminium wedge: Part I. Experimental study. *Ocean Engineering*, 279, 114510.  
<https://doi.org/10.1016/j.oceaneng.2023.114510>
- III Hosseinzadeh, S., Tabri, K., Topa, A., & Hirdaris, S. (2023). Slamming loads and responses on a non-prismatic stiffened aluminium wedge: Part II. Numerical simulations. *Ocean Engineering*, 279, 114309.  
<https://doi.org/10.1016/j.oceaneng.2023.114309>

and the following relevant publications in the peer-reviewed conference proceedings:

- IV Hosseinzadeh, S., Izadi, M., & Tabri, K. (2020). Free fall water entry of a two-dimensional asymmetric wedge in oblique slamming: a numerical study. In *International Conference on Offshore Mechanics and Arctic Engineering* (Vol. 84409, p. V008T08A013). American Society of Mechanical Engineers.  
<https://doi.org/10.1115/OMAE2020-18645>
- V Hosseinzadeh, S., & Tabri, K. (2020). Numerical investigation of hydroelastic response of a three-dimensional deformable hydrofoil. In *HSMV 2020* (pp. 77–86). IOS Press.  
<http://doi.org/10.3233/PMST200029>
- VI Hosseinzadeh, S., & Tabri, K. (2021). Free-fall water entry of a variable deadrise angle aluminium wedge: An experimental study. In *Developments in the Analysis and Design of Marine Structures* (pp. 29–37). CRC Press.  
<http://doi.org/10.1201/9781003230373-4>
- VII Hosseinzadeh, S., Topa, A., & Tabri, K. (2023). A Numerical Sensitivity Analysis of Fluid-Structure Interaction Simulations on Slamming Loads and Responses. In *IOP Conference Series: Materials Science and Engineering* (Vol. 1288, No. 1, p. 012017).  
<http://doi.org/10.1088/1757-899X/1288/1/012017>

## Author's Contribution to the Publications

Contribution to the papers in this thesis are:

- I In Publication I, **“Hydroelastic effects of slamming impact loads during free-fall water entry”**, the author proposed and developed the numerical approach to simulate hydroelastic slamming on 2D structures. The simulation was analysed by the author and the results were compared with both published experimental data and analytical method. The manuscript was written and revised by the author. K. Tabri reviewed the manuscript and provided valuable comments.
  
- II In Publication II, **“Slamming loads and responses on a non-prismatic stiffened aluminium wedge: Part I. Experimental study”**, the author proposed the experimental study, designed the test setup, conducted the experiments, provided uncertainty analysis of the experimental data, analysed the results, and prepared the manuscript. K. Tabri and S. Hirdaris made valuable comments and feedback on the analysis and the manuscript. T. Sakh prepared and assembled the test tower, conducted the experiments, and provided the initial analysis of the results.
  
- III In Publication III, **“Slamming loads and responses on a non-prismatic stiffened aluminium wedge: Part II. Numerical simulations”**, the author provided numerical models using two different two-way coupling approaches to simulate hydroelastic slamming on a 3D wedge section. The impact-induced loads and responses were compared with the experimental data presented in Publication II by the author. The accuracy of the numerical model was discussed, and the manuscript was written by the author. A. Topa contributed to the preparation of the ALE numerical model and provided valuable information on the results. K. Tabri and S. Hirdaris reviewed the paper, provided valuable recommendations, and contributed to the manuscript.

## Original Features

Ship slamming is a complicated Fluid-Structure Interaction (FSI) phenomenon, which is associated with impulsive hydrodynamic loads and can threaten ship structural integrity. The majority of previous experimental and numerical studies on water entry problems focused on rigid two-dimensional structures for the sake of simplicity. Although modelling 2D rigid bodies can provide valuable insights into the physics of impact problems, it may not be suitable for many practical applications due to the dynamic response of the hull structure. This thesis presents an experimental and numerical analysis of impact-induced loads and responses on a 3D complex body, considering deformations of the structures. The following features of this thesis are believed to be original.

1. A numerical approach was developed to analyse the impact loads and responses on 2D elastic wedge sections in [Publication I]. A two-way coupling technique was utilised between the FVM and FEM solvers to compute the bottom plate deformations with different structural stiffnesses. To evaluate the effect of vertical velocity on bottom plate deformations, the results of constant velocity and free-fall impact were compared.
2. A series of free-fall drop tests were conducted on a non-prismatic aluminium wedge with stiffened and unstiffened bottom. The experimental results of vertical accelerations, hydrodynamic pressures, and strain responses at various drop heights were presented in [Publication II].
3. The importance of hydroelasticity assessment was studied in [Publication II] using a dimensionless factor. The study showed that the hydroelasticity has a significant effect on the unstiffened plate at all examined impact velocities ( $V_i = 2.2 - 5.6 \text{ m/s}$ ), whereas for the stiffened panel, it becomes important only at high impact velocities ( $V_i > 4.0 \text{ m/s}$ ). The effect of the mass of the wedge on the natural frequency of the structure was also investigated.
4. [Publication III] introduces two numerical models: the MMALE method and the combination of RANS CFD and FEM dynamic analysis with a two-way coupling technique. These models were developed to simulate the instantaneous interaction between fluid and a 3D wedge section. The computed structural deformation of the bottom plates was compared at different impact velocities.
5. The results of the numerical studies presented in [Publication III] were validated and compared with the experimental data available in [Publication II]. The study examined the influence of three-dimensionality, impact velocity, deadrise angle, and structural rigidity on vertical acceleration, slamming pressure, and strain response. The effect of three-dimensionality on slamming loads was investigated by comparing the maximum slamming force coefficients of 2D and 3D wedges.



# 1 Introduction

## 1.1 Background

In rough seas, the ship's hull may emerge from the waves and re-enter the water, causing significant loads over a short period of time, which is known as a slamming impact. This phenomenon occurs when a body encounters the water surface or when water forcefully impacts a structure at a small relative angle. In this situation, the water near the interface accelerates suddenly, resulting in high pressure and significant loads. The impact pressure is highly dependent on the relative angle between the structure and the water surface, and it rises sharply at small relative angles [1–3].

The slamming loads are typically much larger than other wave loads, and the structure responds both locally and globally to this load. It is worth noticing that the structural response can be either a local or a global vibration mode (known as whipping), or sometimes a combination of both modes [4–7]. Whipping is characterised by a low level of damping, causing the ship's structure to undergo multiple oscillations before dissipating the energy [4]. It is a long-lasting vibratory response that can persist for several cycles due to minimal energy dissipation. Moreover, the increased number of load cycles associated with whipping can contribute to fatigue damage accumulation in the structure, particularly under seakeeping loads. As a result of local and global dynamic responses, high stresses can occur in specific areas, causing elastic and plastic deformations [8]. In addition, there is a significant impact of slamming loads on ship performance, which is a major reason for ship operators to change course and/or reduce speed.

The dynamic behaviour of slamming loads can exert considerable effects on the structural integrity of ships, potentially leading to structural damage or even collapse. Figure 1 illustrates two major accidents that happened due to severe slamming impacts in rough seas. One of the most tragic maritime incidents of the 20th century took place on September 28, 1994, involving the sinking of the MS Estonia ferry in the Baltic Sea. According to the official report by the Joint Accident Investigation Commission [9], the vessel's bow visor malfunctioned as a result of a significant wave impact, leading to its detachment from the ship. The investigation concluded that the extensive damage was caused by severe slamming in rough sea conditions, characterised by a wind speed of 15–20 m/s and a significant wave height of 4–6 m [9].



Figure 1. Two major accidents due to slamming loads:(a) MS Estonia Ro-Ro passenger ship; (b) MSC Napoli container ship.



The MSC Napoli incident in 2007 serves as another example highlighting the potential consequences of impact loads on the catastrophic failure of a ship's hull. The ship encountered extreme sea conditions with a wave height of 9 meters at 11 knots forward speed, which is considered high for such wave conditions [10]. As a result, the ship experienced significant pitching motions and suffered hull damage near the engine room. The initial investigation conducted by classification societies indicated that, among various potential causes, the whipping load was identified as the primary factor contributing to the ship's failure [11]. The non-linear finite element strength analysis conducted by DNV showed that the buckling strength in the forward part of the ship's engine room was insufficient [11]. These events highlighted the critical importance of understanding and mitigating the effects of extreme wave impacts to ensure that their influences are adequately considered in design and structural analysis, allowing for an appropriate margin of safety.

In general, the impact-induced loads on ship structures can be classified as follows.

- Bottom slamming refers to the phenomenon in which the emerged bottom of a ship's hull re-enters the water surface, resulting in high forces and loads that can potentially cause structural damage, vibrations, and alterations in the ship's stability and maneuverability (Figure 2a).
- Bow-flare slamming occurs when the bow of a ship slams into the water surface with an extreme pitch-and-heave motion at high relative speed (Figure 2b).
- Green water slamming is the phenomenon in which large volumes of water forcefully impact the deck or upper structure of a vessel or an offshore platform, typically in extreme sea conditions (Figure 2c).
- Breaking wave impacts occur when incident waves and bow waves combine and hit the bow of a ship, even during small ship motions. These types of waves pose a higher risk of slamming impacts due to their steepness and the possibility of direct contact with the structure (Figure 2d).

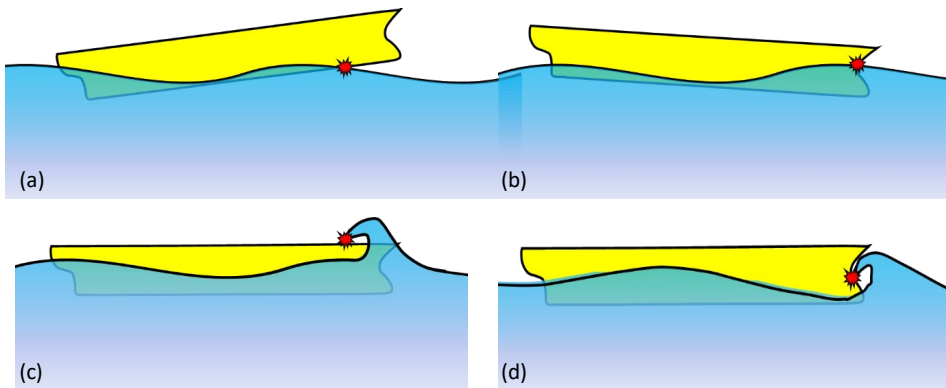


Figure 2. Different types of slamming impact: (a) bottom slamming; (b) bow-flare slamming; (c) green water slamming; (d) breaking wave impact (reproduced from [12]).

In addition to the aforementioned types of slamming impacts, there are other variations that occur under specific sea conditions and on certain structures, which are not the focus of this study. These include stern slamming, wet-deck slamming (observed in catamaran vessels), and wave run-up slamming (relevant to offshore structures).

The analysis of impact loads and water entry problems was initially explored by von Karman [13] and Wagner [14], who analytically addressed the issue with specific simplifications. These simplifications included assumptions of a 2D rigid body, symmetric impact, incompressible fluid, irrotational flow, neglect of gravity, and no flow separation. Since their pioneering works, numerous advancements and developments have been made in this field. Zhao and Faltinsen [15] studied the water entry of 2D bodies and proposed an asymptotic solution for small deadrise angles structures. Later, Vorus [16] extended the Wagner solution by introducing a nonlinear term to the kinematic condition in an incompressible flow for rigid cylinder impact. Following Wagner's work, many analytical and semi-analytical investigations have expanded upon his method, applying it to various shapes and diverse applications [17–19]. Tassin et al. [20] conducted a comprehensive assessment of several analytical models for water entry of rigid bodies, comparing the results of asymptotic method, MLM (Modified Logvinovich Model [21]), and GWM (Generalised Wagner Model [22]) with numerical simulations and experimental data [23].

In addition to the analytical methods, the advancement of supercomputers has led to the development of a wide range of numerical models. These models allow researchers to conduct more detailed and realistic simulations, enabling them to gain more insight into the behaviour of water entry problems [24,25]. Luo et al. [26] used an explicit finite element method to predict the slamming loads on a rigid wedge. In a similar way, Wang and Soares [27] simulated the water entry problem on a 2D rigid wedge based on ALE formulation and compared the results with analytical solutions. A review of capabilities of CFD methods to estimate the impact induced loads on rigid bodies presented by [28]. Izadi et al. [29] simulated the free-fall impact of a 2D rigid wedge with different deadrise angles based on finite volume method. Additionally, the effect of heel angles on pressure distribution and impact loads of oblique slamming on an asymmetric rigid wedge was numerically studied by Hosseinzadeh et al. [30]. These studies contribute to the growing body of research on water entry problems, exploring different numerical approaches, and investigating various factors that affect the slamming phenomenon.

The water entry problems have been extensively investigated in recent decades; however, the majority of these studies have focused on rigid structures with 2D assumptions. It is important to consider that impact-induced problems involve complex air-water-structure interactions, and simplifying the problem to a 2D rigid body impact may not always provide accurate results. Furthermore, implementing analytical models for 3D complex structures can be challenging. The rigidity of a body implies no deformation upon impact, resulting in hydrodynamic pressure remaining unaffected by structural deformation. Additionally, the effect of hydroelasticity, which accounts for the interaction between the structure's deformation and hydrodynamic forces, cannot be considered in the analysis when assuming a rigid body.

Recent research highlights the importance of flexible fluid-structure interaction (FFSI) analysis in studying ship slamming phenomenon. Specifically, investigating the hydroelastic slamming of flexible bodies has emerged as a crucial aspect in gaining a deeper understanding of the dynamic response and structural integrity of ships subjected to water entry impacts [1,3]. By considering the coupled interaction between fluid and structure, it helps identify potential areas of concern and enables the development of improved design strategies to enhance the structural integrity and overall safety of maritime applications. Furthermore, hydroelastic analysis assists in the prediction and mitigation of potential risks associated with ship slamming. By taking into

account the hydroelastic effects, including force redistribution and energy dissipation, designers can optimize the hull form, material selection, and structural arrangements to minimize the risk of structural failure, fatigue, and damage caused by repetitive slamming impacts.

## 1.2 State of the Art

Fluid-structure interaction mechanics can be described as a multidisciplinary area of study that investigates the dynamic behaviour of a coupled system consisting of solid and fluid components. In an FSI problem, the fluid field ( $\Omega_f$ ) and structural field ( $\Omega_s$ ) are considered as a coupled system through a shared interface ( $\Gamma_{FSI}$ ). Figure 3 illustrates how the appropriate solution to a fluid-structure interaction problem is determined by the level of interaction between structural response and fluid loads. Depending on the degree of structural response, the FSI problem can be categorised between the problem where there is negligible deformation in the solid domain and the structure can be considered as a rigid body [31], and the cases where significant structural deformation occurs, influencing the flow field [32,33]. Hydroelasticity, a term used to describe one of the applications of FSI in marine floating structures, involves the fully coupled study of the interaction between the water surface and an elastic structure. It focuses on examining the mutual influence between fluid loads and structural responses, encompassing the dynamics of both fluid and solid components [31,32].

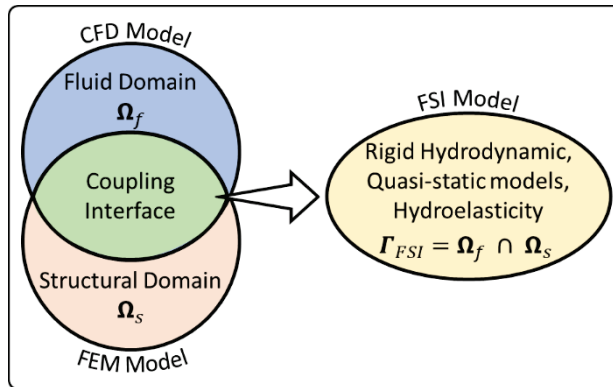


Figure 3. A schematic of FSI problem with  $\Gamma_{FSI}$  as a shared surface (reproduced from [34]).

The dynamic and impulsive nature of impact-induced loads can have severe consequences on marine structures. Ship structures may experience local damage or extensive buckling on the deck due to the impact loads. It is more crucial for moderate to high-speed ships where even small individual impact loads can accelerate fatigue damage to the hull [12]. The presence of slamming loads poses a threat to the safety of ships, making it essential to develop a reliable and practical estimation method for the impact loads. Consequently, employing a fully coupled fluid-structure interaction analysis provides a more comprehensive representation of the intricate physics underlying this phenomenon and enables an accurate estimation of the structural responses. To date, numerous investigations have demonstrated the advancements in analysing hydroelastic slamming through analytical models [35–39], experimental studies [40–43], and numerical simulations [44–48].

In the studies presented by Faltinsen [1, 3, 49], it was discovered that the water entry phenomenon can become severe at high impact velocities and low deadrise angles, thereby intensifying the coupling between hydrodynamic loads and structural responses. Bereznitski [50] conducted a study on the water entry of 2D wedges with low deadrise angles and highlighted that the ratio between the impact duration and the period of the first dry mode of vibration of the structure plays a critical role in determining whether hydroelastic effects should be considered in the solution of structural responses. Kapsenberg [2] presented a review of the state-of-the-art in slamming research, focusing on its implications for ship design and emphasised that in cases of local impacts with small relative surface structure angles, the coupled interaction between the fluid and structure becomes significant when the resonance period of the structure exceeds the impact duration [2]. Korobkin et al. [51] used Wagner theory to calculate the hydrodynamic loads and employed a direct coupling of the finite element method to estimate the structural responses on an elastic 2D body. Later on, Khabakhpasheva and Korobkin [52] developed an approximate model by combining the Wagner solution with Euler beam theory to analyse the elastic wedge impact problem and estimate the maximum bending stress in thick wedge plates. Lv and Grenestedt [53] conducted an analytical study on the structural responses of boat bottom panels subjected to impact loads, utilising a linear elastic Euler-Bernoulli beam to represent the cross section of the panels and presenting the deflections and bending moment of the bottom as functions of time and position.

In addition to the analytical models, various advanced numerical studies have been conducted to estimate the impact-induced loads and responses on marine structures. The possible application of the Arbitrary Lagrangian-Eulerian (ALE) method has been investigated in many studies [54,55]. Stenius et al. [56] simulated the hydroelastic panel water impacts based on an explicit finite element method (LS-DYNA) and compared the results with a simplified in-house developed method. Wang and Soares [57] used an ALE solver to simulate the water impact problem on three-dimensional hemispheres and cones with different deadrise angles. In a more recent study, Wang and Soares [58] conducted a comprehensive review on ship slamming loads and structural responses to provide an in-depth understanding of the phenomenon, including hydroelastic wave impact of wet-decks, water entry of an elastic wedge, and hull girder vibrations induced by impact loads. Yu et al. [59] studied the hydro-plastic response of beams and stiffened panels subjected to extreme water slamming at small impact angles using a multi-material ALE method and compared the results with a proposed analytical model. Their findings revealed that the numerical model accurately captures the interaction between hydrodynamic loads and structural deformations [59]. Moreover, the numerical prediction of slamming loads acting on flat stiffened plates and their dynamic response was conducted by Truong et al. [60], using a non-linear explicit finite element code in LS-DYNA. The numerical uncertainties associated with the ALE method for the prediction of local slamming loads and structural responses on a rigid and elastic flat plate were recently presented by Wang et al. [61].

The coupling between hydrodynamic forces and the structural behaviour subjected to slamming impacts can also be predicted using alternative computational techniques [62, 63]. Maki et al. [64] combined RANS CFD and FEM based on one-way coupling to predict the hydroelastic response of a wedge-shaped body. Panciroli et al. [65] proposed a numerical model based on a coupled FEM and Smoothed Particle Hydrodynamics (SPH) formulation to simulate the hydroelastic effects and compared the computed results with experimental data. More recently, a FSI coupling strategy between boundary

element method (BEM) and modal superposition method was proposed to study the hydroelastic slamming of wedge sections by Feng et al. [66]. They compared the results of quasi-static, decoupling (rigid) and coupling solutions and concluded that the quasi-static solution underestimates structural maximum response [66].

Izadi et al. [67] utilised a two-way coupling (FVM and FEM) to study the hydroelastic impact of deformable wedges with oblique speed and asymmetric conditions, and compared the deformation at the midpoint of wedge with available experimental data. A benchmark study was conducted by Truong et al. [68] to assess the accuracy of different FSI coupling techniques in predicting the slamming loads and responses of stiffened flat plates. They evaluated four different commercial software (ALE, ICFD, ANSYS CFX, and Star-CCM+/ABAQUS) and compared the impact loads with the corresponding bottom deflections under several vertical velocities. Yan et al. [69] applied a CFD-FEA two-way coupling technique to study the impact loads on both stiff and flexible flat plates, revealing the effect of structural rigidity on peak pressure values. Furthermore, Yan et al. [70] presented a systematic comparison of FSI simulations with experiments, focusing on hydroelasticity and air trapping effects, numerical uncertainties, and the validity of modelling assumptions for predicting bottom slamming. In the latter publication, the authors illustrated that the validation uncertainty percentage for peak pressure tends to decrease at higher impact velocities and is generally independent of the velocity for slamming forces.

Fluid-Structure Interaction (FSI) simulations play an important role in addressing slamming problems due to its profound effect on structural integrity. The significance of hydroelasticity effects highlighted in recent studies underscores the indispensability of FSI simulations. Furthermore, the complex interaction between hydrodynamic loads and structural responses remains inadequately explored, necessitating the utilisation of hydroelastic simulations to unveil the complete picture. A thorough experimental exploration of 3D structures in water entry problems not only enhances comprehension of these challenges but also offers a means to validate analytical models.

### **1.3 Objective of the Thesis**

The main goal of this study is to analyse hydroelastic slamming and provide a unified model to predict the impact loads and responses on ship structures. To fully capture the intricacies of fluid-structure interaction involving flexible bodies, it is necessary to develop a comprehensive model that considers various factors such as material properties, geometric characteristics, and fluid mechanics. This requires an in-depth understanding of both the mechanical behaviour of materials and their response to fluid flow dynamics. Additionally, experimental data can be used to validate the numerical models and to make more accurate predictions of behaviour of the system under different conditions. Thus, a series of systematic free-fall drop tests is carried out to provide a benchmark data for impact loads. The importance of two-way coupling technique is discussed in detail. To determine the most efficient coupling technique, some simple FFSI problems are first investigated, and the results are compared with previous experimental data. Subsequently, the validated coupling technique is applied to a 2D elastic wedge section and a 3D deformable stiffened wedge to calculate the slamming and local dynamic loads, as well as to validate the numerical models with experimental study. To achieve these, the following objectives have been outlined:

1. Assessment dynamic loads acting on 2D elastic wedge sections considering both constant velocity and free-fall impact.
2. Conduct systematic free-fall drop tests on a non-prismatic aluminium wedge with stiffened and unstiffened plates and analyse the importance of hydroelastic slamming.
3. Develop and implement an efficient method for coupling computational fluid dynamics (CFD) and computational solid dynamics (CSD) solvers.
4. Simulate the impact-induced problem with two different numerical methods, MMALE and a combination of RANS CFD and FEM.
5. Validate and compare the computed results with measured data and analysing the flexural rigidity as well as 3D effects on the slamming loads and responses.
6. Present frequency analysis of strain responses and study on the effects of impact velocities and wedge masses on the frequency distribution.

## 1.4 Scope of Work

The water entry problem was initially investigated numerically using rigid wedges, and the findings were presented in a peer-reviewed conference paper [30]. Subsequently, to evaluate the capability of the FFSI model for hydroelastic problems, a study was conducted on a 3D deformable hydrofoil with different turbulence models [71]. The investigation focused on analysing the flow-induced deformation and elastic response of both rigid and flexible hydrofoils at different angles of attack [71]. After that, the validated coupling technique was employed to tackle hydroelastic slamming problems.

This thesis encompasses a comprehensive investigation involving both experimental and numerical analyses. Figure 4(a-c) vividly illustrate real-life instances of bottom slamming occurring on various types of vessels. This highlights that regardless of the type of the ships, the impact loads can have a substantial effect on the structural integrity under harsh sea conditions. As already stated, this study aims to evaluate the effect of bottom slamming on the structural responses and estimate the bottom plate deformations at different impact velocities. To achieve this, a wedge section is utilised which resembles a fore body structure of a moderate to high-speed craft. A series of free-fall drop tests is conducted, enabling the measurement of slamming pressure and structural responses on a non-prismatic aluminium wedge. To complement the experimental findings, numerical simulations using both the ALE and CFD-FEM methods are employed to accurately simulate hydroelastic slamming events and predict the corresponding structural responses. As shown in Figure 4(d and e), both 2D and 3D wedge sections are modelled and the hydroelastic slamming is studied in detail. Figure 4(f) presents an example of maximum deformation computed at various locations on the 3D wedge. It is worth noticing that the emphasis of the thesis is placed on understanding how the aluminium structure responds to the applied loads while remaining within its elastic limits. Therefore, the investigation does not incorporate the effects or implications of plastic deformation in the analysis.

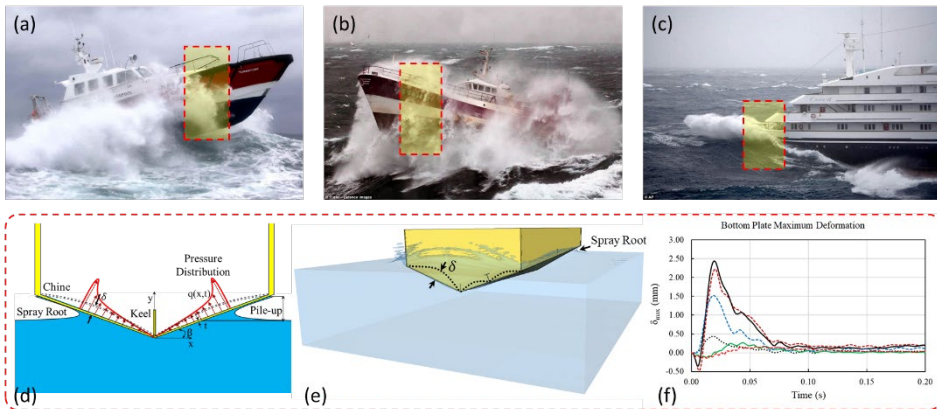


Figure 4. Real slamming and numerical modelling: (a) a pilot vessel in rough weather [72]; (b) a French fishing vessel flounders amid furious waves during a storm in the Irish Sea [73]; (c) Wave-induced loads caused a broken bridge window and affected engine performance on the Clelia II, the American cruise ship [74]; (d) a schematic view of water entry problem of a two-dimensional symmetric flexible wedge [P1]; (e) three-dimensional wedge impact [P3]; (f) a sample of bottom plates maximum deformation at different locations of the 3D wedge [P3].

The scope of this work includes the investigation of various parameters and their effects on the slamming loads and responses. These parameters may include, but are not limited to, impact velocity, deadrise angle, structural properties, and coupling technique. The present investigation comprises both experimental and numerical studies which provide valuable insights into the behaviour of water entry problems and contribute to the development of improved design guidelines for ship structures and other marine applications. The impact-induced loads and responses of a 3D non-prismatic aluminium wedge are experimentally studied. On the basis of the experimental observations, a 2D and a 3D numerical model are developed to simulate the fluid-structure interaction problem by implementing a fully coupled technique. The numerical simulations are performed to estimate the local response of elastic bodies and analyse the bottom deformations under different conditions. To ensure the accuracy and reliability of the proposed models, the computed results are validated and meticulously compared with the experimental data. The entirety of this investigation is documented in three publications, as illustrated in Figure 5.

In publication I, the water entry problem of a 2D elastic wedge is numerically investigated at different impact velocities and deadrise angles. The finite volume method and finite element method are employed to model the FFSI problem based on a two-way coupling technique. The bottom deformation of the wedge is calculated using the solid stress model implemented in Star CCM+ software. This model utilises the finite element method to calculate the displacement of the solid structure, and subsequently determines the associated stresses and strains. The effect of impact velocity is studied by comparing the constant velocity and free-fall impacts. Additionally, two different materials are used to examine the effect of structural stiffness on the impact loads and responses. A detailed study of structural deformation in relation to impact velocity, deadrise angle, and pressure distribution is conducted [P1].

Publication II focuses on the experimental investigation of the impact-induced loads and structural responses of a 3D non-prismatic aluminium wedge with stiffened panel

during free-fall water entry. The study specifically examines the simultaneous structural responses caused by hydrodynamic loads, particularly in cases of high-impact water entry. The bottom of the wedge is made up of a 4 mm plate thickness and the deadrise angle varied from 20° to 30°. The repeatability of the experiments and the analysis of measurement uncertainties are extensively discussed. The effects of flexural rigidity on the slamming parameters are examined by comparing the pressure results and strain responses of unstiffened and stiffened panels. A frequency analysis is conducted on the measured strain responses to determine the relationship between the natural frequency of the wedge and the impact time. The importance of FFSI simulation is assessed using a hydroelasticity factor, which is found to have a significant effect on the unstiffened bottom for all impact velocities studied. This study provides valuable benchmark data for the validation of numerical results of water entry problems [P2].

Publication III presents the validation and comparison of two different numerical models proposed for calculating slamming parameters. The experimental observations presented in [P2] serve as the basis for developing a numerical model, which aims to simulate the impact loads and responses on 3D elastic structures. To achieve this, an explicit nonlinear finite element method based on the ALE algorithm is implemented to design the numerical FFSI model. In addition, the interaction between fluid and structure of the water entry problem is modelled by utilising a strongly two-way coupling technique. The coupling between the FVM and FEM solvers is achieved using STAR-CCM+ and ABAQUS commercial software. The wedge structure is modelled using shell elements in both numerical methods. The study explores the influence of various factors, including three-dimensionality, impact velocity, deadrise angle, and structural rigidity, on vertical acceleration, slamming pressure, and strain responses [P3].

## 1.5 Limitations

This thesis proposes a simulation model for calculating impact-induced loads on elastic bodies and analysing their structural responses. While both numerical and experimental models presented in this study have provided valuable insights into the behaviour of impact problems on ship structures, there are some limitations on the applicability of the models, among which are as follows:

- This study focuses on analysing the behaviour of aluminium materials within their elastic range, without taking into account plastic deformation.
- Both the experimental and numerical studies are conducted under symmetric condition and do not consider heel angles (no asymmetric loads).
- The computational resources and time required for running the simulations may be significant, limiting their practicality for large-scale applications.
- The CFD-FEM model is time-consuming and requires extensive mesh refinement near the free surface.
- The MMALE method exhibits high sensitivity to the coupling factors, necessitating a trial-and-error process to determine the appropriate penalty and damping factors.
- The role of aeration and cavitation on the hydroelastic slamming and structural responses at high impact velocities has not been examined.



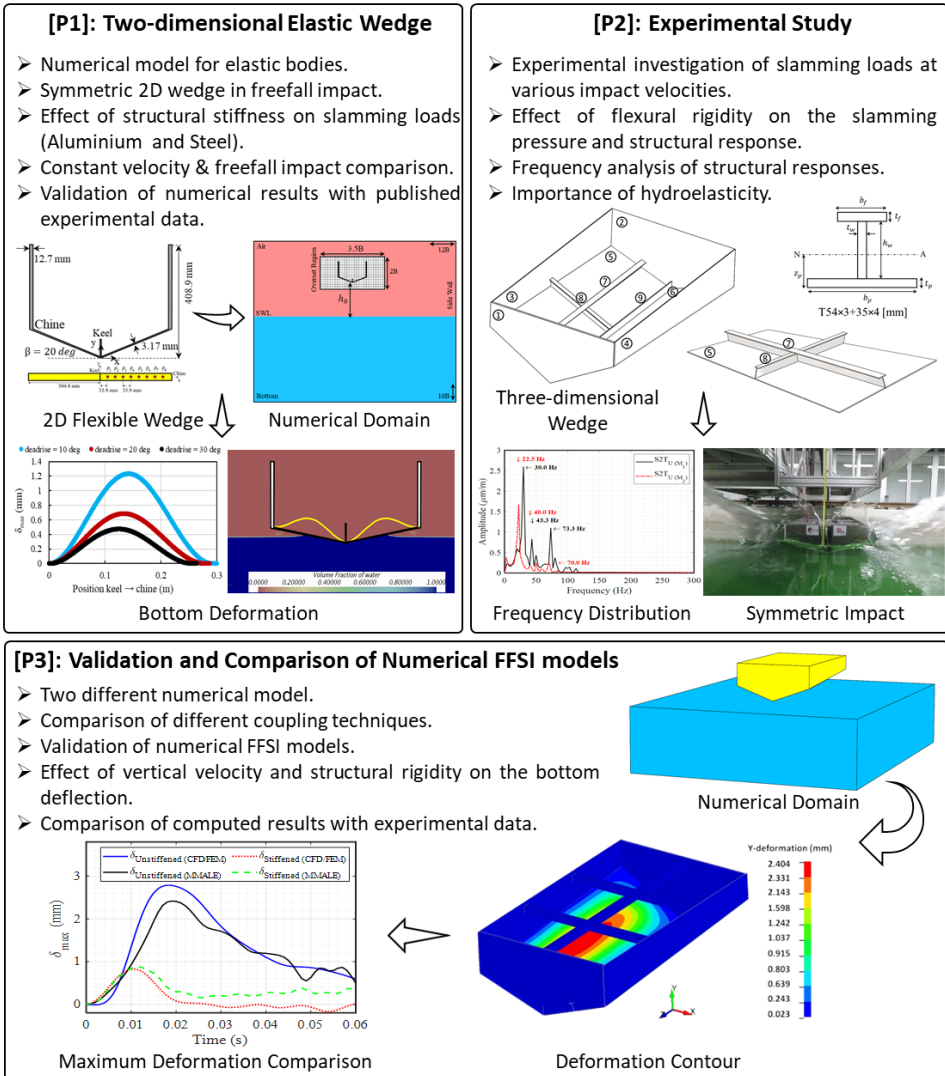


Figure 5. Outline of the investigation.

## 2 Experimental Study

The slamming phenomenon poses challenges when it comes to conducting experimental studies due to its inherent complexity. One of the main difficulties lies in the short duration of the impact event, which typically lasts only milliseconds. It becomes difficult to accurately record and measure the impact pressure and other local variables within this remarkably short period of time [2]. To achieve accurate measurements, high sampling rates are required during the experiment. Additionally, when dealing with structures that have smaller deadrise angles, even higher sampling rates are necessary to capture the rapid changes and intricacies of the slamming event. Tveitnes et al. [75] conducted a series of experiment on symmetric rigid wedges with a deadrise angle ranging from  $5^\circ$  to  $45^\circ$  and constant impact velocities. They measured the vertical forces acting on the wedge section and evaluated the added mass of the impact. In a series of drop tests conducted by Lewis et al. [76], the evolution of spray root, acceleration, and pressure distribution of a constant deadrise angle rigid wedge (2D) were measured. The authors also provided an extensive uncertainty analysis on the experimental data, ensuring their usefulness for validating numerical models and emphasizing the importance of accurate measurements [76].

The study of hydroelastic effects led to a series of experiments aimed at validating the theory that was developed [77–81]. Stenius et al. [42] conducted a study to investigate the importance of hydroelastic effects on rigid and flexible panels in constant velocity and derived semi-empiric expressions for the pressure distributions. Panciroli and Porfiri [82] carried out an experimental study on a flexible aluminium plate with 0.5 mm thickness and  $22^\circ$  deadrise angle during free-fall impact. They employed a particle image velocimetry (PIV) technique to measure the velocity field around the structure. An extensive series of tests were conducted by Duan et al. [83] to study the characteristics of slamming pressures, including propagation speed and pressure coefficient, on rigid and elastic wedges with deadrise angles ranging from  $0^\circ$  to  $45^\circ$  and drop heights ranging from 0.1 m to 1.0 m. In the latter publication, it was found by the authors that the flexibility of the plate in the wedge led to an increase in the duration of the slamming pressure [83]. In recent years, extensive experimental studies have been conducted on flat plates, specifically focusing on their applicability to offshore structures and their role in the development of simplified analytical models for accurately predicting hydroelastic slamming [84–87].

These studies reveal that the experimental investigations of hydroelastic slamming can pose even greater challenges, due to the small thickness of the structure and the influence of plate deformations on the hydrodynamic pressures. In addition, the review of published research indicates a lack of comprehensive understanding regarding the influence of flexural rigidity, deadrise angle, and impact velocity on the structural responses of 3D V-shaped elastic bodies. To shed light on these uncertainties, a systematic experimental investigation was conducted [P2], which forms the focus of this section. The objective of this section is to present the experimental setup and the findings regarding the hydroelastic response of a symmetric wedge section made of aluminium. The aim is to examine the potential influences of hydroelasticity on the loads and responses induced by the impact. Through this investigation, valuable insights are gained into the complex dynamics of hydroelastic slamming and its effects on the structural behaviour.

## 2.1 Test Set-up

A comprehensive series of free-fall drop tests using a self-designed test rig was carried out at the Marine Technology Competence Centre (MARTE) of Tallinn University of Technology. The drop test tower was specifically designed to provide a wide range of impact tests, with drop heights ranging from 25 cm to 2 m. The test rig, as depicted in Figure 6, is situated within a dedicated section of the 60 m long, 5 m wide, and 3 m deep towing tank. To ensure stability and minimize vibrations during testing, one side of the test frame was securely fixed to a carriage, while the other side was firmly screwed out to a heavy beam. The specimen is attached to two linear guide rails, enabling vertical free-fall motion. A movable stopper was also used to adjust the specific drop height for each test.

To reduce friction and enable smooth motion, measures were taken to minimize resistance along the guide rails and bearing mounts. The thick molybdenum grease from the bearings was carefully cleared away, allowing them to roll with minimal resistance. Additionally, the soft cleaning pads from the bearing blocks were removed to further reduce resistance and eliminate friction against the guiding rail. To facilitate unrestricted free-fall motion during the experiments, a distance of 70 cm was maintained between the end of the guide rails and the still water surface. This ensured that the specimen experienced a fully unobstructed descent throughout the testing process.

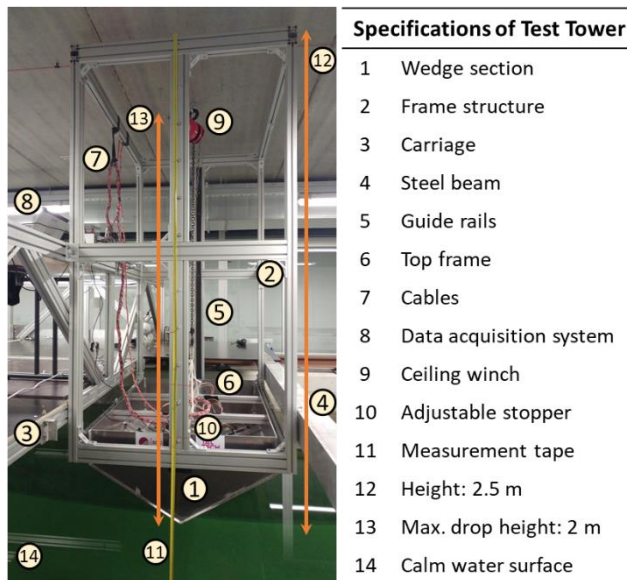


Figure 6. Illustration of drop test tower with installed wedge for 25 cm drop height experiment.

## 2.2 Test Section, Sensors and DAQ

A non-prismatic three-dimensional wedge-shaped specimen made of aluminium (alloy 5083-H111) was designed to resemble the fore body structure of semi-planing and planing vessels. It is worth noticing that the design considered the practicalities of producing the test section at laboratory scale. The wedge section used in the study has principal dimensions of 1500×940×450 mm, with a variable deadrise angle ranging from

20 to 30 degrees (see Figure 7). The consideration of a non-prismatic section allows for the analysis of three-dimensional effects on hydroelastic slamming. To explore the influence of flexural rigidity on the structural response, the section is designed using different plates to ensure sufficient stiffness on the port and starboard sides. The starboard bottom was made up of a 4 mm thick extruded panel with a T-shaped longitudinal and transverse stiffener (Stiffened bottom), while there are no stiffeners on the port bottom of the specimen (Unstiffened bottom). Furthermore, a frame was designed and mounted on top of the wedge to facilitate hoisting using a loop shackle for positioning it in the test tower. Two different wedge masses were employed in the experiments to examine the effect of mass on slamming loads. The designed wedge had a mass of 55 kg ( $M_1$ ), while the heavier wedge weighed 82.5 kg ( $M_2$ ), including sensors, screws, welding, and the top frame. To increase the mass of the lighter wedge, additional weights were evenly distributed along the length of its keel. Further details regarding plates thickness and stiffener dimensions can be found in the table provided in Figure 7(b).

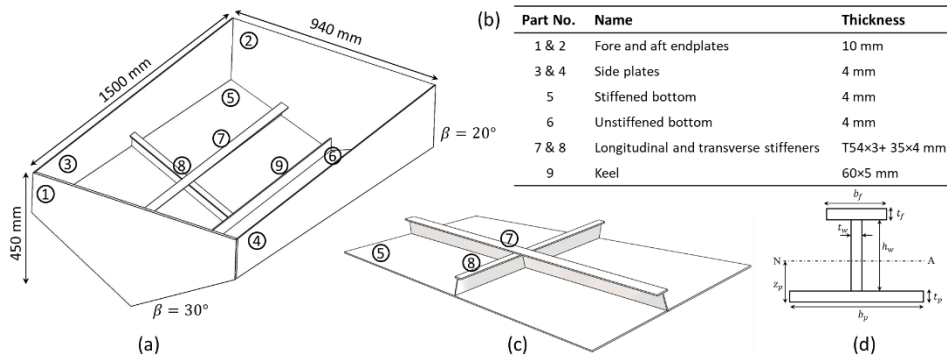


Figure 7. Drawing of the wedge section: (a) general dimensions of the wedge; (b) table of plate thickness; (c) stiffened bottom plate; (d) stiffeners properties [P2].

Figure 8 presents an overview of the arrangement of sensors on the wedge section. During the experiments, the slamming pressures were measured using sixteen piezoelectric dynamic pressure transducers (PCB-CA102B18) arranged along the bottom surface of the wedge. In order to evaluate and compare the pressure measurements obtained from the unstiffened and stiffened bottoms, the sensors were symmetrically mounted on the bottom of the wedge, with different labels assigned to the sensors on the port and starboard sides, such as  $P2_S$  for the second sensor on the stiffened bottom and  $P2_U$  for the second sensor on the unstiffened bottom.

The structural responses of the slamming impact were recorded using twenty liner strain gauges (HBM-1-LY13-6/120), which were positioned on the inner side of the bottom plates of the specimen. As depicted in Figure 8, the strain gauges are distributed in both transverse and longitudinal directions to ensure that the strain responses can be effectively captured from different directions. Similarly, to the pressure sensors, the strain gauges were labelled with subscripts "U" and "S" to distinguish their location on the unstiffened and stiffened sections of the structure, respectively. For instance,  $S1_L$  referred to the first strain gauge on the stiffened bottom in the longitudinal direction, while  $S2_T_U$  indicated the second strain gauge on the unstiffened bottom in the transverse direction.

In addition to measuring impact pressures and strain responses, vertical accelerations were recorded using three Dytran 3176B piezoelectric accelerometers. These accelerometers were positioned on the top of the keel, at the fore, middle, and aft of the wedge, denoted as  $A_f$  ( $\beta = 30$  deg.),  $A_m$  ( $\beta = 25$  deg.), and  $A_a$  ( $\beta = 20$  deg.), respectively. Figure 8 (b-d) present cross-sectional views of the specimen at different locations, providing a clearer depiction of the positions of the pressure and strain sensors.

Data from all sensors were collected simultaneously using a data acquisition (DAQ) system located on the carriage. For the pressure sensors on the unstiffened bottom, two dynamic universal amplifiers with 4 channels each and a sampling rate of 100 kHz were utilised. The pressure data from the stiffened bottom, as well as the acceleration data, were captured using a universal amplifier with a sampling rate of 40 kHz. The strain gauge data were acquired using a bridge amplifier with a sampling rate of 20 kHz. All sensor data were recorded through an HBM CX22B-W data recorder module connected to the HBM proprietary CatmanEASY AP software. Further information regarding sensor specifications and data acquisition system properties can be found in [P2].

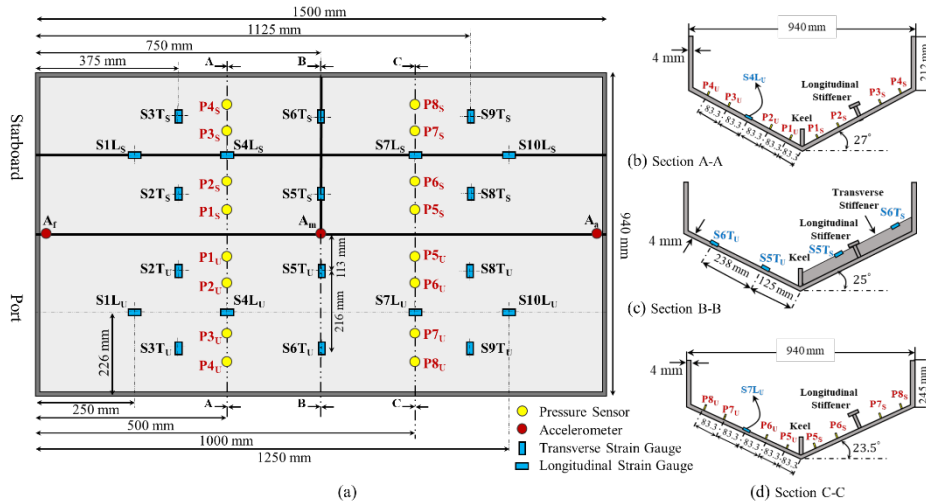


Figure 8. Sensor arrangement: (a) A top view of the wedge showing the distribution of pressure sensors, strain gauges, and accelerometers; (b) A-A cross section at  $\beta = 27^\circ$ ; (c) B-B cross section at  $\beta = 25^\circ$ ; (d) C-C cross section at  $\beta = 23.5^\circ$  [88,P2].

## 2.3 Experiments Procedure

The experimental procedure, as depicted in Figure 9, consisted of several essential steps. Firstly, the bottom plates of the wedge were prepared for sensor installation, ensuring a clean surface. All sensors were calibrated according to the manufacturer's guidelines. Prior to the tests, a thorough check of the test tower was conducted to identify any unexpected errors. The free-fall drop tests were performed at various heights, ranging from 25 cm to 200 cm, with increments of 25 cm. To determine the drop height, a laser level and measurement tape were used, referencing the calm water surface. Between test runs, specific steps were taken, including determining the drop height using a laser level, cleaning the bottom surface of the wedge, checking instrument cables and

reapplying petroleum jelly to the pressure sensors. The data recorder channels were reset, and a waiting period of 30–60 minutes was observed to allow the water surface to calm down before proceeding to the next test. These measures were implemented to maintain consistency, reliability, and accuracy throughout the experimental study.

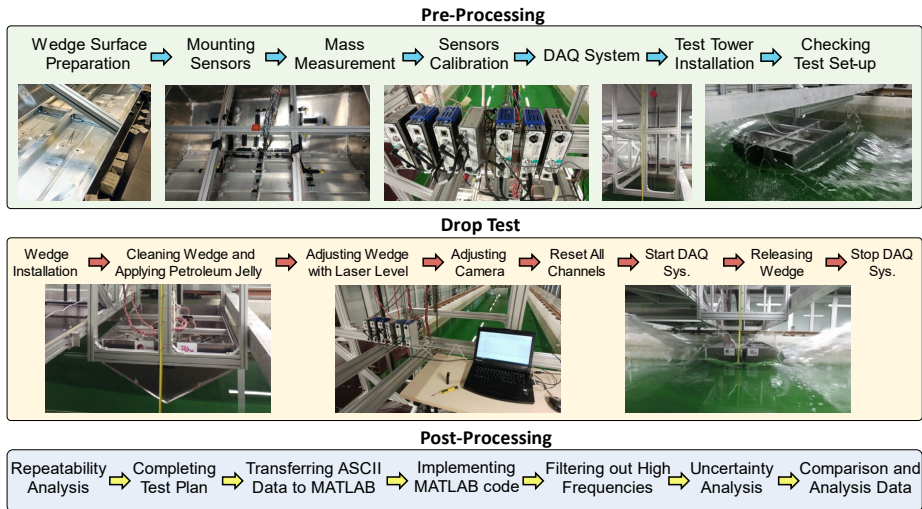


Figure 9. An overview and steps of the experimental studies.

To assess the reproducibility of the experimental measurements, multiple trials were conducted for each test case. The first test case at a drop height of 25 cm was repeated eighteen times, while the remaining cases were repeated at least twice. The time histories of acceleration, pressure, and strain from these runs were analysed to determine the experimental uncertainties. To mitigate high-frequency noise in the sensor data, a Butterworth low-pass filter was applied using MATLAB’s ‘filtfilt’ function that uses a zero-phase digital filtering technique [89,90]. The cut-off frequency for the filter was set at 1000 Hz for acceleration and pressure data, while a frequency of 500 Hz was chosen for strain gauge data.

The mean peak values of acceleration, pressure, and strain from the multiple experiments with a 25 cm drop height were calculated. The statistical uncertainty of the experiments was determined using standard deviation and relative standard deviation for all sensors. These uncertainties, along with other relevant data, can be found in [P2]. The repeatability of the measurements was also assessed across different impact velocities, revealing that the standard deviation tends to increase at higher velocities. This trend was observed consistently across all accelerometers, pressure sensors, and strain gauges.

### 3 Numerical Simulations

In numerical simulations of hydroelastic problems, also known as flexible fluid-structure interaction (FFSI), the main objective is to analyse the dynamic interactions between a fluid and a flexible structure, while considering their mutual influence. The hydroelastic simulations involve solving coupled equations that describe both the fluid flow and the structural deformation, allowing for a comprehensive understanding of the complex behaviour and responses of the flexible structure subjected to fluid loads. Regarding the coupling of solid and fluid variables, the strategies employed to address hydroelastic problems can be broadly categorized into two distinct approaches: the monolithic approach and the partitioned approach [91,92]. The monolithic algorithms involve formulating the governing equations for both the fluid and solid components together, allowing them to be solved simultaneously within a single solver. This approach treats the fluid and solid domains as a unified continuum, automatically considering the boundary conditions at the interface. The monolithic approach is known for its accuracy and stability, making it suitable for strong fully coupled simulations. However, due to the nonlinear nature of the coupling and the large number of unknowns involved, the solution process of the monolithic algorithm can be computationally expensive and time-consuming [91]. As a result, implementing the monolithic approach in practical problems can be challenging.

On the other hand, the partitioned approach involves solving the fluid and solid domains separately using different solvers, with data exchange at the interface. This method can be implemented in two ways: one-way coupling, where dynamic response is not considered, and two-way coupling, where continuous information exchange captures the dynamic behaviour of the structure. The one-way coupling method is employed when the fluid flow is minimally affected by the structural response. Typically, this occurs when the structure is sufficiently rigid, and its deformation does not significantly change the fluid dynamics. In contrast, two-way coupling becomes crucial when both the fluid and structural responses are significant for the dynamic behaviour of the system [93]. As demonstrated in Figure 10, depending on the nature of the FSI problem, the two-way coupling can be implemented through explicit coupling (weak) with a single force-displacement exchange per coupling time step, or through implicit coupling (strong) utilising iterative exchange with a relaxation function until convergence is reached for a given coupling step.

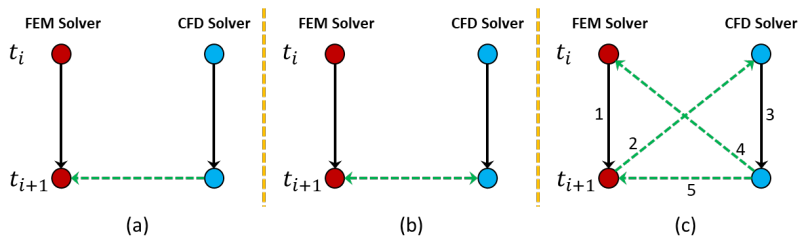


Figure 10. Different schemes of partitioned FSI coupling methods: (a) one-way coupling (explicit); (b) two-way coupling (explicit); (c) two-way coupling (implicit) (reproduced from [94]).

The partitioned approach offers advantages such as lower memory usage and easier implementation using existing codes. This method is often preferred in marine engineering applications due to extensive development, verification, validation, and focused research

dedicated to improving the solvers. However, sometimes the dynamic behaviour of force at the interface can result in instabilities and convergence issues (explicit partitioned), especially when the interaction between the fluid and solid is highly pronounced, and a small number of iterations per time step may be inadequate for correctly computing the interface properties [91].

In this section, the numerical approaches used to compute impact-induced loads and responses of a 3D non-prismatic aluminium wedge are presented. The wedge is modelled using two different coupling methods in free-fall conditions. Firstly, the FFSI problem is simulated using an explicit nonlinear FE scheme in LS-DYNA. The fluid domain, consisting of water and air, is modelled using a multi-material Eulerian formulation, while the deformations of the structure are described using the Lagrangian formulation. In the second approach, a two-way coupled FVM and FEM methods is employed to model the slamming phenomenon.

### 3.1 MMALE Coupling Method

The multi material ALE algorithm combines Lagrangian and Eulerian formulations in FEA to apply conservation equations. It utilises Lagrangian formulations to represent structural dynamics through the boundaries of a Eulerian mesh that forms the fluid domain. Details of the equations and mesh motion in the ALE method can be found in [95–99]. As shown in Figure 3, the FSI interface ( $\Gamma_{fsi}$ ) acts as a boundary between the fluid domain ( $\Omega_f$ ) and solid domain ( $\Omega_s$ ). At this interface, fluid pressure is transferred to the structure, and fluid nodal velocities are constrained to be equal to the structural nodal velocities. Velocity and stress normal components are continuous on both sides of the  $\Gamma_{fsi}$  boundary. To model the interaction between fluid and structure, a Euler-Lagrange penalty coupling method is utilised, combining the MMALE formulation and classical master-slave penalty contact method. This approach ensures momentum and energy conservation [98]. In the Euler-Lagrange coupling, the advection strategy is used to update velocity and history variables as the MMALE fluid flows across the mesh.

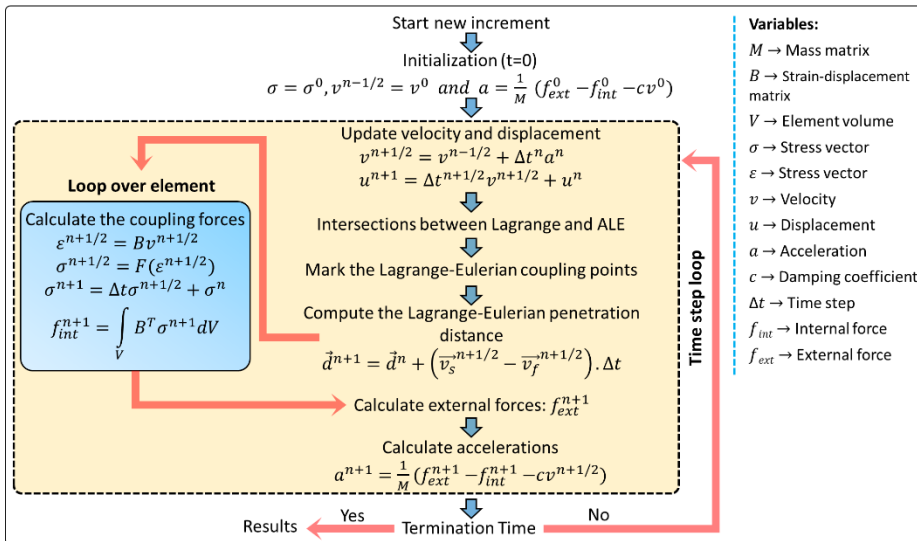


Figure 11. Schematic of explicit time integration algorithm in LS-DYNA [98,99].



Figure 11 illustrates a detailed description of the MMALE algorithm. In an explicit time integration algorithm, the coupling forces between fluid and structure nodes on the fluid-structure interface are computed after determining the nodal forces for both entities. At each time step, a depth penetration vector  $\vec{d}$  is iteratively updated for each structure node based on the relative velocity  $(\vec{v}_s - \vec{v}_f)$ , where  $\vec{v}_s$  represents the velocity of the slave node and  $\vec{v}_f$  denotes the fluid velocity at the location of the master node. The structure node is considered the slave node, while the master node belongs to the Eulerian element. By employing the isoperimetric coordinates of the fluid element, the position of the master node is calculated. The penetration vector  $\vec{d}^{n+1}$  is then updated at time  $t^n = t^{n-1} + \Delta t$ . It is important to note that the coupling force only comes into effect when penetration occurs ( $\vec{n}_s \cdot \vec{d}^n < 0$ ), where  $\vec{n}_s$  is obtained by averaging the normal of the structure elements connected to the structure node [99].

The experimental case discussed earlier is simulated numerically using the ALE method and penalty coupling algorithm. The numerical model, as shown in Figure 12, comprises the fluid domain (air and water) and the aluminium wedge. The wedge is modelled using the Lagrangian method with shell elements, except for the top support frame, which is assumed to have no deformations or rotations. The materials are defined as “Rigid” for the support frame and “Elastic” for the aluminium wedge. The top frame of the wedge is constrained in the horizontal directions, allowing only free-fall motion in the y-direction. An initial velocity ( $V_i$ ) corresponding to the impact velocity of the wedge during the experiments is applied in all simulations. For the fluid domain, solid hexahedral elements with one-point ALE multi-material formulation is used to model water and air. The Grüneisen equation of state (EOS) [99,100] is employed to simulate the behaviour of water. In addition, both gravity and water surface tension effects are considered in the simulations. A sufficiently fine mesh region in the impact area is used to minimize numerical issues and ensure accurate results. The results of a mesh sensitivity study are presented in [P3], which aimed to determine the optimal mesh size for precise simulations.

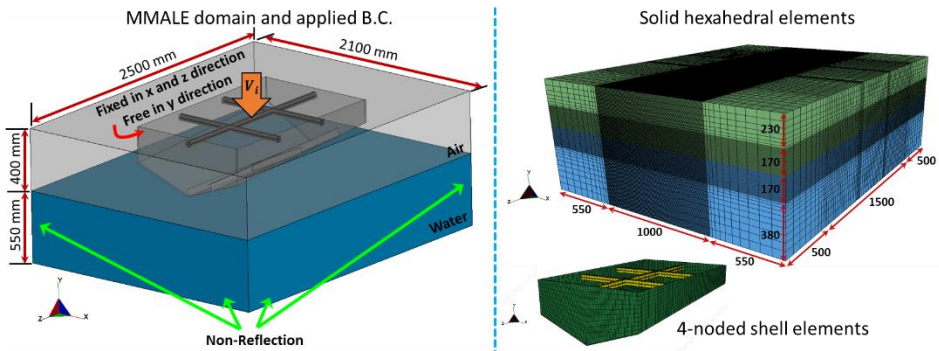


Figure 12. MMALE numerical domain and boundary conditions including mesh distribution in fluid region and shell structure (Unit: mm) [P3].

As already stated, a penalty coupling method was employed to model the coupling between a Lagrangian formulation (structure) and an ALE formulation (fluid). This method behaves like a spring system and the penalty forces are proportional to the penetration depth and spring stiffness. The choice of the penalty factor  $p_f$  ( $0 \leq p_f \leq 1$ ) is crucial for

impact problems, as it affects the allowed interpenetration at the contact interface. Increasing  $p_f$  reduces interpenetration but can lead to numerical instabilities due to frequent spring-damper interactions [24,98,101,102]. Conversely, insufficient penalty contact allows large non-physical penetrations, disrupting the flow field and causing leakage on the Lagrangian structure, particularly at high impact velocities [103]. To mitigate these issues, a viscous contact damping coefficient ( $\xi$ ) can be applied to the coupling algorithm to damp out the high-frequency oscillations. Hosseinzadeh et al. [104] conducted a comparative study on a 3D elastic wedge, finding that simulations with  $p_f = 0.02$  and  $\xi = 0.1$  exhibited fewer numerical instabilities (see Figure 13). Additionally, they discovered that an excessively large damping coefficient can lead to an unstable FSI coupling.

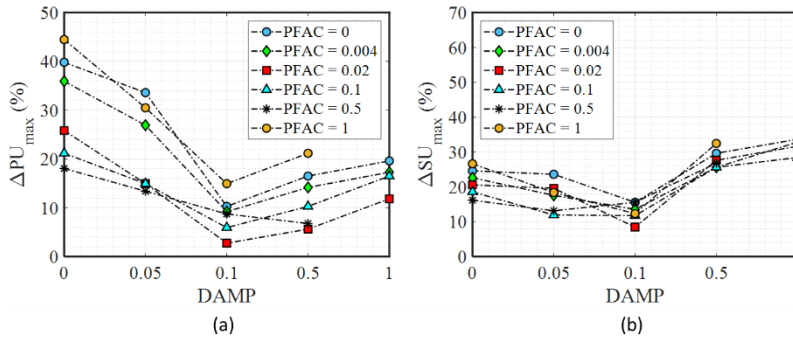


Figure 13. Effect of penalty factor (PFAC) and damping factor (DAMP) at 4.00 m/s impact velocity on the maximum value of (a) pressure on the unstiffened plate (b) strain response on the unstiffened plate [104].

### 3.2 CFD-FEM Coupling Method

To assess the efficiency and accuracy of numerical methods, the described FFSI problem is simulated using an implicit two-way coupling approach in addition to the ALE method. The CFD-FEM method is employed, where Star-CCM+ serves as the CFD solver for fluid flow and hydrodynamic pressure, while ABAQUS acts as the FEM solver for structural responses to slamming loads (see Figure 14). The Reynolds-averaged Navier-Stokes equations (RANS) and continuity equations are solved using a Finite Volume Method (FVM) with an implicit unsteady solver and a  $k-\epsilon$  turbulence model. The simulation includes both inviscid and viscous flow analyses to assess the impact of viscosity on load responses. The complex evolution of the free surface during impact is accurately captured using the volume-of-fluid (VOF) technique. The FVM and Semi-Implicit Method for Pressure-Linking Equations (SIMPLE) are employed to describe the fluid domain around the wedge during impact [105]. The wedge structure is modelled using shell elements in ABAQUS. The FEM solver utilises non-linear, dynamic, implicit analysis with the Hilber-Hughes-Taylor time integration method [106]. The simulation considers free-fall vertical translation, including gravity load and predefined initial impact velocity. The outer sides of the shell elements are designated as a coupled surface to facilitate the transfer of structural responses to the fluid domain in the co-simulation model.

As shown in Figure 14, in each time step, the CFD model calculates pressure load and shear stress, which are then applied as surface loads in the FE model. The computed

nodal displacement of the structure is transferred back to the fluid domain, allowing the fluid mesh to be updated using a mesh morphing technique based on the structure's deformation. The simulation utilises an implicit coupling scheme with a constant coupling time step matching the fluid solver time step. The co-simulation setup includes a minimum of twenty exchanges per time step and one inner iteration with an active morpher-solver. The choice of the FSI under-relaxation parameter ( $\beta_r$ ) and the number of inner iterations is crucial for achieving convergence. For problems requiring dynamic accuracy, choosing a low under-relaxation factor ( $\beta_r < 0.5$ ), as this might necessitate more iterations and longer computation time. Conversely, using a large  $\beta_r$  may affect the simulation's convergence and lead to an underestimation of pressure loads [105,107]. In this study,  $\beta_r$  is set to 0.6. To prevent numerical instabilities at the simulation's start, a pressure ramping parameter of [0, 004] is applied.

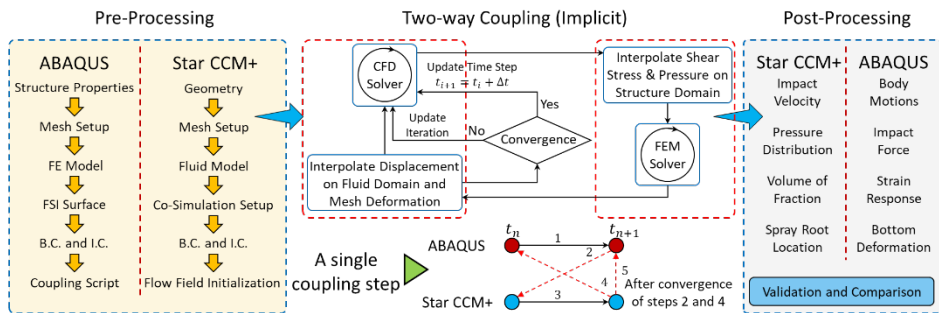


Figure 14. An overview of CFD-FEM FSI model including the two-way coupling flowchart and a single coupling step [P1, P3].

As depicted in Figure 15, a trimmed cell mesh is used to accurately simulate free surface problems. The overset mesh technique is employed to reduce computation time by establishing a smaller mesh near the structure's walls and free surface. The nodal values in both background and overset regions are linearly interpolated. The mesh morpher method is utilised to update the fluid mesh based on structural deformations by modifying boundaries and nodes according to the displacements from the FE solver. A preliminary assessment of the numerical model indicates the need for grid refinement in the fluid domain surrounding the structure to resolve the water volume distribution near the wedge surface. Consequently, several controls are applied to the overset region, including volumetric control around the wedge and surface control on the bottom of the wedge section. The FE solver models the wedge structure using a four-node shell element (S4R) with reduced integration to enable hourglass control and eliminate shear lock-in [106]. To determine the most accurate mesh for the present coupling method, a mesh convergence study was conducted and presented in [P3]. The study also examines the effect of viscosity on the wedge water entry problem. By comparing the results of turbulent flow and inviscid flow, it is observed that there is no significant difference in computed results between the two scenarios, allowing for the neglect of viscosity effects on impact-induced loads and responses [P3].

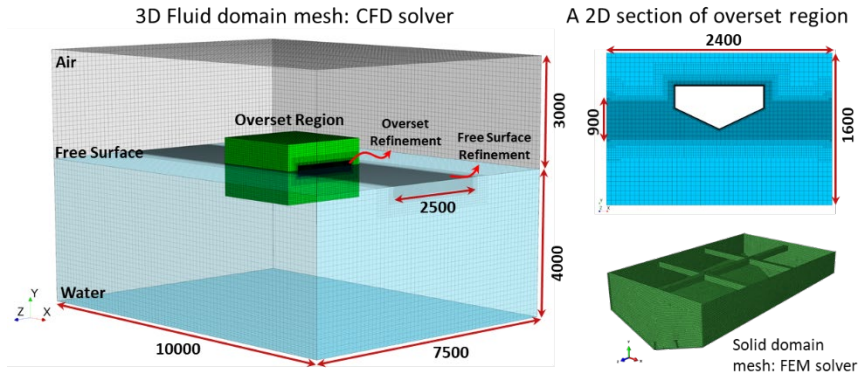


Figure 15. Mesh distribution in fluid and solid domains of CFD-FEM model (Unit: mm) [P3].

## 4 Results and Discussions

This section highlights the key findings of the thesis, focusing on the extensive investigation of various parameters on impact-induced loads and structural responses. Figure 16(a) presents a comparison between numerical results and experimental measurements [108–110] for a 2D wedge with a 20° deadrise angle and 25.4 cm drop height. The effect of impact velocity on the plate deflection is examined by comparing the outcomes of freefall impact with constant velocity simulations. The results demonstrate that employing a constant velocity may lead to an overprediction of the bottom deflection in the wedge [P1]. Furthermore, to assess the influence of structural rigidity, simulations were conducted on two wedges with a 10° deadrise angle and different materials (steel and aluminium). Figure 16(b) illustrates the bottom deflection from keel to chine, indicating a greater deflection in the aluminium wedge due to its higher flexibility [P1]. These findings provide valuable insights into the FFSI simulations of slamming problems and the relationship between parameters and bottom deflections in wedge structures.

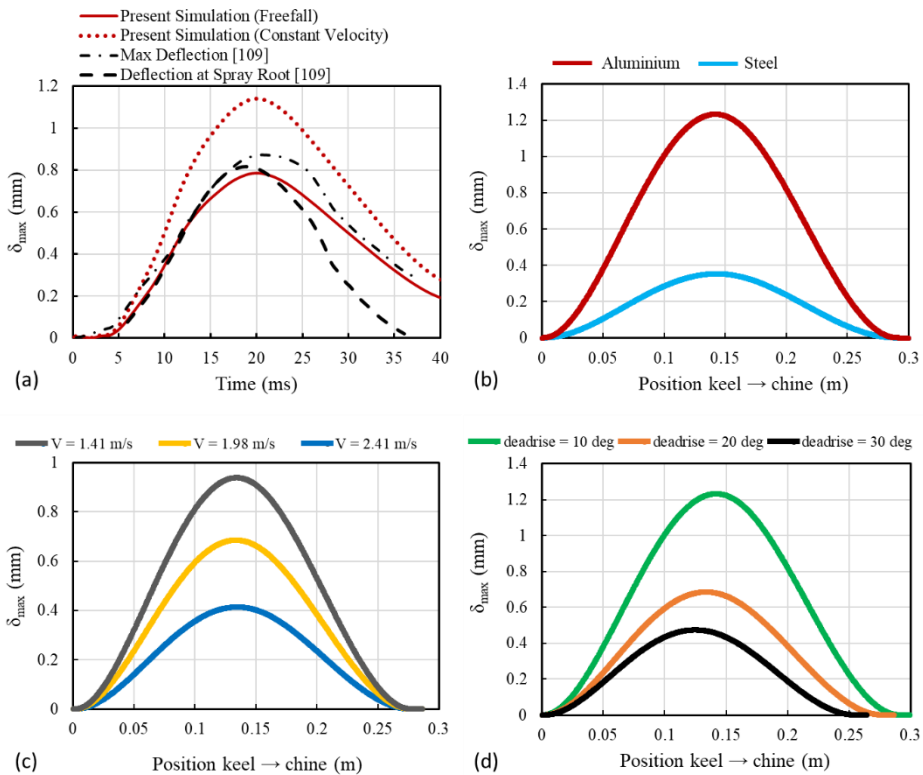


Figure 16. Computed results of 2D elastic wedge section: (a) effect of free-fall and constant velocity on the bottom deflection and its comparison with the experiment ( $\beta = 20^\circ$ ,  $h_0 = 25.4$  cm); (b) structural rigidity effect on bottom deflection ( $\beta = 10^\circ$ ,  $h_0 = 20$  cm); (c) effect of impact velocity on the bottom deflection of the aluminium wedge ( $\beta = 20^\circ$ ); (d) deadrise angle effects on the bottom deflection of the aluminium wedge ( $h_0 = 20$  cm) [P1].

In addition, the influence of different impact velocities and deadrise angles on the deflection of the bottom plate is investigated, with the results presented in Figure 16(c) and (d), respectively. The findings reveal that increasing the initial drop height leads to an increase in the maximum deflection. Moreover, the deflection of the plate is closely associated with the shape and magnitude of the pressure distribution [P1]. It is also observed that the wedge with a lower deadrise angle ( $\beta = 10^\circ$ ) exhibits the highest deflection due to the greater impact load [P1]. These observations indicate that the hydroelasticity effect becomes noticeable in cases where there is a small angle between the impacting surface and the structure.

In addition to the 2D wedge simulation, a 3D non-prismatic aluminium wedge section was also simulated using two different coupling methods, and the results were compared to the experimental data [P2, P3]. Figure 17 presents the experimental (left) and numerical (right) impacts of the case with an initial drop height of 100 cm at various time instants. The results demonstrate that the numerical method accurately captures the entire process of the water entry problem [P3]. Hence, numerical simulations serve as a valuable tool in examining the additional aspects of the slamming phenomenon that may not be observable through experimental studies.

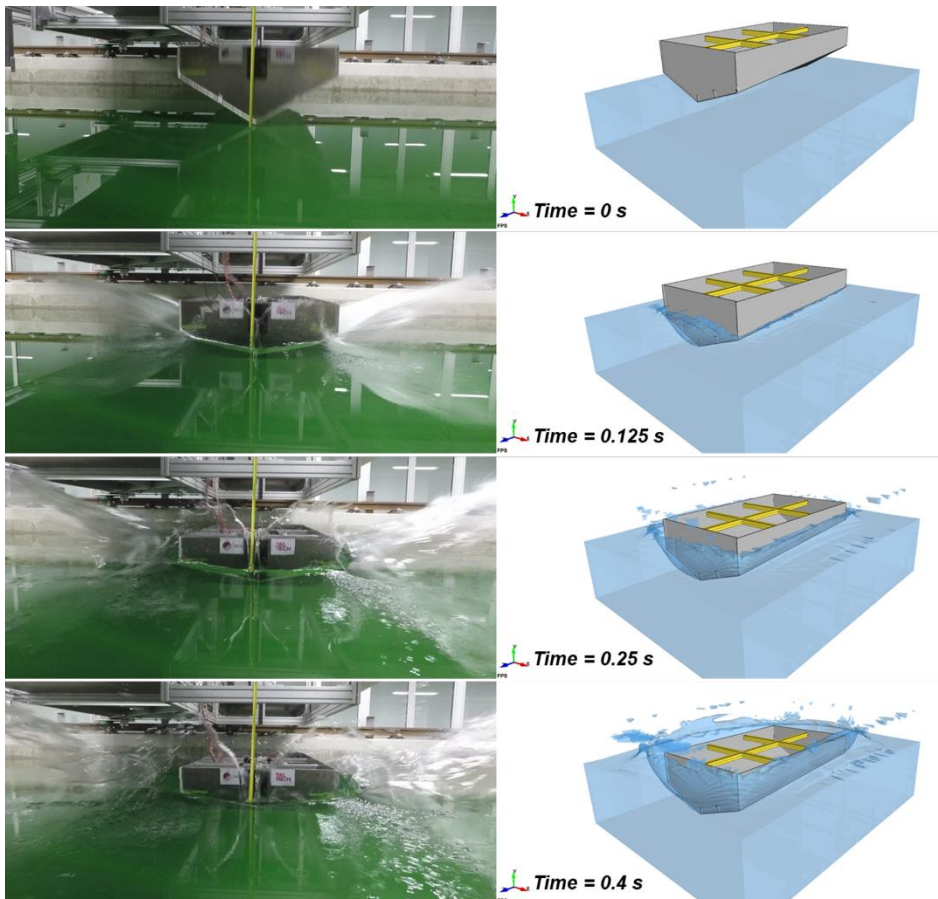


Figure 17. Comparison of experimental and numerical water entry of the wedge with 100 cm initial drop height at different time instants [P2, P3].

The effect of structural stiffness on the deflection of the bottom plates of the 3D wedge is investigated using two different FFSI numerical models. The distributions of the bottom deflection (ABAQUS) and pressure (Star CCM+) at the time instant of bottom maximum deflection are illustrated in Figure 18(a) and (b), respectively. In addition, Figure 18(c) compares the time histories of the maximum deflection on the unstiffened and stiffened bottom plates computed by MMALE and CFD/FEM two-way coupling methods for the case with 4.0 m/s initial impact velocity. As expected, the maximum deflection differs significantly between the stiffened and unstiffened plates and increases with higher impact velocity [P3]. It is shown that the maximum deflection on the unstiffened bottoms of the wedge is 2.774 mm, occurring at  $t = 0.018$ s of the simulation time, while the maximum deflection on the stiffened plate is 0.825 mm, happening at  $t = 0.012$ s. These findings emphasize that the outcomes of both numerical approaches are comparable and have the capability to predict the bottom deflection of the structure. In addition, a comparison of the maximum deflection on both stiffened and unstiffened plates is presented in Table 1, which is calculated using two different coupling techniques at various impact velocities. The discrepancies between the two numerical methods are also outlined in the table.

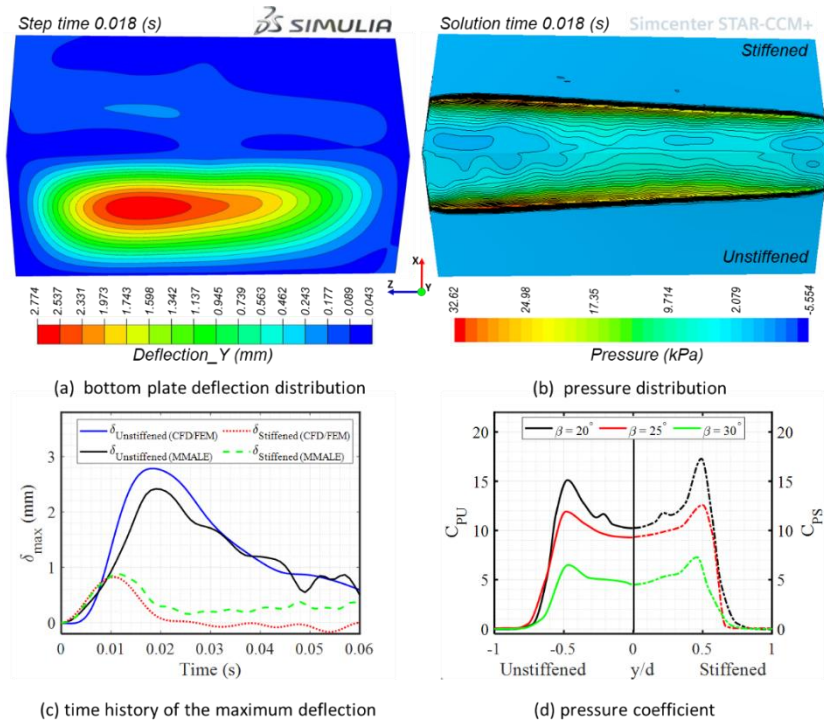


Figure 18. Numerical results of the case with 4.0 m/s initial impact velocity: (a) bottom deflection distribution; (b) pressure distribution on the bottom of the wedge; (c) comparison of maximum deflection on the unstiffened and stiffened bottom plates with two different coupling methods; (d) and pressure coefficient of stiffened and unstiffened bottom at 0.1 of wedge [P3].

Figure 18 (d) provides a comparison of pressure coefficient ( $C_p = P/0.5\rho V_i^2$ ) calculated on the stiffened ( $C_{PS}$ ) and unstiffened ( $C_{PU}$ ) bottom at different locations along the 3D wedge. This computation is performed at a time interval on the order of 0.005s,

corresponding to the moment when the spray root reaches 0.1 of the wedge wall length. These results display that the structural rigidity affects the pressure coefficients, particularly at lower deadrise angles ( $\beta = 20^\circ$ ).

*Table 1. The differences in maximum deflection calculated with two different coupling methods at various impact velocities [P3].*

$V_i$ (m/s)	Unstiffened plate ( $\delta_{max}$ )		Difference (%)	Stiffened plate ( $\delta_{max}$ )		Difference (%)
	[mm]			[mm]		
	MMALE	CFD-FEM	MMALE	CFD-FEM		
2.20	0.720	0.835	14.7	0.267	0.234	13.1
3.00	1.355	1.563	14.2	0.535	0.463	14.4
3.55	1.872	2.152	13.9	0.746	0.651	13.6
4.00	2.401	2.774	14.4	0.951	0.825	14.1

Based on experimental and numerical findings, it has been discovered that the choice of modelling the structure as either 2D or 3D can affect the results. Table 2 presents a comparison of numerical results of the maximum slamming force and coefficients between 2D and 3D wedges. The purpose of this comparative analysis is to examine the effect of dimensionality on the impact-induced loads. The results are compared using a non-dimensional maximum force coefficient  $C_{Fmax}$ , which is calculated as  $C_{Fmax} = F_{max}/0.5\rho V_i^2 L \tan \beta$ . It is shown that the value of  $C_{Fmax}$  decreases for both 2D and 3D models as the initial impact velocity increases. The findings indicate that, depending on the impact velocity and deadrise angle, the maximum slamming force predictions from the 3D calculations are between 10.31% and 27.61% lower than those from the 2D models where  $\Delta C_{Fmax} = (C_{Fmax2D} - C_{Fmax3D})/C_{Fmax2D}$ . Furthermore, the results highlight that as the impact velocities increase, the differences in the maximum force coefficient between the 2D and 3D models become more significant. These findings emphasize the importance of considering the three-dimensionality effect in slamming analysis, as it can lead to notable variations in the predicted slamming force.

*Table 2. A comparison of the numerical results of the maximum slamming force and coefficient between the 2D and 3D wedges at different impact velocities [P3].*

$V_i$ (m/s)	Deadrise (deg.)	$F_{2D}$ (N)	$C_{Fmax}$ (2D)	$F_{3D}$ (N)	$C_{Fmax}$ (3D)	$\Delta C_{Fmax}$ (%)
2.20	20	59.85	2.74	2750	2.10	23.42
	25	45.83	1.64	2139.5	1.32	19.79
	30	36.66	1.06	1826	0.95	10.31
3.00	20	108.49	2.65	4702.5	1.98	25.12
	25	85.08	1.62	4059	1.29	20.48
	30	68.29	1.05	3470.5	0.93	11.54
3.55	20	148.32	2.59	6380	1.92	25.97
	25	117.41	1.60	5555	1.26	21.14
	30	95.05	1.05	5043.5	0.91	12.93
4.00	20	192.49	2.58	8360	1.87	27.61
	25	143.66	1.50	6490	1.13	24.70
	30	123.19	1.04	6325	0.89	14.43



The time histories of pressure results and strain responses of all sensors were compared between numerical simulations and experimental data, and the differences were reported in [P3]. Figure 19 illustrates an example of the entire duration of transverse strain responses of two sensors that are located at different positions on the unstiffened plate of the wedge (Figure 8). The measured strain values are compared with the numerical results, demonstrating the capability of the numerical model to accurately simulate the structural response and post-impact behaviour. The time history of the strain response also highlights the influence of the deadrise angle, with sensors positioned in the section with a smaller deadrise angle (S8T<sub>U</sub>) exhibiting higher peak values. These findings provide valuable insights for further analysis of the structural responses in the frequency domain and can contribute to a more comprehensive understanding of the hydroelastic effect on the slamming impact.

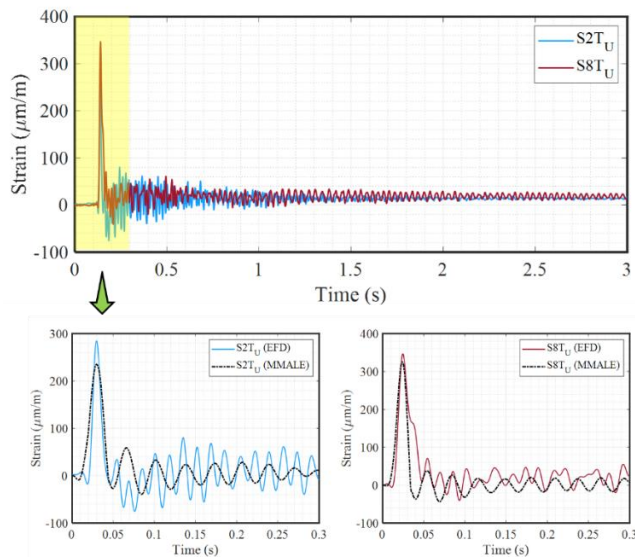


Figure 19. An example of strain response time history of the 3D wedge along with its comparison against numerical calculations at 100 cm initial drop height [P2, P3].

The research conducted by Faltinsen in [3] highlights the significant influence of various factors on hydroelastic slamming. These factors include the ratio between the wetting time (i.e., load period) and the first natural period of the structure, as well as parameters such as impact velocity and deadrise angle. The research findings indicated that when load periods exceed the natural period of a structure, it becomes possible to neglect certain hydroelastic effects [3]. As a result, in cases where these conditions are satisfied, it may be appropriate to simplify analysis using quasi-static or one-way coupling methods for modelling slamming problems. However, if these conditions are not met and there is a significant interaction between fluid and structure, a fully coupled FSI simulation becomes necessary. It should be noted that understanding how these various factors interact can contribute to the development of more precise theoretical models for predicting hydroelastic slamming phenomena.

In order to examine the effect of impact loads on the structural responses, an analysis was conducted to study the relationship between the natural frequency of the wedge and the impact time. This analysis was performed using fast Fourier transformation (FFT), allowing for a comprehensive understanding of the structural behaviour under different

impact conditions. Additionally, a comparison of the FFT analysis was made between the port and starboard sides of the wedge to account for their differing structural rigidities, as discussed in [P2]. Figure 20 presents the frequency distribution obtained from the sensors located on the unstiffened plate of the wedge. Through the frequency analysis of the strain responses, it is determined that the frequency of 30 Hz is the wet natural frequency of the structure, which remained consistent regardless of the increasing impact velocity. It is also observed that the frequency amplitude of S8T<sub>U</sub> is higher than that of S2T<sub>U</sub>. This difference can be attributed to the lower deadrise angle, which leads to higher impact loads in the section where S8T<sub>U</sub> is positioned.

The frequency distribution of the sensor S2T<sub>U</sub> obtained from numerical strain response is also compared with the corresponding experimental findings, as illustrated in Figure 20(c). The results indicate that while the first natural frequency can be accurately predicted through the numerical analysis using FFT, the accuracy decreases for the second and third frequencies. As already stated, the experimental study involved two wedges with different masses, and Figure 20(d) demonstrates the influence of wedge mass on the frequency distribution of strain responses. The analysis of the strain response time histories revealed that the mass of the wedge affects the natural frequency of the structure. Specifically, the natural frequency of the heavier wedge is found to be 22.5 Hz, which is lower than that of the lighter wedge. These findings confirm that the mass of the wedge plays a significant role in effecting both the frequency distribution and amplitude of the strain responses. An increase in the mass of the structure results in a noticeable decrease in its natural frequency.

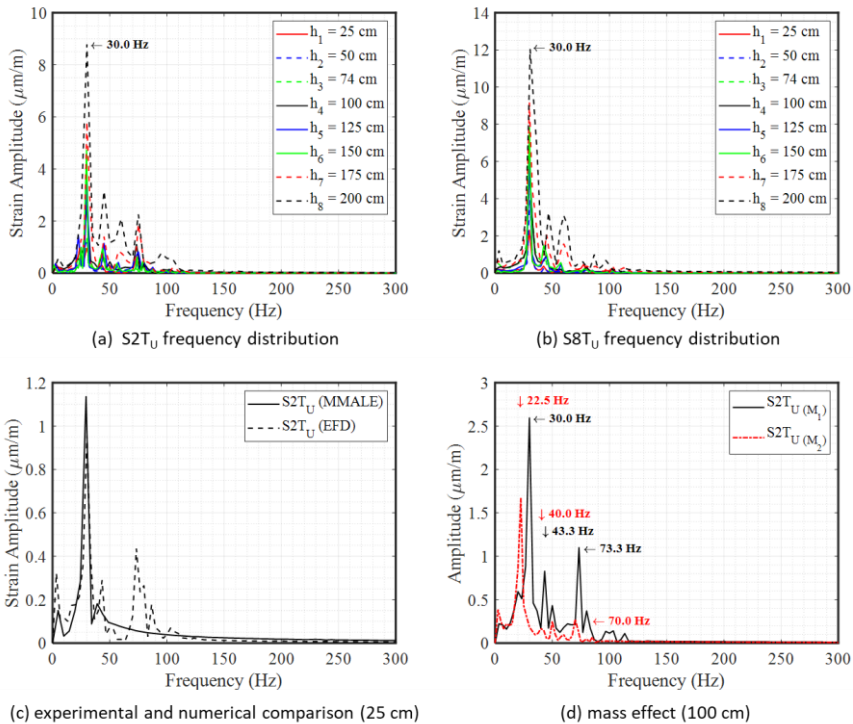


Figure 20. Frequency distribution of recorded strain responses on both unstiffened (U) and stiffened (S) bottom plates of the 3D wedge [P2, P3].

As a noteworthy outcome of this study, a valuable contribution is made by presenting a detailed guideline for conducting FSI simulations to predict the slamming loads and responses on ship structures. Table 3. provides an overview encompassing the computational resources employed and FSI models utilised with commercial software packages. By examining the different numerical models and coupling techniques used in this study, valuable insights can be gained into the factors that affect and contribute to the variability and uncertainty encountered in FSI simulations. Furthermore, it is highly recommended to undertake rigorous convergence studies to address any issues that may arise during FSI simulations. Particularly, conducting a trial-and-error analysis for penalty coupling factors is crucial in the MMALE method. Furthermore, in the case of the CFD-FEM two-way coupling method, it is crucial to carefully consider and investigate the coupling parameters, including the number of exchanges per time step, the number of inner iterations, and the FSI coupling under relaxation factor (URF). Moreover, using the adaptive refinement mesh technique, rather than the overset mesh method, can reduce the computational time in the CFD-FEM method. These practices ensure stability, consistency, and accurate outcomes in numerical computations by verifying solution independence from mesh refinement and determining suitable boundary conditions while minimizing potential uncertainties.

Table 3. A comparison of different numerical models employed in this thesis: features, advantages, and disadvantages [91, 97, 98, 111–113].

Software	Star CCM+	LS-DYNA	Star CCM+/ABAQUS
Version	13.06.012	R11.0.0	13.06.012/R2018
Structure	2D wedge	3D wedge	3D wedge
Computer feature	PC: 40 cores	PC: 40 cores	HPC: 40 cores
Formulation	CFD-FEM	ALE	CFD-FEM
Time integration	Explicit/Implicit	Explicit	Explicit/Implicit
Coupling method	FSI coupling (solid stress)	Penalty coupling	Co-simulation
Coupling scheme	Weak/Strong	Weak	Weak/Strong
Mesh technique	DFBI morphing	Mesh motion	Morphing mesh
Fluid domain	Hexahedral mesh	Hexahedral elements	Trimmed cell mesh
Solid domain	Solid elements	Shell elements	Shell elements
Time step	1.0E-4 s	5.0E-7 s	5.0E-5 s
Simulation time	0.05 s	0.05 s	0.05 s
Computation time	10 hrs for two-way coupling (implicit)	Single precision	SMP: 51 hrs MPP: 15 hrs
			92 hrs for two-way coupling (implicit)

- |           |  |
|-----------|--|
| Star CCM+ | <ul style="list-style-type: none"> <li>• Effortless pre-processing.</li> <li>• Integration of fluid and solid solvers within a single software package.</li> <li>• Utilization of adaptive mesh refinement (AMR) technique.</li> <li>• Implementation of adaptive time step for improved efficiency.</li> <li>• Straight forward convergence.</li> <li>• Customizable post-processing data.</li> </ul> |
| Pros      |  |
| LS-DYNA   | <ul style="list-style-type: none"> <li>• Convenient handling of coupling parameters.</li> <li>• Single software package implementation of coupling technique.</li> <li>• Independent mesh motion in the fluid and solid domains.</li> <li>• Avoid data transfer errors or inconsistencies between software.</li> <li>• Enhanced convergence and stability.</li> </ul>                                  |

Table 3. Continued.

Pros	Star CCM+/ ABAQUS	<ul style="list-style-type: none"> <li>• Flexible choice of coupling methods (one- and two-way).</li> <li>• Adaptive time step and mesh refinement to optimize simulations.</li> <li>• Can handle large-scale or complex FSI problems more efficiently.</li> <li>• Better accuracy and robustness for certain FSI problems.</li> <li>• User-controlled data transfer scheme between solvers.</li> <li>• Flexibility for user-defined post-processing.</li> </ul>
	Star CCM+	<ul style="list-style-type: none"> <li>• Limited applicability (2D or simple 3D structures).</li> <li>• Requires mesh refinement, particularly near the FSI interface.</li> <li>• Sensitivity to time step and number of inner iterations.</li> <li>• High computational time consumption.</li> </ul>
Cons	LS-DYNA	<ul style="list-style-type: none"> <li>• Reduced accuracy at high impact velocities</li> <li>• Trial and error analysis required for coupling factors.</li> <li>• Insufficient Lagrangian mesh refinement can lead to coupling failure.</li> <li>• Distorted shaped elements can cause instabilities and inaccuracies.</li> <li>• ALE method is both case- and parameter-specific.</li> <li>• Double precision improves accuracy but is extremely time-consuming.</li> <li>• High fluctuations in slamming pressure results require mitigation.</li> </ul>
	Star CCM+/ ABAQUS	<ul style="list-style-type: none"> <li>• Implementation of fluid and solid domains in different software.</li> <li>• Potential errors and inconsistencies in data transfer and interpolation.</li> <li>• Convergence and stability issues for some FSI problems.</li> <li>• High requirement for user input and expertise in setting up FSI interface.</li> <li>• High computational time consumption.</li> <li>• Sensitivity to mesh size, time step, data exchange, FSI under-relaxation parameter, and number of inner iterations.</li> </ul>

## 5 Conclusions

In this thesis, the dynamics of ship's bottom slamming have been comprehensively studied through a combination of experimental and numerical approaches. The study focused on examining the effects of hydroelasticity on the hydrodynamic pressure and structural response of both 2D and 3D flexible V-shaped structures. A series of systematic drop tests were performed on a non-prismatic aluminium wedge section, which resembles a fore body of semi-planing to planing vessels. These tests enabled the study of simultaneous structural responses induced by slamming loads and provided a high-quality dataset for hydroelastic slamming analysis. To assess the influence of flexural rigidity on the impact loads and responses, the wedge section was designed with both stiffened and unstiffened bottom plates. The experimental study extensively investigated the effects of three-dimensionality, impact velocity, deadrise angle, structural rigidity, and mass of the wedge on vertical acceleration, slamming pressure, and strain responses. The findings from experiments emphasised the importance of coupling analysis between fluid dynamics and structural response for accurately capturing the slamming phenomenon.

On the basis of experimental observations conducted in this study, a two-way coupling technique was implemented in the numerical simulations to model the water entry problem. This enables a more accurate prediction of the hydrodynamic pressures and structural behaviour, ultimately enhancing the understanding and analysis of slamming events in ship structures. The hydrodynamic loads acting on the wedge were effectively simulated using three different numerical methods, resulting in accurate capture of the corresponding structural responses. The observed slight variations in the maximum values of pressure and strain can be attributed to the different coupling techniques employed in the FFSI simulations. The characteristics, implementation challenges, as well as the advantages and disadvantages of each numerical method were discussed in detail.

This thesis provides an in-depth analysis of the various aspects of impact induced loads and responses. The following findings represent the most important conclusions that can be drawn from this study:

- As the impact velocity increases, the deflection of the bottom plate also increases. This highlights the importance of conducting a coupled FSI assessment.
- Hydroelasticity plays a significant role, influenced by factors such as deadrise angle, impact velocity, bending stiffness, and the first natural period of the structure. The impact of hydroelasticity is prominent in the unstiffened bottom at all impact velocities, while for the stiffened bottom, it becomes important primarily at high impact velocities and small deadrise angles.
- Stiffened bottom plates experience higher peak pressure compared to unstiffened bottom plates, and the pressure relaxation in the unstiffened bottom results in a delayed peak pressure, particularly evident at higher impact velocities and lower deadrise angles.
- The time history of strain responses exhibits two phases: maximum strain and elastic vibrations. During the partially wetted phase, bottom plates undergo significant strain and deformation, with more pronounced elastic vibrations observed in the unstiffened bottom at high impact velocities.

- Comparing 2D and 3D wedge sections, it was found that three-dimensional effects influenced slamming loads, with the 3D model predicting lower maximum force coefficients than the 2D model. Specifically, the 3D calculations showed approximately 10% to 14% lower maximum slamming force coefficients for a wedge with a deadrise angle of 30° and around 23% to 27% lower coefficients for a wedge with a deadrise angle of 20°.
- It was found that the numerical models employed in this study are highly dependent on the coupling parameters. In the MMALE method, the penalty factors play a significant role, while in the CFD-FEM method, the coupling setup, including data exchange and under-relaxation factor, is crucial. Furthermore, the study revealed that the effect of viscosity on pressure distribution and structural responses is negligible.
- Based on the numerical results, it was determined that the CFD-FEM method provides higher accuracy compared to the ALE method, although it does come at the cost of longer computational time. Moreover, it was noted that the accuracy of the ALE method decreases at high impact velocities.

The results of this thesis contribute to a deeper understanding of the hydroelastic nature of impact loads, which can have significant implications for the structural integrity of ships and high-speed marine vehicles. These findings provide valuable insights into the behaviour of ship structures during slamming events, emphasizing the importance of fluid-structure coupling, hydroelasticity, and three-dimensional effects in achieving accurate prediction and analysis. To further improve future numerical simulations, several modifications are suggested. For the CFD-FEM method, it is advisable to incorporate adaptive time step and mesh refinement to reduce computational time. Although utilising double precision in the ALE method increases computational time, it can enhance the accuracy and reliability of the results. Additionally, conducting an asymmetric analysis of hydroelastic slamming can provide a more realistic representation of the problem and examine the influence of heel angle on the results.

## References

- [1] Faltinsen, O. M. (1997). The effect of hydroelasticity on ship slamming. *Philosophical Transactions of the Royal Society of London. Series A: Mathematical, Physical and Engineering Sciences*, 355(1724), 575-591.
- [2] Kapsenberg, G. K. (2011). Slamming of ships: where are we now?. *Philosophical Transactions of the Royal Society A: Mathematical, Physical and Engineering Sciences*, 369(1947), 2892-2919.
- [3] Faltinsen, O. M. (2000). Hydroelastic slamming. *Journal of Marine Science and Technology*, 5, 49-65.
- [4] Kapsenberg, G. K. (2018). On the slamming of ships: Development of an approximate slamming prediction method. *Doctoral Thesis*.
- [5] Kim, J. H., Kim, Y., Yuck, R. H., & Lee, D. Y. (2015). Comparison of slamming and whipping loads by fully coupled hydroelastic analysis and experimental measurement. *Journal of Fluids and Structures*, 52, 145-165.
- [6] Lakshmyarayanan, P. A. K., & Hirdaris, S. (2020). Comparison of nonlinear one-and two-way FFSI methods for the prediction of the symmetric response of a containership in waves. *Ocean engineering*, 203, 107179.
- [7] Hirdaris, S., & Temarel, P. (2009). Hydroelasticity of ships: recent advances and future trends. *Proceedings of the Institution of Mechanical Engineers, Part M: Journal of Engineering for the Maritime Environment*, 223(3), 305-330.
- [8] Faltinsen, O. M. (2005). *Hydrodynamics of high-speed marine vehicles*. Cambridge university press.
- [9] Joint Accident Investigation Commission (JAIC). (1997). Final report on the capsizing on 28 September 1994 in the Baltic Sea of the Ro-ro passenger vessel MV Estonia. Helsinki: Edita Books.
- [10] Marine Accident Investigation Branch (MAIB). (2008). Report on the investigation of the structural failure of MSC Napoli English Channel on 18 January 2007. Southampton, United Kingdom.
- [11] Det Norske Veritas (DNV). (2007). MSC Napoli report load and strength assessment. In: 2007-1928; R. N.; Det Norske Veritas.
- [12] Bertram, V. (2011). *Practical Ship Hydrodynamics, Second Edition*. Pract. Sh. Hydrodyn. Second Ed., pp. 1-382.
- [13] Von Karman, T. (1929). The impact on seaplane floats during landing. National Advisory Committee for Aeronautics.
- [14] Wagner, H. (1932). The phenomena of impact and planing on water. National Advisory Committee for Aeronautics Translation 1366, ZAMM, 12, 193-215.
- [15] Zhao, R., & Faltinsen, O. (1993). Water entry of two-dimensional bodies. *Journal of fluid mechanics*, 246, 593-612.
- [16] Vorus, W. S. (1996). A flat cylinder theory for vessel impact and steady planing resistance. *Journal of ship research*, 40(02), 89-106.

- [17] Korobkin, A. (1996). Water impact problems in ship hydrodynamics. In *Advances in Fluid Mechanics* (pp. 323-371).
- [18] Korobkin, A. A., & Khabakhpasheva, T. I. (2006). Regular wave impact onto an elastic plate. *Journal of engineering mathematics*, 55, 127-150.
- [19] Mei, X., Liu, Y., & Yue, D. K. (1999). On the water impact of general two-dimensional sections. *Applied Ocean Research*, 21(1), 1-15.
- [20] Tassin, A., Jacques, N., Alaoui, A., Nême, A., & Leblé, B. (2010). Assessment and comparison of several analytical models of water impact. *The International Journal of Multiphysics*, 4(2), 125-140.
- [21] Korobkin, A. (2004). Analytical models of water impact. *European Journal of Applied Mathematics*, 15(6), 821-838.
- [22] Zhao, R., Faltinsen, O., & Aarsnes, J. (1996). Water entry of arbitrary two-dimensional sections with and without flow separation. In *Proceedings of the 21st symposium on naval hydrodynamics* (pp. 408-423).
- [23] Constantinescu, A., Alaoui, A. E. M., Nême, A., Jacques, N., & Rigo, P. (2011). Numerical and Experimental studies of simple geometries in slamming. *International Journal of Offshore and Polar Engineering*, 21(03).
- [24] Aquelet, N., Souli, M., & Olovsson, L. (2006). Euler–Lagrange coupling with damping effects: Application to slamming problems. *Computer methods in applied mechanics and engineering*, 195(1-3), 110-132.
- [25] Stenius, I. (2006). Finite element modelling of hydroelasticity in hull-water impacts (Doctoral dissertation, KTH).
- [26] Luo, H., Wang, S., & Soares, C. G. (2011). Numerical prediction of slamming loads on a rigid wedge subjected to water entry using an explicit finite element method. *Advances in marine structures*, 41-48.
- [27] Wang, S., & Soares, C. G. (2012). Analysis of the water impact of symmetric wedges with a multi-material Eulerian formulation. *International Journal of Maritime Engineering*, 154(A4).
- [28] Southall, N., Choi, S., Lee, Y., Hong, C., Hirdaris, S., & White, N. (2015). Impact analysis using CFD—a comparative study. In *ISOPE International Ocean and Polar Engineering Conference* (pp. ISOPE-I). ISOPE.
- [29] Izadi, M., Ghadimi, P., Fadavi, M., & Tavakoli, S. (2018). Numerical modeling of the freefall of two-dimensional wedge bodies into water surface. *Journal of the Brazilian Society of Mechanical Sciences and Engineering*, 40, 1-19.
- [30] Hosseinzadeh, S., Izadi, M., & Tabri, K. (2020). Free fall water entry of a two-dimensional asymmetric wedge in oblique slamming: a numerical study. In *International Conference on Offshore Mechanics and Arctic Engineering* (Vol. 84409, p. V008T08A013). American Society of Mechanical Engineers.
- [31] Lewis, EV. (1989). Principles of naval architecture. SNAME, 365.
- [32] Bishop, R. E., & Price, W. G. (1979). Hydroelasticity of ships. Cambridge University Press. vol. 15, no. 6, pp. 949-949.



- [33] Bishop, R. E., Price, W. G., & Wu, Y. (1986). A general linear hydroelasticity theory of floating structures moving in a seaway. *Philosophical Transactions of the Royal Society of London. Series A, Mathematical and Physical Sciences*, 316(1538), 375-426.
- [34] Hirdaris, S. E., & Chunhua, G. (2005). Review and introduction to hydroelasticity of ships. *Lloyd's Register*.
- [35] Wang, S., Karmakar, D., & Soares, C. G. (2016). Hydroelastic impact of a horizontal floating plate with forward speed. *Journal of Fluids and Structures*, 60, 97-113.
- [36] Shams, A., Zhao, S., & Porfiri, M. (2017). Hydroelastic slamming of flexible wedges: Modeling and experiments from water entry to exit. *Physics of Fluids*, 29(3).
- [37] Sun, Z., Korobkin, A., Sui, X. P., & Zhi, Z. (2021). A semi-analytical model of hydroelastic slamming. *Journal of Fluids and Structures*, 101, 103200.
- [38] Yu, Z., Amdahl, J., Greco, M., & Xu, H. (2019). Hydro-plastic response of beams and stiffened panels subjected to extreme water slamming at small impact angles, part II: Numerical verification and analysis. *Marine Structures*, 65, 114-133.
- [39] Lv, J., & Grenestedt, J. L. (2013). Some analytical results for the initial phase of bottom slamming. *Marine structures*, 34, 88-104.
- [40] Huera-Huarte, F. J., Jeon, D., & Gharib, M. (2011). Experimental investigation of water slamming loads on panels. *Ocean Engineering*, 38(11-12), 1347-1355.
- [41] Tenzer, M., Moctar, O. E., & Schellin, T. E. (2015). Experimental investigation of impact loads during water entry. *Ship Technology Research*, 62(1), 47-59.
- [42] Stenius, I., Rosén, A., Battley, M., & Allen, T. (2013). Experimental hydroelastic characterization of slamming loaded marine panels. *Ocean Engineering*, 74, 1-15.
- [43] Yan, F., Zhang, C., Sun, L., & Zhang, D. (2015). Experimental study on slamming pressure and hydroelastic vibration of a flat plate during water entry. *Journal of Coastal Research*, (73), 594-599.
- [44] Facci, A. L., Porfiri, M., & Ubertini, S. (2016). Three-dimensional water entry of a solid body: A computational study. *Journal of Fluids and Structures*, 66, 36-53.
- [45] Takami, T., Matsui, S., Oka, M., & Iijima, K. (2018). A numerical simulation method for predicting global and local hydroelastic response of a ship based on CFD and FEA coupling. *Marine Structures*, 59, 368-386.
- [46] Yan, D., Hosseinzadeh, S., Lakshmyanarayana, A., Mikkola, T., & Hirdaris, S. (2021). Comparative study on numerical hydroelastic analysis of impact-induced loads. In *Proceedings of the 23rd numerical towing tank symposium. NuTTs* (p. 6).
- [47] Tavakoli, S., Babanin, A. V., & Hirdaris, S. (2023). Hydroelastic Analysis of Hard Chine Sections Entering Water—Observations for Use in Preliminary Design Stage. *Journal of Offshore Mechanics and Arctic Engineering*, 145(5), 051901.
- [48] Tavakoli, S., Mikkola, T., & Hirdaris, S. (2023). A fluid–solid momentum exchange method for the prediction of hydroelastic responses of flexible water entry problems. *Journal of Fluid Mechanics*, 965, A19.

- [49] Faltinsen, O. M. (1999). Water entry of a wedge by hydroelastic orthotropic plate theory. *Journal of ship research*, 43(03), 180-193.
- [50] Bereznitski, A. (2001). Slamming: the role of hydroelasticity. *International Shipbuilding Progress*, 48(4), 333-351.
- [51] Korobkin, A., Gueret, R., & Malenica, Š. (2006). Hydroelastic coupling of beam finite element model with Wagner theory of water impact. *Journal of Fluids and Structures*, 22(4), 493-504.
- [52] Khabakhpasheva, T. I., & Korobkin, A. A. (2013). Elastic wedge impact onto a liquid surface: Wagner's solution and approximate models. *Journal of Fluids and Structures*, 36, 32-49.
- [53] Lv, J., & Grenestedt, J. L. (2015). Analytical study of the responses of bottom panels to slamming loads. *Ocean Engineering*, 94, 116-125.
- [54] Wang, S., & Guedes Soares, C. (2014). Numerical study on hydroelastic water entry of a wedge. In *Developments in maritime transportation and exploitation of sea resources* (pp. 199-208). London, UK: Francis & Taylor Group.
- [55] Aghaei, A., Schimmels, S., Schlurmann, T., & Hildebrandt, A. (2020). Numerical investigation of the effect of aeration and hydroelasticity on impact loading and structural response for elastic plates during water entry. *Ocean Engineering*, 201, 107098.
- [56] Stenius, I., Rosén, A., & Kutteneuler, J. (2011). Hydroelastic interaction in panel-water impacts of high-speed craft. *Ocean Engineering*, 38(2-3), 371-381.
- [57] Wang, S., & Soares, C. G. (2014). Numerical study on the water impact of 3D bodies by an explicit finite element method. *Ocean Engineering*, 78, 73-88.
- [58] Wang, S., & Guedes Soares, C. (2017). Review of ship slamming loads and responses. *Journal of Marine Science and Application*, 16, 427-445.
- [59] Yu, Z., Amdahl, J., Greco, M., & Xu, H. (2019). Hydro-plastic response of beams and stiffened panels subjected to extreme water slamming at small impact angles, Part I: An analytical solution. *Marine Structures*, 65, 53-74.
- [60] Truong, D. D., Jang, B. S., Ju, H. B., & Han, S. W. (2022). Prediction of slamming pressure considering fluid-structure interaction. Part I: numerical simulations. *Ships and Offshore Structures*, 17(1), 7-28.
- [61] Wang, S., Islam, H., & Soares, C. G. (2021). Uncertainty due to discretization on the ALE algorithm for predicting water slamming loads. *Marine Structures*, 80, 103086.
- [62] Piro, D. J., & Maki, K. J. (2013). Hydroelastic analysis of bodies that enter and exit water. *Journal of Fluids and Structures*, 37, 134-150.
- [63] Panciroli, R., Pagliaroli, T., & Minak, G. (2018). On air-cavity formation during water entry of flexible wedges. *Journal of Marine Science and Engineering*, 6(4), 155.
- [64] Maki, K. J., Lee, D., Troesch, A. W., & Vlahopoulos, N. (2011). Hydroelastic impact of a wedge-shaped body. *Ocean Engineering*, 38(4), 621-629.

- [65] Panciroli, R., Abrate, S., Minak, G., & Zucchelli, A. (2012). Hydroelasticity in water-entry problems: Comparison between experimental and SPH results. *Composite Structures*, 94(2), 532-539.
- [66] Feng, S., Zhang, G., Wan, D., Jiang, S., Sun, Z., & Zong, Z. (2021). On the treatment of hydroelastic slamming by coupling boundary element method and modal superposition method. *Applied Ocean Research*, 112, 102595.
- [67] Izadi, M., Ghadimi, P., Fadavi, M., & Tavakoli, S. (2018). Hydroelastic analysis of water impact of flexible asymmetric wedge with an oblique speed. *Meccanica*, 53, 2585-2617.
- [68] Truong, D. D., Jang, B. S., Janson, C. E., Ringsberg, J. W., Yamada, Y., Takamoto, K., ... & Ju, H. B. (2021). Benchmark study on slamming response of flat-stiffened plates considering fluid-structure interaction. *Marine Structures*, 79, 103040.
- [69] Yan, D., Mikkola, T., Kujala, P., & Hirdaris, S. (2022). Hydroelastic analysis of slamming induced impact on stiff and flexible structures by two-way CFD-FEA coupling. *Ships and Offshore Structures*, 1-13.
- [70] Yan, D., Mikkola, T., Lakshmyanarayanan, A., Tödter, S., Schellin, T. E., Neugebauer, J., ... & Hirdaris, S. (2022). A study into the FSI modelling of flat plate water entry and related uncertainties. *Marine Structures*, 86, 103296.
- [71] Hosseinzadeh, S., & Tabri, K. (2020). Numerical investigation of hydroelastic response of a three-dimensional deformable hydrofoil. In *HSMV 2020* (pp. 77-86). IOS Press.
- [72] Safehaven Marines Interceptor 48 Pilot Vessel. [Online]. Available: <http://www.safehavenmarineold.com/2012TURNSTONE.htm>.
- [73] French fishing vessel in the Irish Sea. [Online]. Available: [https://www.dailymail.co.uk/travel/travel\\_news/article-4701314/Terrifying-photos-ships-vicious-storms.html](https://www.dailymail.co.uk/travel/travel_news/article-4701314/Terrifying-photos-ships-vicious-storms.html).
- [74] The terrifying moment a cruise ship was slammed by giant Antarctic waves. [Online]. Available: <https://www.dailymail.co.uk/news/article-1337062/Cruise-ship-slammed-enormous-Antarctic-waves.html>.
- [75] Tveitnes, T., Fairlie-Clarke, A. C., & Varyani, K. (2008). An experimental investigation into the constant velocity water entry of wedge-shaped sections. *Ocean Engineering*, 35(14-15), 1463-1478.
- [76] Lewis, S. G., Hudson, D. A., Turnock, S. R., & Taunton, D. J. (2010). Impact of a free-falling wedge with water: synchronized visualization, pressure and acceleration measurements. *Fluid Dynamics Research*, 42(3), 035509.
- [77] Chuang, S. L. (1973). Slamming tests of three-dimensional models in calm water and waves. Naval Ship Research and Development Center Bethesda, MD, US Department of Commerce, National Technical Information Service, 10.
- [78] Aarsnes JV. (1994). An experimental investigation of the effect of structural elasticity on slamming loads and structural response. Technical Report, MARINTEK A/S.

- [79] Peseux, B., Gornet, L., & Donguy, B. (2005). Hydrodynamic impact: numerical and experimental investigations. *Journal of fluids and structures*, 21(3), 277-303.
- [80] Panciroli, R., Ubertini, S., Minak, G., & Jannelli, E. (2015). Experiments on the dynamics of flexible cylindrical shells impacting on a water surface. *Experimental Mechanics*, 55, 1537-1550.
- [81] Panciroli, R., Shams, A., & Porfiri, M. J. O. E. (2015). Experiments on the water entry of curved wedges: High speed imaging and particle image velocimetry. *Ocean Engineering*, 94, 213-222.
- [82] Panciroli, R., & Porfiri, M. (2015). Analysis of hydroelastic slamming through particle image velocimetry. *Journal of Sound and Vibration*, 347, 63-78.
- [83] Duan, L., Zhu, L., Chen, M., & Pedersen, P. T. (2020). Experimental study on the propagation characteristics of the slamming pressures. *Ocean Engineering*, 217, 107868.
- [84] Tödter, S., El Moctar, O., Neugebauer, J., & Schellin, T. E. (2020). Experimentally measured hydroelastic effects on impact-induced loads during flat water entry and related uncertainties. *Journal of Offshore Mechanics and Arctic Engineering*, 142(1), 011604.
- [85] Mai, T., Mai, C., Raby, A., & Greaves, D. M. (2020). Hydroelasticity effects on water-structure impacts. *Experiments in Fluids*, 61, 1-19.
- [86] Spinosa, E., & Iafrati, A. (2021). Experimental investigation of the fluid-structure interaction during the water impact of thin aluminium plates at high horizontal speed. *International Journal of Impact Engineering*, 147, 103673.
- [87] Meziane, B., Alaoui, A. E. M., Nême, A., Leble, B., & Bellanger, D. (2022). Experimental investigation of the influence of the panel stiffness on the behaviour of a wedge under slamming. *Journal of Fluids and Structures*, 114, 103702.
- [88] Hosseinzadeh, S., & Tabri, K. (2021). Free-fall water entry of a variable deadrise angle aluminium wedge: An experimental study. In *Developments in the Analysis and Design of Marine Structures: Proceedings of the 8th International Conference on Marine Structures (MARSTRUCT 2021, 7-9 June 2021, Trondheim, Norway)* (p. 29). CRC Press.
- [89] Mitra, S. K. (2011). *Digital signal processing: a computer-based approach* (Vol. 1221). New York, NY, USA: McGraw-Hill.
- [90] Swidan, A., Thomas, G., Ranmuthugala, D., Amin, W., Penesis, I., Allen, T., & Battley, M. (2016). Experimental drop test investigation into wetdeck slamming loads on a generic catamaran hullform. *Ocean Engineering*, 117, 143-153.
- [91] Bna, S. (2014). Multilevel domain decomposition algorithms for monolithic fluid-structure interaction problems with application to haemodynamics.
- [92] Aghaei, A. (2022). Numerical modelling of aeration and hydroelasticity in slamming loads and responses of marine structures. Doctoral Thesis.

- [93] Benra, F. K., Dohmen, H. J., Pei, J., Schuster, S., & Wan, B. (2011). A comparison of one-way and two-way coupling methods for numerical analysis of fluid-structure interactions. *Journal of applied mathematics*.
- [94] Oliveira, D., Santiago, A., & Rigueiro, C. (2016). Fluid structure interaction in offshore environment. In *Proc. 5th Int. Conf. on Integrity-Reliability-Failure, Porto (Portugal)*.
- [95] Benson, D. J. (1992). Computational methods in Lagrangian and Eulerian hydrocodes. *Computer methods in Applied mechanics and Engineering*, 99(2-3), 235-394.
- [96] Donea, J., Huerta, A., Ponthot, J. P., & Rodríguez-Ferran, A. (2004). Arbitrary Lagrangian–Eulerian Methods. *Encyclopedia of computational mechanics*.
- [97] Aquelet, N., & Souli, M. (2003). Damping effect in fluid-structure interaction: application to slamming problem. In *ASME pressure vessels and piping conference (Vol. 41553, pp. 175-184)*.
- [98] Souli, M. H., & Benson, D. J. (Eds.). (2013). *Arbitrary Lagrangian Eulerian and fluid-structure interaction: numerical simulation*. John Wiley & Sons.
- [99] LS-DYNA Theory Manual. (2022). Technology, Livermore Software, An Ansys Company.
- [100] Heuzé, O. (2012). General form of the Mie–Grüneisen equation of state. *Comptes Rendus Mécanique*, 340(10), 679-687.
- [101] Cheon, J. S., Jang, B. S., Yim, K. H., Lee, H. D., Koo, B. Y., & Ju, H. (2016). A study on slamming pressure on a flat stiffened plate considering fluid–structure interaction. *Journal of Marine Science and Technology*, 21, 309-324.
- [102] Ladeira Napoleao de Souza, I. J. (2019). *Simulation of Slamming on a Fiber Reinforced Composite Structure Using the ALE/Eulerian Numerical Approach*. Master Thesis.
- [103] Stenius, I., Rosén, A., & Kuttenkeuler, J. (2006). Explicit FE-modelling of fluid–structure interaction in hull–water impacts. *International Shipbuilding Progress*, 53(2), 103-121.
- [104] Hosseinzadeh, S., Topa, A., & Tabri, K. (2023). A Numerical Sensitivity Analysis of Fluid-Structure Interaction Simulations on Slamming Loads and Responses. In *IOP Conference Series: Materials Science and Engineering (Vol. 1288, No. 1, p. 012017)*. IOP Publishing.
- [105] STAR-CCM+. (2020). *STAR-CCM+ Version 15.06 Manual*.
- [106] D. Systèmes. (2016). *Abaqus Analysis User’s Guide Volume IV: Elements*. Dassault Systèmes Simulia Corp.: Providence, RI, USA.
- [107] Causin, P., Gerbeau, J. F., & Nobile, F. (2005). Added-mass effect in the design of partitioned algorithms for fluid–structure problems. *Computer methods in applied mechanics and engineering*, 194(42-44), 4506-4527.
- [108] Ren, Z., Wang, Z., Stern, F., Judge, C., & Ikeda-Gilbert, C. (2019). Vertical water entry of a flexible wedge into calm water: A fluid-structure interaction experiment. *Journal of ship research*, 63(01), 41-55.

- [109] Javaherian, M. J., Ren, Z., & Gilbert, C. M. (2019). Flow visualization, hydrodynamics, and structural response of a flexible wedge in water entry experiments. In SNAME Maritime Convention (p. D033S004R008). SNAME.
- [110] Ren, Z., Javaherian, M. J., & Gilbert, C. M. (2021). Kinematic and inertial hydroelastic effects caused by vertical slamming of a flexible V-shaped wedge. *Journal of Fluids and Structures*, 103, 103257.
- [111] Hosseinzadeh, S., & Tabri, K. (2021). Hydroelastic effects of slamming impact loads during free-fall water entry. *Ships and Offshore Structures*, 16(sup1), 68-84.
- [112] Hosseinzadeh, S., Tabri, K., Hirdaris, S., & Sahk, T. (2023). Slamming loads and responses on a non-prismatic stiffened aluminium wedge: Part I. Experimental study. *Ocean Engineering*, 279, 114510.
- [113] Hosseinzadeh, S., Tabri, K., Topa, A., & Hirdaris, S. (2023). Slamming loads and responses on a non-prismatic stiffened aluminium wedge: Part II. Numerical simulations. *Ocean Engineering*, 279, 114309.



## Appendix 1 (Publication I)

**[P1]** Hosseinzadeh, S., & Tabri, K. (2021). Hydroelastic effects of slamming impact loads during free-fall water entry. *Ships and Offshore Structures*, 16(sup1), 68-84.







# Hydroelastic effects of slamming impact Loads During free-Fall water entry

Saeed Hosseinzadeh  and Kristjan Tabri 

School of Engineering, Department of Civil Engineering and Architecture, Tallinn University of Technology, Tallinn, Estonia

## ABSTRACT

This paper examines the hydroelastic problems of a two-dimensional symmetric flexible wedge water entry through free-fall motion. Water entry is numerically investigated by coupled Finite Volume Method and Finite Element Method using a strong two-way coupling approach. The emphasis of this study is on numerical approach and the paper provides an accurate two-way FSI coupling method for the water entry of two-dimensional symmetric elastic wedge section in different conditions. The effect of freefall velocity is investigated by comparing the constant velocity and freefall impacts. It is shown that the bottom deflection is overestimated by using the constant velocity. In order to evaluate the accuracy of the numerical model, the numerical results are compared and validated against published experimental data and favourable agreement is reported. The vertical position, impact velocity, acceleration, pressure distribution, and deflection along the bottom plate of the elastic wedge are evaluated and compared to experimental data. For better understanding of the hydroelastic slamming, the results are presented for different deadrise angles and vertical velocities. The relation between the structural deflection and vertical velocity, deadrise angle, and pressure distribution is investigated. It is observed that the significance of hydroelasticity increases with decreasing deadrise angle and increasing impact velocity.

## ARTICLE HISTORY

Received 29 October 2020  
Accepted 1 July 2021

## KEYWORDS

Fluid–Structure Interaction;  
Free-fall Water Entry; Flexible  
Wedge; Hydroelastic  
Slamming

## 1. Introduction

In recent decades, due to the importance of the effect of slamming loads on the marine structures, many studies have been conducted on water entry problems. The phenomenon of slamming is a complex problem of air–water–structure coupling, and it is simplified by many researchers to a two-dimensional rigid body impact. However, it may not always be accurate to make this assumption. When the duration of the impact loads is much shorter than the natural period of the structure, the phenomenon is referred to as hydroelastic slamming and it affects the ship structures, the performance of the vessels and the crew on board. Such loads of short duration stimulate the dynamic response of the ship structures and initiate vibratory response and fatigue problems. In turn, the hydrodynamic load itself is also affected by the structural response. The impact loading causes the wedge to deflect, which influences the fluid flow and the instantaneous pressure loading on the structure. This dependency makes the flexible wedge water entry problems a challenging task for a numerical assessment.

Solving the water entry problem provides structural loads for marine structures (Faltinsen 2001), and it can be used for evaluating the dynamic motions of planing hulls by extending the 2-D sectional forces in longitudinal direction (Akers 2014; Hosseinzadeh et al. 2018). Comprehensive literature review for wedge water entry phenomena and hull slamming is made by Abrate (2013). Hirdaris et al. (2014) presented an extensive overview of the methods for impact loads and hydroelasticity in the design of ships and offshore structures. Numerous studies have attempted to explain the fluid dynamics phenomena and hydrodynamic impact around a symmetric wedge at constant vertical velocity. Zhao et al. (1996) investigated vertical water entry of a symmetric wedge and used an approximate solution without considering flow separation. Judge et al. (2004) studied asymmetric wedge-impact flows at vertical and oblique angles with horizontal as well as vertical impact velocity and found good agreement between

the experimental data and the numerical predictions. Southall et al. (2014) predicted impact loads using OpenFOAM and compared the results with the experiment data of WILS wedge test cases. They calculated the time history of the impact pressure and forces of 2D wedges for different deadrise angles and tilt angles and concluded that the presented CFD method is a suitable tool for the prediction of slamming pressures and loads. In addition, a review of the capabilities of CFD to predict the impact of a rigid wedge-shaped body on the water surface can be found in Southall et al. (2015). Bilandi et al. (2018) simulated a finite volume method (FVM) for the two-dimensional symmetrical and asymmetrical wedges entering calm water at constant vertical velocity. To find more realistic and applicable results, the free-fall condition for water entry problems is considered by many researchers. The water entry problem of a wedge through free-fall in three degrees of freedom was studied through the velocity potential theory for the incompressible fluid by Xu et al. (2010). Izadi et al. (2018b) investigated a numerical simulation pattern based on FVM approach for the free-fall of two-dimensional rigid wedges in different deadrise angles. Furthermore, the hydrodynamic problem of oblique water entry of an asymmetrical wedge was analysed by Hosseinzadeh et al. (2020) and concluded that the heel angle dramatically affects the wedge dynamics, pile-up evolution, and pressure distribution.

While the water entry problems of rigid bodies have been widely studied and there are some analytical solutions capable to predict the slamming loads, the effect of deformation of the flexible structures on the hydrodynamic pressure is still a complicated problem and needs more studies. Faltinsen (1997) and Faltinsen et al. (1997) carried out two major works, which analysed the interaction of the fluid and the structure during water impact. Theoretical and experimental drop tests of the horizontal elastic plates were reviewed by Faltinsen (2001). Berezniński (2001) developed various numerical

codes which calculated potential velocity around the wedge for consideration of the effects of elasticity on slamming phenomena and noted that the ratio of the duration of the water impact to the natural frequency of the structure is the most important factor to be considered in the computations. Later, Stenius et al. (2007) solved Fluid–Structure Interaction (FSI) during the water entry impact by developing one of Berezinski (2001) codes. Korobkin and Khabkhpasheva (2006) solved the hydroelastic problem of water impact of the wedge section bodies by using one-way coupling between the Wagner solution and Finite Element Method (FEM). Maki et al. (2011) studied the constant-velocity impact of an elastic wedge-shaped body using a one-way-coupled simulation method. Panciroli (2012) investigated the slamming phenomenon experienced during the water entry of deformable bodies by experimental and numerical methods. Moreover, the water impact of deformable wedges was experimentally and numerically investigated by Panciroli et al. (2013) and suggested that the occurrence of hydroelasticity depends on the ratio between the natural frequency of the structure and the characteristic wetting time. Wagner solution and the Euler beam theory were used by Shams and Porfiri (2015) to find the structural response of the wedge entering water. Mesa and Maki (2017) established a coupled fluid–structure interaction algorithm for a flat plate entering water with high horizontal velocity. The hydroelastic impact of asymmetric and symmetric 2D wedge sections with constant vertical velocity into calm water were numerically studied by Izadi et al. (2018a). Ren et al. (2019) investigated the dynamic structural response of the bottom plate of a wedge both experimentally and computationally. They used a one-way coupling approach for predicting the deflection of the plate and found a slightly higher prediction for deflection. Their experimental studies further developed to different drop heights by Javaherian et al. (2019). As a recent experiment, Tödter et al. (2019) experimentally measured hydroelastic effects on impact-induced loads acting on flat bottom ship structures and investigated the hydroelasticity of the flexible flat plate by studying the time histories of pressures, forces, and deformations. Although water entry problems have received much attention in the past decades with a focus mainly on 2D rigid bodies, ship slamming still requires further investigation in regard to structural deformation and elasticity effects. Besides, the effects of the vertical velocity, deadrise angle and structural elasticity on the hydroelastic slamming are not fully understood.

In the current study, the hydroelastic slamming of a two-dimensional symmetric flexible wedge through free-fall motion is investigated computationally. The aim of the paper is to examine the hydroelastic effect of a deformable wedge section by implementing an accurate numerical model. In addition, a parametric study is conducted to identify the influence of different parameters on pressure distribution and structural response. This paper presents the kinematics results of the wedge, hydrodynamic loading, free surface elevation, and the structural response of the bottom plate. In order to achieve near-realistic results, the physically admissible vertical velocity is considered during the simulation. The governing fluid dynamic equations are solved using Finite Volume Method (FVM) with overset mesh technique, while the fluid is assumed to be viscous. For the structural domain, the FEM scheme is utilised. This fluid–structure interaction problem is simulated under two-way fully coupled assumptions and the implicit unsteady solver is employed for both fluid and structure domain. The obtained results are compared against analytical solution and previous experimental data for validation and verification of the simulations. Main results of the current study are presented in various drop heights and deadrise angles to analyse the effect of hydroelasticity. The vertical acceleration, bottom plate deflection, and pressure coefficients

are compared in different conditions. In addition, the free surface elevation around the wedge wall and time history of the pressure and strain at the midpoint of the wedge are computed.

## 2. Problem description

In this paper, a two-dimensional symmetric flexible wedge with a width of  $B$  and deadrise angle of  $\beta$  is assumed. The schematic of the problem is illustrated in Figure 1. It is considered that the wedge can freely fall into the water, while its angular and horizontal motions are confined. The initial vertical velocity of the wedge is assumed to be zero and the impact velocity is defined via the drop height. Before the water impact, the wedge is free of any deflections. Once the wedge touches the calm water surface, the hydrodynamic pressure develops over the wedge resulting in the deflection on the bottom plate.

The deflection of the bottom plate is denoted as  $\delta$  and it is considered positive when the plate is deflected towards interior of the wedge. The same pressure distribution and deformation patterns are assumed for both sides of the wedge. see Figure 2. It is obvious that the bottom deflection will lead to the variation of pressure in comparison with a rigid wedge.

### 2.1. Fluid domain

As shown in Figure 1, the fluid domain consists of the air and water, separated by the free surface. The fluid is assumed to be laminar and incompressible. The continuity equation and the Navier-Stokes's equation can be written in differential form as

$$\nabla \cdot v = 0 \quad (1)$$

$$\frac{D(\rho v)}{Dt} = -\nabla p + \nabla \cdot (\mu v) + \rho g \quad (2)$$

where  $v$  is the fluid velocity vector,  $\rho$  the fluid density,  $\mu$  the fluid viscosity,  $p$  the fluid pressure, and  $g$  the acceleration due to gravity. The nature of hydroelastic free-surface phenomena requires the solution of the free-surface position. The water entry problem has a complex evolution of the free surface during the impact stage. In order to achieve an accurate solution for the nonlinear and complex free surface, the volume-of-fluid (VoF) interface-capturing technique is used. The density ( $\rho$ ) at each cell is computed by Equation (3) and the kinematic viscosity ( $\mu$ ) is found by Equation (4):

$$\rho = \alpha \rho_w + (1 - \alpha) \rho_a \quad (3)$$

$$\mu = \alpha \mu_w + (1 - \alpha) \mu_a \quad (4)$$

where  $w$  and  $a$  subscripts are for water and air, respectively. The volume fraction of the fluid is  $\alpha$  and the governing equation on  $\alpha$  is:

$$\frac{\partial \alpha}{\partial t} + \nabla \cdot (\alpha v) = 0 \quad (5)$$

The FVM and Semi-Implicit Method for Pressure-Linking Equations (SIMPLE) are used to study the fluid domain around the wedge during the impact. Additionally, the volume fraction of the fluid  $\alpha$  is solved by VoF approach by using the High-Resolution Interface Capturing (HRIC) scheme (Star CCM+ 2019).

### 2.2. Structural domain

The structural part of the problem is solved using the finite element method. The bottom panel is considered as an Euler–Bernoulli beam subjected to the slamming load  $q(x,t)$  which moves from one end to the another. The deflection of the beam is  $\delta(x,t)$ ,

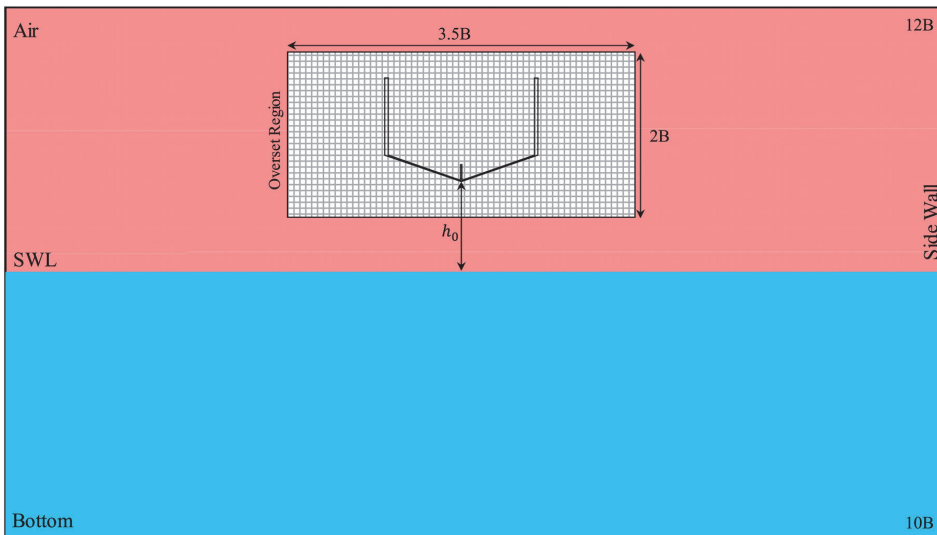


**Figure 1.** Problem domain and boundary condition of the numerical model with overset region and initial drop height in 20° derdrise angle. (This figure is available in colour online.)

where  $x(0 < x < L)$  is the position within the beam,  $t$  is time and  $L$  is the length of the beam from keel to chine. To define the governing equation, deflections are assumed to be small, the wedge material is homogeneous, and the wedge plate cross-section is constant along its bottom. Neglecting the rotations and using the Euler–Bernoulli beam assumptions the governing equation on the wedge structure is

$$EI \frac{\partial^4 \delta(x, t)}{\partial x^4} + \mu^* \frac{\partial^2 \delta(x, t)}{\partial t^2} = q(x, t) \tag{6}$$

where  $EI$  is bending stiffness (assumed constant) and  $\mu^*$  is total mass per unit length of the beam. The dynamic behaviour of the wedge’s flexible bottom is described via displacement field  $\mathbf{u}$  and its time derivatives as

$$M\ddot{\mathbf{u}} + K\dot{\mathbf{u}} + C\mathbf{u} = \mathbf{q} \tag{7}$$

where  $M$ ,  $K$ , and  $C$  are the structural mass, damping, and stiffness  $n \times n$  matrix, respectively. The structural problem is solved by using finite element method.

### 2.3. Coupling method

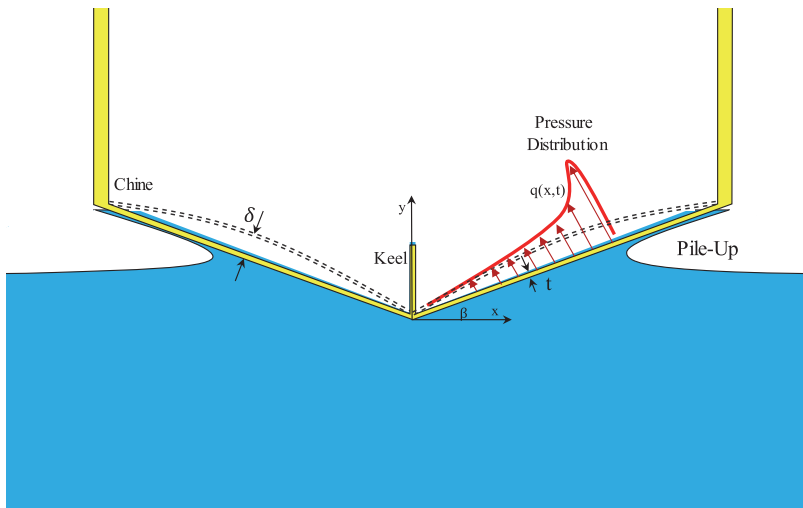
To solve the fluid-structure problems (FSI), different types of coupling methods can be used between fluid and structural domain. Due to the dependency between the hydrodynamic forces and the structural response, the one-way or two-way coupling method can be employed. According to previous studies, results from the two-way coupling method are more accurate and promising than results from the one-way coupling (Benra et al. 2011; Lakshmyraranana and Hirdaris 2020). Moreover, as the slamming problem is under short-term dynamic load and to obtain an applicable solution, the strongly two-way coupling method is used in this study. As shown in Figure 3, the FSI boundary is adopted on the walls of the structure. Numerically computed values of the fluid vector are set to be at the rate of deformations of the wedge at each instant. The idea is to use a coupled equation that uses the pressure in the fluid domain  $p$ , and the structural displacements  $\mathbf{u}$ , as the working variables. Accordingly, a partitioned solution scheme with implicit coupling is employed.

Figure 4 provides an overview of the algorithm used for the numerical computations. The algorithm explains the two-way coupling scheme employed for the FSI co-simulation. The simulations are run from the STAR CCM+ (STAR-CCM+ 2019) environment, which includes the FVM and FEM analysis in its solver process. Lakshmyraranana and Hirdaris (2020) explained the differences between one-way and two-way coupling methods. There are different coupling algorithms, and for loosely coupled problems, it is adequate to update the fields between each time step, which is known as explicit coupling. It is necessary to update the fields at each iteration for strongly coupled problems, which is called implicit coupling. In the present study, the implicit coupling approach is implemented in the two-way coupling scheme, which uses the fixed-point iterative method with under-relaxation to accelerate the convergence. As illustrated in Figure 4, after the pre-processing step, the fluid solver creates the initial field variables and maps the pressure loading to the contacting surface of the wedge structure. The implicit unsteady solver and the segregated flow solver are employed to solve the discretised set of governing equations. After applying the hydrodynamic loads on the structure, the finite element structural solver calculates the dynamic structural response directly in the time domain employing the second-order Newmark method. The structural solver updates the nodal displacements, which are obtained using a sparse direct matrix solver algorithm, MUMPS (STAR-CCM+ 2019). The mesh morphing solver is applied to transform the structure displacements to the fluid domain, after which the overset mesh is updated. The process is continued to reach either the convergence criterion or the maximum number of iterations, after which the algorithm advances to the next time step.

## 3. Numerical modelling

### 3.1. Problem setup

The hydroelastic wedge entering water constitutes a transient problem with large deformations relative to the thickness of the bottom plate. Therefore, a fully coupled method with free-fall motion is considered for analysing the flexible wedge. In the current study,



**Figure 2.** A schematic water entry problem of a two-dimensional symmetric flexible wedge with the deflection ( $\delta$ ) on the bottom. (This figure is available in colour online.)

a two-dimensional symmetric wedge with a deformable bottom plate is simulated. The setup resembles the laboratory experiments of Javaherian et al. (2019). The computational domain of the FSI problem is illustrated in Figure 1. Two side walls are considered on the right and left sides of the fluid domain. On the side plating of the wedge, a free-slip condition is applied, and the gradient of the volume fraction is considered to be zero. The fluid domain is assumed to consist of water and air. The length of the considered domain is  $12B$  and its depth is taken as  $10B$ , see Figure 1. To give an accurate description of physical impacts, where the impacting object is accelerated in any degree of freedom, the dynamic fluid body interaction (DFBI) method should be chosen for the wedge. Figure 5(a) displays a schematic of the front view of the 2D wedge section. In addition, the principal characteristics of the wedge can be seen in Table 1.

The thickness of the bottom ( $t_b$ ) and side ( $t_s$ ) plates are designed to be 3.17 and 12.7 mm, respectively then the side plates are much more rigid compared with the bottom plates. In order to obtain comparable results between numerical and experimental study, a

2D section of the wedge is modelled and the weight of the wedge equals to 0.644 kg as in the reported experiment. Figure 5(b) shows the top view of the bottom flexible plate with eight pressure points ( $P_1$ - $P_8$ ) with 33.9 mm spacing starting from the keel.

### 3.2. Mesh setup

The finite volume method (FVM) is used as the fluid solver and the governing equations are discretised over a grid of cells, with the nodal values evaluated at the centre of each cell. The fluid grid is built up by hexahedral cells that lead to an accurate solution and are particularly well suited for free surface problems. The overset mesh follows the body, and nodal values are interpolated between the background mesh and the moving mesh. The overset mesh method decreases computational time by producing small mesh sizes near the wedge walls and free surface. The overset region which surrounds the wedge is a rectangle with a length of  $3.5B$  and  $2B$  width (Figure 1). The minimum grid size is 2 mm at the overset region which a refinement on the bottom surface with 0.5 mm grid size is considered. As the mesh must be updated to account for the deformations, the mesh morpher method is employed. This method allows boundaries and nodes to move within the domain and deforms the mesh for each time step. For the structural domain, the finite element method with tetrahedron mesh using mid-side vertex (quadratic) is applied. The mid-side vertex adds mid-side nodes as interpolates of the corner nodes. The minimum grid size for the structural region is 1 mm. The generated mesh both in the overset region and structural domain is shown in Figure 6. The time-step size for both the fluid and solid solvers is selected to be  $\Delta t = 0.1$  ms with 15 internal iterations. During the simulation, care was taken to ensure that the mesh and time-step size are fine enough to limit mesh distortion issues after each structural calculation.

In order to find the most optimum mesh that is appropriate for the current freefall simulation, the response of a wedge of  $20^\circ$  dead-rise angle with 2.23 m/s impact velocity is examined. Three different mesh sizes are considered, see Table 2. The mesh study is organised for both the fluid and solid domains of the described problem. Accordingly, the time history of the pressure at the midpoint

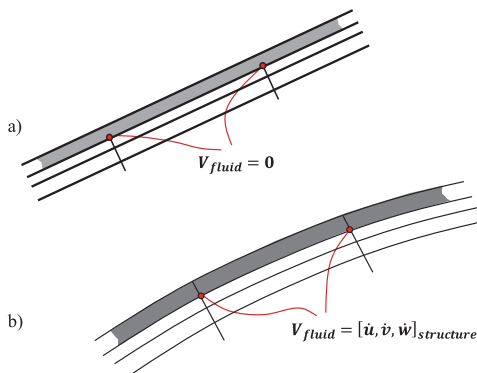


**Figure 3.** Fluid-structure interaction boundary condition (a) rigid body (b) FSI model. (This figure is available in colour online.)

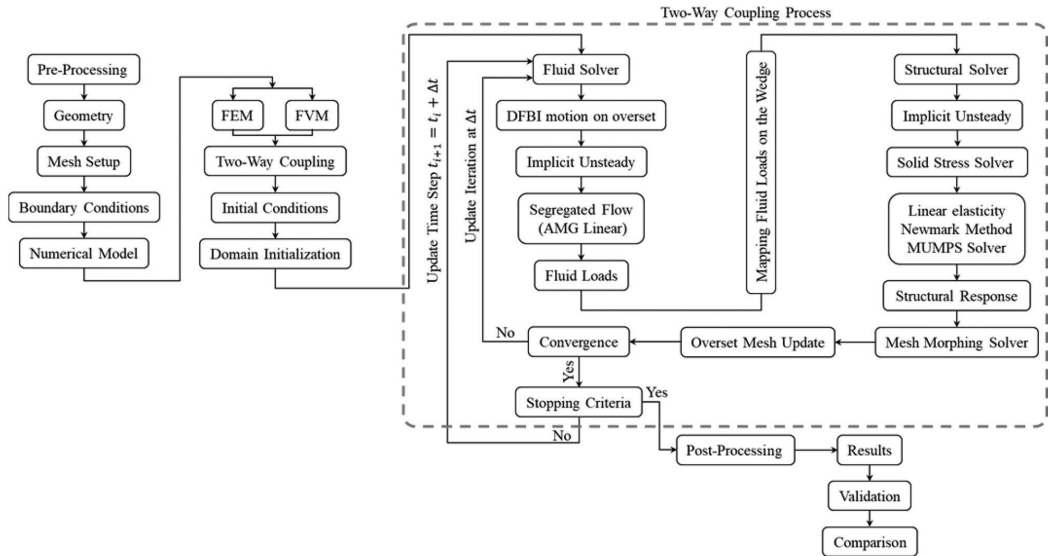


Figure 4. Algorithm used for the water entry problem of the flexible wedge includes the strongly two-way coupling scheme. (This figure is available in colour online.)

and the deflection of the bottom plate are computed from the beginning of the impact for each of these mesh sizes and the results are compared against each other. The results of these three different mesh sizes are shown in Figure 7.

As illustrated in Figure 7, large fluctuations are observed in the computed midpoint pressure and deflection when the coarse mesh is used. Therefore, the results of coarse mesh are undesirable. Furthermore, it is apparent that the deflection results of the medium

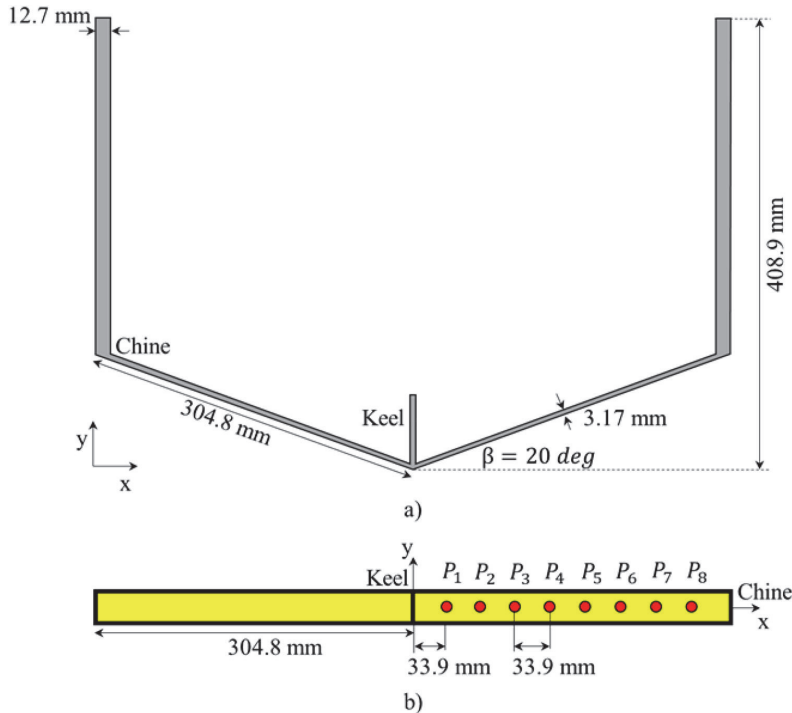


Figure 5. A drawing of the midsection of the flexible wedge (a) the dimension of the wedge and (b) arrangement of pressure points with 33.9 mm spacing. (This figure is available in colour online.)

**Table 1.** Main particulars of the flexible wedge.

Parameter	Value
Breadth (B)	573 mm
Overall Depth (D)	408.9 mm
Deadrise angle ( $\beta$ )	20 deg
Panel thickness ( $t_b$ )	3.17 mm
Side thickness ( $t_s$ )	12.7 mm
Material	Aluminium, 6061-T6
Density of Structure ( $\rho_s$ )	2700 kg/m <sup>3</sup>
Young's modulus (E)	68.9 GPa
Poisson's ratio ( $\nu$ )	0.33

mesh are smaller than fine mesh and the maximum deflection on the bottom of the wedge is underestimated using medium mesh. Consequently, the fine mesh is adopted for modelling the present water entry problem.

### 3.3. Validation of numerical model with experiments

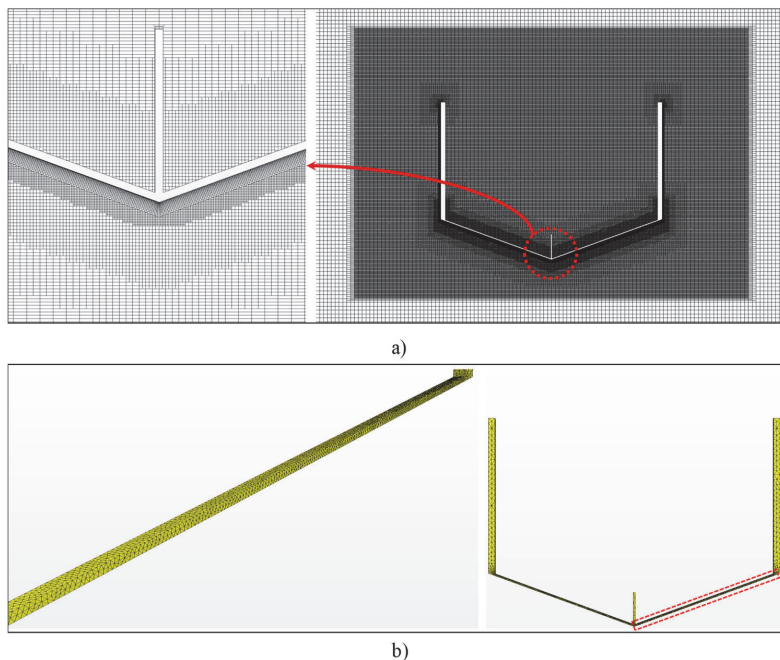
To verify the validity of the current hydroelastic simulations, the computed results are compared against the experimental data presented by Javaherian et al. (2019) and Ren et al. (2019). The results of the numerical simulations with initial drop height of 0.254 [m] and zero initial velocity are compared with analytical solution and experimental results. For the analytical solution, the modified Wagner method presented by Zhao and Faltinsen (1993) is used. Figure 8(a) displays the time history of the vertical position and good agreement can be observed.

Figure 8(b) depicts the time history of the vertical velocity. As shown, the curve has a good agreement for the falling period before the impact moment, but the deviation becomes discernible after impact and it is due to the velocity is calculated by integrating

the acceleration in the experiment (Javaherian et al. 2019). In the vertical velocity, the maximum negative values are very close to the experiment, and the corresponding error is about 2.9%. The acceleration time history of the wedge illustrated in Figure 8(c). The small error associated with the prediction of the maximum vertical acceleration increases by increasing drop height. Therefore, larger initial drop height means a higher impact velocity at the time the wedge reaches the water, which leads to larger errors. It is evident that the errors highly decrease after this time instant. That is, the larger drop height adversely affects the accuracy at the onset of the impact, and subsequently, errors reduce. Moreover, it is shown that the analytical method has less accuracy to predict the acceleration peak of the elastic wedge and cannot capture the post-impact stage of the water entry problem. Based on the results illustrated in Figure 8, there is a good agreement between numerical and experimental results. The discrepancy is likely due to friction in the bearings that are used in experiment.

Hydrodynamic pressures acting on the wedge with 20-degree deadrise angle for different pressure points, as defined in Figure 5, are computed and compared against the experimental results. Pressure time histories due to the 0.079 and 0.254 [m] drop height are illustrated in Figure 9. Generally, the results reveal that the proposed numerical approach is suitable to simulate such experiments.

As demonstrated in Figure 10, the results of computed pressure coefficient along the wedge, in dimensionless variables, are compared against Wagner's method and previous experimental data for the wedge in different deadrise angles. The vertical axis represents the pressure coefficient ( $C_p = P/(0.5\rho(V(t))^2$ ) where  $V(t)$  is the instantaneous wedge velocity, and the horizontal axis normalised by the vertical distance ( $y/vt$ ). In comparison with the Øien (2015) and Yettou et al. (2006) experiment, the peak pressures are relatively similar, and the trends are in good agreement.



**Figure 6.** Generated mesh, (a) mesh of the overset region with a close view around the wedge apex (b) close up view of the generated mesh on the structure. (This figure is available in colour online.)

**Table 2.** Considered grids size for fluid and structure domain for wedge with 20-degree deadrise angle and 0.254 [m] drop height.

Fluid Domain			
Type of Mesh	Coarse	Medium	Fine
Number of Cells	44266	109000	407273
Structural Domain			
Number of Cells	2170	21660	102540

There is a difference between the computed and experiment  $C_p$  because the simulated wedge is elastic. Therefore, due to the flexibility of the computed results, the maximum  $C_p$  is smaller than the analytical method and experiment.

In addition to hydrodynamics loads, the predicted deformations of the wedge are calculated and compared against the experimental data. A wedge with 20-degree deadrise angle with initial drop height of 0.254 [m] is simulated. Comparison of the predicted bottom plate deflection time histories against experimental data are displayed in Figure 11. In order to examine the effect of free fall velocity on bottom deflection, the results of the same wedge in constant vertical velocity are presented. As shown in Figure 11, using constant velocity leads to an increase in the difference between the computed results and the experiment. The error at the peak value of plate deflection compare with experimental maximum deflection and the deflection at the spray root is 9.8% and 3.6%, respectively. It is observed that the results are in good agreement, and the trend of the current results is similar to the experimental data.

The deflection from keel to chine can be seen in Figure 12. The predicted maximum deflection ( $\delta_{\max}$ ) at 15 and 20 ms after impact are compared against the experimental data. Based on this figure, the numerical maximum deflection happens earlier than experimental. In other words, friction in the experiment setup affects the pressure peak, spray root, and the maximum deflection. There could be several reasons for the deviation. To avoid numerical instabilities, the number of iterations in each time step, the simulation time step, and the mesh set-up should be considered in an efficient and accurate way. The mesh distortion was also a reason for many failed simulations, which is a cause for pressure divergence. Using overset mesh with a morphing method can overcome this problem and reduce computational costs. According to the comparison, there is a good agreement between computational results and experimental data, and it is concluded that the numerical model setup does accurately describe the physics of the experiment. The effect of

constant velocity and freefall impact on the deflection distribution is shown in Figure 12.

## 4. Results and discussion

### 4.1. Effect of structural rigidity

In order to examine the influence of structural elasticity, the wedges with different bending stiffness are simulated. This is achieved by simulating wedges assuming either steel or aluminium structure. In both cases, the structural mass is kept the same for both materials. The material parameters for steel are  $\rho_s = 7800 \text{ kg/m}^3$  (density of structure),  $E = 210 \text{ GPa}$  (Young's modulus), and  $\nu = 0.3$  (Poisson's ratio). The material parameters of aluminium are presented in Table 1. Pressure time histories due to the 20 cm drop height with a 10-degree deadrise angle for two different wedges are shown in Figure 13. As illustrated, each pressure point reaches the peak value in a very short period of time. As expected, due to lower flexibility of aluminium wedge and thus the higher deflection on the bottom plate, the pressure points reach the maximum peak value later than for the steel wedge. This short period of time affects also the maximum peak value of pressure.

Comparison of the bottom plate deflection time histories for steel and aluminium is displayed in Figure 14. As the results show, the steel has higher rigidity, and it leads to lower deflection on the bottom plates. As illustrated, the structural elasticity has a certain influence on the deflection and the slamming loads, and this influence should be considered when determining the impact loads on the structure.

The results of the current paper are presented in different sections. The influence of hydroelasticity on pressure coefficient in different deadrise angles is investigated in the next section. Later, the effect of vertical velocity on acceleration, plate deflection, and strain is studied. The effect of the deadrise angle on the acceleration and structure response is analysed in the last section. It should be noted in all conducted simulations, material of the elastic wedge is assumed to be aluminium 6061-T6, the initial vertical velocity is zero, and the mesh settings are constant throughout the entirety of this research.

### 4.2. Effect of hydroelasticity on $C_p$

The free surface elevations around the wedge wall at different deadrise angles are shown in Figure 15. It is necessary to investigate the

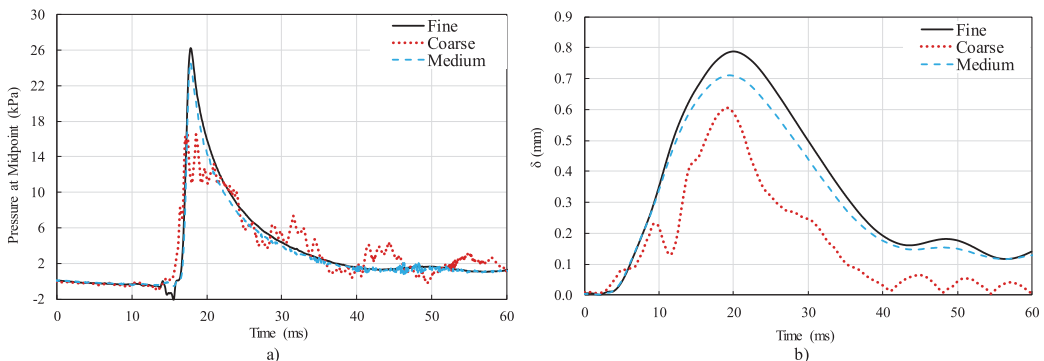


**Figure 7.** Mesh study of the simulation for a wedge with deadrise angle of 20° during free fall water entry with 0.254 [m] drop height (a) time history of pressure at midpoint of the wedge wall and (b) time history of deflection at midpoint. (This figure is available in colour online.)



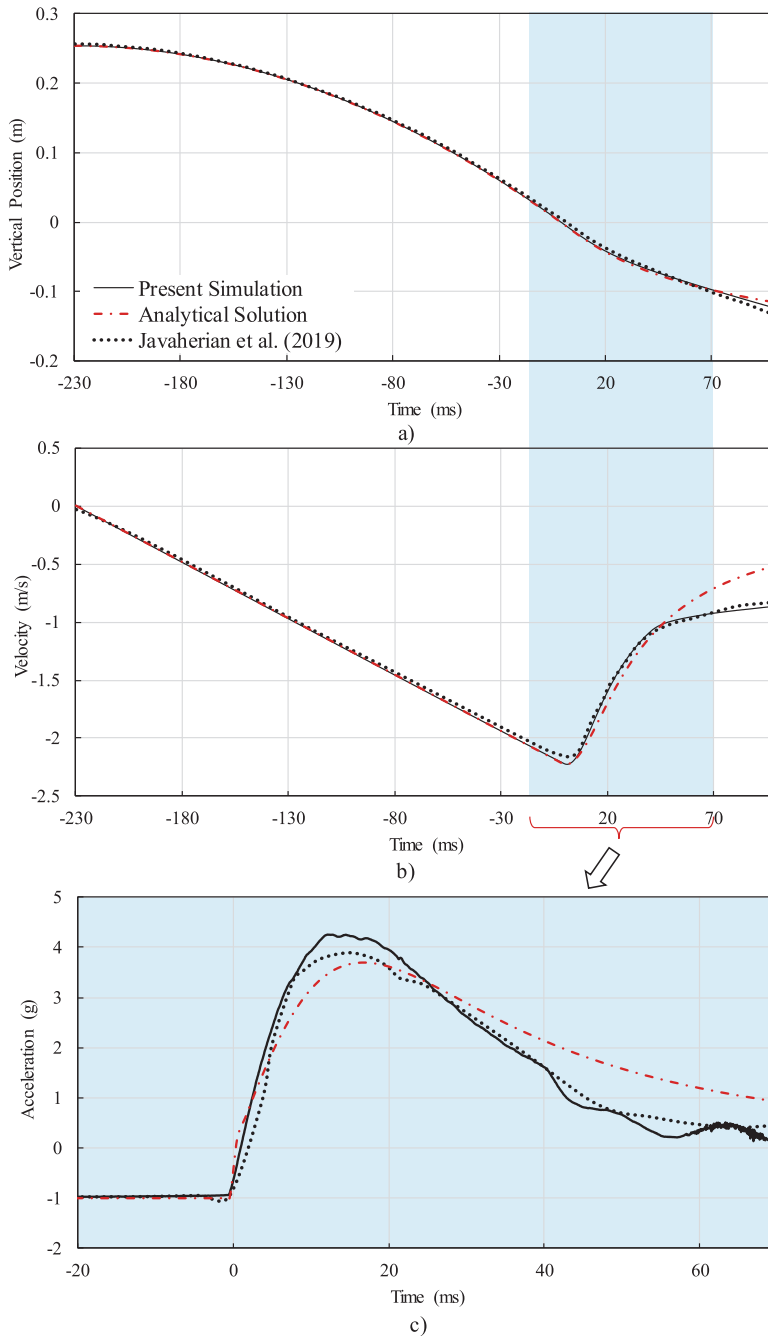


**Figure 8.** Comparison of the computed results against analytical solution and experimental data Javaherian et al. (2019) (a) time history of vertical position, (b) time history of vertical velocity (c) time history of vertical acceleration. (This figure is available in colour online.)

wetted surface of the wedge which can provide valuable information about the structural response. In Figure 15, the horizontal axis is non-dimensionalised using  $c$ , the half beam wetted by

water, and the vertical axis is dimensionless using  $d$ , the wedge penetration at each instant. Based on the comparison of the results at different deadrise angles, it can be concluded that when the deadrise

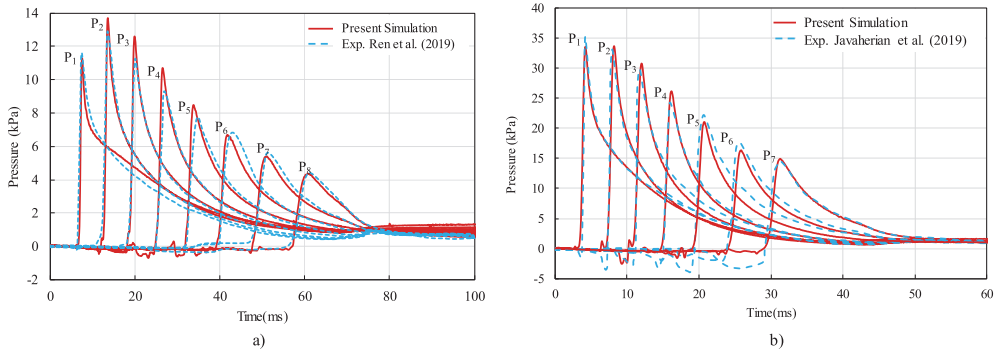


Figure 9. Comparison of pressure time history at different locations of the elastic wedge with 20-degree deadrise angle (a) 0.079 [m] initial drop height (b) 0.254 [m] initial drop height. (This figure is available in colour online.)

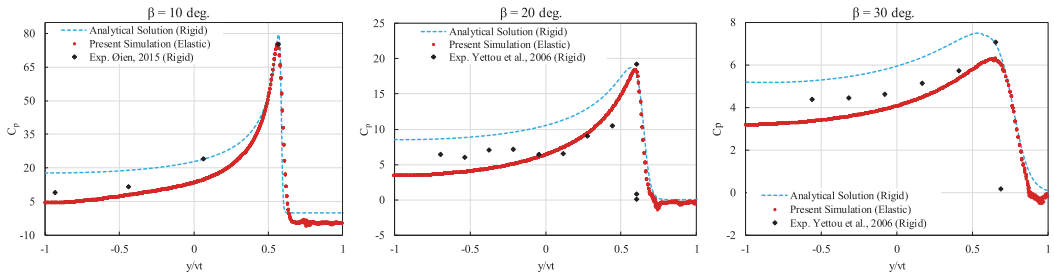


Figure 10. Comparison of pressure coefficient ( $C_p$ ) with analytical solution and experimental results for a wedge with different deadrise angles. (This figure is available in colour online.)

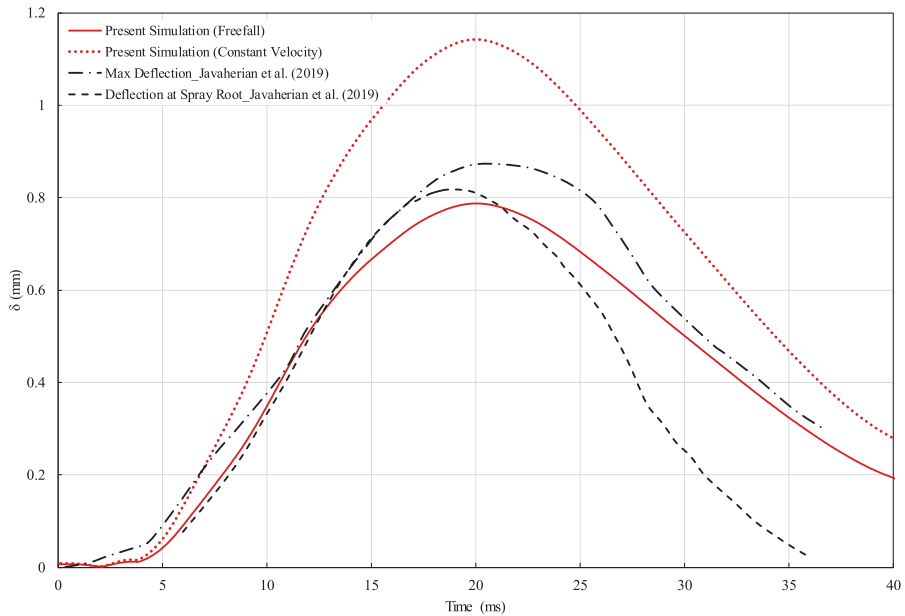
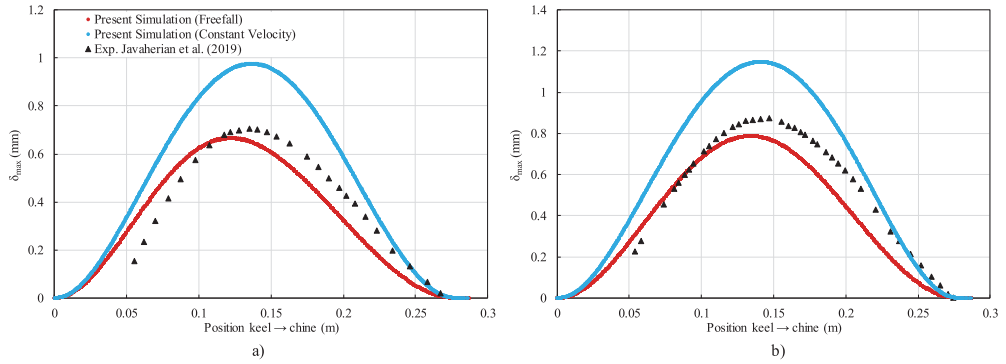
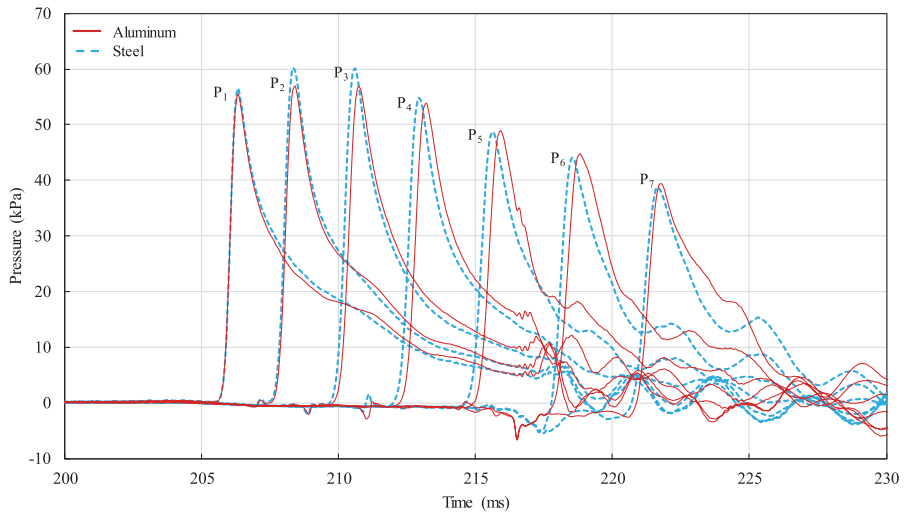


Figure 11. Comparison of the maximum deflection versus time for 20-degree deadrise angle elastic wedge with constant velocity and freefall impact ( $h_0 = 0.254$  m). (This figure is available in colour online.)



**Figure 12.** Comparison of the deflection distribution along the bottom plate of a 20-degree deadrise angle elastic wedge with constant velocity and freefall impact ( $h_0 = 0.254$  m) (a) time = 15 ms and (b) time = 20 ms. (This figure is available in colour online.)



**Figure 13.** Comparison of the pressure time history at different locations of aluminium and steel wedges with 10° deadrise angle and 20 cm drop height. (This figure is available in colour online.)

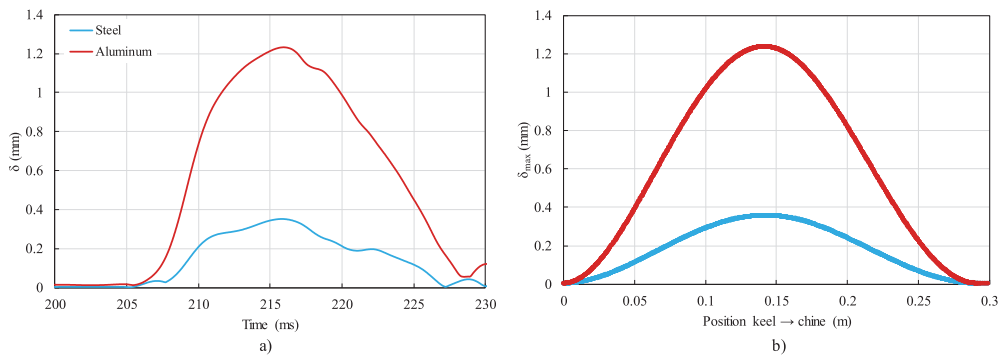


**Figure 14.** Comparison of steel and aluminium wedges with 10° deadrise angle and 20 cm drop height (a) maximum deflection versus time and (b) deflection distribution along the wedge. (This figure is available in colour online.)

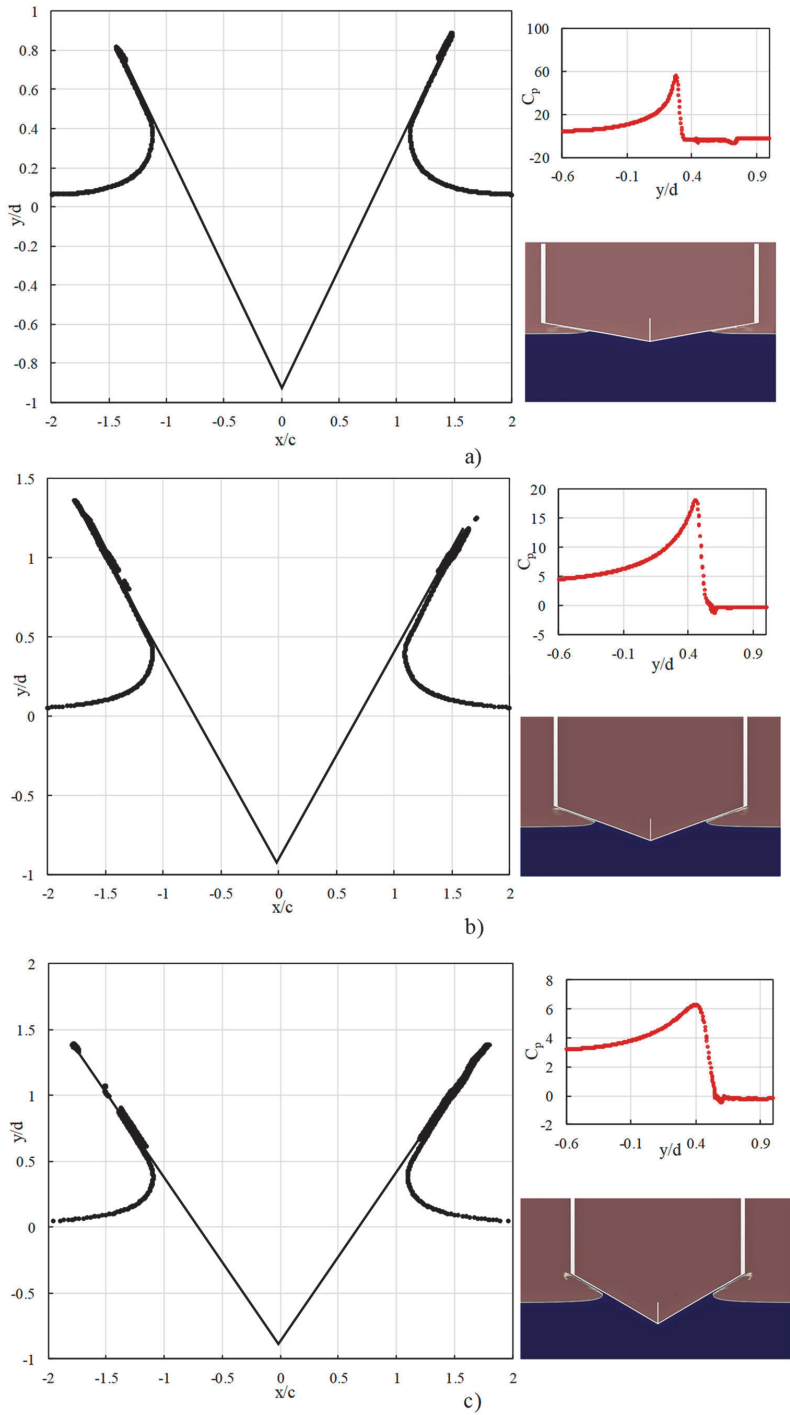


Figure 15. Free surface elevation (left) and pressure coefficient (right top) of the flexible wedges at  $h_0 = 20$  cm drop height (a) 10-degree deadrise angle, (b) 20-degree deadrise angle and (c) 30-degree deadrise angle. (This figure is available in colour online.)

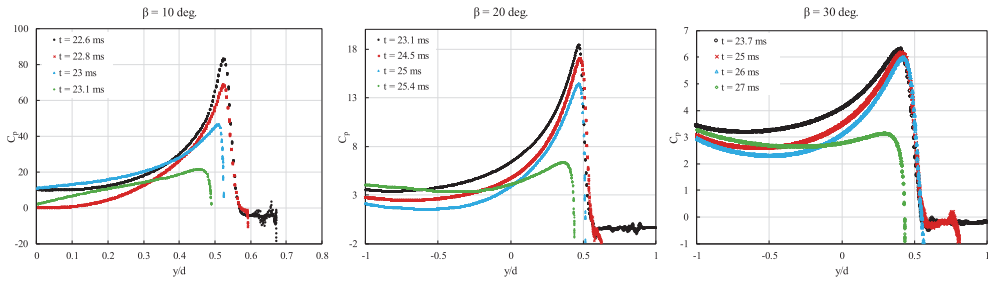


Figure 16. Computed pressure coefficient over the wedge wall at different time and different deadrise angles ( $h_0 = 20$  cm). (This figure is available in colour online.)

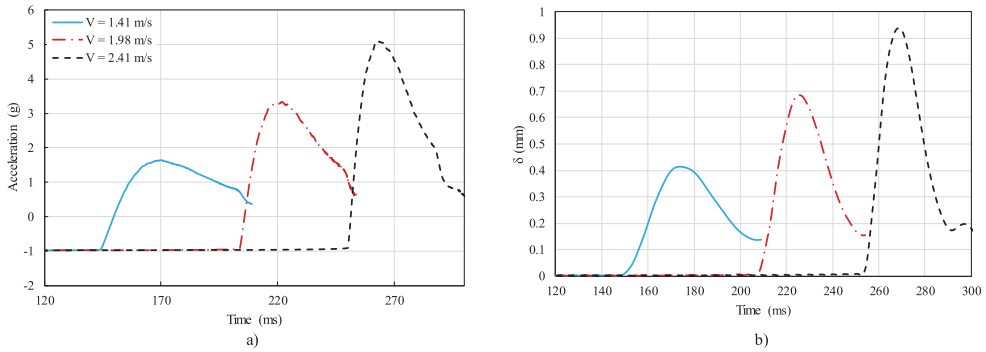


Figure 17. Comparison of different impact velocity for the flexible wedge with  $20^\circ$  deadrise angle (a) time history of acceleration and (b) time history of deflection. (This figure is available in colour online.)

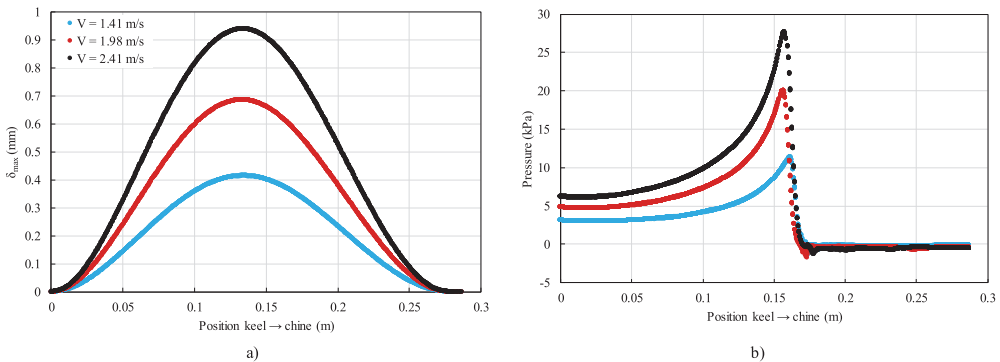


Figure 18. Effect of impact velocity for the  $20^\circ$  deadrise angle wedge (a) maximum deflection distribution along the wedge and (b) pressure distribution along the wedge. (This figure is available in colour online.)

angle increases, the variation of the free surface profile in time becomes less significant.

Since the deadrise angle is the most important parameter influencing the pressure coefficient, its distribution over the wedge wall, when the water reaches the midpoint, is also presented in Figure 15. The vertical axis represents the pressure coefficient as defined before, and the horizontal axis normalised by the vertical distance  $y/d$  ( $d$  the wedge penetration at each

instant). Pressure coefficients at four different times are presented for each deadrise angle in Figure 16. As expected, the peak pressure decreases over time. The difference between pressures at the first computed instant and the last computed instant becomes larger when the angle decreases. The results show that the pressure coefficient profile is dependent on the deadrise angle and for the small angle, the profile illustrates a sharper peak with a larger amplitude.

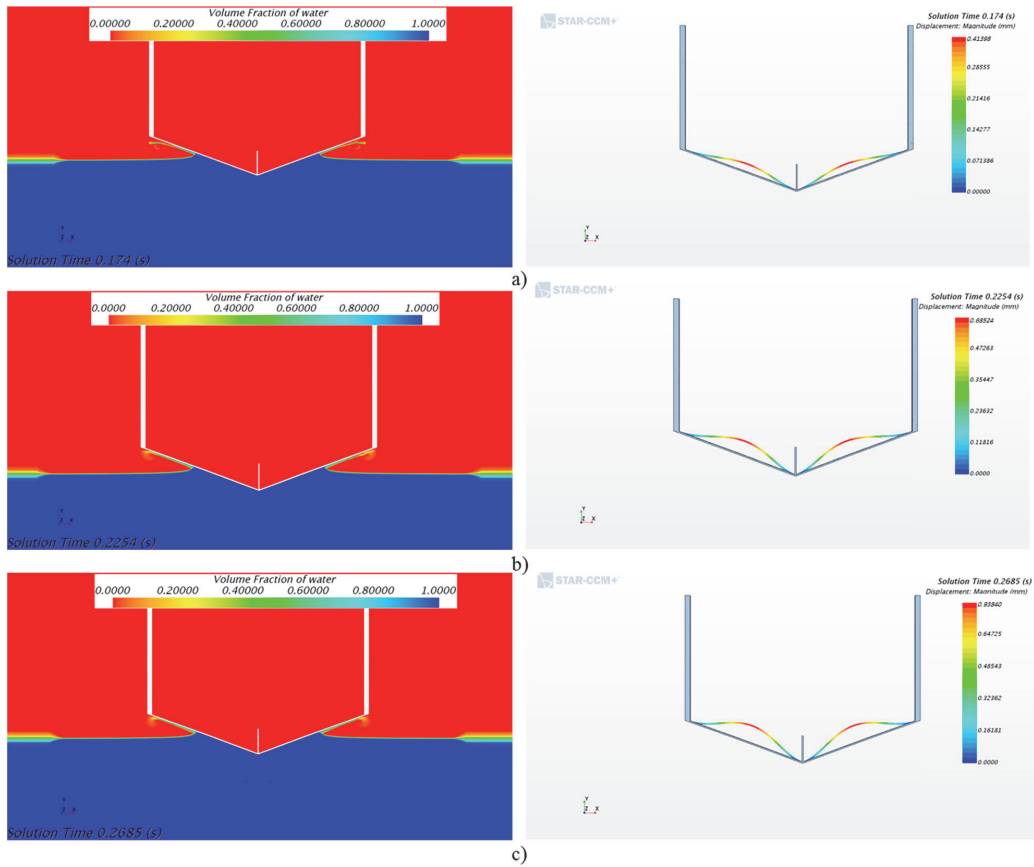


Figure 19. Free surface elevation (left) and deflections (right) of the flexible wedge with 20° deadrise angle (a) 1.41 m/s impact velocity, (b) 1.98 m/s impact velocity and (c) 2.41 m/s impact velocity. (This figure is available in colour online.)

### 4.3. Effect of impact velocity on $\delta$

To evaluate the effect of impact velocity on the plate deflection, simulations have been conducted with different drop heights. The flexible wedge with the same geometry for all cases falling freely

in the water at 10, 20, and 30 cm drop heights. As shown in Figure 17(a), the time histories of acceleration at three different vertical velocities are compared. The time histories of deflection on the bottom plate of the wedge are displayed in Figure 17(b). As expected,

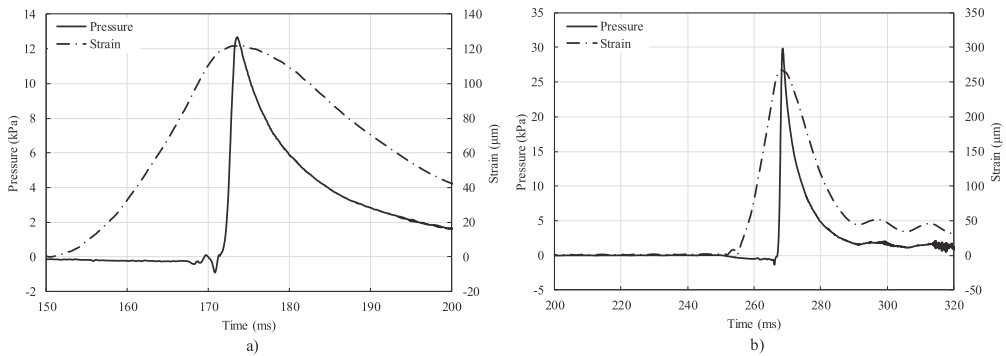
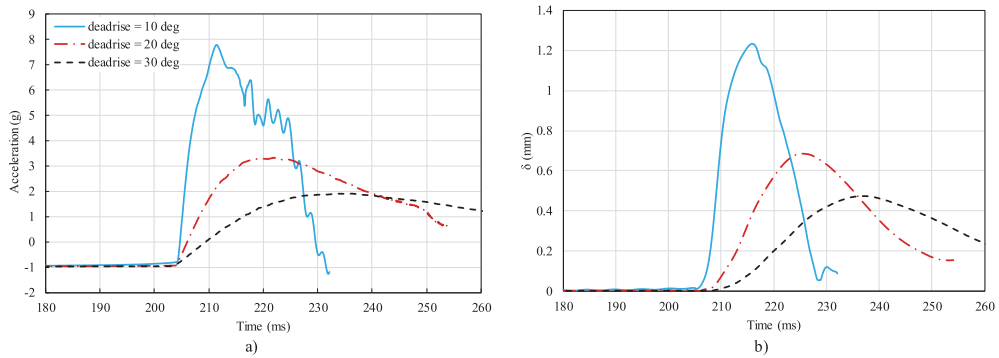


Figure 20. Time series of pressure and strain at the midpoint of the wedge with 20° deadrise angle (a) 10 cm drop height and (b) 30 cm drop height. (This figure is available in colour online.)



**Figure 21.** Comparison of different deadrise angle for the flexible wedges at 20 cm initial drop height (a) time history of acceleration and (b) time history of deflection. (This figure is available in colour online.)

by increasing the impact vertical velocity (higher drop height) the peak value of deflection increases.

To further analyse the structural response of the wedge, the maximum deflections along the bottom plate are illustrated in different drop heights in Figure 18(a). The results show the maximum deflection increases by increasing drop height. The pressure distribution along the wedge is studied at the time that the bottom plate is on the maximum deflection. Figure 18(b) illustrates the computed pressure distribution at the time when the maximum deflection occurred in different drop heights. It appears that the plate deflections are associated with the shape of the pressure distribution and its magnitude at certain locations.

Free surface elevation and maximum deflection of the bottom plate of the flexible wedge are shown in Figure 19. All the results are related to the time at which the maximum deflection condition begins. As demonstrated, when the spray root reaches near the middle of the plate, the maximum deflection happens. Accordingly, by analysing the location of the spray root, a better view of the structural response can be observed.

Figure 20 illustrates overlaying time histories of midpoint pressure and strain for the elastic wedge with 20° deadrise angle in two different initial drop heights. The behaviour of pressure and strain, as shown by the results, is distinctly similar. As a result of this section, for higher vertical velocity, the effect of hydroelasticity will be significant and it should be considered in the structural studies of marine structures.

#### 4.4. Effect of deadrise angle on $\delta$

In this section, the relation of the deadrise angle with acceleration, deflection, and free surface elevation is studied. The computed acceleration for these different wedges is shown in Figure 21(a). Based on the obtained results, the maximum peak value of acceleration appears on the wedge with a deadrise angle of 10°. As illustrated in Figure 21(a), some numerical fluctuations are observed after impact for the flexible wedge acceleration with 10° deadrise angle. It has happened as a cause of numerical instabilities. The time history of the bottom plate deflection is displayed in Figure 21(b) for all wedges. This figure shows the behaviour of the deflection during the elastic impact. As indicated, immediately following the impact, the wedge experiences a sharp deflection and reaches a peak and after that decays gradually. As expected from acceleration curves, the deflection of the wedge with a deadrise angle of 10° is larger than that of other wedges. The reason for this fact is that the wedge with a deadrise angle of 10° is exposed to larger pressure impact, and therefore the hydrodynamic loads acting on it become larger.

To evaluate the elastic effect, the deflection and pressure distribution along the bottom plate in different deadrise angles is demonstrated in Figure 22. As shown, the deflection of the wedge with 10° is larger than that of other wedges and the maximum pressure peak value has happened smaller deadrise angle.

The simulated free surface elevation, pile-up around the wedges, and maximum deflection on the bottom plate with

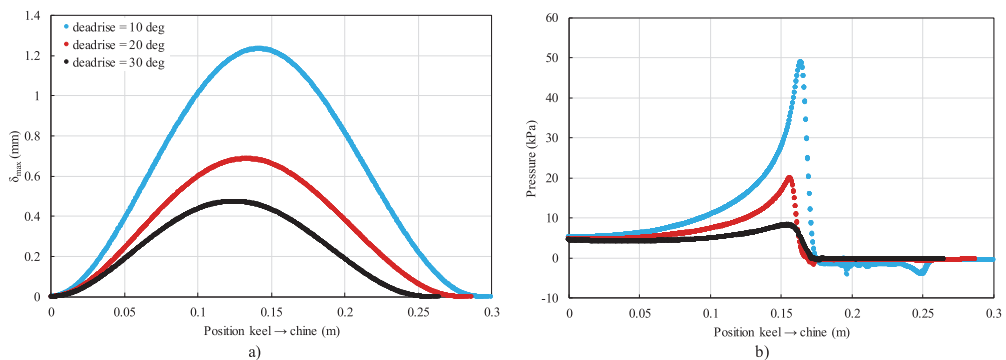


**Figure 22.** Effect of deadrise angle for the wedge at 20 cm initial drop height (a) maximum deflection distribution along the wedge and (b) pressure distribution along the wedge.

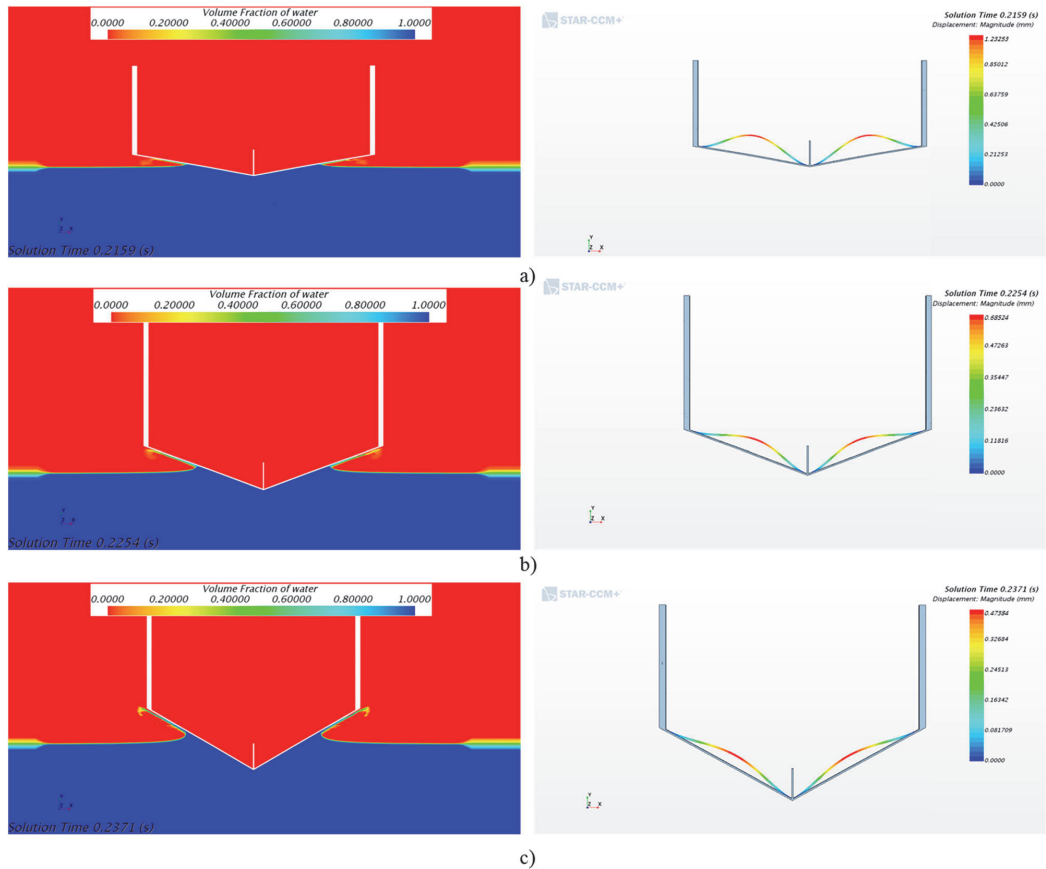


**Figure 23.** Free surface elevation (left) and deflections (right) of the flexible wedges at 20 cm initial drop height (a) 10-degree deadrise angle, (b) 20-degree deadrise angle and (c) 30-degree deadrise angle. (This figure is available in colour online.)

deadrise angles of 10°, 20°, and 30° are displayed in Figure 23. All the results are related to the time at which the maximum deflection condition happens on the bottom plate. A comparison between the results of different wedges shows that wedge with a deadrise angle of 10° experiences the largest deformation, while the wedge with deadrise angle of 30° experiences the smallest deformation. As observed, the vertical velocity for all wedges is same but as a cause of different deadrise angle, the time to reach

the maximum deflection is different for the wedges. Therefore, as a result, when the angle between the impacting free surface and the body surface is small, hydroelasticity effect is significant and must be considered. Figure 24 depicts the overlaying of mid-point pressure and strain time histories for the elastic wedge with different deadrise angles at 20 cm initial drop height. As expected, the pressure and strain have the same behaviour during freefall impact.

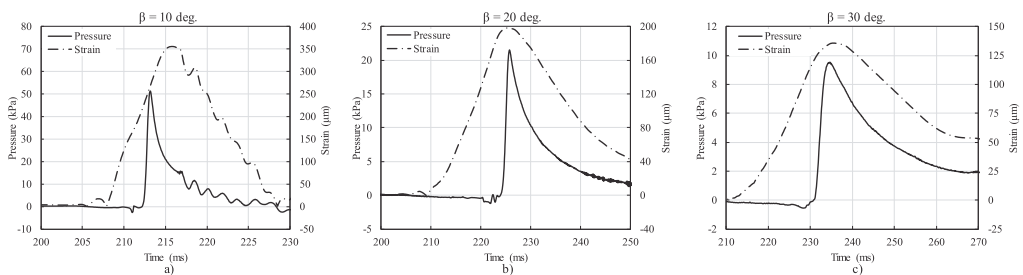


**Figure 24.** Time series of pressure and strain at the midpoint of the wedge with different deadrise angles and 20 cm initial drop height. (This figure is available in colour online.)



## 5. Conclusions

The aim of this paper has been to simulate and investigate the hydroelastic slamming of a two-dimensional symmetric flexible wedge. A numerical model is established to conduct coupled simulations between fluid and structural domain. This has been achieved by using the commercial software STAR CCM+ and the problem is simulated by coupling FVM and FEM by using a two-way coupled approach. The validity of the proposed numerical model is evaluated by comparing the results against an analytical solution and previously published experimental data. It is seen that vertical translation, impact velocity, and acceleration of the elastic wedge are predicted well and that there is good agreement between the numerical results and previous experiments. The pressure distribution acting on the elastic wedge at different locations has been determined and compared against the experiment, suggesting that the numerical model is suitable for predicting the pressure distribution and its peak values. Furthermore, the time history of the bottom plate deflection of the wedge has been computed and compared against the experimental data.

Parametric study has been conducted to identify the influence of different parameters of the pressure distribution and structural response. The influence of the freefall velocity is investigated by comparing the constant velocity and freefall impact, and it is discovered that the bottom deflection is overestimated by using the assumption of constant velocity. The effect of the bending stiffness on the deflection of the wedge is investigated as well. Eventually, some simulations are conducted in different conditions to provide further insight into the hydroelastic effect of the wedge-shaped bodies. By studying the effect of vertical velocity, it has been shown that the importance of hydroelasticity depends on the impact velocity and for higher drop height, the hydroelastic impact is significant. In addition, the simulations of the flexible wedge are carried out for three different wedges with deadrise angles of  $10^\circ$ ,  $20^\circ$  and  $30^\circ$ . It is observed that the maximum value of acceleration for the deadrise angle of  $10^\circ$  is greater than the other wedges. Similarly, it is seen that the deflection of the bottom plate of the wedge with a deadrise angle of  $10^\circ$  is larger than other cases. Increasing deadrise angle obviously increases the magnitude of the hydrodynamic impact loads and the bottom deformations and thus the importance of coupled assessment increases.

Improvements in these studies will lead to a better understanding of the hydroelastic characteristics of high-speed crafts and can be used for other kinds of fluid–structure interaction problems. In the future, the numerical simulation will be continued on optimising the mesh in both fluid and structural domains to examine the three-dimensional effects. Moreover, different structural elements can also be added to the wedge structure to estimate more realistic hydroelastic effects.

## Acknowledgement

This research work has been financially supported by the Estonian Research Council via grant PRG83 (Numerical simulation of the FSI for the dynamic loads and response of ships). This help is here kindly appreciated.



## Disclosure statement

No potential conflict of interest was reported by the author(s).

## Funding

This research work has been financially supported by the Estonian Research Council via grant PRG83 (Numerical simulation of the FSI for the dynamic loads and response of ships).

## ORCID

Saeed Hosseinzadeh  <http://orcid.org/0000-0002-5830-888X>  
 Kristjan Tabri  <http://orcid.org/0000-0001-8560-8477>

## References

- Abrate S. 2013. Hull slamming. *Appl Mech Rev.* 64(6):060803. DOI:10.1115/1.4023571.
- Akers RH. 2014. “A method of structural load prediction for high-speed planning craft. Portland: Maine Marine Composites LLC.
- Benra F-K, Dohmen HJ, Pei J, Schuster S, Wan B. 2011. A Comparison of One-Way and Two-Way coupling methods for numerical analysis of fluid-structure interactions. *J Appl Math.* 2011;16. DOI:10.1155/2011/853560.
- Bereznitski A. 2001. Slamming: the role of hydroelasticity. *Int Shipbuild Prog.* 48:333–351.
- Bilandi RN, Jamei S, Roshan F, Azizi M. 2018. Numerical simulation of vertical water impact of asymmetric wedges by using a Finite Volume Method combined with a volume-of-fluid technique. *Ocean Eng.* 160(July):119–131. DOI:10.1016/j.oceaneng.2018.04.043.
- Faltinsen OM. 1997. “The effect of hydroelasticity on ship slamming. *Philos Trans R Soc A: Math Phys Eng Sci.* 355(1724):575–591. DOI:10.1098/rsta.1997.0026.
- Faltinsen OM. 2001. Hydroelastic slamming. *J Mar Sci Technol.* 5(2):49–65. DOI:10.1007/S007730070011.
- Faltinsen OM, Kvålsvold J, Aarnesen JV. 1997. Wave impact on a horizontal elastic plate. *J Mar Sci Technol.* 2(2):87–100. DOI:10.1007/BF02491523.
- Hirdaris SE, Bai W, Dessi D, Ergin A, Gu X, Hermundstad OA, Huijsmans R, Lijima K, Nielsen UD, Parunov J, et al. 2014. “Loads for Use in the design of ships and offshore structures. *Ocean Eng.* DOI:10.1016/j.oceaneng.2013.09.012.
- Hosseinzadeh S, Izadi M, Tabri K. 2020. Free fall water entry of a two-dimensional asymmetric wedge in oblique slamming: a numerical study. In 39th International Conference on Ocean, Offshore & Arctic Engineering. <https://doi.org/10.1115/OMAE2020-18645>.
- Hosseinzadeh S, Khorasanchi M, Seif MS. 2018. “Investigation of planning vessels motion using nonlinear strip theory—an experimental and numerical study. *Ships Offsh Struct.* DOI:10.1080/17445302.2018.1552342.
- Izadi M, Ghadimi P, Fadavi M, Tavakoli S. 2018a. Numerical modeling of the freefall of two-dimensional wedge bodies into water surface. *J Braz Soc Mech Sci Eng.* 40(1):24. DOI:10.1007/s40430-017-0941-3.
- Izadi M, Ghadimi P, Fadavi M, Tavakoli S. 2018b. Hydroelastic analysis of water impact of flexible asymmetric wedge with an oblique speed. *Meccanica.* 53(10):2585–2617. DOI:10.1007/s11012-018-0846-y.
- Javaherian MJ, Ren Z, Christine Marie G. 2019. “Flow visualization, hydrodynamics, and structural response of a flexible wedge in water entry experiments.” In SNAME Maritime Convention, 30 October - 1 November, Tacoma, Washington, USA. The Society of Naval Architects and Marine Engineers.
- Judge C, Troesch A, Perlin M. 2004. Initial water impact of a wedge at vertical and Oblique angles. *J Eng Math.* 48:279–303. <https://link.springer.com/content/pdf/10.1023%2FB%3A98000018187.33001.e1.pdf>.
- Korobkin AA, Khabakhpasheva TI. 2006. Regular Wave impact onto an elastic plate. *J Eng Math.* 55(1–4):127–150. DOI:10.1007/s10665-005-0191-8.
- Lakshmyarayanana PAK, Hirdaris S. 2020. Comparison of nonlinear one- and two-way FFSI methods for the prediction of the symmetric response of a containership in waves. *Ocean Engineering.* DOI:10.1016/j.oceaneng.2020.107179.
- Maki KJ, Lee D, Troesch AW, Vlahopoulos N. 2011. Hydroelastic Impact of a wedge-shaped body. *Ocean Eng.* 38(4):621–629. DOI:10.1016/j.oceaneng.2010.12.011.
- Mesa JD, Maki KJ. 2017. Numerical hydroelastic analysis of slamming for high speed vessels. In Proceedings of the 14th International Conference on FAST SEA TRANSPORTATION, Nantes, France.
- Oien PK. 2015. Physical investigation of slamming loads on a 2D Body.
- Panciroli R. 2012. Hydroelastic impacts of deformable wedges. *Solid Mech Appl.* 192:1–45. DOI:10.1007/978-94-007-5329-7\_1.
- Panciroli R, Abrate S, Minak G. 2013. Dynamic response of flexible wedges entering the water. *Compos Struct.* 99(May):163–171. DOI:10.1016/j.compstruct.2012.11.042.
- Ren Z, Wang Z, Stern F, Judge C, Ikeda-Gilbert C. 2019. Vertical water entry of a flexible wedge into calm water: a fluid-structure interaction experiment. *J Ship Res.* 63(1):41–55. DOI:10.5957/JOSR.09180087.
- Shams A, Porfiri M. 2015. Treatment of hydroelastic impact of flexible wedges. *J Fluids Struct.* 57(August):229–246. DOI:10.1016/j.jfluidstructs.2015.06.017.

- Southall N, Choi S, Lee Y, Hong C, Hirdaris S, White N. 2015. Impact analysis using CFD – a comparative study. *OnePetro*.
- Southall NR, Lee Y, Johnson MC, Hirdaris SE, White NJ. 2014. Towards a pragmatic method for prediction of whipping: wedge impact simulations using OpenFOAM. *OnePetro*.
- STAR-CCM+. 2019. STAR-CCM+ Version 14.04 Manual.
- Stenius I, Rosén A, Kutteneuler J. 2007. Explicit FE-modelling of fluid – structure interaction in hull – water impacts. *Int Shipbuild Prog*. 53:103–121.
- Tödter S, Moctar OE, Neugebauer J, Schellin TE. 2019. Experimentally measured hydroelastic effects on impact-induced Loads During flat water entry and related uncertainties. *Journal of Offshore Mechanics and Arctic Engineering*. DOI:10.1115/1.4044632.
- Xu GD, Duan WY, Wu GX. 2010. Simulation of water entry of a wedge through free fall in three degrees of freedom. *Proc R Soc A*. 466:2219–2239. DOI:10.1098/rspa.2009.0614.
- Yettou EM, Desrochers A, Champoux Y. 2006. Experimental study on the water impact of a symmetrical wedge. *Fluid Dyn Res*. 38(1):47–66. DOI:10.1016/j.fluiddyn.2005.09.003.
- Zhao R., Faltinsen OM. 1993. Water entry of two-dimensional bodies. *J Fluid Mech*. 246:593–612.
- Zhao R, Faltinsen OM, Aarsnes J. 1996. Water entry of arbitrary Two-dimensional sections with and without flow separation. In *Proceedings of the 21st Symposium on Naval Hydrodynamics*, Trondheim, Norway: National Academy Press, Washington, DC, USA. p. 408–423.



## Appendix 2 (Publication II)

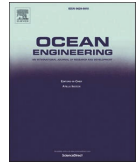
**[P2]** Hosseinzadeh, S., Tabri, K., Hirdaris, S., & Sahk, T. (2023). Slamming loads and responses on a non-prismatic stiffened aluminium wedge: Part I. Experimental study. *Ocean Engineering*, 279, 114510.





Contents lists available at ScienceDirect

## Ocean Engineering

journal homepage: [www.elsevier.com/locate/oceaneng](http://www.elsevier.com/locate/oceaneng)

# Slamming loads and responses on a non-prismatic stiffened aluminium wedge: Part I. Experimental study

Saeed Hosseinzadeh<sup>a,\*</sup>, Kristijan Tabri<sup>a,b</sup>, Spyros Hirdaris<sup>c</sup>, Tarmo Sakh<sup>a,b</sup>

<sup>a</sup> Department of Civil Engineering and Architecture, Tallinn University of Technology, Tallinn, Estonia

<sup>b</sup> Marine Technology Competence Center, Tallinn University of Technology, Kuressaare, Estonia

<sup>c</sup> Marine Technology Group, Department of Mechanical Engineering, Aalto University, Espoo, Finland

## ARTICLE INFO

Handling Editor: A.I. Incecik

## Keywords:

Flexible fluid structure interactions (FFSI)  
Experimental study  
Free-fall water entry  
Slamming loads  
Dynamic response

## ABSTRACT

Hydroelastic slamming is a phenomenon that occurs when there is a fully coupled interaction between the water surface and a deformable structure, and it has a significant effect on the local and global loads of the structure during high impact velocities in rough seas. Estimating the simultaneous structural responses caused by hydrodynamic loads during high impact water entry is a challenging task. This article, which is Part I of a two-part companion paper, deals with the experimental studies of the impact-induced loads and structural responses of a three-dimensional non-prismatic aluminium wedge with stiffened panel during free-fall water entry. Two different plates were considered on the bottom of the wedge in order to study the influence of flexural rigidity on hydroelastic slamming. A description of the experimental conditions, including the geometry of the wedge, material properties, and the test plan is provided. The effects of water impact velocity, deadrise angle, mass of the wedge, and bending stiffness on the slamming pressures and structural responses are discussed in detail. It is shown that the maximum strain and deformation occur during the partially wetted phase of the slamming problem. The study concludes that the hydroelasticity effects on slamming responses generally increase at lower deadrise angles and higher impact velocities. The importance of FSI simulation is assessed using a hydroelasticity factor ( $R_F$ ), which is found to have a significant effect on the unstiffened bottom for all impact velocities studied. For a stiffened bottom panel, hydroelasticity is only significant at high impact velocities.

## 1. Introduction

As marine and material technology advances, advanced marine vehicles can become increasingly exposed to the influence of extreme events. Therefore, it is important to properly evaluate vessel performance, seakeeping properties, and the effect of vessel motions on the crew.

Ship slamming occurs over a short period of time when a ship or part of it enters the water at high impact velocity in rough seas. The phenomenon may be associated with large amplitude motions and may pose a threat to ship structural integrity. Modelling slamming impacts and understanding flow physics between the hull of a vessel and the water surface present a challenging problem in hydrodynamics and naval architecture. This is due to local loads that change rapidly, the hydroelastic effects that occur, and the interaction between trapped air pockets and water (Faltinsen, 2000; Hirdaris and Temarel, 2009; Hirdaris et al., 2014). In addition, slamming events produce noise and a vibratory

response (whipping) but can also cause local buckling and plastic deformations (Cui et al., 1999; Southall et al., 2014).

The theory of water entry impact on two-dimensional bodies was first developed analytically by von Karman (1929) and later refined by Wagner (1932). Early studies mostly focused on two-dimensional (2D) rigid bodies (Vorus, 1996; Korobkin, 1996; Mei et al., 1999; Royce, 2001; Korobkin and Iafrati, 2005; Faltinsen and Chezhian, 2005; Yettou et al., 2007; Tassin et al., 2014), numerical simulations (Fairlie-Clarke and Tveitnes, 2008; Wang and Guedes Soares, 2014; Facci et al., 2016; Kamath et al., 2017; Izadi et al., 2018; Hosseinzadeh et al., 2020; Yan et al., 2022) and experimental studies (Chuang, 1966; Peterson et al., 1997; Judge et al., 2004; Yettou et al., 2006; De Backer et al., 2009; Lewis et al., 2010; J. Wang et al., 2015). Since slamming involves air-water-structure interactions, it may not always be accurate to simplify the problem as a two-dimensional rigid body impact. A rigid structure does not deform, the hydrodynamic pressure is not affected by structural deformation, and so the hydroelasticity cannot be taken into

\* Corresponding author. Department of Civil Engineering and Architecture, Tallinn University of Technology, Tallinn, Estonia.  
E-mail address: [Saeed.Hosseinzadeh@taltech.ee](mailto:Saeed.Hosseinzadeh@taltech.ee) (S. Hosseinzadeh).

<https://doi.org/10.1016/j.oceaneng.2023.114510>

Received 4 January 2023; Received in revised form 25 March 2023; Accepted 7 April 2023

Available online 24 April 2023

0029-8018/© 2023 Elsevier Ltd. All rights reserved.

**Table 1**  
A review of previous experiments information (NR: not reported).

Authors	Tank dimension (m)	Wedge dimension (m)	Deadrise (deg.)	Mass (kg)	Material	Plate thickness (mm)	Drop height/Impact velocity (m, m/s)
Chuang (1973)	7.62 × 4.57 × 2.59	1.82 × 0.4 × 0.22	0, 10, 20	132.44	Aluminium	1.6, 9.5	0.076–0.457 m
Peseux et al. (2005)	1.2 × 1	R = 0.32 (Cone)	6–14	NR	Aluminium, Steel	0.5,1,1.5, 25	2–8 m/s
Tveitnes et al. (2008)	NR	0.3 × 0.6	0–45	2.8, 5.2	PVC with Aluminium	10	0.24–1.19 m/s (Constant Velocity)
Luo et al. (2012)	24 × 8 × 8	2.88 × 3.36 × 1.3	22	3250	Steel	3.4	0.3–2.5 m
Panciroli et al. (2012)	1.6 × 1 × 0.6	0.3 × 0.25	15–35	NR	Al 6068 T6, GFRP	2.4	0.5–3 m
Stenius et al. (2013)	3.5 × 1.3–1.4	1 × 0.5	10, 20	18.3, 10.1, 31.9	GFRP	9.5, 2.5,3	0.5–7.0 m/s
Luo et al. (2014)	5 × 4.4 × 1.2	1.44 × 1.35 × 0.75	20	180	Steel	3.4	0.3–1.4 m
Tenzer et al. (2015)	6 × 1.5 × 0.55	0.3 × 0.3 × 0.2	5, 10	17.8, 20.9	Aluminium (5083)	2.81,2.85,12	0.5–2.5 m/s
Eastridge (2017)	30.8 × 4.6 × 2.4	1.45 × 1.19 × 0.53	20	186.9	Aluminium (5086H116)	6.35	0.15–0.61 m
Shams et al. (2017)	0.8 × 0.32 × 0.1	0.203 × 0.193	25	NR	Aluminium	0.6	1.25 m/s
Hassoon et al. (2017)	3 × 2 × 1.1	0.5 × 0.25	10	3.7, 6, 8	Composite Panels	8,13	4–10 m/s
Sun and Wang (2018)	4 × 4 × 2	1.6 × 1.2 (Flat Plate)	0	112	Steel	2.5	0.5–2.0 m
Dong et al. (2019)	108 × 7 × 3.5	1.5 × 0.9 × 0.75	45	553	Aluminium, Steel	4.5	0.25–1 m
Tödter et al. (2019)	6 × 1.5 × 0.75	0.3 × 0.3 × 0.2 (Flat Plate)	0	18.5,20.3	Al 5083, POM	4.7,12	0.52–1.04 m/s
Duan et al. (2020)	30 × 4 × 1	0.3 × 0.7	0–40	282	Aluminium, Steel	1, 2, 4,10	0.1–1 m
Spinosa and Iafrazi (2021)	470 × 13.5 × 6.5	1 × 0.5 (Flat Plate)	0	NR	Aluminium (2024-T3)	0.8,3,15	Horizontal Impact
Ren et al. (2021)	4.4 × 2.4 × 1.2	0.635 × 0.57 × 0.409	20	40.65	Al 6061-T6 Composite	3.17,12.7	0.079–0.508 m
Hosseinzadeh and Tabri (2021a)	60 × 5 × 3	1.5 × 0.94 × 0.45	Variable Deadrise	55, 82.5	Aluminium (5083-H111)	4	0.25 m
Meziane et al. (2022)	hydraulic shock test-rig	0.56 × 1.1 × 0.34	30	47.26	Aluminium (6061-T651)	5	Up to 10 m/s (Constant Velocity)

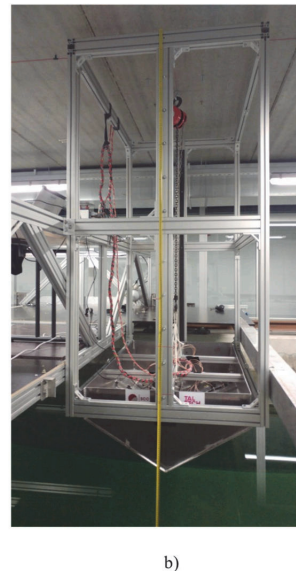
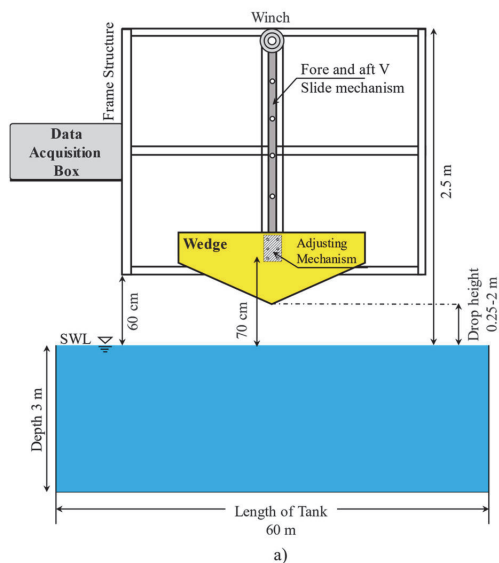


**Fig. 1.** Illustration of the experimental setup: a) schematic view of test rig, location of data acquisition box, and adjusting mechanism (reproduced from Hosseinzadeh and Tabri, 2021a); b) view of the frame structure for vertical motion and installed wedge.

account. Hydroelastic slamming occurs when hydrodynamic loads induce elastic deformations which simultaneously affect the fluid flow and pressure field. This coupled interaction is particularly significant for

local impacts at small relative surface-structure angles and when the duration of the impact is short relative to the resonance period of the structure.

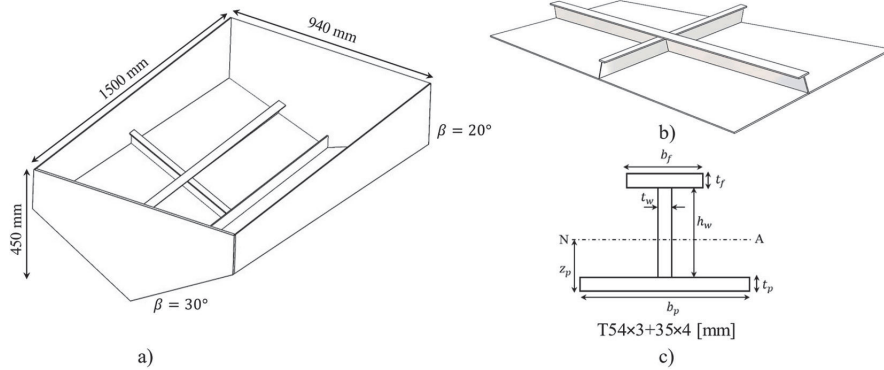


Fig. 2. Drawing of the of the non-prismatic aluminium wedge: a) dimensions of the wedge section in mm; b) stiffened bottom with longitudinal and transverse stiffeners; c) configuration of the stiffener.

**Table 2**  
Specifications and material properties of the aluminium wedge.

Material properties	Value
Density ( $\rho_{Al}$ )	2700 [kg/m <sup>3</sup> ]
Modulus of Elasticity (E)	68 [GPa]
Shear Modulus (G)	26 [GPa]
Poisson Ratio ( $\nu$ )	0.33
Tensile Strength	300 [MPa]
Longitudinal and Transverse Stiffener	T54 × 3 + 35 × 4 [mm]
Keel flat bar	60 × 5 [mm]
Thickness of Bottom plates	4 [mm]
Thickness of Endplates	10 [mm]
Thickness of Side plates	4 [mm]
Mass of the wedge ( $M_1$ )	55 kg
Mass of the wedge ( $M_2$ )	85.5 kg

**Table 3**  
Characteristics of the PCB-CA102B18 miniature dynamic pressure sensor.

Useful Overrange	689.4 [kPa]
Measurement Range	344.7 [kPa]
Maximum Pressure (static)	6895 [kPa]
Sensitivity ( $\pm 15\%$ )	14.5 [mV/kPa]
Resonant Frequency	$\geq 500$ [kHz]
Resolution	0.007 [kPa]
Rise Time	$\leq 1.0$ [ $\mu$ s]
Mounting Thread	7.9 [mm]
Measurement Diameter	8.6 [mm]

According to the numerical model proposed by Berezniński (2001), the role of hydroelasticity on slamming becomes important for small incidence angles and low natural frequencies of the structure. To date, several studies have investigated the effect of hydrodynamic loads on ships and offshore structures. Wang and Guedes Soares (2017b) provided a comprehensive literature review of ship slamming loads and responses. Khabakhpasheva and Korobkin (2013) studied the water entry problem of a two-dimensional elastic wedge at a constant velocity by combining an Euler–Bernoulli beam theory and the Wagner method. This analytical model was further developed by deriving an exact solution to the boundary value problem of the hydroelastic impact of elastic wedges under free-fall conditions and was validated against available experimental results in terms of strains, deflections, and total forces (Shams and Porfiri, 2015). Sun et al. (2021) investigated hydroelastic slamming for 2D symmetric elastic bodies using a semi-analytical model in both free-fall and constant water entry cases and compared the results with the existing experimental data.

In addition to analytical and numerical methods, high-quality experimental data on slamming loads and responses are essential to help us gain a deeper understanding of hydroelasticity, as well as improve existing theories and validate numerical simulations. Experimental research on the subject has been previously carried out with flat plates, prismatic wedges, cylinders, and even with ship hull models or sections of a ship. An extensive study by Chuang (1970, 1973) used wedges with different deadrise angles and drop heights. The findings of the investigation show that elasticity may reduce impact pressure. The hydroelastic slamming of three different composite panels with a relative deadrise angle of 10° was experimentally studied by Stenius et al. (2013). They analysed the importance of hydroelastic effects of rigid and flexible panels in constant velocity water impacts by comparing quasi-static finite element simulations with experimental results. A particle image velocimetry (PIV) technique was applied by Panciroli and Porfiri (2015) to measure the velocity field around an aluminium wedge during free-fall water entry. They indirectly evaluated hydrodynamic pressure by solving the Navier–Stokes equations with the measured velocity field. Shams et al. (2017) and Jalalisendi and Porfiri (2018) presented additional details about semi-analytical models derived on the basis of systematic experiments. Sun and Wang (2018) measured the impact pressure and effective stress on a stiffened panel at various drop heights using three-dimensional elastic stiffened plates. Dong et al. (2019) found that the structural elasticity affects slamming loads, which should be considered when modelling hydroelastic slamming. The authors used two models made of aluminium and steel to compare the effects of pressures and strains between elastic and rigid bodies. Tödter et al. (2019) conducted an experimental study with the aim to observe pressure differences due to rigid and elastic effects. Their results show that the pressure peaks were higher on the rigid plate than on the elastic due to the local deformations. A high-speed video recorded during their test gave insight into the different shapes of the trapped air underneath the rigid and elastic bottom plate. Two different experiments were conducted by Mai et al. (2020) to explore the role of elasticity in slamming and wave impacts. They investigated the free-falling impact of rigid and elastic flat plates on water surface, as well as the wave impacts on truncated vertical rigid and elastic walls. Duan et al. (2020) conducted an extensive series of tests with a wedge with different deadrise angles and drop heights to systematically study the effects of pressure distribution, and propagation. Their findings show that up to a 1-degree deadrise angle, the pressure coefficient increases and the pressure duration decreases slowly. Another finding was that at small deadrise angles, the duration of the slamming pressure is close to the wet natural frequency of the plate. The water impact of aluminium plates of different thickness at high horizontal velocity was carried out based on



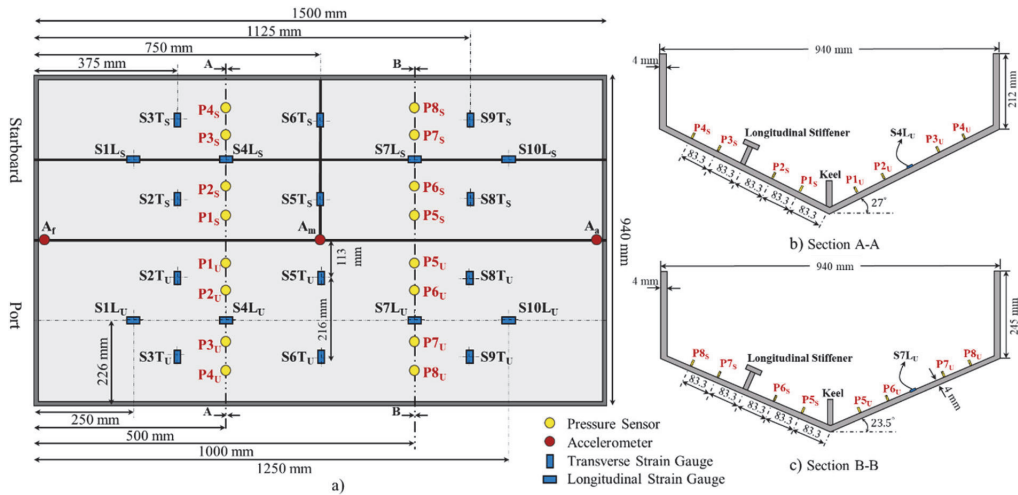


Fig. 3. Locations and arrangements of sensors: a) top view of the wedge with distribution of pressure sensors, strain gauges, and accelerometer; b) A-A cross section with the location of pressure sensors at  $\beta = 27^\circ$ ; c) B-B cross section with the location of pressure sensors at  $\beta = 23.5^\circ$ .

Table 4  
Specifications of data acquisition system.

Module	Number of Channel	Sampling Rate per Channel	Signal Bandwidth	Measuring Ranges
One MX840B universal amplifier	8	40 kHz	7.2 kHz	$\pm 10$ mV/V
Two MX440B universal amplifier	4	40 kHz	7.2 kHz	$\pm 10$ mV/V
Two MX410B highly dynamic universal amplifier	4	100 kHz	40 kHz	$\pm 20$ mV/V
One MX1615B strain gauge bridge amplifier	16	20 kHz	3 kHz	$\pm 20$ mV/V
One HBM CX22B-W data recorder	-	4 MHz for 56 Ch.	-	-

experimental measurements in Spinoso and Iafrati (2021). The authors found that structural behaviour changes considerably due to both stiffness changes and fluid-structure interaction effects. The flexural rigidity of a wedge with a constant deadrise angle of  $20^\circ$  was examined by Ren et al. (2021). According to their study, the hydrodynamic pressure may be coupled with the spray root in such a way that its peak magnitude is proportional to the square of spray root velocity and its peak location is proportional to the spray root position. Recently, Meziane et al. (2022) investigated the effect of panel stiffness on pressure and strain in an aluminium wedge with controlled vertical velocity, using three different types of panels with varying stiffnesses. Table 1 provides a summary of the dimensions of the towing tanks as well as the geometrical details of

Table 5  
The wedge impact velocities for different drop heights.

Drop Height ( $h$ ) [cm]	25	50	75	100	125	150	175	200
Theoretical impact velocity ( $V_t$ ) [m/s]	2.21	3.13	3.84	4.43	4.95	5.42	5.86	6.26
Experimental impact velocity ( $V_e$ ) [m/s]	2.20	3.00	3.55	4.00	4.50	4.90	5.25	5.60
Difference (%)	0.45	4.1	7.5	9.7	9.0	9.5	10.4	10.5

several important published experimental studies.

The review of published studies reveals that there is a lack of experimental research on the hydroelastic slamming of three-dimensional V-shaped sections with longitudinal and transverse stiffeners. The effect of impact velocity, deadrise angle, and flexural rigidity on the hydrodynamic pressures and structural responses of 3D complex bodies is not completely understood. Based on this, the objective of the present study is to gain a deeper understanding of the hydroelastic effects of slamming loads on 3D elastic structures. The influence of hydroelasticity (and hence structural rigidity) on hydrodynamic pressures and structural responses is experimentally investigated. The experimental studies are conducted on a non-prismatic aluminium wedge with stiffened and unstiffened bottoms that may freely fall into the calm water at varying drop heights (different impact velocities). The bottom plates of the wedge are designed with two different bending stiffnesses to study the effect of flexural rigidity on the structural responses. Two different wedge masses were used in the experiment to examine the effect of the wedge's mass on slamming loads.

The rest of the paper is structured as follows. The geometry of the aluminium wedge, experimental setup, sensor arrangement, and test plan of the experiments are all detailed in Section 2. A description of the post-processing of the results, including repeatability and uncertainty analysis, is presented in Section 3. The results of the experiment under different test conditions are described and discussed in Section 4. Section 5 provides a summary of the final remarks and conclusions.

## 2. Experimental set-up

### 2.1. Drop test rig

The experiments described in this paper were conducted at the Marine Technology Competence Centre (MARTE) at Tallinn University of Technology (TalTech). The towing tank with 60 m length, 5 m breadth,

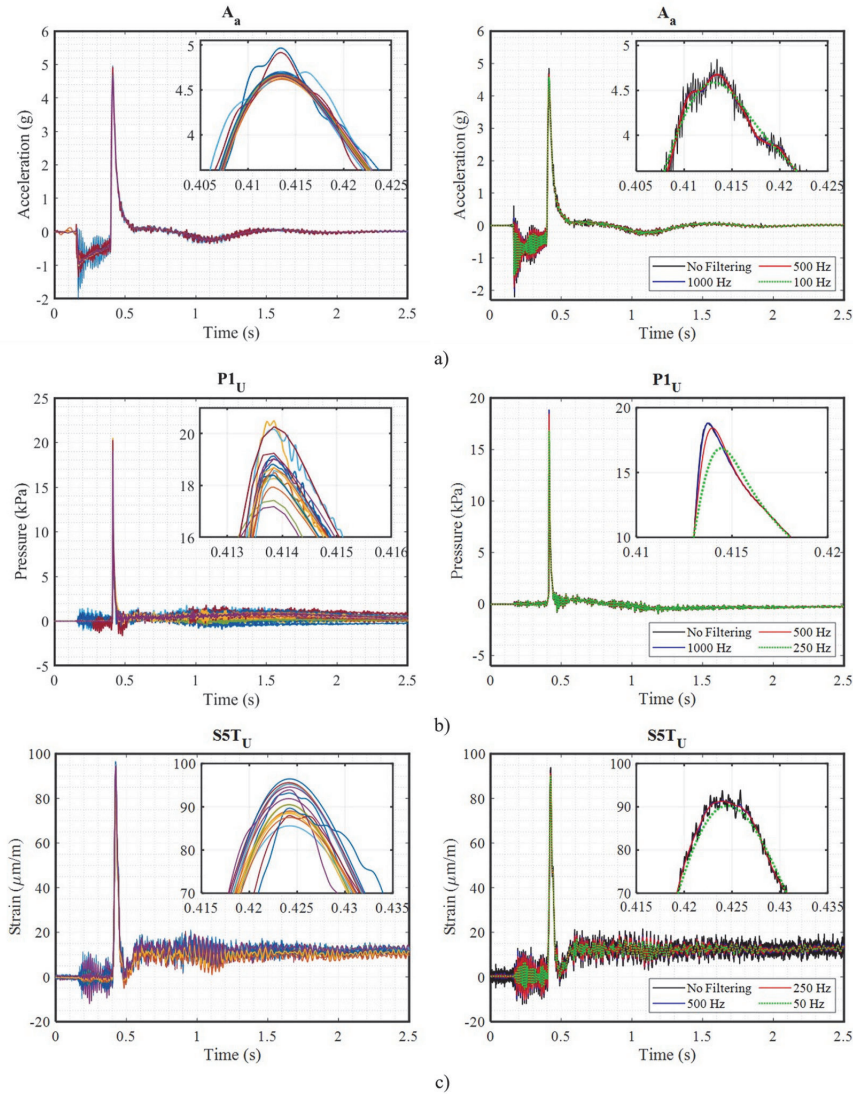


Fig. 4. Repeatability of the 18 impact tests (left) and effect of different low-pass Butterworth filter rates (right) on the: a) time history of acceleration; b) time history of pressure; c) time history of strain at 25 [cm] drop height.

and 3 m water depth was used to install the drop test rig. The test rig was designed and constructed using Norcan 45 × 90 mm anodised aluminium profiles and Norcan 88 × 43 mm corner triangles. Fig. 1a shows a schematic of the drop test rig and the installed equipment. As shown in Fig. 1b, one side of the test tower is mounted on the carriage of the towing tank, and the other side is fixed with a steel beam. The depth of the water in the towing tank remains constant during the experiment. Two linear guide rails (HepcoMotion 44-1-1796) were attached on the front and back of the test frame to allow vertical free-fall motion. A distance of 70 cm between the end of the guide rails and the undisturbed water surface was considered to allow a totally free-falling motion (Fig. 1). In addition, the thick molybdenum grease from the bearings was cleared away to reduce the friction of the guide rails and bearing mount and allow for smoother rolling with minimal resistance. The soft

cleaning pads from the bearing blocks were also removed. The test tower was assembled on level ground to adjust the guide rails and ensure that there is no binding between the guide sleds and rails. To install the test rig and lift the wedge to the proper drop height, an adjusting mechanism and a manually operated winch were employed. The winch was mounted on the ceiling of the tank and aligned with the centre axis of the test tower.

## 2.2. Model description

A non-prismatic aluminium (alloy 5083-H111) wedge section was designed to measure the slamming pressure and the structural responses during the experiment. The dimensions of the structure used in the experiment are shown in Fig. 2. As illustrated in Fig. 2a, the deadrise

**Table 6**

Mean, standard deviations ( $\sigma$ ), and RSD of the maximum acceleration, pressure and strain data for each sensor obtained from 18 runs of a test with 25 [cm] drop height (2.20 [m/s] impact velocity).

Accelerometer	$A_a$			$A_m$			$A_f$			
Mean Peak Acceleration (g)	4.67			4.20			3.49			
Standard Deviation ( $\sigma$ )	0.15			0.20			0.1			
RSD (%)	3.02			4.76			2.86			
Pressure Sensors (Unstiffened Bottom)	$P1_U$	$P2_U$	$P3_U$	$P4_U$	$P5_U$	$P6_U$	$P7_U$	$P8_U$		
Mean Peak Pressure (kPa)	18.6	8.40	2.60	1.67	21.6	12.0	4.69	1.85		
Standard Deviation ( $\sigma$ )	0.59	0.51	0.25	0.16	0.74	0.49	0.43	0.15		
RSD (%)	3.17	6.00	9.61	9.58	3.42	4.00	9.16	8.10		
Pressure Sensors (Stiffened Bottom)	$P1_S$	$P2_S$	$P3_S$	$P4_S$	$P5_S$	$P6_S$	$P7_S$	$P8_S$		
Mean Peak Pressure (kPa)	20.4	11.4	2.75	1.92	23.2	13.6	6.03	2.13		
Standard Deviation ( $\sigma$ )	0.73	0.64	0.26	0.19	0.53	0.56	0.53	0.19		
RSD (%)	3.57	5.60	9.45	9.89	2.28	4.11	8.78	8.92		
Strain Gauges (Unstiffened Bottom)	$S1L_U$	$S2T_U$	$S3T_U$	$S4L_U$	$S5T_U$	$S6T_U$	$S7L_U$	$S8T_U$	$S9T_U$	$S10L_U$
Mean Peak Strain ( $\mu\text{m/m}$ )	51.97	81.04	32.88	55.38	90.04	75.01	15.29	122.72	28.64	74.39
Standard Deviation ( $\sigma$ )	3.51	2.79	2.36	1.86	2.26	1.34	1.37	3.17	2.05	1.82
RSD (%)	6.75	3.44	7.16	3.35	2.50	1.78	8.90	2.58	7.15	2.44
Strain Gauges (Stiffened Bottom)	$S1L_S$	$S2T_S$	$S3T_S$	$S4L_S$	$S5T_S$	$S6T_S$	$S7L_S$	$S8T_S$	$S9T_S$	$S10L_S$
Mean Peak Strain ( $\mu\text{m/m}$ )	13.53	72.47	19.98	15.66	28.20	18.95	29.73	94.87	28.66	39.34
Standard Deviation ( $\sigma$ )	1.25	3.31	1.87	1.21	2.31	1.45	1.79	3.27	1.44	1.60
RSD (%)	9.23	4.56	9.30	7.72	8.19	7.65	6.00	3.44	5.02	4.06

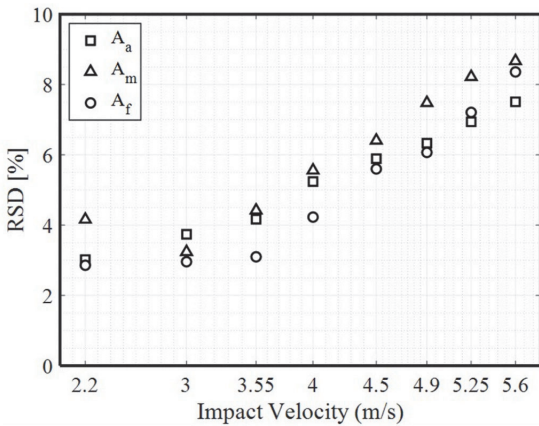


Fig. 5. RSD of the maximum acceleration of three accelerometers located at fore ( $A_f$ ), middle ( $A_m$ ) and aft ( $A_a$ ) of the wedge.

angle varies from 20 to 30° along the length of the wedge. This was done to examine the three-dimensional effects on the structural response and pressure results. To study the flexural rigidity of the structure, the bottom of the wedge was comprised of two different plates. The bottom of the starboard was made of a 4 mm thick extruded aluminium panel with a single T-shaped longitudinal stiffener and, hereafter referred to as “stiffened side”. Additionally, a transverse stiffener was welded to the wedge’s mid-bottom plate (Fig. 2b and c). A detailed description of stiffener dimensions can be found in Table 2. There are no stiffeners on the port side of the wedge. Hence, it is idealised as an “unstiffened elastic side” with 4 mm thickness. Two end plates with 10 mm thickness are attached on the fore and aft of the wedge structure. The keel is made of a 60 × 5 mm flat bar that is vertically welded to the apex of the wedge. An additional frame is designed and mounted on the top of the wedge to add more stiffness to the sides and allow a loop shackle to be attached for hoisting the wedge up into the test rig. To investigate how the wedge mass affects the slamming loads, two different wedge masses were used in the experiments. The designed wedge has a mass of 55 kg ( $M_1$ ) and 82.5 kg ( $M_2$ ), including all sensors, screws, welding, and top frame (Table 2). In order to increase the wedge’s mass, some weights were attached to the keel of the lighter wedge. These weights were evenly distributed along the length of the wedge.

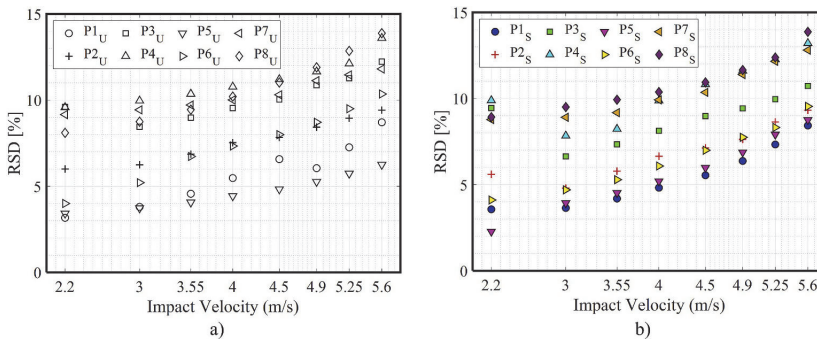


Fig. 6. RSD of peak pressure of all pressure sensors: a) pressure sensors on unstiffened bottom; b) pressure sensors on stiffened bottom.

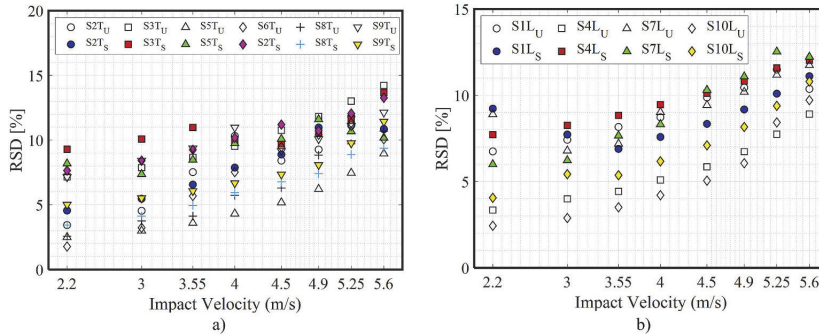


Fig. 7. RSD of maximum strain value of all strain gauges: a) strain gauges located on transverse direction; b) strain gauges located on longitudinal direction.

### 2.3. Data acquisition system and sensors

To measure the slamming pressures during water entry, sixteen piezoelectric pressure transducers (PCB-CA102B18) were employed. The characteristics of the miniature dynamic pressure sensors used during the experiment are shown in Table 3. Fig. 3a illustrates the top view of the arrangement of measuring cells on the wedge. To compare the pressure results of unstiffened and stiffened bottoms, the pressure sensors were mounted symmetrically on the bottom of the wedge. The pressure sensors (referred to as P) are labelled differently on the port and starboard sides of the wedge. For instance,  $P2_S$  denotes the second pressure sensor on the stiffened bottom, and  $P2_U$  refers to the second pressure sensor on the unstiffened bottom. As shown in Fig. 3a, the pressure data were measured from pressure transducers distributed along a characteristic line from the keel to the hard chine. To study the three-dimensional effect, the sensors were placed in two different characteristic lines with a 500 mm longitudinal distance from fore and aft of the wedge section. Fig. 3b and c shows the location of pressure sensors on the wedge section with a deadrise angle of 23.5 and 27°, respectively. As shown in Fig. 3b, the first sensor on the unstiffened bottom,  $P1_U$ , is located 83.3 mm away from the keel, and the others are installed at increments of 83.3 mm. The pressure sensors have a mounting thread length of 7.9 mm and because the bottom plates are 4 mm thick, different spacers were used. A Medium Strength Loctite thread glue was applied to all threads to ensure that there were no leaks between the mounting hole and the threads of the sensors. As well as pressure measurements, vertical acceleration was also recorded in the experiment. To examine the effects of deadrise angles on the vertical acceleration, three Dytran 3176B piezoelectric type accelerometers were adhesively mounted on the top of the keel. The accelerometers were located on the fore, middle, and aft of the wedge and indicated as  $A_f$  ( $\beta = 30$  deg.),  $A_m$  ( $\beta = 25$  deg.), and  $A_a$  ( $\beta = 20$  deg.), respectively (Fig. 3a).

To assess structural response during the impact, twenty linear strain gauges (HBM-1-LY13-6/120) were installed on the inner side of the bottom plates of the aluminium wedge. To achieve a flat surface and improve adhesion between the strain gauges and the wedge surface, the locations of the strain gauges were wet sanded to 400 grits. Fig. 3a shows the arrangement of the strain gauges (denoted as S). To measure the strain distribution in the different directions on the structure, twelve strain gauges were positioned in the transverse direction and eight in the longitudinal direction. In the same way as the pressure sensors, the U subscript indicates the sensor on the unstiffened bottom, and the S subscript represents the sensor on the stiffened bottom. The strain gauges are marked differently on the stiffened and unstiffened bottom of the wedge. For example,  $S1L_S$  is the first strain gauge on the stiffened bottom in the longitudinal direction, whereas  $S2T_U$  is the second strain gauge on the unstiffened bottom in the transverse direction.

During the experiment, data from all the sensors were simultaneously gathered using a data acquisition (DAQ) system located on the towing carriage. Two highly dynamic universal amplifiers with a 100 kHz sampling rate were employed for the pressure sensors. The three accelerometers were connected to a universal amplifier with a sampling rate of 40 kHz. The strain gauge data were gathered using a bridge amplifier with a sampling rate of 20 kHz. All sensor data were collected using an HBM CX22B-W data recorder module connected to the HBM proprietary CatmanEASY AP software. The FireWire cables were used to connect the amplifiers and the data recorder module. The specifications of the data acquisition (DAQ) system and the modules used in the experiment are shown in Table 4.

### 2.4. Experimental procedures

The free-fall drop tests were conducted at various drop heights ranging from 25 cm to 200 cm, with each increment of 25 cm. To ensure that the experimental results would be repeatable, the 25 cm drop height test case was repeated eighteen times and the remaining tests were conducted a minimum of two times. Using the calm water surface as a reference, the drop height was measured from the water surface to the wedge apex. To conduct the test, the wedge was tied to the winch's shackle with nylon rope and hoisted to the height of the test until it firmly touched the movable stopper. A measurement tape was also attached to one side of the test rig to ensure that the adjustable stopper and drop height were properly positioned, and the correct drop height was determined using a laser level. The arrangement of the cables inside the wedge was checked before each test to reduce the possibility of the cables snagging and damaging the sensors. In addition, a thin layer of petroleum jelly was applied to all pressure sensors, as recommended by the manufacturer, to minimise the temperature shock when the sensor was rapidly moved from one environment to another. After each test, the CatmanEASY AP analysis module was used to check the experiment results to ensure that all sensors had operated properly, and that all relevant data had been recorded. The following steps were considered between two test runs:

- The drop height was determined using a laser level and a measurement tape.
- The wedge was positioned at the correct drop height.
- The bottom surface of the wedge was cleaned of excess water (also inside of the wedge for high impact velocities).
- All instrument cables and sensors were checked, and the petroleum jelly was re-applied to the pressure sensors.
- Reset all channels of the data recorder.
- A wait time of 30–60 min was applied between two runs to ensure that the water surface had calmed down.

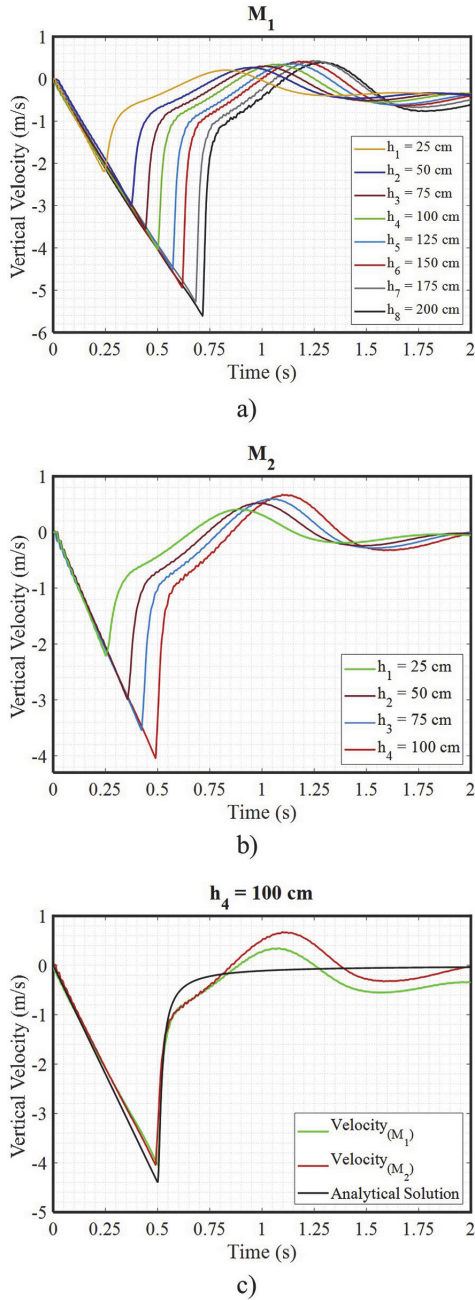


Fig. 8. Time histories of vertical water entry velocity calculated by integrating the acceleration measurements with different masses of the wedge: a) wedge with  $M_1 = 55$  kg mass; b) wedge with  $M_2 = 82.5$  kg mass; c) comparison of vertical velocity of two different masses of the wedge and analytical solution ( $V_a$ ) at 100 [cm] drop height.

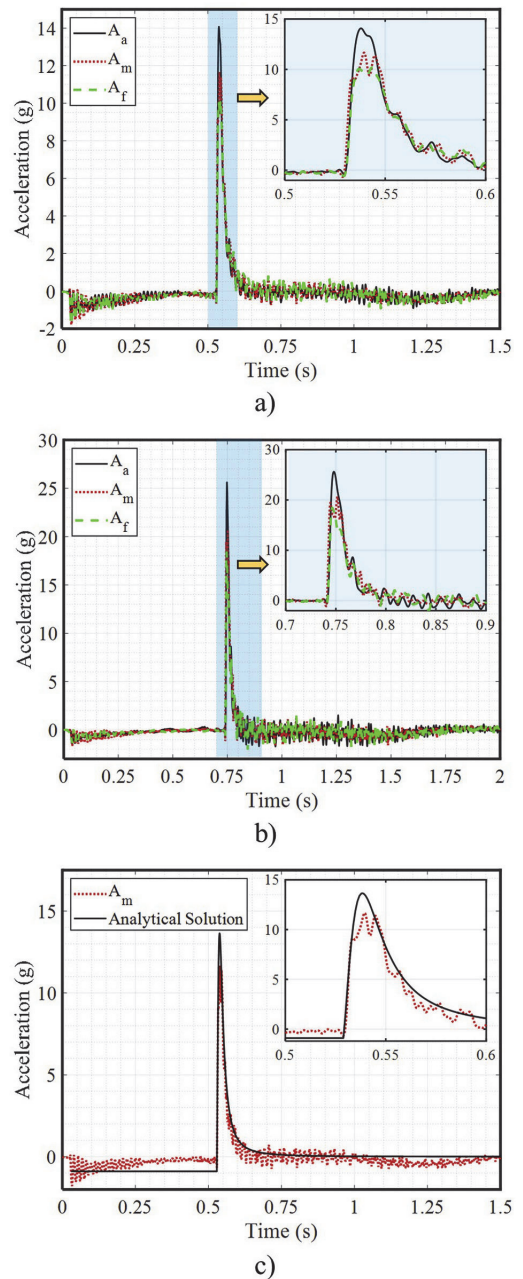


Fig. 9. Comparison of the measured vertical acceleration at different location of the wedge: a) 100 [cm] initial drop height; b) 200 [cm] initial drop height; c) difference of experimental and analytical acceleration at  $\beta = 25$  deg. ( $A_m$ ) and 100 [cm] initial drop height.

For numerical simulation of the slamming problem, it is common practice to start with a velocity rather than with the wedge at rest to minimise the associated computation time. Therefore, the velocity of the wedge during the free-fall impact was calculated using cumulative trapezoidal numerical integration. The difference between theoretical

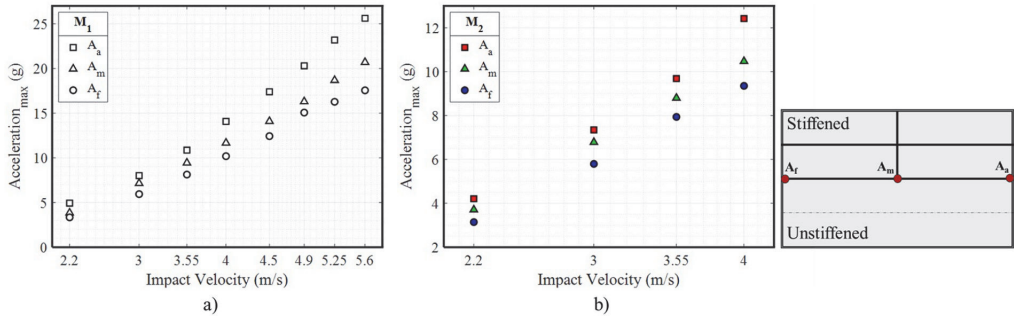


Fig. 10. Comparison of maximum vertical acceleration in various impact velocities and different masses of the wedge: a)  $M_1 = 55$  kg; b)  $M_2 = 82.5$  kg.

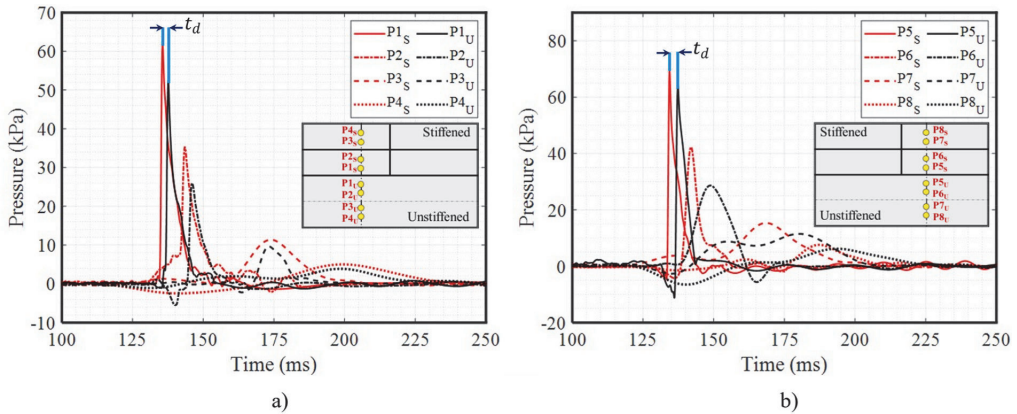


Fig. 11. Comparison of measured pressure of 100 [cm] initial drop height on different locations along the wedge: a) time history of pressure on stiffened and unstiffened bottoms at  $\beta = 27$  deg.; b) time history of pressure on stiffened and unstiffened bottoms at  $\beta = 23.5$  deg. (Note: Each graph refers to a sensor).

( $V_t = \sqrt{2gh}$ ) and calculated water entry impact velocities ( $(V_t - V_i) / V_t \times 100$ ) for different drop heights are shown in Table 5.

### 3. Post-processing of results

To investigate the reproducibility of the experimental measurements, eighteen trials were carried out for the first test case ( $h_1 = 25$  cm) and rest of cases were repeated at least twice. The time histories of all 18 runs for acceleration, pressure, and strain are compared and shown in Fig. 4 (left). To determine the experimental uncertainties associated with the tests, the results were analysed. In order to filter out high frequency noise from the sensors signal during the experiments, a low-pass filtering was employed on the raw data. The variation in the acceleration, pressure, and strain sensors with different Butterworth low-pass filter frequencies are illustrated in Fig. 4 (right) at  $h_1 = 25$  cm. The filters were generated using MATLAB's 'filtfilt' function, which utilises a zero-phase digital filtering technique that processes the current point in relation to both forward and reverse points in the frequency domain to retain the signal time history in line with the original signal (Mitra and Kuo, 2006; Swidan et al., 2016). As depicted in Fig. 4, for acceleration and pressure data, the low-pass Butterworth filter with a cut-off frequency of 1000 Hz has a negligible to no effect on the results and is thus applied to all sensors. Furthermore, a low-pass filter frequency of 500 Hz was chosen for strain gauges data (Fig. 4c).

Table 6 represents the mean of the acceleration, pressure, and strain peak values from different sensors for 18 experiments with 25 [cm] drop height. The statistical uncertainty of the experiment is calculated using

standard deviation ( $\sigma$ ) and relative standard deviation (RSD) for different sensors according to Eq. (1).

$$\sigma = \sqrt{\frac{1}{N-1} \sum_{i=1}^N (x_i - \bar{x})^2}, RSD(\%) = (\sigma / \bar{x}) \times 100 \quad (1)$$

where  $N$  is the number of repeated tests,  $x_i$  the maximum value of individual test, and  $\bar{x}$  the mean peak value of the measurement. Table 6 shows that the RSDs for acceleration sensors are less than 5%. Furthermore, the repeatability of the tests is considerably better for pressure sensors near to the keel and with smaller deadrise angles. The RSDs for all pressure and strain sensors calculated from 18 runs are less than 10%, confirming that the experimental setup presented in this study is reproducible and could provide reliable results.

In order to obtain reliable benchmark data, the repeatability of measurements was examined for all impact velocities. Fig. 5 shows the relative standard deviation of the maximum acceleration measured by the accelerometers at different locations and various drop heights. The repeatability of the experiment can be evaluated using the plot of RSDs for all cases. It can be seen that the acceleration RSDs for all tests are less than 9%, indicating good repeatability of the experimental set-up.

In addition to the acceleration measurements, the relative standard deviations of all pressure sensors and strain gauges are calculated and presented in Figs. 6 and 7, respectively. It is shown that the pressure and strain RSDs for all tests are less than 15%. Besides that, the pressure sensors placed close to the keel have better repeatability than those

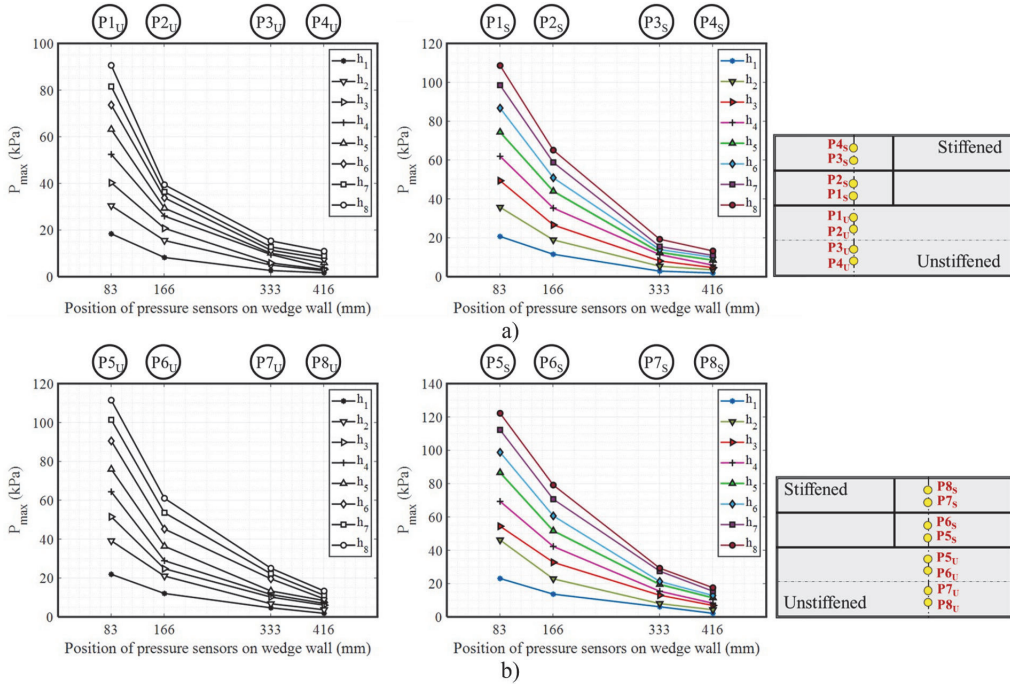


Fig. 12. Comparison of maximum pressure measured at different initial drop heights and 55 kg mass of the wedge: a) peak pressure value of sensors located on section A-A ( $\beta = 27 \text{ deg}$ ); b) peak pressure value of sensors located on section B-B ( $\beta = 23.5 \text{ deg}$ .) Note: unstiffened (left plot) and stiffened (right plot).

located near the chine. It can be concluded that the standard deviation increases as impact velocities increase. This behaviour was observed for all accelerometers, pressure sensors, and strain gauges.

4. Experimental results and discussion

4.1. Motion kinematics

A comparison between experimental results in different conditions is presented and discussed in this section. As stated in the previous section, two different masses were used to test the described non-prismatic wedge. The time histories of vertical velocity of the wedge with mass of  $M_1$  at different drop heights are shown in Fig. 8a. The velocity profile was calculated by integrating the experimental data from an accelerometer located on the mid-section of the wedge ( $\beta = 25 \text{ deg}$ ). As shown, after releasing the wedge, the velocity increases linearly and reaches its maximum negative value which corresponds to the moment when the vertical acceleration is zero in Fig. 9a. Subsequently, the velocity of impact begins to decrease, indicating the start of the exit phase in the water entry problem, which occurs when the velocity profile changes from a downward to an upward direction. The velocity profile of the wedge with a mass of  $M_2$  ( $=1.5M_1$ ) is presented in Fig. 8b. As expected, the mass of the wedge affects the post-impact phase of the water entry problem. According to the two-dimensional (2D) Wagner theory (Wagner, 1932; Duan et al., 2020), the water entry velocity can be calculated as

$$V_a = \frac{V_t}{\sqrt{1 + \rho \pi^3 L \frac{V_t^2}{4M \tan^2 \beta}}} \tag{2}$$

where  $\rho$  is the density of water,  $M$  is the mass of the wedge,  $t$  is the penetration time,  $L$  is the length of the wedge,  $g$  is the acceleration of

gravity, and  $V_t$  is theoretical impact velocity that presented in Table 5 for each drop height. Fig. 8c compares the velocity profile calculated by the analytical method with the experimental results for the case of drop height equal to 100 [cm].

Fig. 9 shows the vertical acceleration over time determined by measuring it on the top of the keel at different longitudinal locations along the wedge's length. As displayed in Fig. 3, the accelerometers were placed on fore ( $A_f$ ), middle ( $A_m$ ) and aft ( $A_a$ ) of the wedge ( $\beta = 30, 25, 20 \text{ deg}$ , respectively). Fig. 9a compares the vertical acceleration time history for the case of drop height equal to 100 [cm]. The influence of deadrise angle on the vertical acceleration for 200 [cm] drop height is illustrated in Fig. 9b. Impact with the water surface induces a rapid acceleration peak reached within a short period. The acceleration values at different locations on the wedge indicate that the wedge is undergoing a slight rotation around the transverse axis. However, due to the small angle of rotation, it did not significantly affect the water entry process. The measured vertical acceleration for the sensor located on 25-degree deadrise angle at 100 [cm] initial drop height is compared with the acceleration calculated by Wagner theory (Wagner, 1932) and is shown in Fig. 9c. The analytical method predicts a maximum acceleration of 13.6g whereas the experiment shows 11.6g. The discrepancy between the analytical and experimental results may be due to three-dimensional effects. Aside from the time histories of vertical acceleration, Fig. 10 presents the maximum values of acceleration measured at various drop heights and two different weights of the wedge. It is demonstrated that for the heavier wedge, the maximum acceleration becomes smaller which leads to a slower decrease in vertical velocity. Additionally, the heavier body reach their acceleration peak later.

4.2. Slamming pressure

This section investigates the effects of impact velocity, structural

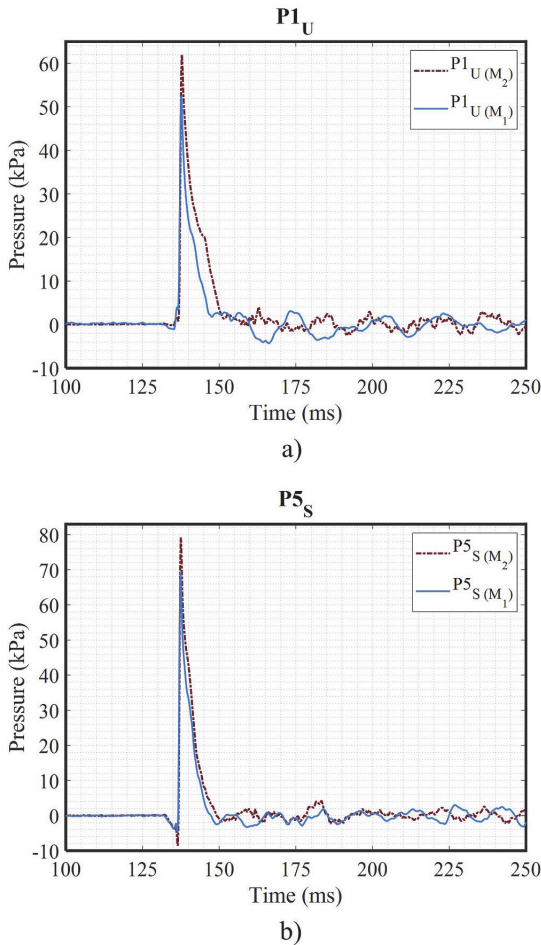


Fig. 13. Effect of mass of the wedge on the pressure distribution at 100 [cm] drop height: a) pressure sensor located on unstiffened bottom ( $\beta = 27 \text{ deg.}$ ); b) pressure sensor placed on stiffened bottom ( $\beta = 23.5 \text{ deg.}$ ).

rigidity, and deadrise angle on hydrodynamic pressure. The experimental results of all pressure sensors at 100 [cm] drop height ( $V_i = 4.0 \text{ m/s}$ ) are presented in Fig. 11. To study how stiffness affects the pressure results, the pressure measurements of sensors located on the unstiffened (U) and stiffened (S) bottom were measured and compared along the wedge's length. As expected, the pressure maximum values are highest near the keel and gradually decrease toward the chine. On the stiffened bottom, the pressure transducer, P1 and P5, are the first sensors to be in contact with the water surface, and pressure peaks propagate from P1 to P4 and P5 to P8. The pressure distribution of the sensors located on the unstiffened bottom shows a similar behaviour. Because of the influence of structural rigidity, the pressure values on the stiffened bottom of the wedge are constantly higher than those on the unstiffened bottom. In addition, the pressure peaks for the sensors located on the fore of the wedge (Fig. 11a), where the deadrise angle is  $27^\circ$ , are smaller than those located on the aft with a  $23.5^\circ$  deadrise angle (Fig. 11b).

During the experiments, it was discovered that some pressure sensors in way of the chine recorded negative values. In some cases, these negative pressures may occur as a result of temperature shock when the sensor rapidly moves between different environments. Van Nuffel et al.

(2013) studied the parameters that affect the accuracy of dynamic pressure measurements during water impact. They observed that several factors, including the data sampling rate, the condition of the surface of the structure, how the sensor is mounted, the water surface conditions, and the temperature sensitivity of the pressure transducers, may lead to inaccurate pressure measurement. It is possible to avoid temperature shocks by using piezoelectric pressure sensors with a preloaded sleeve, which is available for the sensors used in this experiment. Moreover, covering the sensor diaphragm with electrical tape or a thin layer of petroleum jelly could help reduce unexpected phenomena during the experiment.

As explained in section 2, before each test, the water surface must be completely calmed down, the pressure sensors must be dry, and the cables inside the wedge need to be secured. Fig. 11 shows that negative pressures are evident on the unstiffened bottom and far away from wedge apex. However, it almost disappears on the stiffened bottom. Consequently, the negative pressure can be a result of a pressure relaxation caused by the plate deflection. A similar phenomenon was found for pressure points near the chine in numerical simulations (Hosseinzadeh and Tabri, 2021b; Hosseinzadeh et al., 2023). It can also be observed that the pressure points on the unstiffened bottom reach their peak values slightly later than those on the stiffened bottom (see Fig. 11). Due to the rigidity of the unstiffened and stiffened plates, the time lag ( $t_d$ ) in the pressure time history will become greater for each sensor that is further away from the keel. This phenomenon becomes more noticeable for smaller deadrise angles and higher impact velocities (Fig. 11b).

The peak values of pressure sensors along the wedge's bottom plates at various initial drop heights obtained from experimental data are compared in Fig. 12. The x-axis presents the location of each sensor. As expected, because of more flexibility on the unstiffened bottom of the aluminium wedge, the peak pressure of the unstiffened bottom is smaller than that of the stiffened bottom.

The experiments were conducted using wedges with two different masses in order to assess the influence of mass on the pressure distribution. Fig. 13 compares the pressure time histories of two different masses of the wedge for the sensors on unstiffened ( $P1_U$ ) and stiffened bottom ( $P5_S$ ) at 100 [cm] drop height. It is shown that for the lighter wedge, the pressure load becomes smaller, and the pressure peak happens slightly later for the heavier wedge.

A comparison of unstiffened (U) and stiffened (S) maximum pressure with two different masses of the wedge obtained from experimental data at various impact velocities on section A-A of the wedge is presented in Fig. 14. Detailed results of the wedge with the mass of  $M_2$  are shown in the smaller plots on each figure. Fig. 15 shows a comparison between unstiffened and stiffened maximum pressure with two different masses at various impact velocities on section B-B of the wedge. It is also shown that the hydrodynamic pressures are very sensitive to the change of deadrise angle. Due to rigidity of the stiffened panel, the maximum pressure on the starboard side of the wedge is higher than those on port side. This is more evident for the case of higher impact velocities. Furthermore, the wedge's weight does not appear to significantly affect the maximum pressure at low-impact velocities, but it makes a significant difference at higher impacts.

#### 4.3. Structural response

The structural response of the non-prismatic aluminium wedge was examined using twenty strain gauges positioned at different locations on the unstiffened and stiffened bottom plates. Fig. 3 demonstrates the arrangement of the strain gauges in the transverse and longitudinal directions. It is worth noticing that the location of the strain gauges is symmetric on the bottom plates. It is expected that fluid-structure interaction phenomena can have a considerable effect on the dynamics of the structural response for the unstiffened bottom with 4 mm thickness. Fig. 16 compares experimental measurements of transverse



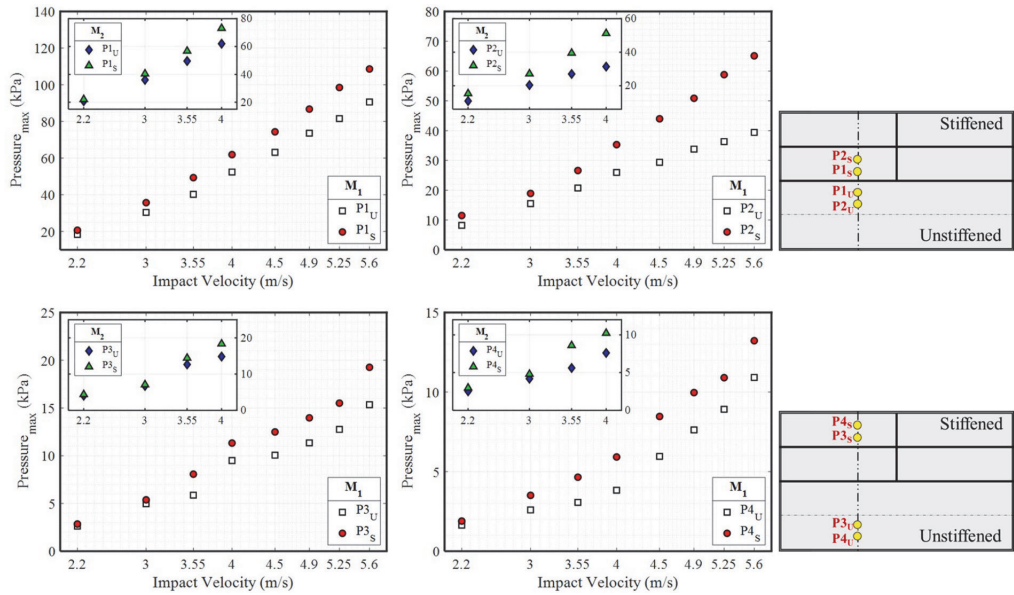


Fig. 14. Comparison of unstiffened (U) and stiffened (S) maximum pressure with two different masses obtained from experimental data at various impact velocities on section A-A of the wedge ( $\beta = 27 \text{ deg.}$ ) (Note: Smaller plot on each figure illustrates maximum pressure of the heavier wedge).

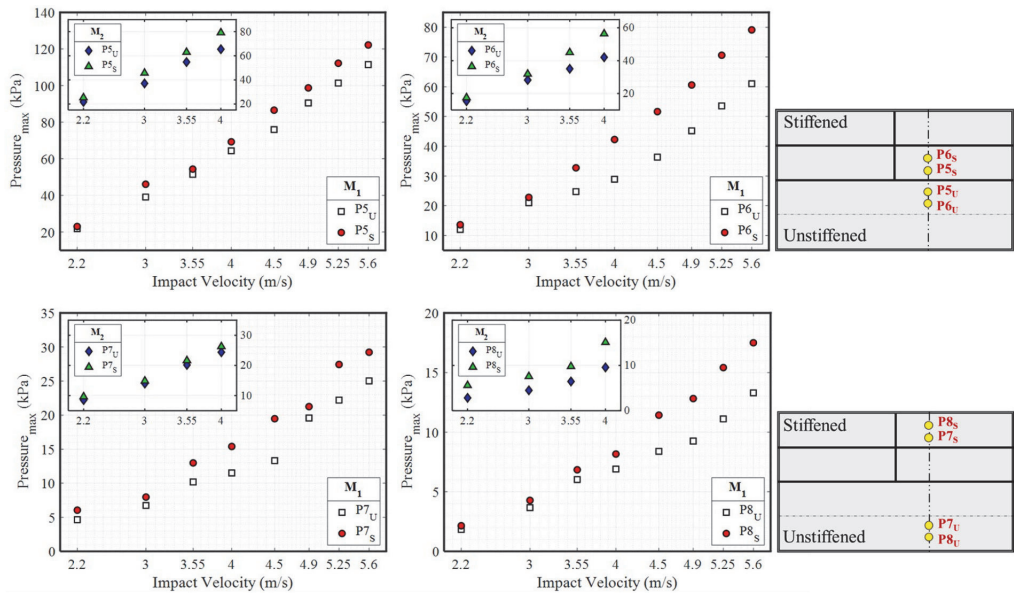


Fig. 15. Comparison of unstiffened (U) and stiffened (S) maximum pressure with two different masses obtained from experimental data at various impact velocities on section B-B of the wedge ( $\beta = 23.5 \text{ deg.}$ ) (Note: Smaller plot on each figure illustrates maximum pressure of the heavier wedge).

strain gauges on unstiffened and stiffened bottom plates with 100 [cm] initial drop height. The measured strain follows similar behaviour in time for strain gauges that were placed close to the keel on both bottom plates (S2T, S5T, and S8T). The transverse strains begin at zero, reach a maximum, and then gradually decrease back to zero. As expected, the strain values on the unstiffened plate are much higher than those on the

stiffened plate. Since the S5T<sub>S</sub> and S6T<sub>S</sub> strain gauges were positioned on top of the transverse stiffener, their peak values are relevantly lower. Moreover, it is found that the behaviour of the strain time history for the gauges located close to the chine of the wedge is different (S3T, S6T, and S9T). For these sensors, transverse strain values start at zero, reach the maximum negative value, increase until the maximum positive value,

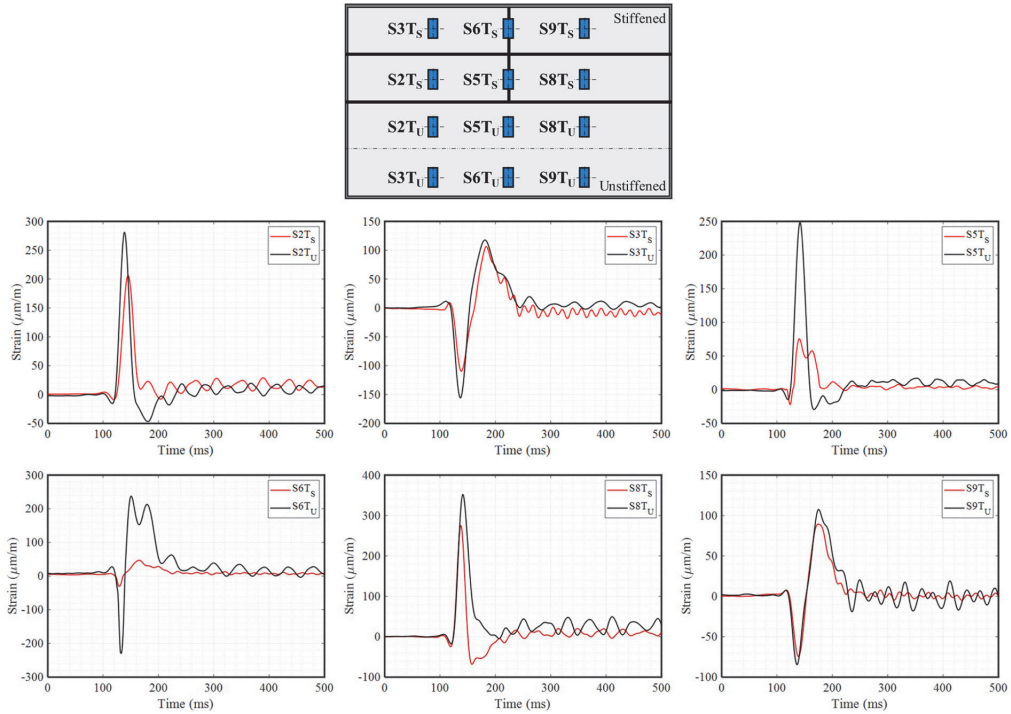


Fig. 16. Comparison of the experimental strains results over time in transverse direction on unstiffened and stiffened bottoms with 100 [cm] initial drop height.

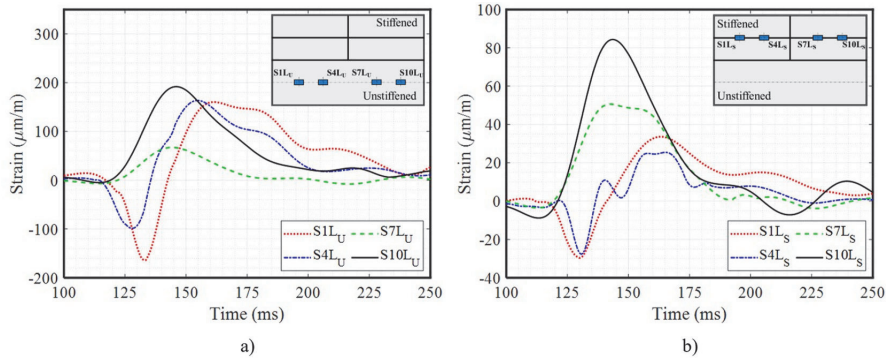


Fig. 17. Comparison of the experimental strains results over time in longitudinal direction with 100 [cm] initial drop height: a) unstiffened bottom; b) stiffened bottom.

and then gradually decay to zero. It is worth noting that at the time of maximum positive strain on the gauges near the keel, the strain gauges close to the chine reach their maximum negative value, which is due to the deformation of the bottom plate. The effect of the deadrise angle on strain results is clear, as the gauges placed on the section with a lower deadrise angle (S8T and S9T) have a higher peak value.

The time history of strain responses reveals two phases. During phase one, the structure experiences the maximum strain. During phase two, the strain begins to decrease, while the influence of structural dynamics becomes increasingly evident. Fig. 16 clearly shows that the elastic vibration on the unstiffened plate is more remarkable than that on the stiffened plate. In fact, the elastic vibration is not evident in the results of

sensors located on the top of the transverse stiffener (S5T<sub>S</sub> and S6T<sub>S</sub>). It is important to note that the hydroelasticity behaviour of the bottom plates differs from that described by Faltinsen (2000, 2005), who discovered that the maximum strain occurs during the free vibration phase. This could be attributed to the fact that in Faltinsen's (2000) study, the whole plate is wet at the end of the structural inertia phase. Then, the plate starts to vibrate freely. In the study presented, the bottom plates are wet by the end of phase two and the maximum deflection and strain occur in the partially wetted phase. These observations are confirmed by Luo et al. (2012) and Ren et al. (2021).

The time histories of the experimental strain responses in the longitudinal direction with an initial drop height of 100 [cm] for a short

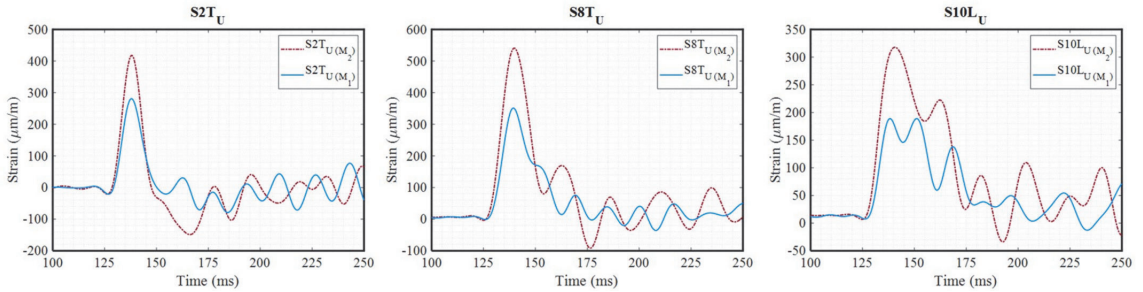


Fig. 18. Influence of mass of the wedge on the strain values on transverse direction (S2T<sub>U</sub>, S8T<sub>U</sub>) and longitudinal direction (S10L<sub>U</sub>) of unstiffened bottom at 100 [cm] drop height.

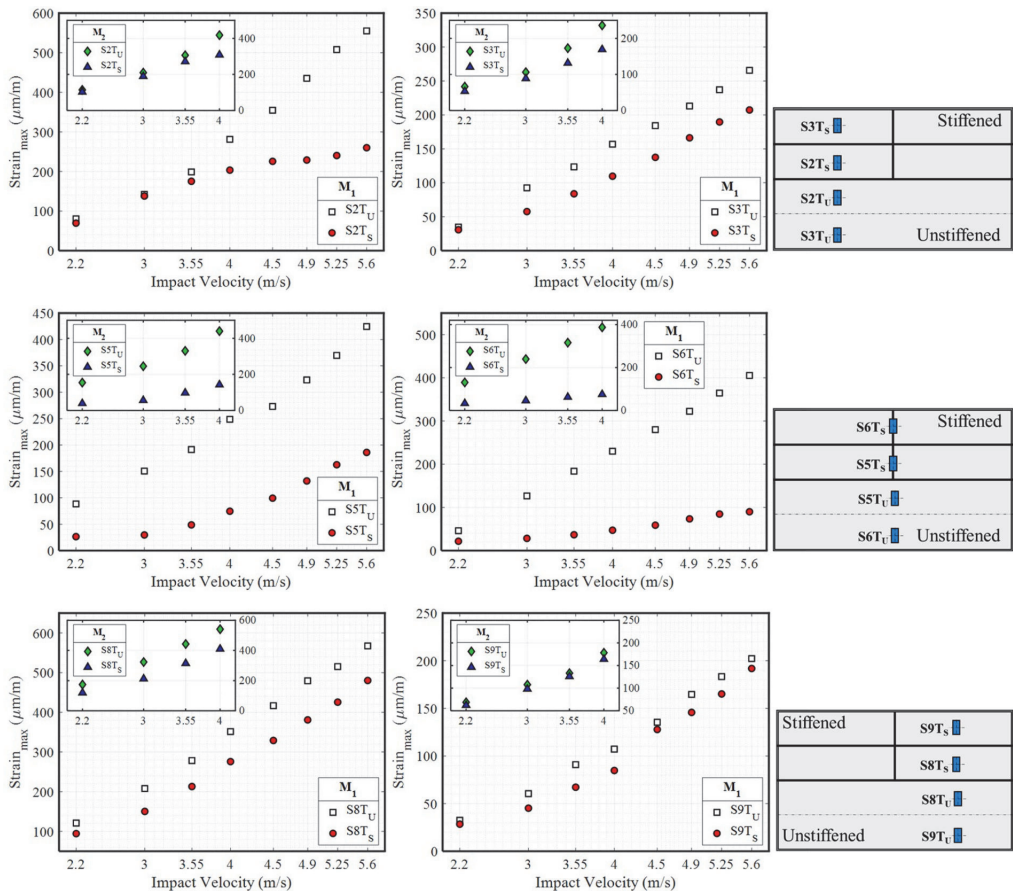


Fig. 19. Comparison between unstiffened (U) and stiffened (S) maximum transverse strain values of two different masses of the wedge at various impact velocities (Note: Smaller plot on each figure illustrates maximum strain of the heavier wedge).

period of time are illustrated in Fig. 17. The longitudinal direction strain gauges on the stiffened bottom were located on the top of the longitudinal stiffener, as shown in Fig. 3. It is observed that on the unstiffened plate, the maximum strain value gradually increases with decreasing the deadrise angle (Fig. 17a). The strain peak values for sensors placed on the stiffened plate are significantly lower than those of the unstiffened

plate (Fig. 17b). The gauges S1L and S4L ( $25 < \beta < 30$ ) have a negative maximum value at the same time that the gauges S7L and S10L ( $20 < \beta < 25$ ) reach their maximum value. This is caused by the deformation of the bottom plates.

Fig. 18 shows a comparison of strain time histories of the wedge with two masses in both transverse (S2T<sub>U</sub>, S8T<sub>U</sub>) and longitudinal (S10L<sub>U</sub>)

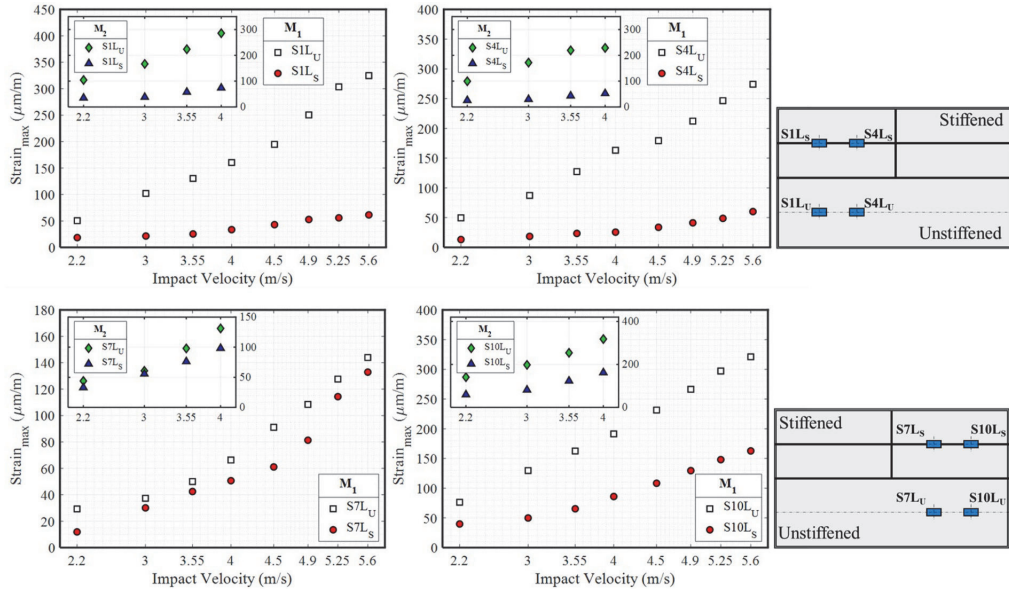


Fig. 20. Comparison between unstiffened (U) and stiffened (S) maximum longitudinal strain values of two different masses of the wedge at various impact velocities (Note: Smaller plot on each figure illustrates maximum strain of the heavier wedge).

directions of the unstiffened bottom at 100 [cm] drop height. The body mass seems to affect the structural response of the wedge. In fact, as the mass reduces (i.e., for a lighter wedge), the strain peak value becomes smaller. Elastic vibrations become more prominent for the heavier wedge.

The maximum transverse strain values on the unstiffened bottom plate of the wedge obtained from experimental data are compared against those of the stiffened bottom plate at various impact velocities (see Fig. 19). The maximum strain of the heavier wedge is shown in the smaller plot in each figure. Similarly, the strain peak values of the gauges located in the longitudinal direction for both stiffened and unstiffened plates are presented in Fig. 20. The results of the unstiffened bottom show that the maximum strain increased at a greater rate for the gauges close to the centre than for those near the chine as the drop height increases (i.e., the impact velocity becomes higher).

#### 4.4. Hydroelastic effects

To further analyse the effect of impact-induced loads on the structural responses, the relationship between the natural frequency of the wedge and the impact time is studied. Fig. 21 illustrates the frequency distribution of recorded strain responses of two gauges on both unstiffened (U) and stiffened (S) bottom plates at different initial drop heights. An FFT (Fast Fourier Transformation) analysis of the time histories of strain responses is conducted to obtain the frequency distribution of the wedge model. Due to the different structural rigidities of the port and starboard of the wedge, a comparison of the FFT results is also presented.

In Fig. 21, a frequency peak of 3.3 Hz is depicted, which can be attributed to the immersion of the structure. It is shown that even at high impact velocities, the effect of this peak on both strain gauges is relatively minimal. As a result of the frequency analysis of the strain responses, the frequency of 30 Hz is the natural frequency of the structure, and as expected, it remains constant with increasing impact velocity. In addition, from the time histories of measured strain (see Fig. 16), it is observed that the oscillation period after the maximum strain value is

approximately 0.032 s. The FFT analysis reveals a frequency component of around 43–46 Hz, which is the frequency of the wedge at the water surface and slightly increases with increasing impact velocity. It is observed that the frequency amplitude of strain responses on the port is higher than that on the starboard due to the stiffer structure on the starboard. According to the frequency analysis, it may be concluded that the third frequency component in Fig. 21 occurs due to the hydroelastic impact on the bottom plates. As shown in Fig. 21 c, the strain gauges S2 and S8 present peak frequencies of 75 Hz and 85 Hz, respectively, for the experiment with a 200 [cm] initial drop height. Depending on the impact velocity and the location of sensors, this peak frequency refers to the second natural frequency of the bottom plates.

Additionally, the influence of the wedge’s mass on the frequency distribution of the strain responses on the unstiffened bottom plate for the experiment with two different initial drop heights is compared in Fig. 22. From the time histories of strain responses (see Fig. 18), it was expected that the mass of the wedge affects the natural frequency of the structure. As shown in Fig. 22, the natural frequency of the heavier wedge is 22.5 Hz, which is lower than the natural frequency of the lighter wedge presented in Fig. 21. It can be concluded that the mass of the wedge affects the frequency distributions and its amplitude of the strain responses, and an increase in the structure’s mass leads to a decrease in its natural frequency.

To comprehend the importance of hydroelasticity on slamming loads, the effect of structural stiffness, deadrise angle, and impact velocity on the impact-induced loads have also been examined. Based on the findings of Faltinsen (2000), hydroelastic slamming is highly dependent on the ratio between the wetting time (load period) and the first natural period of the structure, the impact velocity, and the deadrise angle. Accordingly, for load periods above the natural period, the effects of hydroelasticity can be ignored, and the quasi-static method may be suitable for the idealisation of slamming problems. In this paper, the hydroelastic effect on both stiffened and unstiffened plates of the wedge is studied by comparing the experiment results against a quasi-static method. The structural response can be calculated in a simplified way by assuming that the panel is subjected to a uniform pressure

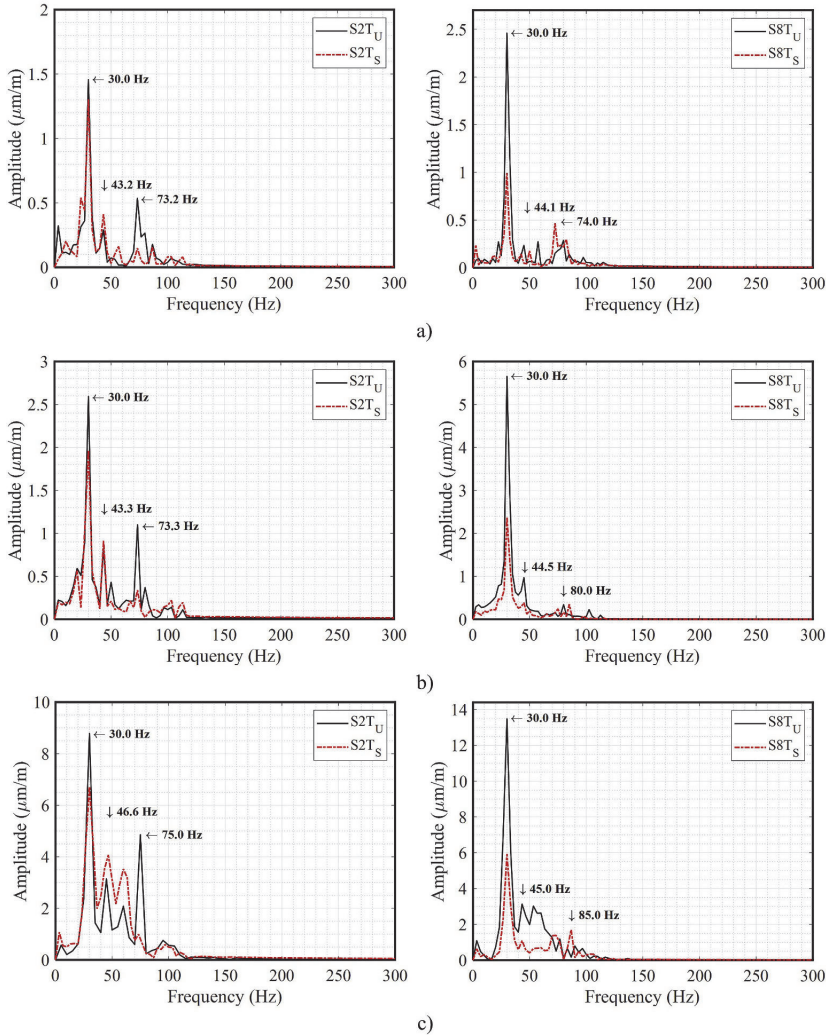


Fig. 21. Frequency distribution of recorded strain responses on both unstiffened (U) and stiffened (S) bottom plates at: a) 25 [cm]; b) 100 [cm]; c) 200 [cm] initial drop height.

distribution (Stenius, 2006; I. Stenius et al., 2011). According to engineering beam theory, the quasi-static maximum strain can be expressed as

$$\epsilon_{max}^q = \mu_\epsilon \frac{y_a \rho_w \pi^2 L^2 V_i^2}{48 D \tan \beta} \quad (3)$$

where  $\rho_w$  is the density of water,  $V_i$  is impact velocity,  $\beta$  is deadrise angle,  $L$  is the length from wedge apex to the chine,  $D$  is bending stiffness, and  $y_a$  is maximum normal distance from neutral plane to panel surface. In Eq. (3),  $\mu_\epsilon$  is boundary condition factor and equals to 1 for clamped-clamped (CC) and 1.5 for simply supported (SS) boundary. According to the plate theory, the unstiffened plate flexural rigidity ( $D_U$ ) is determined by the Young's modulus ( $E$ ), the Poisson's ratio ( $\nu$ ), and cube of the plate's thickness ( $t$ ) and expressed as

$$D = \frac{Et^3}{12(1 - \nu^2)} \quad (4)$$

The values of the parameters used in this equation were presented in Table 2. The stiffened plate flexural rigidity ( $D_S$ ) with longitudinal and transverse stiffeners was calculated using a numerical study. A non-dimensional maximum strain parameter is used to determine the importance hydroelasticity

$$\epsilon_{nd}^e = \frac{\epsilon_{max}^e}{\epsilon_{max}^q} \quad (5)$$

where  $\epsilon_{max}^e$  is the maximum strain measured by experimental study and  $\epsilon_{max}^q$  is the maximum strain calculated by Eq. (3). A normalised parameter proposed by Faltinsen (2000) can be used to assess the hydroelasticity of the structure in slamming studies. As expressed in Eq. (6), a non-dimensional parameter called hydroelasticity factor ( $R_F$ ) can be employed for quantifying inertial and elastic effects

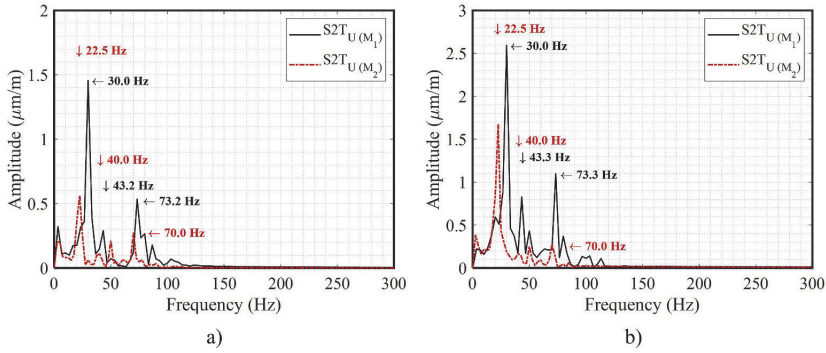


Fig. 22. Effect of mass of the wedge on the frequency distribution of recorded strain responses on the unstiffened bottom plate at: a) 25 [cm]; b) 100 [cm] initial drop height.

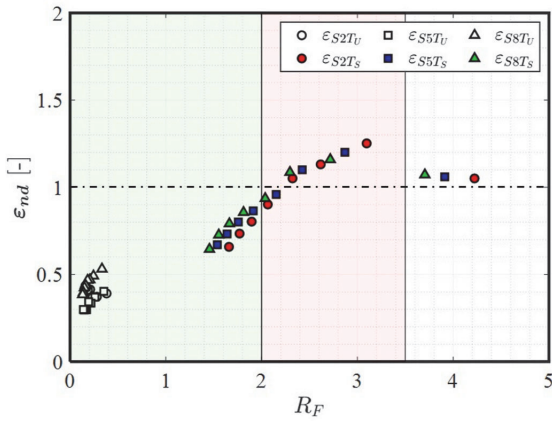


Fig. 23. Nondimensional maximum strain ratio calculated by quasi-static formula and experimental data versus hydroelasticity factor on both unstiffened and stiffened plates.

$$R_F = \frac{\tan \beta}{V_i} \sqrt{\frac{D}{\rho_w L^3}} \quad (6)$$

The smaller values of  $R_F$  correspond to a stronger coupling effect between fluid and structure. For the critical value of  $R_F$ , hydroelasticity has a significant effect on the water entry problem, and a strong two-way coupling should be applied to investigate slamming loads (Faltinsen, 2000; Piro and Maki, 2013; Panciroli et al., 2015). A plot of the ratio of maximum strain against the hydroelasticity factor is shown in Fig. 23. When  $R_F$  tends to infinity, the ratio is close to 1. This indicates that the quasi-static solution is sufficient to predict maximum structural response. For  $R_F > 3.5$ , the hydroelastic effect may become negligible, and thus the wedge can be analysed as a rigid body. The hydroelastic influence on impact loads is moderate for  $2 < R_F < 3.5$  confirming a weakly coupling between fluid and structure. Accordingly, the role of hydroelasticity is significant for  $R_F < 2$  as the quasi-static solution is not able to predict the structural response precisely. In addition, it is shown that the quasi-static method always overestimates the structural response on the unstiffened bottom of the wedge due to different bending stiffness on that side.

Since the stiffened and unstiffened bottoms have different flexural rigidities, the hydroelasticity factor has been calculated separately for each plate and named  $R_{FS}$  and  $R_{FU}$ , respectively. The variations of

hydroelasticity factors of the unstiffened and stiffened bottoms at different deadrise angles along the wedge and at various impact velocities are demonstrated in Fig. 24. There is a noticeable influence of hydroelasticity on the unstiffened plate for all considered impact velocities (presented in Table 5). It is also shown that hydroelasticity becomes more important by decreasing the deadrise angle. However, in the case of the stiffened plate, the behaviour is different and hydroelasticity only matters at high impact velocities. For instance, at 25° deadrise angle the hydroelastic effects appear after 4 [m/s] impact velocity ( $R_{FS} < 2$ ).

## 5. Conclusions

This paper examined the effects of hydroelasticity on the hydrodynamic pressure and structural response of a complex three-dimensional V-shaped structure. The simultaneous structural responses caused by hydrodynamic loads were studied experimentally for the cases of high impact water entry on a non-prismatic aluminium wedge. The bottom of the wedge was made up of a 4 mm plate thickness and the deadrise angle varied from 20 to 30°. The starboard bottom of the wedge was stiffened with longitudinal and transverse stiffeners, whereas the port bottom was unstiffened to provide different structural flexibility and allow for hydroelastic responses. Two masses of the wedge were tested to examine the effect of mass on the results. A series of free-fall drop tests were conducted at a variety of drop heights ranging from 25 cm to 200 cm, with an increment of 25 cm. Experimental uncertainty analysis confirmed the high-quality dataset made available. The experimental data presented provided additional insights into the influence of hydroelasticity on slamming induced loads experienced by complex structures. The latter has been supported through parametric studies that explored the effects of three-dimensionality, drop height (impact velocity), deadrise angle, and structural rigidity on the vertical acceleration, slamming pressure, and strain responses.

The following conclusions can be drawn:

- The comparison between the stiffened and unstiffened bottom pressure explains that the peak pressure of the stiffened bottom is higher than that of the unstiffened bottom. The pressure relaxation caused by the plate deflection influences the pressure values of the unstiffened bottom, and as a result, the peak pressure value is reached later than that of the stiffened bottom. This is more evident for higher impact velocities and lower deadrise angles. The three-dimensionality of the structure also influences the distribution of hydrodynamic pressures.
- The time history of strain responses can be decomposed into two phases. During phase (1), the structure experiences the maximum strain. Elastic vibrations appear in phase (2). The bottom plates

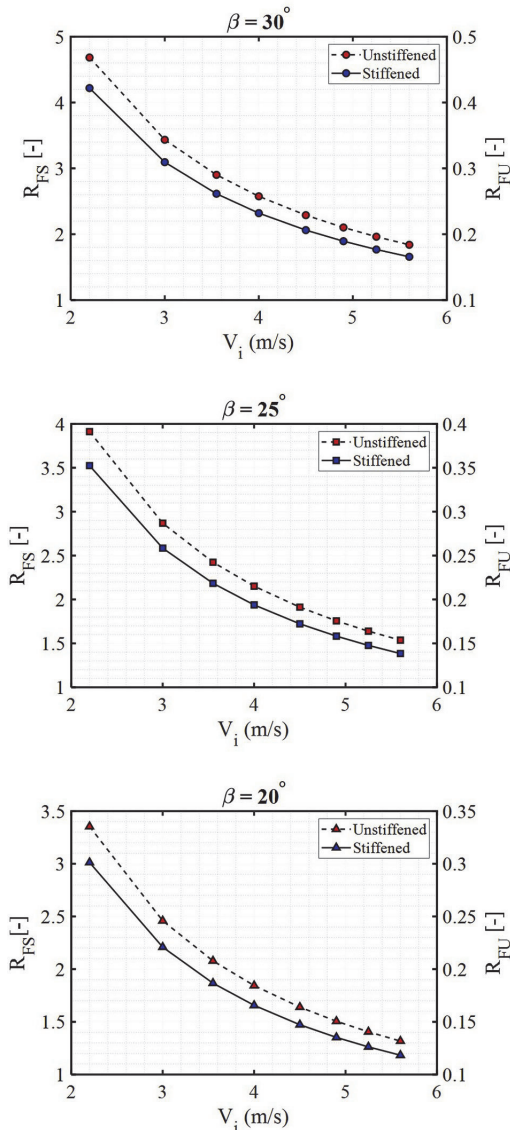


Fig. 24. Nondimensional hydroelasticity factor at different deadrise angles versus the impact velocity for both unstiffened ( $R_{FU}$ ) and stiffened ( $R_{FS}$ ) plates of the wedge (Note the different y-axis for  $R_{FU}$  and  $R_{FS}$ ).

experience maximum strain and deformation during the partially wetted phase. The elastic vibrations become more noticeable on the unstiffened bottom at high impact velocities.

- The importance of hydroelasticity can be assessed by a factor which is dependent on the deadrise angle, impact velocity, bending stiffness, and the first natural period of the structure. It was shown that the hydroelasticity has a significant effect on the unstiffened bottom ( $R_{FU}$ ) at all examined impact velocities, whereas for the stiffened bottom ( $R_{FS}$ ), it becomes important only at high impact velocities and small deadrise angles.
- An FFT analysis of the measured strain responses reveals that the impact velocity has a negligible effect on the wedge's first natural

frequency, while it influences the second natural frequency of the bottom plates. This highlights the importance of coupled FSI analysis on the unstiffened plate. The study also concludes that the mass of the wedge affects its natural frequency and that as the mass of the structure increases, the natural frequency decreases.

The results presented lead to better understanding of the hydroelastic nature of the impact-induced loads that may influence structural integrity of ships and high-speed advanced marine vehicles subject to slamming loads. Future research could focus more on the influence of asymmetric loads.

#### Credit author statement

**Saeed Hosseinzadeh:** Conceptualization, Formal analysis, Data processing, Experimental setup, Software, Writing – original draft, Writing – review & editing. **Kristjan Tabri:** Resources, Supervision, Project administration, Funding acquisition, Writing – review & editing. **Spyros Hirdaris:** Writing – review & editing, Supervision. **Tarmo Sahk:** Test implementation, Software, Data curation, Data processing.

#### Declaration of competing interest

The authors declare that they have no known competing financial interests or personal relationships that could have appeared to influence the work reported in this paper.

#### Data availability

Data will be made available on request.

#### Acknowledgements

This research work has been financially supported by the Estonian Research Council via the grants PRG83 (Numerical simulation of the FSI for the dynamic loads and response of ships) and PRG1820 (Dynamic response of offshore structures). The authors would also like to thank the staff of the Marine Technology Competence Center at Tallinn University of Technology (TALTECH MARTE) for their valuable support of the experimental study.

#### References

- Berezitski, A., 2001. Slamming: the role of hydroelasticity. *Int. Shipbuild. Prog.* 48, 333–351.
- Chuang, S.L., 1966. Slamming of rigid shaped bodies with various deadrise angles. David Taylor Model Basin (DTMB). Report Number-2268 (USA). <https://apps.dtic.mil/sti/pdfs/AD0643235.pdf>.
- Chuang, S.L., 1970. Investigation of Impact of Rigid and Elastic Bodies with Water. Naval Ship Research and Development Center (NSRDC), Washington, D. C. Report Number-3248. <https://apps.dtic.mil/sti/pdfs/AD0702727.pdf>.
- Chuang, S.L., 1973. Slamming tests of three-dimensional models in calm water and waves. David Taylor Model Basin (DTMB). Report Number-4095 (USA). <https://apps.dtic.mil/sti/pdfs/AD0767021.pdf>.
- Cui, S., Kiat Cheong, H., Hao, H., 1999. Experimental study of dynamic buckling of plates under fluid-solid slamming. *Int. J. Impact Eng.* 22 (7), 675–691. [https://doi.org/10.1016/S0734-743X\(99\)00022-6](https://doi.org/10.1016/S0734-743X(99)00022-6). Elsevier Science Ltd.
- De Backer, G., Vantorre, M., Beels, C., De Pré, J., Victor, S., De Rouck, J., Blommaert, C., Van Paepegem, W., 2009. Experimental investigation of water impact on axisymmetric bodies. *Appl. Ocean Res.* 31 (3), 143–156. <https://doi.org/10.1016/j.apor.2009.07.003>.
- Dong, C., Sun, S., Song, H., Wang, Q., 2019. Numerical and experimental study on the impact between a free-falling wedge and water. *Int. J. Nav. Archit. Ocean Eng.* 11 (1), 233–243.
- Duan, L., Zhu, L., Chen, M., Pedersen, P.T., 2020. Experimental study on the propagation characteristics of the slamming pressures. *Ocean. Eng.* 217, 107868.
- Eastridge, J.R., 2017. An experimental study in the hydroelastic response of an aluminum wedge in drop tests. Available at: <https://scholarworks.uno.edu/td/2317>.
- Facci, A.L., Porfiri, M., Ubertini, S., 2016. Three-dimensional water entry of a solid body: a computational study. *J. Fluid Struct.* 66, 36–53. <https://doi.org/10.1016/j.jfluidstruct.2016.07.015>.

- Fairlie-Clarke, A.C., Tveitnes, T., 2008. Momentum and gravity effects during the constant velocity water entry of wedge-shaped sections. *Ocean. Eng.* 35 (7), 706–716. <https://doi.org/10.1016/j.oceaneng.2006.11.011>.
- Faltinsen, O.M., 2000. Hydroelastic slamming. *J. Mar. Sci. Technol.* 5 (2), 49–65.
- Faltinsen, O.M., 2005. *Hydrodynamics of High-Speed Marine Vehicles*. Cambridge University Press.
- Faltinsen, O.M., Chezhian, M., 2005. A generalized Wagner method for three-dimensional slamming. *J. Ship Res.* 279–287. <https://doi.org/10.5957/jsr.2005.49.4.279>.
- Hassoon, O.H., Tarfaoui, M., Alaoui, A.E.M., 2017. An experimental investigation on dynamic response of composite panels subjected to hydroelastic impact loading at constant velocities. *Eng. Struct.* 153, 180–190. <https://doi.org/10.1016/j.engstruct.2017.10.029>.
- Hirdaris, S.E., Temarel, P., 2009. Hydroelasticity of ships: recent advances and future trends. *Proc. IME M J. Eng. Marit. Environ.* 223 (3), 305–330. <https://doi.org/10.1243/14750902JMEME160>.
- Hirdaris, S.E., Bai, W., Dessi, D., Ergin, A., Gu, X., Hermundstad, O.A., et al., 2014. Loads for use in the design of ships and offshore structures. *Ocean. Eng.* <https://doi.org/10.1016/j.oceaneng.2013.09.012>.
- Hosseinzadeh, S., Tabri, K., 2021a. Free-fall water entry of a variable deadrise angle aluminium wedge: an experimental study. *Dev. Anal. Design Mar. Struct.* 29–37. <https://doi.org/10.1201/9781003230373-4>.
- Hosseinzadeh, S., Tabri, K., 2021b. Hydroelastic effects of slamming impact loads during free-fall water entry. *Ships Offshore Struct.* 16 (Suppl. 1), 68–84. <https://doi.org/10.1080/17445302.2021.1954320>.
- Hosseinzadeh, S., Izadi, M., Tabri, K., 2020. Free fall water entry of a two-dimensional asymmetric wedge in oblique slamming: a numerical study. In: 39th International Conference on Ocean, Offshore & Arctic Engineering. <https://doi.org/10.1115/OMAE2020-18645>.
- Hosseinzadeh, S., Tabri, K., Topa, A., Hirdaris, S.E., 2023. Slamming loads and responses on a non-prismatic stiffened aluminium wedge: Part II. *nu. simulat. Ocean Eng.*
- Izadi, M., Ghadimi, P., Fadavi, M., Tavakoli, S., 2018. Numerical modeling of the freefall of two-dimensional wedge bodies into water surface. *J. Braz. Soc. Mech. Sci. Eng.* 40 (1), 24. <https://doi.org/10.1007/s40430-017-0941-3>.
- Jalalilendi, M., Porfiri, M., 2018. Water entry of cylindrical shells: theory and experiments. *Waves*. <https://doi.org/10.2514/1.J056797>.
- Judge, C., Troesch, A., Perlin, M., 2004. Initial water impact of a wedge at vertical and oblique angles. *J. Eng. Math.* 48 (3), 279–303.
- Kamath, A., Bihs, H., Arntsen, Ø.A., 2017. Study of water impact and entry of a free falling wedge using computational fluid dynamics simulations. <https://doi.org/10.1115/1.4035384>.
- Khabakhpasheva, T.I., Korobkin, A.A., 2013. Elastic wedge impact onto a liquid surface: Wagner's solution and approximate models. *J. Fluid Struct.* 36, 32–49.
- Korobkin, A.A., 1996. Water impact problems in ship hydrodynamics. In: *Advances in Marine Hydrodynamics*; Computational Mechanics Publications, 5, pp. 323–371.
- Korobkin, A.A., Iafrafi, A., 2005. Hydrodynamic loads during initial stage of floating body impact. *J. Fluid Struct.* 21, 413–427.
- Lewis, S.G., Hudson, D.A., Turnock, S.R., Taunton, D.J., 2010. Impact of a free-falling wedge with water: synchronized visualization, pressure and acceleration measurements. *Fluid Dynam. Res.* 42 (3), 35509 <https://doi.org/10.1088/0169-5983/42/3/035509>.
- Luo, H., Wang, H., Guedes Soares, C., 2012. Numerical and experimental study of hydrodynamic impact and elastic response of one free-drop wedge with stiffened panels. *Ocean. Eng.* 40, 1–14. <https://doi.org/10.1016/j.oceaneng.2011.11.004>.
- Luo, H., Zhao, Z., Xie, P., Wu, H., Li, X., 2014. Experimental and numerical investigation on hydroelastic impact of one free-drop wedge with aluminum stiffened panels. In: *OCEANS 2014 - TAIPPEI*. IEEE, pp. 1–7. <https://doi.org/10.1109/OCEANS-TAIPPEI.2014.6964307>.
- Mai, T., Mai, C., Raby, A., Greaves, D.M., 2020. Hydroelasticity effects on water-structure impacts. *Exp. Fluid* 61 (9), 1–19. <https://doi.org/10.1007/s00348-020-03024-3>.
- Mei, X., Liu, Y., Yue, D.K., 1999. On the water impact of general two-dimensional sections. *Appl. Ocean Res.* 21 (1), 1–15. [https://doi.org/10.1016/S0141-1187\(98\)00034-0](https://doi.org/10.1016/S0141-1187(98)00034-0).
- Meziane, B., Alaoui, A.E.M., Nème, A., Leble, B., Bellanger, D., 2022. Experimental investigation of the influence of the panel stiffness on the behaviour of a wedge under slamming. *J. Fluid Struct.* 114, 103702 <https://doi.org/10.1016/J.JFLUIDSTRUCTS.2022.103702>.
- Mitra, S.K., Kuo, Y., 2006. In: *Digital Signal Processing: a Computer-Based Approach*, vol. 2. McGraw-Hill, New York.
- Panciroli, R., Porfiri, M., 2015. Analysis of hydroelastic slamming through particle image velocimetry. *J. Sound Vib.* 347, 63–78. <https://doi.org/10.1016/j.jsv.2015.02.007>.
- Panciroli, R., Abrate, S., Minak, G., Zucchelli, A., 2012. Hydroelasticity in water-entry problems: comparison between experimental and SPH results. *Compos. Struct.* 94 (2), 532–539. <https://doi.org/10.1016/j.compstruct.2011.08.016>.
- Panciroli, R., Shams, A., Porfiri, M., 2015. Experiments on the water entry of curved wedges: high speed imaging and particle image velocimetry. *Ocean. Eng.* 94, 213–222. <https://doi.org/10.1016/j.oceaneng.2014.12.004>.
- Peseux, B., Gornet, L., Donguy, B., 2005. Hydrodynamic impact: numerical and experimental investigations. *J. Fluid Struct.* 21, 277–303. <https://doi.org/10.1016/j.jfluidstruct.2005.04.011>.
- Peterson, R., Wyman, D., Frank, C., 1997. Drop tests to support water-impact and planing boat dynamics theory. <https://apps.dtic.mil/dtic/tr/fulltext/u2/a351983.pdf>.
- Piro, D.J., Maki, K.J., 2013. Hydroelastic analysis of bodies that enter and exit water. *J. Fluid Struct.* 37, 134–150. <https://doi.org/10.1016/j.jfluidstruct.2012.09.006>.
- Ren, Z., Javaherian, M.J., Gilbert, C.M., 2021. Kinematic and inertial hydroelastic effects caused by vertical slamming of a flexible V-shaped wedge. *J. Fluid Struct.* 103 <https://doi.org/10.1016/j.jfluidstruct.2021.103257>.
- Royce, R.A., 2001. *Two-dimensional Impact Theory Extended to Planing Craft with Experimental Comparisons*. Ph.D. Thesis. Naval Architecture and Marine Engineering. University of Michigan.
- Shams, A., Porfiri, M., 2015. Treatment of hydroelastic impact of flexible wedges. *J. Fluid Struct.* 57, 229–246. <https://doi.org/10.1016/j.jfluidstruct.2015.06.017>.
- Shams, A., Zhao, S., Porfiri, M., 2017. Hydroelastic slamming of flexible wedges: modeling and experiments from water entry to exit. *Phys. Fluids* 29, 37107. <https://doi.org/10.1063/1.4978631>.
- Southall, N.R., Lee, Y., Johnson, M.C., Hirdaris, S.E., White, N.J., 2014. Towards a pragmatic method for prediction of whipping: wedge impact simulations using OpenFOAM. June. In: *The Twenty-Fourth International Ocean and Polar Engineering Conference*. OnePetrol.
- Spinoso, E., Iafrafi, A., 2021. Experimental investigation of the fluid-structure interaction during the water impact of thin aluminium plates at high horizontal speed. *Int. J. Impact Eng.* 147, 103673 <https://doi.org/10.1016/J.IJIMPENG.2020.103673>.
- Stenius, I., 2006. Doctoral dissertation. In: *Finite Element Modelling of Hydroelasticity in Hull-Water Impacts*. KTH. <https://www.diva-portal.org/smash/get/diva2:11713/FULLTEXT01.pdf>.
- Stenius, I., Rosén, A., Kutteneuler, J., 2011. Hydroelastic interaction in panel-water impacts of high-speed craft. *Ocean. Eng.* 38 (2–3), 371–381. <https://doi.org/10.1016/j.oceaneng.2010.11.010>.
- Stenius, I., Rosén, A., Battley, M., Allen, T., 2013. Experimental hydroelastic characterization of slamming loaded marine panels. <https://doi.org/10.1016/j.oceaneng.2013.09.007>.
- Sun, H., Wang, D.-Y., 2018. Experimental and numerical analysis of hydrodynamic impact on stiffened side of three-dimensional elastic stiffened plates. *Res. Article Adv. Mech. Eng.* 10 (4) <https://doi.org/10.1177/1687814018767705>.
- Sun, Z., Korobkin, A.A., Sui, X.P., Zhi, Z., 2021. A semi-analytical model of hydroelastic slamming. *J. Fluid Struct.* 101, 103200 <https://doi.org/10.1016/J.JFLUIDSTRUCTS.2020.103200>.
- Swidan, A., Thomas, G., Rannuthugala, D., Amin, W., Penesis, I., Allen, T., Battley, M., 2016. Experimental drop test investigation into wetdeck slamming loads on a generic catamaran hullform. *Ocean. Eng.* 143–153. <https://doi.org/10.1016/j.oceaneng.2016.03.059>.
- Tassin, A., Korobkin, A.A., Cooker, M.J., 2014. On analytical models of vertical water entry of a symmetric body with separation and cavity initiation. *Appl. Ocean Res.* 48, 33–41. <https://doi.org/10.1016/j.apor.2014.07.008>.
- Tenzen, M., Moctar, O.E., Schellin, T.E., 2015. Experimental investigation of impact loads during water entry. *Ship Technol. Res.* 62 (1), 47–59. <https://doi.org/10.1179/0937725515Z.0000000003>.
- Tödter, S., Moctar, O.E., Neugebauer, J., Schellin, T.E., 2019. Experimentally measured hydroelastic effects on impact-induced loads during flat water entry and related uncertainties. <https://doi.org/10.1115/1.4044632>.
- Tveitnes, T., Fairlie-Clarke, A.C., Varyani, K., 2008. An experimental investigation into the constant velocity water entry of wedge-shaped sections. *Ocean. Eng.* 35 (14–15), 1463–1478. <https://doi.org/10.1016/j.oceaneng.2008.06.012>.
- Van Nuffel, D., Vepa, K.S., De Baere, I., Degrieck, J., De Rouck, J., Van Paepegem, W., 2013. Study on the parameters influencing the accuracy and reproducibility of dynamic pressure measurements at the surface of a rigid body during water impact. *Exp. Mech.* 53 (2), 131–144. <https://doi.org/10.1007/s11340-012-9619-z>.
- von Karman, T., 1929. *The Impact on Seaplane Floats during Landing*. National Advisory Committee for Aeronautics, Washington, DC. Technical Note No. 321.
- Vorus, W.S., 1996. A flat cylinder theory for vessel impact and steady planing resistance. *J. Ship Res.* 40, 89–106.
- Wagner, H., 1932. Über Stoß- und Gleitvorgänge an der Oberfläche von Flüssigkeiten. *Angew Math Mech* 12 (4), 193–215.
- Wang, S., Guedes Soares, C., 2014. Numerical study on the water impact of 3D bodies by an explicit finite element method. *Ocean. Eng.* 78, 73–88. <https://doi.org/10.1016/j.oceaneng.2013.12.008>.
- Wang, S., Guedes Soares, C., 2017b. Review of ship slamming loads and responses. *J. Mar. Sci. Appl.* 16, 427–445. <https://doi.org/10.1007/s11804-017-1437-3>.
- Wang, J., Lugni, C., Faltinsen, M., 2015. Experimental and numerical investigation of a freefall wedge vertically entering the water surface. *Phys. Procedia* 51, 181–203. <https://doi.org/10.1016/j.apor.2015.04.003>.
- Yan, D., Mikkola, T., Kujala, P., Hirdaris, S., 2022. Hydroelastic analysis of slamming induced impact on stiff and flexible structures by two-way CFD-FEA coupling 1–13. <https://doi.org/10.1080/107445302.2022.2116231>.
- Yettou, M.E., Desrochers, A., Champoux, Y., 2006. Experimental study on the water impact of a symmetrical wedge. *Fluid Dynam. Res.* 38 (1), 47–66. <https://doi.org/10.1016/j.fluidyn.2005.09.003>.
- Yettou, M.E., Desrochers, A., Champoux, Y., 2007. A new analytical model for pressure estimation of symmetrical water impact of a rigid wedge at variable velocities. *J. Fluid Struct.* 23 (3), 501–522. <https://doi.org/10.1016/j.jfluidstruct.2006.10.001>.





## Appendix 3 (Publication II)

**[P3]** Hosseinzadeh, S., Tabri, K., Topa, A., & Hirdaris, S. (2023). Slamming loads and responses on a non-prismatic stiffened aluminium wedge: Part II. Numerical simulations. *Ocean Engineering*, 279, 114309.





Contents lists available at ScienceDirect

## Ocean Engineering

journal homepage: [www.elsevier.com/locate/oceaneng](http://www.elsevier.com/locate/oceaneng)

# Slamming loads and responses on a non-prismatic stiffened aluminium wedge: Part II. Numerical simulations

Saeed Hosseinzadeh<sup>a,\*</sup>, Kristijan Tabri<sup>a,b</sup>, Ameen Topa<sup>c</sup>, Spyros Hirdaris<sup>d</sup>

<sup>a</sup> Department of Civil Engineering and Architecture, Tallinn University of Technology, Tallinn, Estonia

<sup>b</sup> Marine Technology Competence Center, Tallinn University of Technology, Kuressaare, Estonia

<sup>c</sup> Department of Maritime Technology, Universiti Malaysia Terengganu, Kuala Nerus, Malaysia

<sup>d</sup> Marine Technology Group, Department of Mechanical Engineering, Aalto University, Espoo, Finland

## ARTICLE INFO

Handling Editor: Prof. A.I. Incecik

## Keywords:

Flexible fluid structure interactions (FFSI)

Modelling and validation

Two-way coupling

Slamming loads & responses

Stiffened panels

## ABSTRACT

An experimental study was carried out to examine the impact-induced loads and structural responses of a three-dimensional non-prismatic aluminium wedge. The findings of the experimental study were presented in the first part of this publication, entitled "Slamming loads and responses on a non-prismatic stiffened aluminium wedge: Part I. Experimental study." This paper describes the second part of the study, which deals with numerical simulations of slamming loads acting on the wedge and its dynamic responses. Two different two-way coupling methods are assessed and compared to simulate the water entry problem. Initially, an explicit nonlinear finite element method with a Multi-Material Arbitrary Lagrangian-Eulerian (MMALE) solver is employed to evaluate the elastic response of the structure following a free-fall water impact. Subsequently, the hydroelastic slamming problem is modelled using a two-way coupled technique with a  $k-\epsilon$  turbulence model and implicit unsteady solver for both the fluid and structural domains (Star-CCM+/ABAQUS). The effect of viscosity on slamming loads and responses was examined, and numerical results are compared with experimental data. To investigate the effect of rigidity on structural response and bottom deflection, the wedge was designed with bottom plates of varying thickness. The computed results from the two numerical models and the experimental data are in good agreement. The study concluded that the bottom plates deformation affects hydrodynamic loads during slamming. It is also observed that impact-induced loads depend on the water impact velocity and the flexibility of the bottom plates. This suggests that the slamming pressure increases with an increase in impact velocity and decreases when the structures become more flexible. According to this study, both numerical models are suitable for accurate and efficient computations of hydroelastic slamming; however, the MMALE method results in larger numerical fluctuations.

## 1. Introduction

Hull slamming is a common problem in ship hydrodynamics that occurs due to the large relative motions between a ship's hull and the water surface, particularly in rough seas over short durations. Impulsive loads generated by slamming impact can cause significant local structural damage and induce global transient elastic vibrations of the structure, known as whipping (Abrate, 2013; Faltinsen, 2000, 2005; Hirdaris et al., 2014). One of the worst maritime disasters of the 20th century occurred on September 28, 1994, when the M/S Estonia sank in the Baltic Sea. According to the official report (JointAccident Investigation Commission, 1997), the bow visor malfunctioned due to extreme

wave impact, causing it to detach from the vessel. The damage has been attributed to severe slamming in a rough sea with a wind speed of 15–20 m/s and a significant wave height of 4–6 m (JointAccident Investigation Commission, 1997).

The water entry problem was initially studied by von Karman (1929), who applied momentum theory to predict slamming loads acting on a two-dimensional (2D) flat wedge model. Wagner (1932) developed von Karman's analytical model by considering the effect of free surface on the hydrodynamic pressures to achieve more realistic results. This asymptotic solution was extended by Vorus (1996) by incorporating a nonlinear term to the kinematic boundary condition in an incompressible flow for a rigid cylinder impact. Later, Savander et al.

\* Corresponding author. Department of Civil Engineering and Architecture, Tallinn University of Technology, Tallinn, Estonia.

E-mail address: [Saeed.Hosseinzadeh@taltech.ee](mailto:Saeed.Hosseinzadeh@taltech.ee) (S. Hosseinzadeh).

<https://doi.org/10.1016/j.oceaneng.2023.114309>

Received 4 January 2023; Received in revised form 6 March 2023; Accepted 22 March 2023

Available online 2 May 2023

0029-8018/© 2023 Elsevier Ltd. All rights reserved.

(2002) generalised Vorus's model to predict the slamming loads on three-dimensional planing surfaces. These analytical models relied on the potential theory, in which the viscosity and surface tension of the fluid were ignored and the potential flow around a rigid body was estimated. More recently, researchers discovered that the water entry phenomenon might become more severe at high impact velocities and low deadrise angles, for which the coupling between hydrodynamic pressures and structural responses intensifies (Faltinsen, 1999; Kapsenberg, 2011). In hydroelastic slamming, impact loads cause elastic deformations in the structure, which in turn affect fluid flow, causing the pressure field to decrease. Numerous studies have been conducted to investigate the effects of slamming loads on ships and offshore structures. Abrate (2013) provided an overview of the literature on the water entry phenomenon in both marine and aerospace applications. A comprehensive research summary on ship slamming loads and structural responses is presented by Wang and Soares (2017a).

In recent decades, various numerical methods have been employed by scientists thanks to the development of supercomputers. Wang and Soares (2012) used an explicit finite element method based on an Arbitrary Lagrangian-Eulerian (ALE) formulation to simulate two-dimensional (2D) water entry of rigid wedges and compared the results with analytical calculations. A review of the capabilities of Computational Fluid Dynamics (CFD) methods to estimate impact-induced loads on rigid wedge-shaped bodies can be found in Southall et al. (2015). By utilizing potential-based and CFD methods, Kim et al. (2017) investigated the pressure distribution, free surface evolution, and local slamming force on a wedge and a ship-like section. Kamath et al. (2017) presented an open-source numerical model to evaluate the water impact problem of a symmetrical rigid wedge and examined the ability of the CFD model to simulate the impact of a freely falling wedge. A finite volume method (FVM) was employed by Izadi et al. (2018) to simulate the free-fall of 2D rigid wedges in different deadrise angles. The effect of heel angle on pressure distribution, pile-up evolution, and impact loads of oblique water entry problems on an asymmetrical wedge was numerically analysed by Hosseinzadeh et al. (2020). The water entry process of a freefall lifeboat at various drop heights and angles was investigated by Huang et al. (2021), who discovered that a higher drop angle can reduce the risk of colliding and slamming pressure on the hull.

The majority of the analytical and numerical methods mentioned above were applied to rigid and simplified two-dimensional bodies. However, it could be challenging to implement them in complex three-dimensional (3D) flexible structures. In an attempt to tackle this problem, Stenius et al. (2007) used an explicit finite element method to study the influence of hydroelastic effects during the water entry impact of an elastic panel. The hydroelastic responses of flat stiffened panels under slamming loads were numerically investigated by Luo et al. (2010). They employed the ALE method to predict the slamming loads acting on rigid and elastic structures. Luo et al. (2012) investigated the slamming loads and responses of a complex 3D steel wedge with longitudinal and transverse stiffeners both experimentally and numerically. They simplified the coupled problem into a decoupled model and neglected the effect of elastic vibration on fluid motion. In their study, the pressure distribution was predicted using Wagner theory and applied to a FEM model to calculate stress responses. Stenius et al. (2011) provided numerical simulations of an elastic panel water impact for high-speed craft and concluded that both inertial and kinematic effects need to be explicitly considered to fully understand the hydroelastic problem. The effect of slamming pressure on a deformable flat stiffened plate using the ALE algorithm was investigated by Cheon et al. (2016). By examining the relation between the loading period and the natural period of vibration of the structure, Wang and Soares (2017b) studied the importance of hydroelasticity for local slamming induced responses on a rectangular plate. The water impact problem of a stiffened steel panel was simulated by using the fully coupled ALE algorithm (Wang and Guedes Soares, 2018). A comparison of the predicted slamming loads of

rigid and flexible panels revealed that flexibility could reduce the slamming-induced loads on the structure. Yu et al. (2019a) investigated the hydroelasticity of a wedge with stiffened panels in constant-velocity water entry. A semi-analytical hydrodynamic impact theory was used to model the fluid domain, while the structural response was solved using a modal superposition method. Yu et al. (2019b) used the multi-material ALE method in LS-DYNA to verify a proposed analytical model and examine the hydro-plastic slamming response of beams and stiffened panels. They discovered that the proposed hydro-plastic model accurately predicts permanent deflections of stiffened panels, and the coupling between hydrodynamic loads and structural deformations can be well captured. A numerical investigation of slamming loads acting on flat stiffened plates and their dynamic response presented by Truong et al. (2020). They employed a MMALE solver to simulate the slamming impact. The similarity of two FSI models, namely the structure dropping case and the water hitting case, was examined in their study. A comprehensive study by Truong et al. (2021) was carried out to demonstrate the FSI simulation methodology and modelling technique for predicting the slamming loads acting on stiffened plates of offshore structures. The authors employed FSI methods from four different commercial software and compared slamming pressure results of flat-stiffened steel plates against the analytical models proposed by the DNV Classification Standards (DNV-RP-C205, 2010) and existing experimental data (Mori, 1977). The numerical uncertainties due to discretization for the ALE method in predicting impact-induced loads on a rigid and elastic flat plate were investigated by Wang et al. (2021). These results illustrated that numerical errors affect the analysis of slamming loads, associated structural responses, and hydroelasticity analysis. Based on the results, they concluded that uncertainty due to domain discretization when using the ALE method is both case- and parameter-specific.

Strongly coupled methods combining Finite Volume Method (FVM) and Finite Element Method (FEM) can also be used to predict slamming loads and structural responses. A numerical investigation of hydroelastic slamming of symmetric flexible wedges was conducted by Hosseinzadeh and Tabri (2021a). In the latter publication, the authors study the effect of constant vertical velocity and free-fall impact on slamming pressures and bottom plate deflections. The results showed that the assumption of constant velocity causes overestimated slamming loads and associated structural responses on the elastic wedges as compared to the free-falling cases. Yan et al. (2022a) also applied a two-way coupled FVM-based CFD-FEA modelling procedure to study the slamming impact on stiff and flexible flat plates and wedge structures and discovered that stiff plates reach their peak pressure earlier and with a higher maximum pressure when compared to flexible plates. Recently, uncertainties of numerical simulations and experiments of relevance to flat plate impact based in ITTC procedure (ITTC, 2017) were assessed by Yan et al. (2022b). This work demonstrated that the percentage of validation uncertainty for peak pressure tends to be smaller at high impact velocities and is generally independent of the velocity for slamming forces.

The published literature shows that there are limited studies on the application of numerical approaches to assess hydroelastic slamming on three-dimensional bodies. It is also critical to recognize whether the fully two-way coupling method should be considered during the numerical analysis of impact-induced loads. The purpose of this paper is to verify and compare the results of slamming loads and responses on a 3D elastic structure. Numerical studies are carried out on a non-prismatic aluminium wedge with stiffened and unstiffened bottoms that freely falls into water at different impact velocities. Results are compared with experimental data presented in Hosseinzadeh et al. (2023). In order to assess the three-dimensional effects on the maximum slamming force, the numerical results of 2D and 3D wedges are compared at various impact velocities. The described flexible fluid structure interactions (FFSI) problem is simulated with two different numerical methods, namely: (a) an explicit nonlinear FEA method with a MMALE solver; (b) a two-way coupled assumption with a k- $\epsilon$  turbulence model and implicit

**Table 1**  
Material properties and specifications of the non-prismatic aluminium wedge.

Material parameters	Value
Length × Breadth × Height	1.5 × 0.94 × 0.45 [m]
Density ( $\rho_{Al}$ )	2700 [kg/m <sup>3</sup> ]
Modulus of Elasticity (E)	68 [GPa]
Shear Modulus (G)	26 [GPa]
Poisson Ratio ( $\nu$ )	0.33
Tensile Strength	300 [MPa]
Longitudinal and Transverse Stiffener	154 × 3 + 35 × 4 [mm]
Keel flat bar	60 × 5 [mm]
Thickness of the Endplates	10 [mm]
Thickness of the Side plates	4 [mm]

unsteady solver (CFD/FEM) for both the fluid and structural domains. To examine the influence of viscosity on the impact loads and dynamic response of elastic structures, the described water entry problem is analysed in an inviscid flow using the CFD and FEM coupling methods. All numerical idealisations assume free fall water entry.

A summary of the experimental work, including specifications of the non-prismatic aluminium wedge and sensor arrangement, is presented in Section 2. Section 3 describes the two-way coupling algorithm and the numerical settings employed, as well as the mesh study of the two computational methods. The results of the numerical studies are verified and compared with the experimental data in Section 4. Finally, Section 5 presents the main conclusions of this study.

**2. A summary of experimental work**

Hosseinzadeh et al. (2023) conducted a series of experiments to measure the slamming pressure and structural responses during free-fall water impact by designing a non-prismatic aluminium wedge made of alloy 5083-H111. The wedge section resembled a fore body structure of a medium-speed small craft. The test set-up was defined based on the practicalities involving the production of the wedge section on the laboratory scale and achieving sufficient stiffness difference on the port and starboard sides of the specimen. The bottom of the wedge was manufactured using two different plates with varying deadrise angles from 20° to 30°. The starboard side of the wedge was constructed with a

4 mm thick extruded aluminium panel with T-shaped longitudinal and transverse stiffeners (stiffened bottom), while the port side was unstiffened with a 4 mm thickness (unstiffened bottom). The material properties and dimensions of the wedge are summarized in Table 1. The wedge weighs 55 kg including all sensors, screws, welding, and the top frame.

Piezoelectric pressure transducers (16 in total) were used to measure the slamming pressures. The pressure sensors were symmetrically installed on the bottom of the wedge to compare the pressure data of the unstiffened and stiffened bottom plates. The structural responses of the wedge were measured using twenty linear strain gauges mounted on the inner side of the bottom plates in both transverse and longitudinal directions. In addition, three accelerometers were installed at the fore, middle, and aft of the keel and named  $A_f$ ,  $A_m$ , and  $A_a$ , respectively. Fig. 1 shows a schematic of the top view of the wedge containing the location of pressure sensors, strain gauges, and accelerometers. The pressure sensors on the wedge’s port and starboard sides are marked differently. For example,  $P1_S$  indicates the first pressure sensor on the stiffened bottom. On the other hand,  $P1_U$  represents the first pressure sensor on the unstiffened bottom. Similarly, the strain gauges on the stiffened and unstiffened bottoms of the wedge are labelled differently. For example,  $S1_L_S$  is the first strain gauge on the stiffened bottom in the longitudinal direction, and  $S1_T_U$  is the first strain gauge on the unstiffened bottom in the transverse direction. Detailed information on the experimental study including the test plan, data acquisition system, and uncertainties associated with the tests can be found in Hosseinzadeh et al. (2023).

**3. Numerical modelling**

In this section, two numerical approaches utilised for the computation of impact-induced loads and responses on a three-dimensional character is presented. The aluminium wedge with non-prismatic characteristics is numerically modelled using two different coupling methods under free-fall conditions. At first, the described FFSI problem is simulated with an explicit nonlinear FE scheme in LS-DYNA that accounts for the free surface of water by taking advantage of a MMALE solver. In this way both air and water can be idealized in the same element. It was assumed that the water free surface is undisturbed and that the fluid is

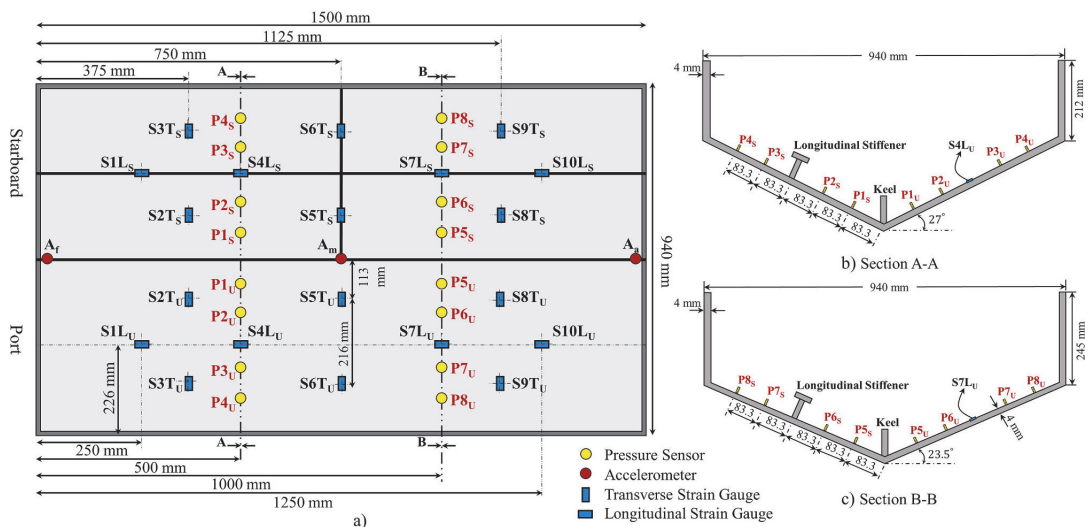


**Fig. 1.** Arrangement of sensors used in the experiment: a) location of pressure sensors, strain gauges, and accelerometers; b) A-A cross section with pressure sensor locations at 27-degree deadrise angle; c) B-B cross section with pressure sensor locations at 23.5-degree deadrise angle (reproduced from Hosseinzadeh and Tabri, 2021b).

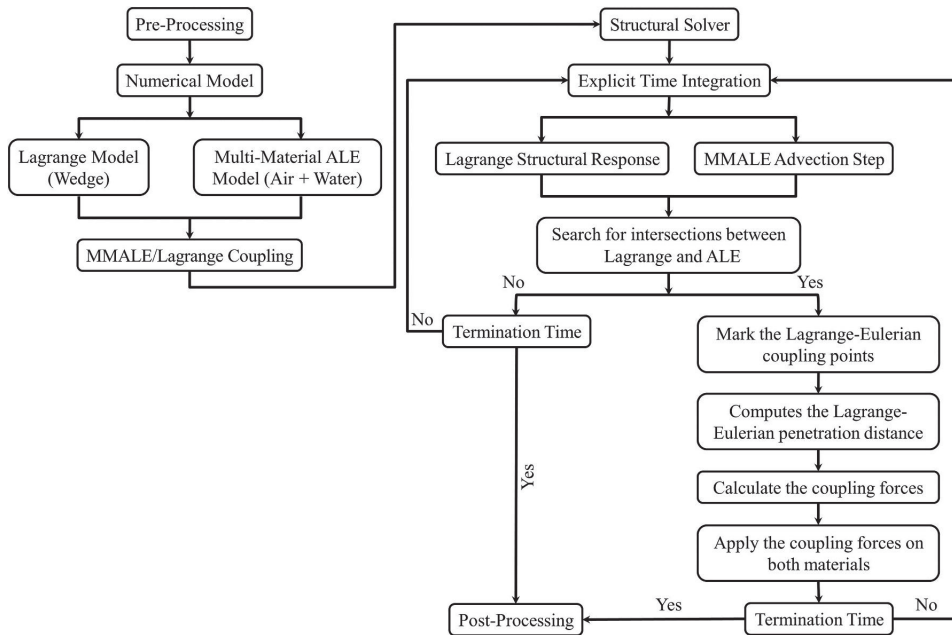


Fig. 2. The detail of the Multi Material Arbitrary Lagrangian-Eulerian (MMALE) algorithm (LS-DYNA Theory Manual, 2022; Souli and Benson, 2013).

incompressible and inviscid. The multi-material Eulerian formulation was applied to the fluid domain including water and air and the Lagrangian formulation was used to describe the deformations of the structure. In the second idealization method, a two-way coupled FVM (based on RANS CFD) and FEM approach was employed to model the defined phenomenon under viscous and inviscid assumptions. Therefore, part of the effort was dedicated to comparing the effects of viscosity on slamming loads.

### 3.1. Arbitrary Lagrangian-Eulerian (ALE) algorithm

The ALE algorithm is a computational method consisting of both Lagrangian and Eulerian formulations that applies conservation equations in FEA. Lagrangian formulations can be used to idealise structural dynamics by means of boundaries of Eulerian mesh forming the fluid domain (Souli and Benson, 2013). A detailed explanation of the mesh motion in the ALE method can be found in (Benson, 1992; Donea et al., 2004; Aquelet and Souli, 2008; Souli and Benson, 2013; LS-DYNA Theory Manual, 2022).

In FFSI problems, coupling between fluid and solid domains is a challenging task and may affect the accuracy of the results. Taking  $\Gamma_s$  and  $\Gamma_f$  as the boundaries of the solid and fluid domains, respectively, therefore,  $\Gamma_{fsi}$  is the FSI interface and can be defined as  $\Gamma_{fsi} = \Gamma_s \cap \Gamma_f$ . A coupling occurs between the fluid and the structure at the interface ( $\Gamma_{fsi}$ ) where the fluid pressure is transferred to the structure while the nodal velocities of the fluid are constrained to be equal to the nodal velocities of the structure. There is continuity of velocity and stress normal components on both sides of  $\Gamma_{fsi}$  boundary. In this study, an Euler-Lagrange penalty coupling method is employed to model the interaction between the fluid and the structure. This method combines the MMALE formulation and the classical master-slave penalty contact method and guarantees the conservation of momentum and energy (Souli and Benson, 2013). In the Euler-Lagrange coupling, the structure is embedded in an Eulerian fixed mesh. The Eulerian mesh contains the Lagrangian structure and the MMALE fluid, which flows across the mesh using the

advection strategy to update velocity and history variables. A detailed description of MMALE algorithm can be found in Fig. 2.

In an explicit integration problem, after calculating the nodal forces for fluid and structure, the coupling forces of the nodes on the fluid structure interface are computed. A depth penetration  $\vec{d}$  is incrementally updated at each time step for each structure node, using the relative velocity  $(\vec{v}_s - \vec{v}_f)$ . The structure node is considered as a slave node and the master node within the Eulerian element. Using the isoparametric coordinates of the fluid element, the location of the master node is computed. At time  $t^n = t^{n-1} + \Delta t$ , the penetration vector is updated as in

$$\vec{d}^{n+1} = \vec{d}^n + (\vec{v}_s^{n+1/2} - \vec{v}_f^{n+1/2}) \cdot \Delta t \quad (1)$$

where  $\Delta t$  is the increment of time,  $\vec{v}_s$  is the velocity of the slave node, and  $\vec{v}_f$  is the fluid velocity at the master node location. The fluid velocity is interpolated from the nodes of fluid element at the current time step. It should be noted that the coupling force acts only if penetration occurs ( $\vec{n}_s \cdot \vec{d}^n < 0$ ), where  $\vec{n}_s$  is built up by averaging normal of structure elements connected to the structure node.

A penalty coupling method is used to solve the FSI problem between a Lagrangian formulation (structure) and an ALE formulation (fluid). This method allows the fluid to flow in the parallel direction to the Lagrangian segments, but not to penetrate the contact surface (LS-DYNA Theory Manual, 2022). The ALE algorithm searches for the elements that overlap or intersect between the Lagrangian segments and the ALE multi-material groups. If an overlap is detected, a coupling force is applied to the penetrating segments. Then, the state variables of the deformed ALE material are mapped back onto the reference ALE mesh in the advection step. The penalty coupling behaves like a spring system and the penalty forces are proportional to the penetration depth and spring stiffness. The spring head is attached to the structure (slave node), and the spring tail is connected to the master node within a fluid element intercepted by the structure (Souli and Benson, 2013). The coupling force is defined by

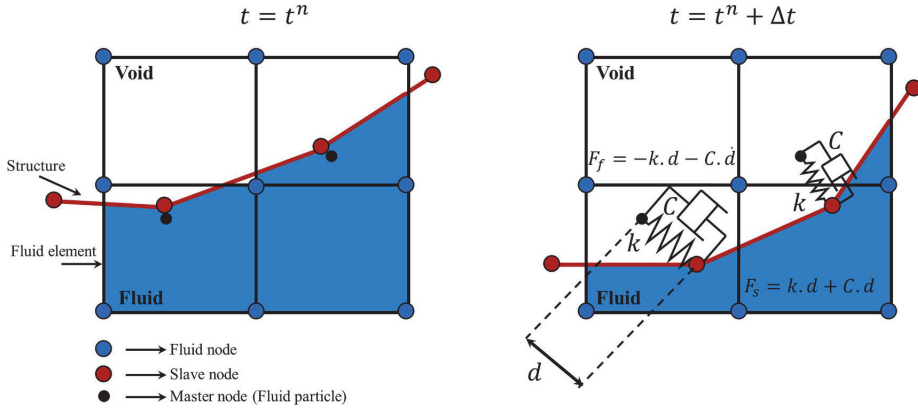


Fig. 3. Description of the Arbitrary Lagrangian-Eulerian coupling scheme with penalty factor (reproduced from Souli and Benson, 2013).

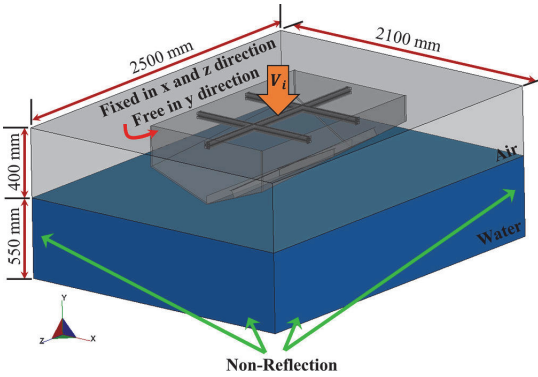


Fig. 4. MMAL domain and applied boundary conditions with the initial impact velocity in LS-DYNA.

$$F = kd \tag{2}$$

where  $d$  represents the penetration and  $k$  is the spring stiffness. To satisfy the equilibrium at the interface coupling, the force is applied to both master and slave nodes in opposite direction. The stiffness value is problem dependent, and a desirable value for the stiffness should minimise the energy interface to satisfy total energy conservation and prevent fluid leakage through the structure. This study uses the explicit penalty contact algorithm in LS-DYNA (LS-DYNA Theory Manual, 2022) to determine the stiffness of the spring. The numerical stiffness is expressed in terms of the bulk modulus ( $K$ ) in the coupling containing the structure node, the fluid element volume ( $V$ ) that contains the master node, and the average area ( $A$ ) of the structure elements attached to the structure node.

$$k = p_f \frac{KA^2}{V} \tag{3}$$

A penalty factor  $p_f$  ( $0 \leq p_f \leq 1$ ) is introduced for scaling the estimated stiffness of the coupling system to avoid the numerical instabilities. For impact problems, it is always necessary to examine the effect of  $p_f$  on the solution. Cheon et al. (2016) investigated the effect of penalty factor on the slamming pressure distribution on a flat stiffened plate and found that the influence of  $p_f$  on the impact load is small. A significant issue with the penalty coupling algorithm is the numerical noise that results from high-frequency oscillations in the coupling

process. Insufficient penalty contact causes large non-physical penetrations, which may disrupt the flow field and cause leakage on the Lagrangian structure, especially at high impact velocities (Stenius et al., 2007). Therefore, a viscous contact damping is added to the coupling algorithm to damp out the high-frequency oscillations. Fig. 3 illustrates the Euler-Lagrange penalty coupling scheme with added viscous damping. By adding the term of viscous damping, the coupling force becomes:

$$F = kd + C\dot{d} \rightarrow C = \xi\sqrt{kM} \tag{4}$$

where  $C$  represents the damping coefficient and  $M$  is the equivalent mass. The damping factor ( $\xi$ ) is used to scale the applied damping and when  $\xi$  is critical, the damping is optimal according to Souli and Benson (2013) and Aquelet et al. (2006). Luo et al. (2011) conducted a parametric study, including the penalty factor, mesh size, and the number of the contact points on a two-dimensional rigid wedge, and validated the results by comparing with the experimental data from Zhao et al. (1996).

### 3.2. ALE numerical setup

The experimental case described in the previous section is simulated numerically employing the ALE method and the penalty coupling algorithm. Fig. 4 illustrates the numerical model including the fluid domain (air and water) and the aluminium wedge. Due to the non-prismatic shape of the 3D wedge and the different bottom plates, the entire structure must be modelled. The properties of the structure with longitudinal and transverse stiffeners are presented in Table 1. The wedge was modelled based on the Lagrangian method with shell element formulation. For the top support frame, it was assumed that there are no deformations or rotations, while the deformable material was considered for all other parts of the wedge. The material types named Rigid and Elastic were used to define the materials of the support frame and the aluminium wedge, respectively. Five integration points through the shell thickness using the Lobatto integration method and 0.83 shear factor were applied in all the analyses (LS-DYNA Theory Manual, 2022). To allow free-fall motion only in the  $y$ -direction, the top frame of the wedge was constrained in the horizontal directions ( $x$  and  $z$  directions). In addition, the non-reflecting boundaries are employed on the numerical domain's left, right, top, and bottom sides to avoid reflection of the impulse wave at the boundaries. An initial velocity ( $V_i$ ) corresponding to the wedge impact velocity is applied in all simulations.

The solid elements with one point ALE multi-material element formulation were used to model the fluid domain including water and air. To describe the nonlinear properties of a fluid-like deformation in



**Table 2**  
Equation of State (EOS) coefficients and material properties of fluid models.

*EOS_Linear_Polynomial Parameter	Air	*EOS_Grüneisen Parameter	Water
$C_0$ [MPa]	0.0	Sound speed of fluid, $C$ [m/s]	1480
$C_1$ [MPa]	0.0	$S_1$ [-]	2.599
$C_2$ [MPa]	0.0	$S_2$ [-]	-1.985
$C_3$ [MPa]	0.0	$S_3$ [-]	0.2286
$C_4$ [-]	0.4	$\gamma_0$ [-]	0.493
$C_5$ [-]	0.4	First-order volume correction, $a$ [-]	1.397
$C_6$ [-]	0.0	Initial internal energy, $E_0$ [MPa]	0.2895
Initial internal energy, $E_0$ [MPa]	0.25	Initial relative volume, $V_0$ [-]	1.0
Initial relative volume, $V_0$ [-]	1.0		
*MAT_NULL (Air)		*MAT_NULL (Water)	
Density, $\rho_0$ [kg/m <sup>3</sup> ]	1.204	Density, $\rho_0$ [kg/m <sup>3</sup> ]	998.2
Dynamic viscosity $\mu$ , [kg/m.s]	1.825E-5	Dynamic viscosity $\mu$ , [kg/m.s]	1.00E-3
Pressure cutoff [Pa]	-10.00	Pressure cutoff [Pa]	-1.00E+4

explicit dynamic codes, a set of constitutive equations with suitable boundary conditions needs to be solved. The constitutive model defines the partial stress of the material and the equation of state (EOS) for the relationship between the volume of deformation and stress. In this case, the solid elements were assigned with \*Mat\_Null with no shear stiffness or yield strength, which behaves as fluid-like material. The air was modelled as a perfect gas with zero shear strength and \*Mat\_Null and \*EOS\_Linear\_Polynomial were used to define its properties. For the air state, the pressure is given by

$$P = C_0 + C_1\mu + C_2\mu^2 + C_3\mu^3 + (C_4 + C_5\mu + C_6\mu^2)E \quad (5)$$

where  $C_0(i = 1, \dots, 6)$  are the hydrodynamic constants and  $E$  is the internal energy per unit reference volume. The parameter  $\mu$  is described by

$$\mu = (\rho / \rho_0) - 1 \quad (6)$$

where  $\rho_0$  is the density at nominal or reference state, usually non-stress or non-deformed state, and  $\rho$  is the current density. The Grüneisen EOS (Heuzé, 2012) based on a cubic shock velocity-particle velocity is used to model the water state. The Grüneisen EOS of the water defines the pressure by

$$P = P_c + P_T = A(\mu) + B(\mu)E \quad (7)$$

where  $B(\mu) = (\gamma_0 + a\mu)$ . For expanded materials ( $\mu < 0$ ),  $A(\mu) = \rho_0 C^2 \mu$

and for compression materials ( $\mu > 0$ ),  $A(\mu)$  is defined as

$$A(\mu) = \frac{\rho_0 C^2 \mu [2 + (2 - \gamma_0)\mu - (\gamma_0 - a)\mu^2]}{2 \left[ 1 - (S_1 - 1)\mu - S_2 \frac{\mu^2}{\mu+1} - S_3 \frac{\mu^3}{(\mu+1)^2} \right]^2} \quad (8)$$

In Eq. (8),  $S_1, S_2, S_3$  are the coefficients of the slope of the shock velocity versus particle velocity curve ( $u_s - u_p$  curve) where  $u_s$  and  $u_p$  are the constant of the shock wave velocity and particle velocity, respectively.  $\gamma_0$  is the Grüneisen gamma,  $a$  is the first-order volume correction to  $\gamma_0$ , and  $C_0$  is the intercept of  $u_s - u_p$  curve, which corresponds to the adiabatic sound speed of fluid. The corresponding parameters for all fluid materials and the constants used in this study are summarized in Table 2. The coupling algorithm between MMALE and elastic wedge is controlled by \*Constrained\_Lagrange\_In\_Solid card, which is used to define the contact between MMALE groups (\*Control\_ALE) and Lagrangian elements. It should be noted that in the current study the effects of water surface tension, as well as the effect of gravity, are considered.

As stated above, the penalty-based method was applied to model the contact between the structure and the fluid. According to Aquelet et al. (2006), increasing the penalty factor ( $p_f$ ) reduces the interpenetration allowed at the nodes of the contact interface. With high contact stiffness and zero penetrations, the interface condition is satisfied, but the virtual spring-damper system of the contact algorithm becomes more frequent and numerical instabilities occur as a result.

Cheon et al. (2016) investigated the influence of penalty factors on pressure values and found that the variations between penalty factors of 0.01, 0.05, 0.1, 0.5, and 1.0 are minimal. However, the combination of penalty ( $p_f$ ) and damping ( $\xi$ ) factors was not taken into consideration in that study. Ladeira (2020) discovered that an excessively high damping coefficient can result in unstable coupling. He conducted a comparative study of the effect of damping and penalty factors on vertical slamming force and concluded that simulations with  $p_f = 0.02$  and  $\xi = 0.1$  have fewer numerical instabilities. Therefore, the same values are used for present simulations. Additionally, the minimum volume fraction is 0.33 and the number of coupling points distributed over each coupled Lagrangian surface is set by default to 2.

The mesh regions of the MMALE numerical domain including solid and shell elements are shown in Fig. 5. The fluid domain is modelled with 1-point ALE multi-material solid hexahedral elements, whereas the Belytschko-Tsay shell element formulation are used for the wedge structure. To minimise numerical issues and achieve accurate results, the mesh regions of the impact area need to be sufficiently fine. Coarser meshes may be used in areas far from the areas of interest to reduce computational time. A mesh sensitivity study was conducted for impact

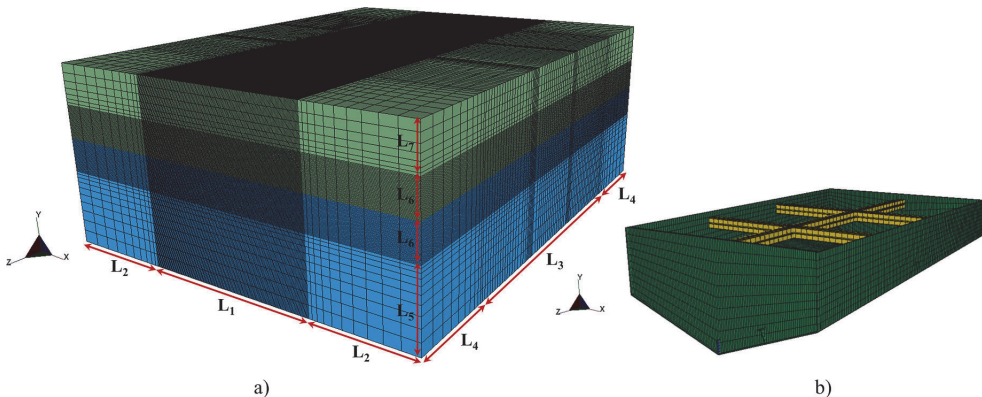
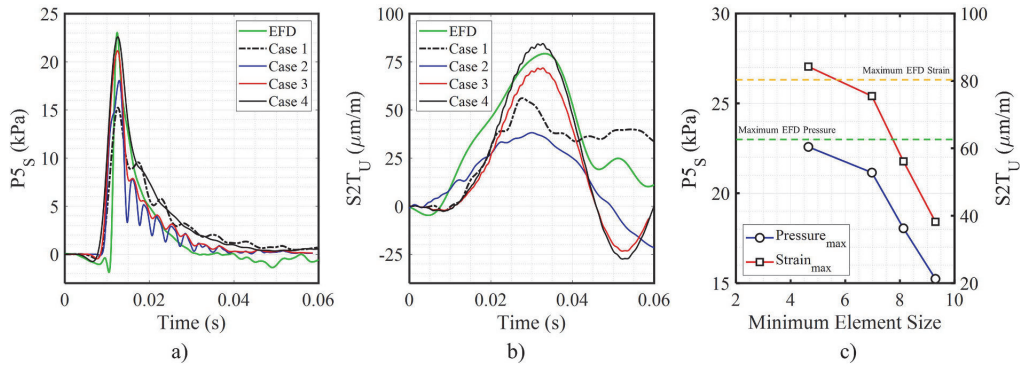


Fig. 5. MMALE computational domain including mesh regions: a) 1-point ALE multi-material solid hexahedral elements; b) 4-noded shell elements.

**Table 3**

Dimensions of different mesh sizes in LS-DYNA (Unit: mm) and a comparison of experimental peak pressure and maximum strain with the MMALE results at 2.20 [m/s] impact velocity.

Fluid Domain								Structure Domain	Comparison	
Length	L <sub>1</sub>	L <sub>2</sub>	L <sub>3</sub>	L <sub>4</sub>	L <sub>5</sub>	L <sub>6</sub>	L <sub>7</sub>		Peak Pressure	Maximum Strain
	1000	550	1500	500	380	170	230			
Minimum cell size								Minimum cell size on the bottom	$\Delta P_{5_S}$ (%)	$\Delta S_{2T_U}$ (%)
Case 1	9.3	18.25	12.5	16.5	12.5	8.5	12.5	14.25 × 10.25	33.80	52.51
Case 2	8.13	18.25	12.5	16.5	12.5	7.43	12.5	14.25 × 10.25	21.59	30.20
Case 3	6.975	18.25	12.5	16.5	12.5	6.375	12.5	12.25 × 9.00	8.12	10.73
Case 4	4.65	18.25	12.5	16.5	12.5	4.25	12.5	12.25 × 9.00 (6.125 × 4.5)	1.87	4.76



**Fig. 6.** Effect of different mesh size in MMALE method at 2.20 [m/s] impact velocity: a) time history of pressure on the stiffened bottom; b) time history of strain on the unstiffened bottom; c) element size versus the accuracy of maximum pressure and strain.

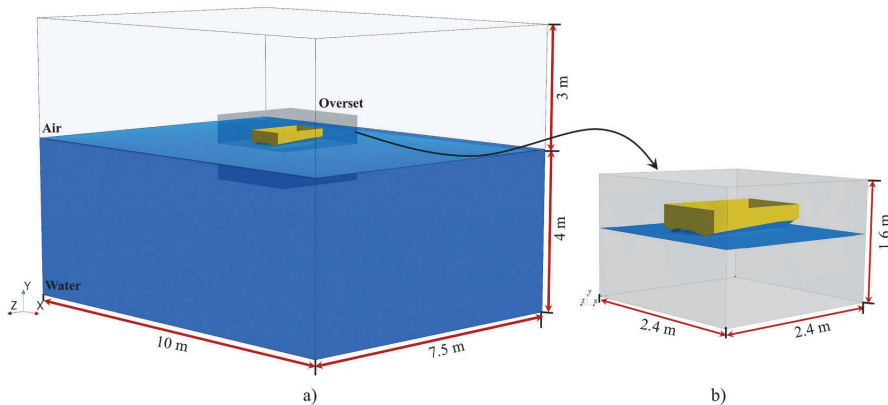


**Fig. 7.** Numerical fluid domain in Star-CCM+: a) dimensions of the background region; b) dimensions of the overset region.

velocity of 2.20 [m/s]. The aim was to determine the most optimal mesh that provides precise results for the simulations presented. The effect of mesh size on simulation results was investigated using four different mesh cases in the fluid and structure domains. Table 3 summarizes the details of the implemented meshes and presents the percentage difference between the experimental fluid dynamics (EFD) data and the corresponding numerical results, where  $\Delta P_{5_S} = (P_{5_S\_EFDmax} - P_{5_S\_MMALEmax}) / P_{5_S\_EFDmax}$ . The same method is applied for comparing the maximum strain ( $\Delta S_{2T_U}$ ) values.

The simulation results of these four different mesh sizes are demonstrated in Fig. 6. A comparison of numerical and experimental results of the slamming pressure on the stiffened bottom of the wedge

with 23.5-degree deadrise angle ( $P_{5_S}$ ) is presented in Fig. 6a. From preliminary simulations, it was found that the coupling between the fluid and the structure cannot be achieved if the Lagrangian mesh is coarser than the fluid mesh in the ALE method. This means if meshes differ significantly, it would be difficult to track the contact boundaries between the fluid and structure, and thus the coupling forces cannot be properly evaluated. As shown in Fig. 6, the numerical fluctuation in the pressure results is significant in cases 1,2. However, it nearly disappears in Case 3. The pressure peak value ( $P_{5_S\_MMALE} = 22.58$  kPa) in case 4 is well agreed with the experimental data ( $P_{5_S\_EFD} = 23.02$  kPa). However, in the other cases, it is underestimated. It should be noted that for Case 4, as shown in Fig. 5, a mesh refinement is applied around all

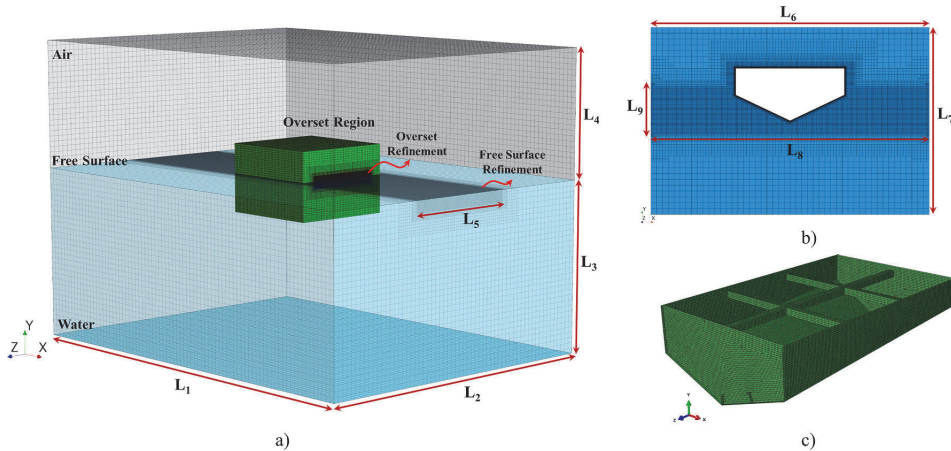


Fig. 8. Properties of mesh elements in CFD/FEM coupling method: a) the mesh size on the background region with a refinement on the free surface; b) close view of trimmed cell mesh in the overset region with its refinement; c) four-node shell element (S4R) in ABAQUS.

Table 4

Dimensions of different mesh sizes in CFD/FEM coupling method (Unit: mm) and a comparison of experimental peak pressure and maximum strain with the numerical results at 2.20 [m/s] impact velocity.

Fluid Domain		Structure Domain								Comparison		
Length	L <sub>1</sub>	L <sub>2</sub>	L <sub>3</sub>	L <sub>4</sub>	L <sub>5</sub>	L <sub>6</sub>	L <sub>7</sub>	L <sub>8</sub>	L <sub>9</sub>	Peak Pressure	Maximum Strain	
	10000	7500	4000	3000	2500	2400	1600	2400	400			
Minimum cell size										Minimum cell size on the bottom	ΔP5 <sub>S</sub> (%)	ΔS2T <sub>U</sub> (%)
Case 1	250	250	250	250	30	100	100	18.75	18.75	10 × 10	29.45	35.27
Case 2	250	250	250	250	30	75	75	12.5	12.5	10 × 10	24.54	27.58
Case 3	250	250	250	250	15	50	50	9.375	9.375	10 × 10	15.77	19.24
Case 4	250	250	250	250	15	50	50	6.25	6.25	10 × 10	4.30	4.17

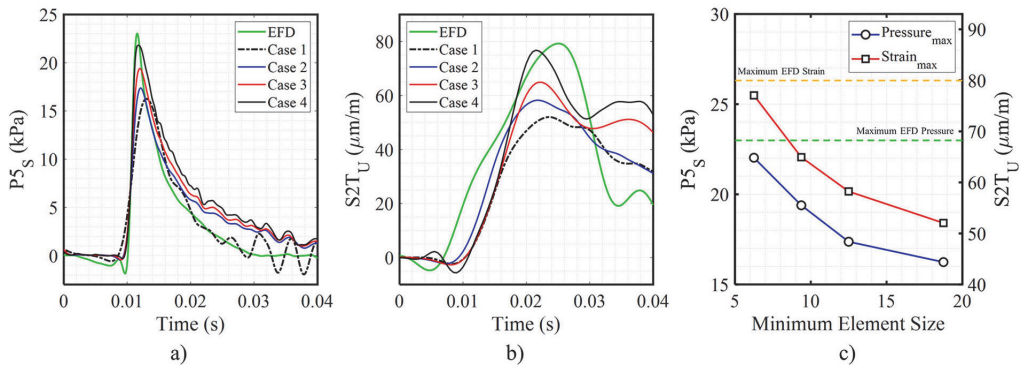


Fig. 9. Effect of different mesh size in CFD/FEM coupling method with 2.20 [m/s] impact velocity: a) time history of pressure on the stiffened bottom; b) time history of strain on the unstiffened bottom; c) element size versus the accuracy of maximum pressure and strain.

pressure sensors. As with the pressure time history, the strain results of second strain sensor on the unstiffened bottom are compared in different mesh sizes (Fig. 6b). This shows that the maximum strain value ( $S2T_{U\_MMALE} = 84.24 \mu\text{m/m}$ ) closely matches the experimental data ( $S2T_{U\_EFD} = 80.41 \mu\text{m/m}$ ). The effect of the element size on the maximum value of pressure and strain is shown in Fig. 6c for each case. According to the results of this mesh study, the numerical model with mesh size applied for Case 4 is suitable to capture the impact pressure and structural responses of the aluminium wedge. Therefore, it is

employed for the remaining simulations presented in this paper.

### 3.3. CFD-FEM numerical setup

In addition to the ALE method, a two-way coupling method is employed to investigate the effect of viscosity on the hydrodynamic pressure and structural response. An explanation of the two-way coupling algorithm can be found in Hosseinzadeh and Tabri (2021a); Yan et al. (2022a). In this numerical model, the CFD solver (Star-CCM+) is

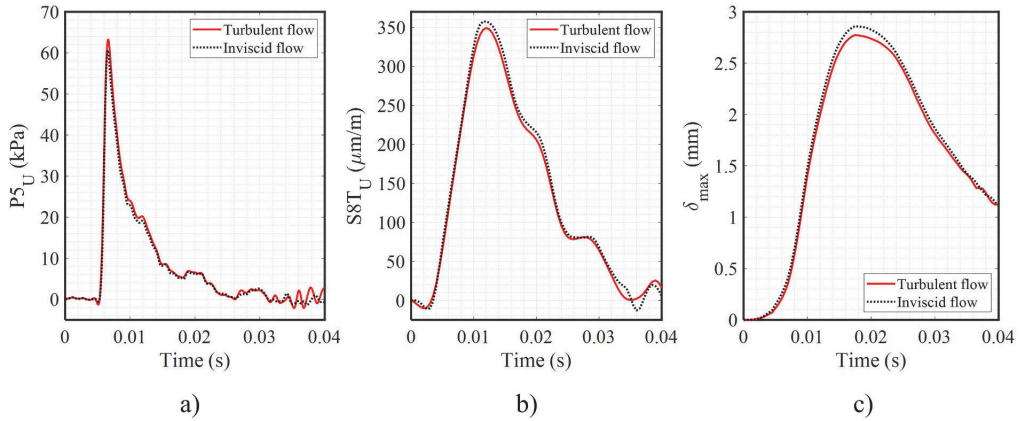


Fig. 10. Comparison of the results of turbulent and inviscid flow at 4.00 [m/s] impact velocity; a) time history of slamming pressure; b) time history of strain response; c) maximum deflection on the unstiffened bottom plate.

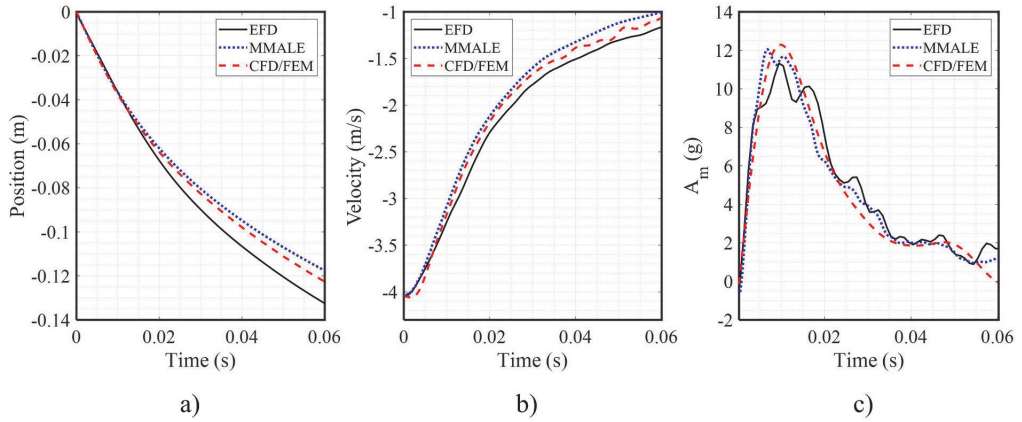


Fig. 11. Comparison of numerical and experimental results at 4.00 [m/s] impact velocity; a) time history of vertical position; b) time history of vertical impact velocity; c) time history of vertical acceleration at the midsection of the wedge.

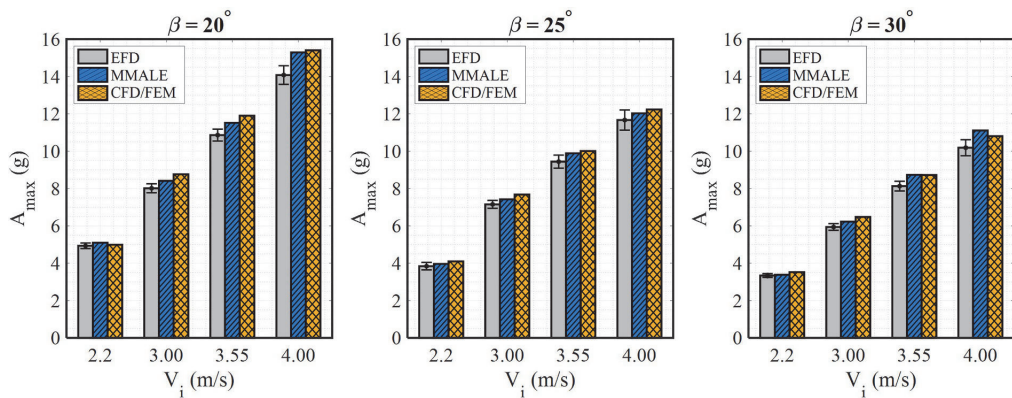


Fig. 12. Comparison of experimental and numerical results for maximum vertical acceleration at different location of the wedge and various impact velocities.

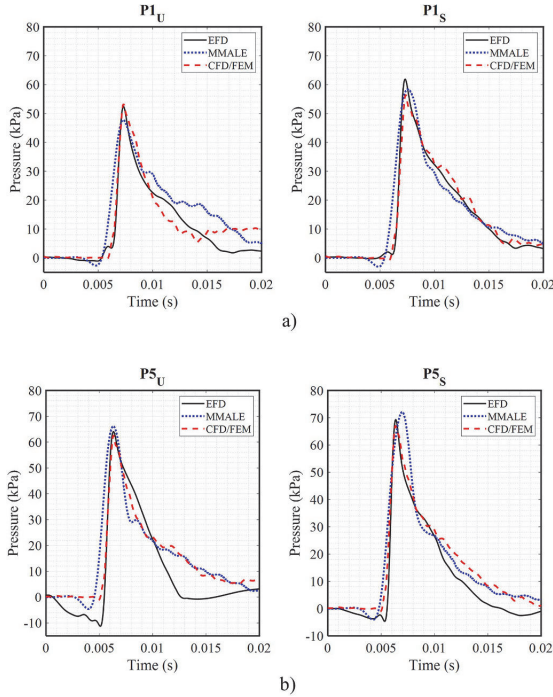


Fig. 13. Comparison of the predicted and measured pressure results at 4.00 [m/s] impact velocity on unstiffened (U) and stiffened (S) bottom plates at: a) 27-degree deadrise angle; b) 23.5-degree deadrise angle.

is used to solve the fluid flow and hydrodynamic pressure, and the FEM solver (ABAQUS) is utilised to solve the structural responses due to slamming loads. The Reynolds-averaged Navier Stokes equations (RANS) and continuity equation are solved using Finite Volume Method (FVM) with an implicit unsteady solver and first-order discretization in time. Moreover, a  $k-\epsilon$  turbulence model is employed and a two-phase Eulerian flow is defined, with the assumption that both, air and water, phases are incompressible. In addition, a simulation of the water entry problem is also carried out in inviscid flow to analyse the influence of viscosity on impact loads. As shown in Fig. 7, the fluid domain consists of air and water that are separated by a free surface. The water entry problem includes a complex evolution of the free surface during the impact stage, and the volume-of-fluid (VOF) interface-capturing technique is employed to provide a precise solution for the nonlinear and complex free surface. Eq. (9) computes the density ( $\rho$ ) at each cell, and Eq. (10) calculates the kinematic viscosity ( $\mu$ ):

$$\rho = \alpha \rho_w + (1 - \alpha) \rho_a \quad (9)$$

$$\mu = \alpha \mu_w + (1 - \alpha) \mu_a \quad (10)$$

where  $w$  and  $a$  subscripts are for water and air, respectively and  $\alpha$  represents volume fraction of the fluid which is defined as

$$\frac{d\alpha}{dt} + \nabla(\alpha w) = 0 \quad (11)$$

To describe the fluid domain around the wedge during the impact, the FVM and Semi-Implicit Method for Pressure-Linking Equations (SIMPLE) are employed. Additionally, the volume fraction of the fluid ( $\alpha$ ) is solved using the VOF technique with a High-Resolution Interface Capturing (HRIC) scheme (STAR-CCM+, 2020).

The wedge structure is modelled with four-node shell element (S4R)

in ABAQUS (Dassault Systèmes, 2016). A nonlinear, dynamic, implicit analysis is defined for the FEM solver that uses the Hilber-Hughes-Taylor time integration by default (Bathe, 2006). To simulate free-fall vertical translation, the free  $y$ -direction boundary condition is applied to the wedge. The outer sides of the shell elements are defined as a coupled surface and assigned to the fluid-structure co-simulation boundary to transfer the structural response to the fluid domain. The model is also subject to a gravity load and the initial impact velocity is defined as a predefined field.

Due to the dynamic nature of the slamming problem, the fluid flow and structure deformations can change dramatically over time. Therefore, the CFD and FEM solvers have been coupled using a strongly two-way coupling method in the present study. In each time step, the pressure load and shear stress from CFD model is first computed and then applied as a surface load in the FE model and the calculated nodal displacement of the structure is transferred back to the fluid domain. Therefore, the fluid domain mesh can be updated for the next time step using a mesh morphing technique based on the deflection and vertical translation of the structure (Lakshmyanarayana and Hirdaris, 2020; Hosseinzadeh and Tabri, 2021a; Yan et al., 2022a). In this study, an implicit coupling scheme with constant coupling time step equal to the fluid solver time step was used. The co-simulation setup was specified as a minimum of twenty exchanges per time step and one inner iteration with an active morpher-solver during the inner iteration. To achieve convergence with a minimal number of iterations, the FSI under-relaxation parameter and number of inner iterations must be properly chosen. According to Eq. (12), the FSI under-relaxation factor ( $\beta_r$ ) is related to the nodal displacements ( $w$ ) imported from FE model.

$$w_{i+1}^{n+1} = (1 - \beta_r) w_i^{n+1} + \beta_r \tilde{w}_{i+1}^{n+1} \quad (12)$$

where  $\tilde{w}$  is unrelaxed nodal displacement,  $n$  is related to the time step, and  $i$  is the iteration counter. A low under-relaxation factor ( $\beta_r < 0.5$ ) should be carefully chosen for the problems demanding dynamic accuracy, as more iterations and a longer computational time would be required. On the other hand, an excessively large  $\beta_r$  may influence the simulation's convergence and underestimate the pressure loads (Causin et al., 2005; Piro and Maki, 2013; STAR-CCM+, 2020). In this study, the FSI under-relaxation factor is set to 0.6. To prevent numerical instabilities at the beginning of the simulation, a pressure ramping parameter of [0, 004] was applied.

As mentioned before, the governing equations are discretised over a grid of cells using the finite volume method, and the nodal values are computed at the centre of each cell. The hexahedral mesh was applied to the fluid domain as it provides an accurate solution and is particularly suitable for simulating the free surface problems. As demonstrated in Fig. 7b, the overset mesh technique is used to reduce the computation time by establishing a smaller mesh near the walls and free surface of the structure. The nodal values of background and overset regions are interpolated linearly. The mesh morpher method, which allows the boundaries and nodes to modify in accordance with the imported displacement from the FE solver, was employed because the fluid mesh needs to be updated depending on the structural deformations. Fig. 8a illustrates the implemented mesh with an overset region and a free surface refinement area in the fluid domain. In the overset region, a prism layer mesher with 15 prism layers was applied to capture the boundary layer and spray root generated during the impact. A preliminary assessment of the numerical model revealed that a grid refinement of the fluid domain around the structure is necessary to resolve the volume distribution of water near the wedge surface. Therefore, various controls are applied to the overset region, including a volumetric control around the wedge and a surface control on the bottom plates of the wedge section (Fig. 8b). As shown in Fig. 8c, the wedge structure is modelled in the FE solver using a four-node shell element (S4R) with reduced integration to allow hourglass control and eliminate shear lock-in (Dassault Systèmes, 2016).

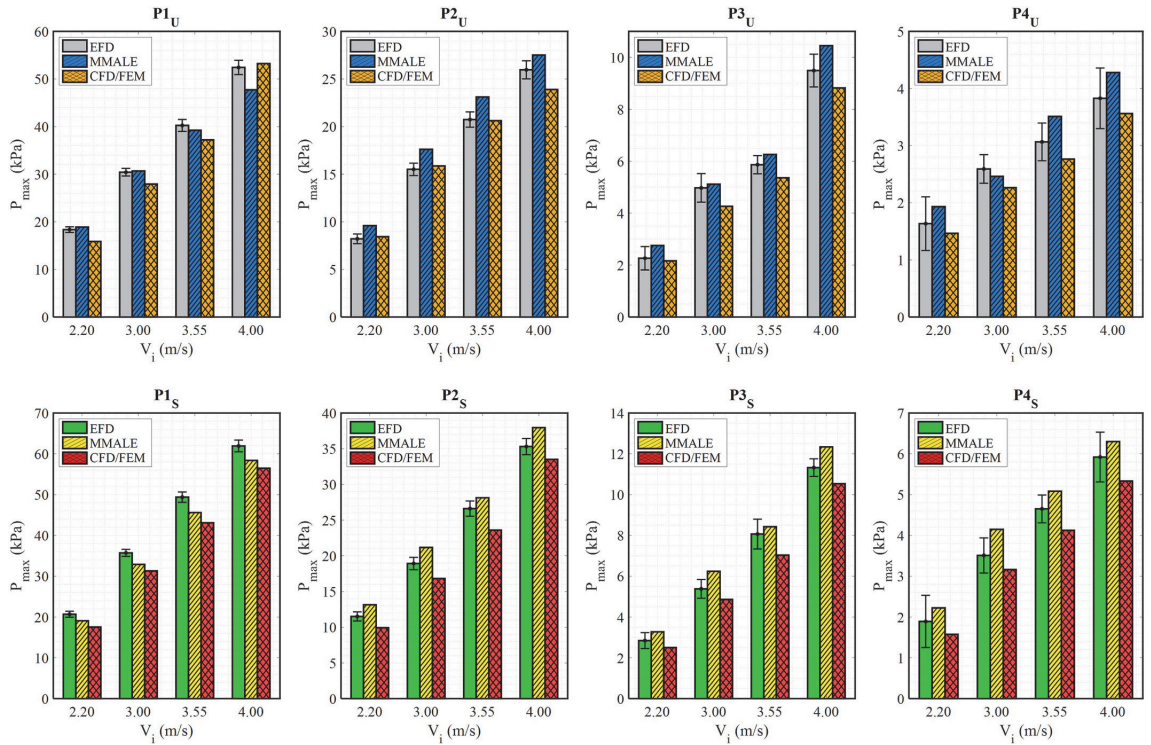


Fig. 14. Comparison of computed and experimental results for maximum pressure at various impact velocities on the unstiffened (U) and stiffened (S) plates of the wedge at 27-degree deadrise angle.

In order to determine the best mesh that provides accurate results for the present coupling method, a mesh convergence study was carried out on the case with an impact velocity of 2.20 [m/s] in a manner similar to the MMALE method. The mesh properties and grid sizes of the four different cases used to examine the effect of mesh size on the slamming pressure and structural response are shown in Table 4. It should be noted that during the mesh study, the cell size in the background region and the element size in the structure solver remain constant. Fig. 9a compares slamming pressure time history of the sensor located on the stiffened bottom with 23.5-degree deadrise angle ( $P5_S$ ) computed with four different mesh sizes. For the first and second cases, the fluid solver ( $\Delta t_f$ ) and coupling ( $\Delta t_{FSI}$ ) time step were 0.1 [ms] and 0.5 [ms], respectively, whereas  $\Delta t_f = \Delta t_{FSI} = 0.05$  ms was used for the third and fourth cases. It is shown that in Case 4, the maximum value of the calculated pressure ( $P5_{S\_CFD/FEM} = 22.03$  kPa) agrees well with the measured pressure from experiments ( $P5_{S\_EFD} = 23.03$  kPa). Similarly, a comparison of the strain values of the second strain sensor on the unstiffened bottom is shown in Fig. 9b, which explains that for the fourth case the maximum strain value ( $S2T_{U\_CFD/FEM} = 77.06$   $\mu\text{m/m}$ ) nearly matches the experimental data ( $S2T_{U\_EFD} = 80.41$   $\mu\text{m/m}$ ). Additionally, Table 4 presents the percentage difference between the experimental data and the numerical results for both pressure and strain values.

As already stated, the effect of viscosity on the wedge water entry problem is examined in the present study. To determine how the turbulent and viscosity assumptions affect the pressure distributions, strain responses, and bottom deflection of the wedge, the results of turbulent flow and inviscid flow are compared at 4.00 [m/s] impact velocity. As illustrated in Fig. 10, there is no significant difference between the computed results of turbulent and inviscid simulations and the viscosity effect on the impact-induced loads and responses can be neglected.

## 4. Results and discussions

### 4.1. Vertical motions

To verify the numerical models, the vertical motions of the wedge presented in section 3 are compared with experimental results (described in Hosseinzadeh et al., 2023). A comparison between the predicted results and the experimental data for 4.00 [m/s] impact velocity is depicted in Fig. 11. A comparison of the vertical position time history of the wedge after the impact is presented in Fig. 11a. It is worth noticing that the experimental vertical position and velocity were calculated by integrating the acceleration data measured during the free-fall test. The calculated vertical velocity matches well with the experiments for the free-falling period after the impact (Fig. 11b). Similarly, Fig. 11c compares the vertical acceleration time history at the middle of the wedge ( $A_m$ ). It is shown that the maximum acceleration value of numerical results is reasonably close to experiments. The relative error in acceleration at the midsection of the wedge is in the order of 3.0% and 4.8% for the MMALE and CFD/FEM methods, respectively.

In addition to the time histories of the accelerations, the maximum acceleration values computed by numerical methods were compared with experimental measurements at different locations of the wedge and various impact velocities. As demonstrated in Fig. 12, acceleration was measured at aft ( $A_a$ ), middle ( $A_m$ ), and fore ( $A_f$ ) of the wedge for deadrise angles of the order of 20°, 25°, and 30°, respectively. The maximum acceleration of the wedge decreases with higher deadrise angles. The slight deviation associated with the prediction of the maximum vertical acceleration increases as the impact velocity also increases. Table A1 compares the maximum acceleration values

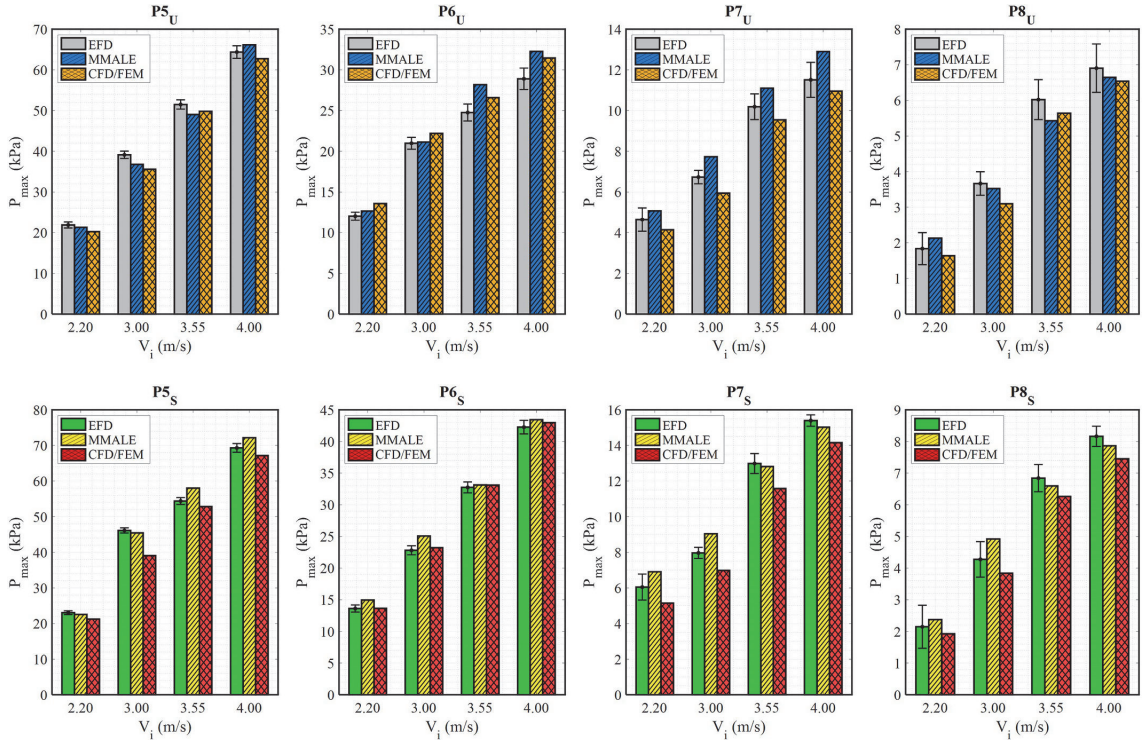


Fig. 15. Comparison of computed and experimental results for maximum pressure at various impact velocities on the unstiffened (U) and stiffened (S) plates of the wedge at 23.5-degree deadrise angle.

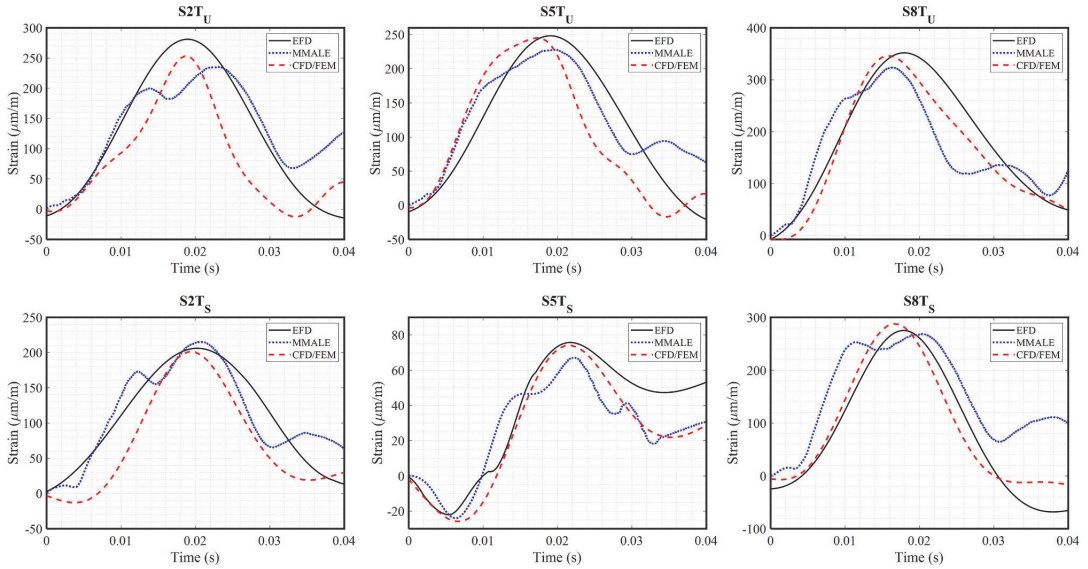


Fig. 16. Comparison of numerical and experimental strains results over time in transverse direction on unstiffened (U) and stiffened (S) plates at 4.00 [m/s] impact velocity.

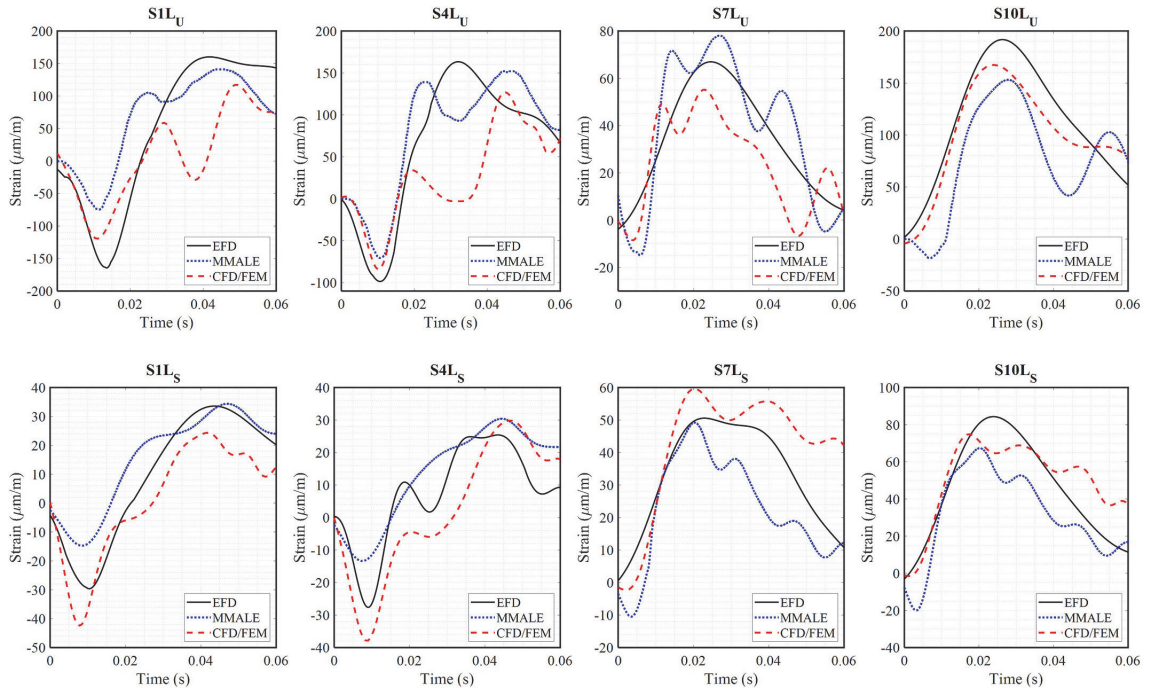


Fig. 17. Comparison of numerical and experimental strains results over time in longitudinal direction on unstiffened (U) and stiffened (S) plates at 4.00 [m/s] impact velocity.

calculated from two numerical models with the experimental data and reports the relative error at various impact velocities.

Throughout the validation study, it was confirmed that the numerical models can simulate the experimental results with reasonable accuracy (see Table A1). The numerical deviations observed in the time history of acceleration could be attributed to several reasons. In the CFD/FEM two-way coupling method, the number of iterations in each time step, the coupling time step itself, the value used to idealise the under-relaxation factor, and last but not least the mesh setup should all be taken into account accurately and efficiently to prevent numerical instabilities. During the preliminary simulations, it was discovered that whereas the results of the CFD/FEM method are smooth, the MMALE method produces noticeable fluctuations in time (Fig. 11). These fluctuations were caused by the penalty coupling method in the MMALE method, which accounts for contact stiffness between fluid and structure. The penalty coupling method can result in high-frequency oscillations due to the nearly incompressible nature of the fluid (Aquelet et al., 2006). Therefore, the penalty coupling factor ( $p_f$ ) and damping factor ( $\xi$ ) were applied to the numerical model to achieve smooth results. Generally, the acceleration results indicate that the set-up of the numerical models presented in this study is suitable to describe the physics of the experiment. The comparison for all pressure and strain sensors at different impact velocities is presented in the following subsections.

#### 4.2. Comparisons of the slamming pressure

The computed pressure distribution of sensors P1 and P5 at 4.00 [m/s] impact velocity was compared against the results available from the experiments (see Fig. 13). In order to investigate the effect of rigidity on the pressure results, the pressure time history of the sensors located on the unstiffened and stiffened bottom plates with the same deadrise angle

are shown in Fig. 13a and b, respectively. As expected, due to the flexibility on the unstiffened bottom of the aluminium wedge, the peak pressure of the unstiffened bottom is lower than that of the stiffened bottom. Additionally, the pressure peaks for the sensors located on aft of the wedge (Fig. 13b), where the deadrise angle is  $23.5^\circ$ , are higher than those located on fore with  $27^\circ$  deadrise angle (Fig. 13a). In the first part of this study (Hosseinzadeh et al., 2023), it was revealed that some pressure sensors recorded negative values. This was particularly apparent for the sensors placed on the smaller deadrise angle. In numerical simulations, the same phenomenon has been observed for the sensors near the chine. According to Fig. 13, the sensor on the unstiffened plate shows a negative pressure that may be caused by pressure relaxation due to plate deflection. The numerical results of both methods have also been demonstrated to be in good agreement with the experiments.

In Fig. 14, maximum pressure values computed by the different numerical methods are compared against experimental measurements at various impact velocities with a 27-degree deadrise angle. The vertical error bar at the peak represents the standard deviation of the experimental peak pressure for each sensor (Hosseinzadeh et al., 2023). In the first row, maximum pressure values are presented for the sensors located on the unstiffened bottom, and in the second row, peak pressures are presented for the sensors positioned on the stiffened bottom. Similarly, the pressure peak values of the sensors located on the section with a 23.5-degree deadrise angle are presented in Fig. 15. It can be observed that there is good agreement between the numerical and experimental pressure results. The discrepancy between numerical and experimental results increases for the sensors on the unstiffened bottom and far away from the keel. In addition, Table A2 presents a comparison of maximum pressure values obtained from two numerical models with the experimental data, along with the relative error of each sensor at an impact velocity of 4.00 [m/s].



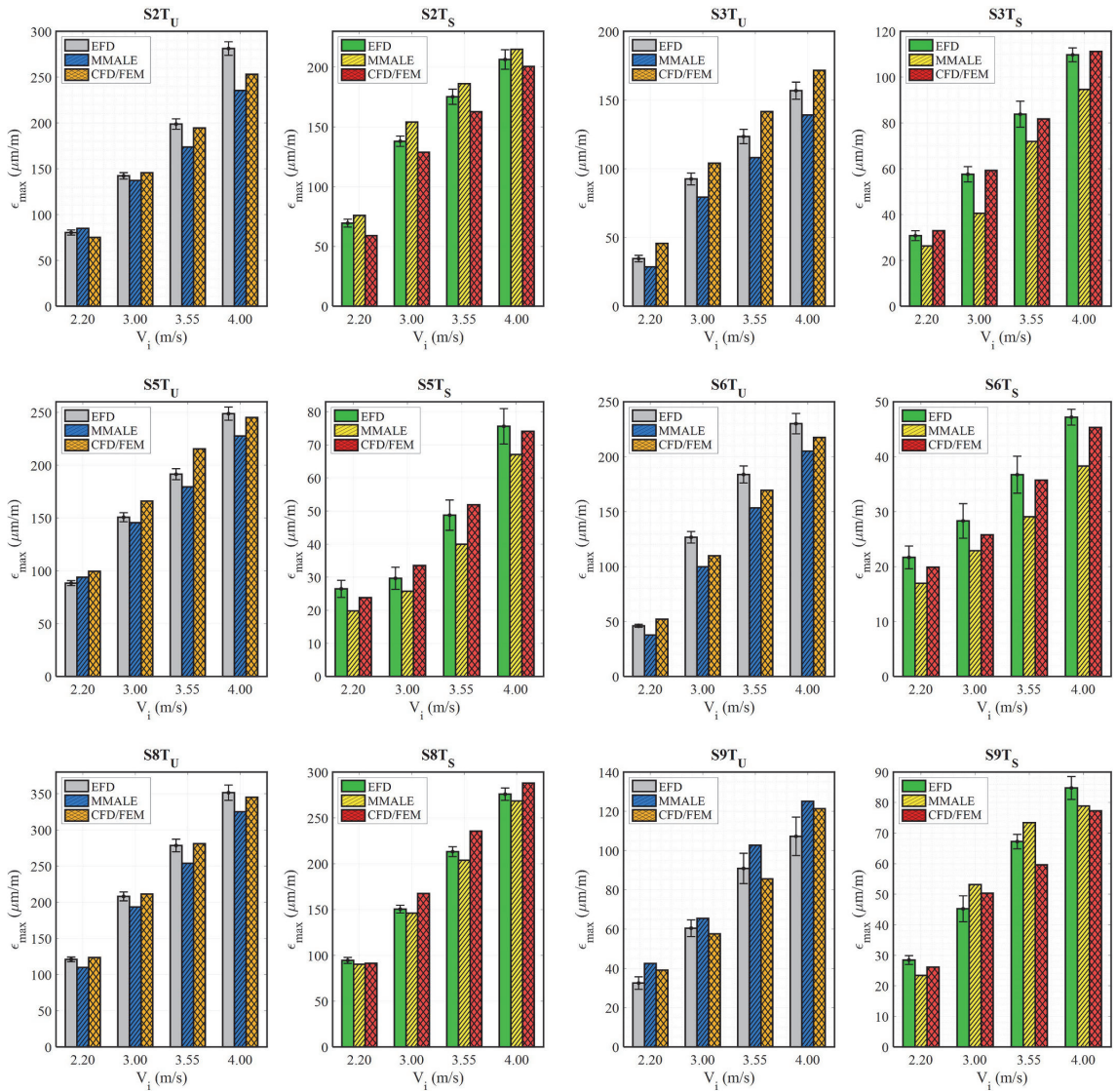


Fig. 18. Comparison of numerical and experimental results of maximum transverse strain at various impact velocities on unstiffened (U) and stiffened (S) plates of the wedge.

### 4.3. Comparisons of structural responses

In addition to the impact velocity, vertical acceleration, and slamming pressure, the numerical strain results of the aluminium wedge are also compared to those from experiments. Fig. 1 shows strain gauge arrangements along transverse and longitudinal directions. The strain gauges were located symmetrically on both the stiffened and unstiffened bottom plates, allowing the results to be assessed based on the structural stiffness. Fig. 16 presents the transverse strain results of the sensors located on the unstiffened (top) and stiffened (bottom) plates of the wedge. The time histories of the transverse strain responses are compared with the experimental data for the case with an impact velocity of 4.00 [m/s]. It is shown that the strain values on the unstiffened plate are considerably higher than those on the stiffened plate. The

strain value of the sensor S5T<sub>S</sub> on the stiffened plate is noticeably lower than that of on the unstiffened plate (S5T<sub>U</sub>) as the sensor was positioned on top of the transverse stiffener. The strain response time history indicates the effect of deadrise angle on the results, with sensors positioned on the section with a smaller deadrise angle (S8T) having a higher peak value.

In addition to the strain values in the transverse direction, the time histories of the numerical strain responses in the longitudinal direction at 4.00 [m/s] impact velocity for a short period of time are compared with the experimental data in Fig. 17. It is worth mentioning that the longitudinal strain gauges were located on the top of the longitudinal stiffener of the stiffened plate for both experimental and numerical models. Fig. 17, shows that the sensors on the stiffened plate display noticeably lower strain values compared to those on the unstiffened

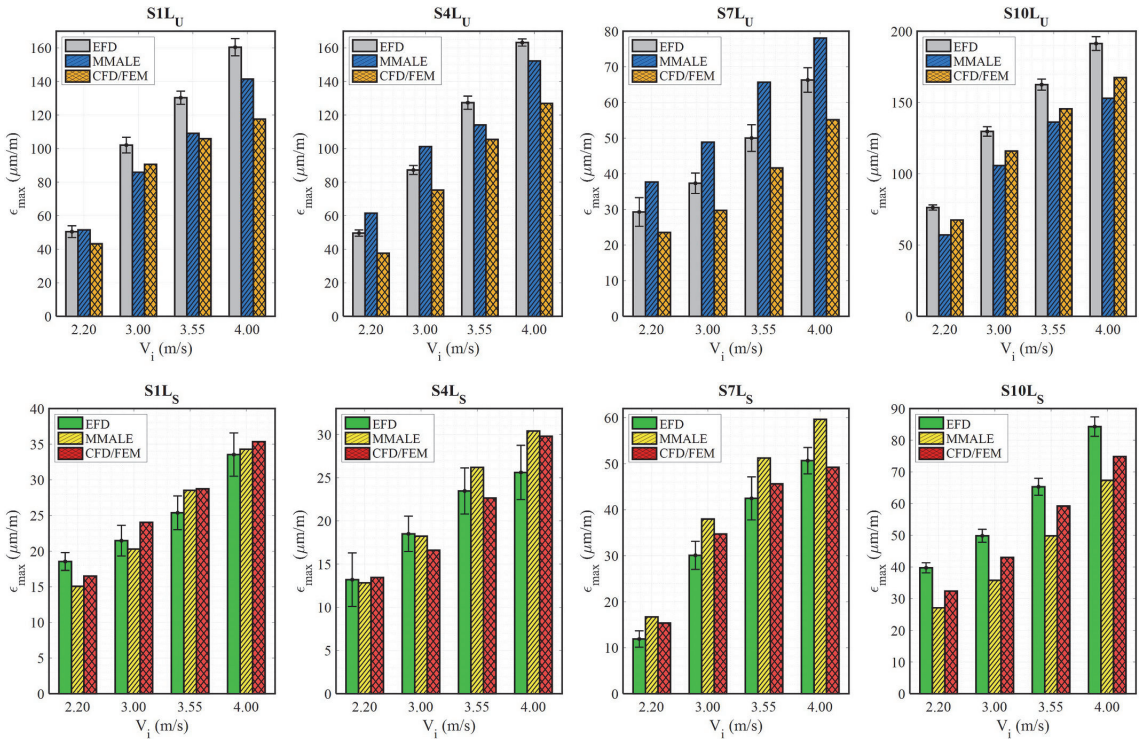


Fig. 19. Comparison of numerical and experimental results of maximum longitudinal strain at various impact velocities on unstiffened (U) and stiffened (S) plates of the wedge.

plate.

The maximum transverse strains computed using numerical methods are compared against the experimental measurements at various impact velocities (see Fig. 18). As shown in this figure, the subscript of U represents the maximum strain values for the gauges located on the unstiffened bottom and the subscript of S shows the maximum strain values for the gauges positioned on the stiffened bottom. In the same way as the pressure results, the vertical error bar at the peak represents the standard deviation of the experimental peak strain for each sensor. The strain results of the numerical simulations were computed at the same location as the experimental strain gauges. Additionally, Fig. 19 compares the numerical strain peak values with experimental data for stiffened and unstiffened plates located in the longitudinal direction. Notably, the predicted and measured maximum strain values coincide with each other quite well. However, the discrepancy between numerical and experimental results increases for the strain gauges close to the chine of the wedge. To further investigate the validity of the numerical models, the maximum strain values obtained from the numerical simulations are compared with the experimental data and reported along with the relative error for each sensor in Table A3 and Table A4.

To comprehend the influence of the two-way FFSI methods on slamming, the effect of structural stiffness and impact velocity on the deflection of the bottom plate is also examined. The time histories of the maximum deflection of the bottom unstiffened and stiffened plates computed by MMALE and CFD/FEM two-way coupling methods are compared at various initial impact velocities. Fig. 20 depicts the distributions of the bottom deflection (ABAQUS) and pressure (Star CCM+) at the time instant of the maximum bottom deflection. As anticipated, the maximum deflection on the stiffened and unstiffened bottoms differs significantly, and it increases with increasing impact velocity. For

instance, the maximum deflection on the unstiffened bottoms of the wedge at 4.00 [m/s] initial impact velocity is 2.77 [mm], which occurs at  $t = 0.018$ s of the simulation time, whereas the maximum deflection on the stiffened plate is 0.82 [mm] and happens at  $t = 0.012$ s (Fig. 20d). It may also be observed that the maximum deflection occurs when the wedge is partially wetted and the stiffened plate experiences maximum deflection earlier than that of the unstiffened bottom (Fig. 20). The effect of rigidity on the pressure peak and structural response is noticeable, and the stiffened bottom's deflection is remarkably negligible for low impact velocities. It is demonstrated that both numerical methods are able to predict the bottom deflection and that the results of the two numerical methods are highly comparable.

#### 4.4. Three-dimensional effects

A comparison of numerical and analytical results of the pressure coefficient ( $C_p = P/0.5\rho V_i^2$ ) on different deadrise angles of the wedge are illustrated in Fig. 21. The aim of this comparison is to investigate the three-dimensional effects on impact-induced loads. The numerical results were computed using the CFD/FEM two-way coupling method presented in Subsection 3.3. The idealisation considered various solution time intervals of the order of 0.005, 0.01, 0.0225, and 0.03s, corresponding to the time instant when the spray root reaches 0.1, 0.25, 0.05, 0.65 of the wedge wall length (L). In Fig. 21a, the vertical axis represents the pressure coefficient as defined before, and the horizontal axis is non-dimensionalised by the vertical distance ( $y/d$ ) where  $d$  is the wedge penetration at each instant. The pressure coefficient results are compared with the asymptotic solution presented by Zhao and Faltinsen (1993). In the latter publication, the authors stated that the asymptotic method can be applied for small deadrise angles ( $\beta < 30$  deg.) and that

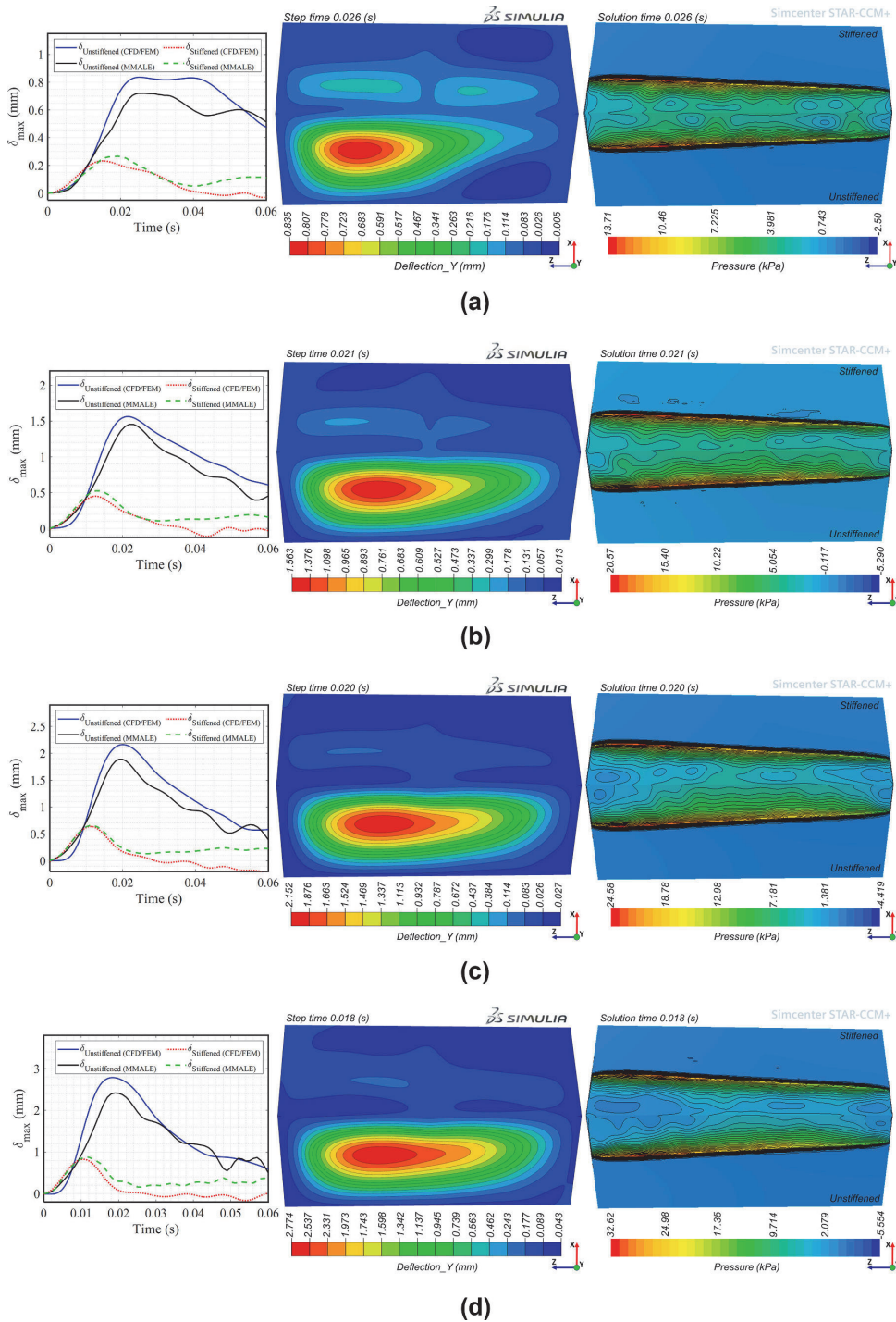


Fig. 20. Time history of the maximum deflection of the bottom unstiffened and stiffened plates computed by two different coupling method (left), bottom deflection distribution (middle), and pressure distribution on the bottom of the wedge (right) with: a) 2.20 [m/s] initial impact velocity; b) 3.00 [m/s] initial impact velocity; c) 3.55 [m/s] initial impact velocity; d) 4.00 [m/s] initial impact velocity.

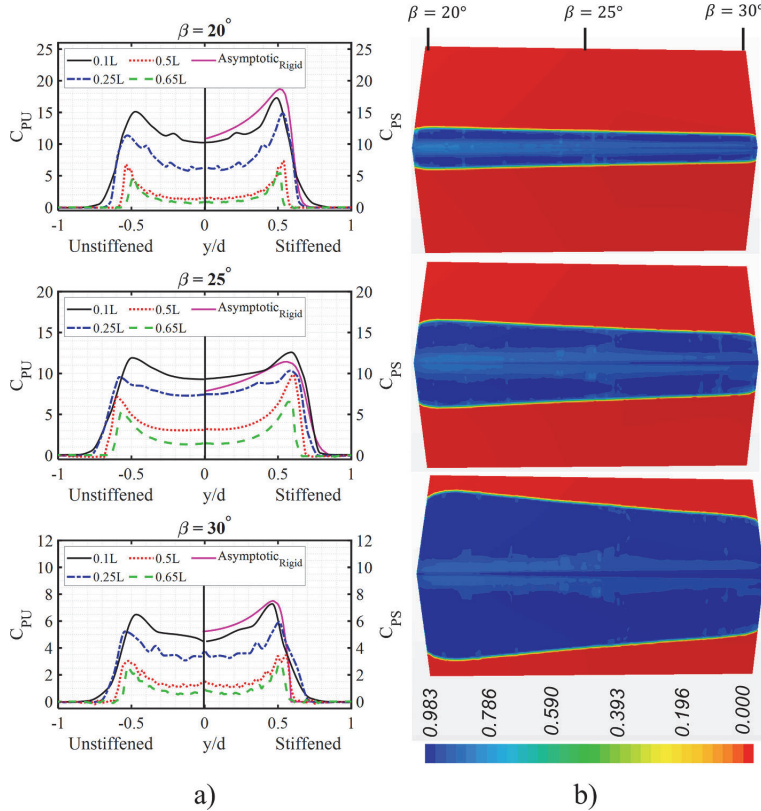


Fig. 21. Comparison of numerical results and asymptotic solution (Zhao and Faltinsen, 1993) at different locations of spray root: a) pressure coefficient at different deadrise angles on the unstiffened and stiffened bottom; b) volume fraction of water at the bottom of the wedge at 0.1L, 0.25L, and 0.5L, respectively.

Table 5 Comparison of the maximum slamming pressure coefficient between numerical stiffened vs unstiffened results and asymptotic solution (Zhao and Faltinsen, 1993).

Deadrise (deg.)	Stiffened vs Unstiffened			Asymptotic vs Unstiffened		Asymptotic vs Stiffened
	$C_{PUmax}$	$C_{PSmax}$	$\Delta C_{Pmax}$ (%)	$C_{Pmax}$ (Asymptotic)	$\Delta C_{PUmax}$ (%)	$\Delta C_{PSmax}$ (%)
20	15.11	17.30	12.61	18.63	18.90	7.20
25	11.95	12.07	0.99	11.35	5.29	6.34
30	6.48	7.27	10.85	7.40	12.32	1.65

Table 6 A comparison of the numerical results of the maximum slamming force between the 2D and 3D wedges.

$V_i$ (m/s)	Deadrise (deg.)	$F_{2D}$ (N)	$C_{Fmax}$ (2D)	$F_{3D}$ (N)	$C_{Fmax}$ (3D)	$\Delta C_{Fmax}$ (%)
2.20	20	59.85	2.74	2750	2.10	23.42
	25	45.83	1.64	2139.5	1.32	19.79
	30	36.66	1.06	1826	0.95	10.31
3.00	20	108.49	2.65	4702.5	1.98	25.12
	25	85.08	1.62	4059	1.29	20.48
	30	68.29	1.05	3470.5	0.93	11.54
3.55	20	148.32	2.59	6380	1.92	25.97
	25	117.41	1.60	5555	1.26	21.14
	30	95.05	1.05	5043.5	0.91	12.93
4.00	20	192.49	2.58	8360	1.87	27.61
	25	143.66	1.50	6490	1.13	24.70
	30	123.19	1.04	6325	0.89	14.43

the air pocket effect during the impact was ignored. It is shown that the pressure coefficient decreases over time and the differences between pressure coefficients at the first and the last computed instants become larger when the deadrise angle decreases.

The effect of structural rigidity on the pressure coefficient is also studied by comparing the results of unstiffened and stiffened bottoms. Fig. 21b displays the volume fraction of water on the bottom of the wedge at  $t = 0.0075, 0.01$  and  $0.0225s$ . According to the findings, the deadrise angle and structural deformation affect the pressure coefficient profile, with a small angle resulting in a profile with a sharper peak and a greater amplitude. However, because of the three-dimensional effect in way of the two ends of the wedge structure, in some instants, the pressure coefficient with a 25-degree deadrise angle is larger than that with a 20-degree deadrise angle (e.g. 0.5L). Furthermore, Table 5 presents the maximum slamming pressure coefficients ( $C_{Pmax} = P_{max}/0.5\rho V_i^2$ ) at various deadrise angles for both stiffened and unstiffened bottom plates. This table lists the variations between the numerical results and the asymptotic solution.

To evaluate the three-dimensional effects on the slamming loads, the maximum value of impact loads on 2D and 3D wedges are numerically calculated and presented in Table 6. The results are compared using a non-dimensional maximum force coefficient  $C_{Fmax}$ , which is calculated as  $C_{Fmax} = F_{max}/0.5\rho V_i^2 L \tan\beta$ , where  $F_{max}$  is the maximum value of the slamming force,  $\beta$  is the deadrise angle,  $\rho$  is the density of the water,  $L$  is the horizontal dimension of the wedge section, and  $V_i$  is the impact velocity. As expected, the value of  $C_{Fmax}$  decreases for both 2D and 3D models as the initial impact velocity increases. Depending on the impact velocity and deadrise angle, the maximum slamming force predictions from 3D calculations are between 10.31% and 27.61% lower than those from 2D models, where  $\Delta C_{Fmax} = (C_{Fmax,2D} - C_{Fmax,3D})/C_{Fmax,2D}$ . In addition, the results demonstrate that as the impact velocities increase, the differences in the maximum force coefficient between the 2D and 3D models become more significant.

## 5. Conclusions

This paper assessed and compared impact induced loads from two different numerical models acting on a complex three-dimensional V-shaped structure. Hydroelastic slamming was simulated on a wedge with a 4 mm bottom plate thickness and a stiffened panel free-falling at different vertical velocities. The numerical FFSI models were validated by direct comparison with the experimental data presented in Part I of this two-part companion paper. An explicit nonlinear LS-DYNA FEA method incorporating a MMALE solver was employed to design the numerical FSI model in LS-DYNA. In addition, the instantaneous interaction between fluid and structure of the described water entry problem was modelled by utilizing a strongly two-way coupling technique in CFD and FEA solvers. The coupling between the FVM and FEM solvers was achieved by STAR-CCM+ and ABAQUS commercial solvers. Following comparison with experimental results, it was concluded that the numerical models properly predict kinematics, slamming pressures, and structural responses. Notwithstanding this, there are some discrepancies in the maximum values of pressure and strain responses for the sensors located close to the chine.

The influence of three-dimensionality, impact velocity, deadrise angle, and structural rigidity on vertical acceleration, slamming pressure, and strain responses were examined in further. It was demonstrated that the slight discrepancy in the maximum value of pressure and strain predicted by numerical methods appears because of the different coupling techniques that were applied in the FFSI simulations. The MMALE method is highly dependent on free surface contact forces, penalty coupling algorithm, and damping factors. Numerical results accounting for the influence of turbulent flow dynamics are in better agreement with experiments. Nevertheless, the viscosity effect on the

pressure distribution and structural responses is almost negligible.

The magnitude of the bottom plate deflection increases as the impact velocity increases, hence making coupled FFSI assessment essential. The structural deformation on the bottom of the wedge affects the hydrodynamic loads during slamming. The dynamic loads change in a short period of time and propagate through hydrodynamic pressure and elastic vibrations. Therefore, the fluid flow could be influenced differently in accordance with the magnitude of the structural response.

The results imply that the slamming loads are influenced by the three-dimensional effects. The maximum slamming force coefficients of 2D and 3D wedges were compared in the study, and it was discovered that the 3D model predicted lower values than the 2D model. In comparison to the 2D simulations, the 3D calculations on the maximum slamming force coefficient are around 10%–14% lower for the wedge with a deadrise angle of 30° and around 23%–27% lower for the wedge with a deadrise angle of 20°.

## CRedit authorship contribution statement

**Saeed Hosseinzadeh:** Writing – original draft, Conceptualization, Formal analysis, Software, Editing. **Kristjan Tabri:** Resources, Supervision, Project administration, Writing – review & editing, Funding acquisition. **Ameen Topa:** Writing – review & editing, Software, Formal analysis. **Spyros Hirdaris:** Writing – review & editing, Supervision.

## Declaration of competing interest

The authors declare that they have no known competing financial interests or personal relationships that could have appeared to influence the work reported in this paper.

## Data availability

Data will be made available on request.

## Acknowledgements

This research work has been financially supported by the Estonian Research Council via the grants PRG83 (Numerical simulation of the FSI for the dynamic loads and response of ships) and PRG1820 (Dynamic response of offshore structures). The assistance of HPC Center in providing access to computational resources is also gratefully acknowledged. The authors would also like to thank the staff of the Marine Technology Competence Center at Tallinn University of Technology (TALTECH MARTE) for their valuable support of the experimental study.

## Appendix A. Comparison of experimental and numerical results

**Table A1**

Comparison of maximum acceleration calculated by two numerical models with experimental data, and the corresponding percentage error ( $|E|_{\%}$ ) at different impact velocities.

$V_i$ (m/s)	Deadrise (deg.)	Maximum Acceleration (g)			$ E _{\%}$	
		EFD	MMALE	CFD/FEM	MMALE	CFD/FEM
2.20	20	4.93	5.10	4.99	3.33	1.18
	25	3.84	3.97	4.10	3.21	6.72
	30	3.34	3.38	3.53	1.31	5.51
3.00	20	8.01	8.41	8.77	4.95	9.39
	25	7.15	7.42	7.68	3.76	7.38
	30	5.94	6.23	6.48	4.84	9.05
3.55	20	10.86	11.52	11.90	6.04	9.55
	25	9.44	9.88	10.01	4.75	6.04
	30	8.13	8.77	8.73	7.46	7.32
4.00	20	14.08	15.29	15.40	8.61	9.42
	25	11.67	12.03	12.23	3.10	4.85

(continued on next page)

Table A1 (continued)

		Maximum Acceleration (g)			$ E _{\%}$	
$V_i$ (m/s)	Deadrise (deg.)	EFD	MMALE	CFD/FEM	MMALE	CFD/FEM
	30	10.19	11.11	10.81	9.08	6.08
Average $ E _{\%}$					5.04	6.87

Table A2

Comparison of maximum pressure computed from two numerical models with experimental data, and the corresponding percentage error ( $|E|_{\%}$ ) at 4.00 [m/s] impact velocity on unstiffened (U) and stiffened (S) bottom plates.

		Unstiffened Plate					Stiffened Plate					
		Peak Pressure (kPa)			$ E _{\%}$		Peak Pressure (kPa)			$ E _{\%}$		
$V_i$ (m/s)	Sensor No.	EFD	MMALE	CFD/FEM	MMALE	CFD/FEM	Sensor No.	EFD	MMALE	CFD/FEM	MMALE	CFD/FEM
4.00	P1 <sub>U</sub>	52.43	47.73	53.24	8.96	1.55	P1 <sub>S</sub>	61.93	58.38	56.46	5.73	8.83
	P2 <sub>U</sub>	25.97	27.51	23.90	5.95	7.96	P2 <sub>S</sub>	35.30	37.96	33.51	7.52	5.09
	P3 <sub>U</sub>	9.49	10.45	8.83	10.11	7.02	P3 <sub>S</sub>	11.33	12.34	10.54	8.94	6.97
	P4 <sub>U</sub>	3.83	4.28	3.56	11.80	6.95	P4 <sub>S</sub>	5.92	6.30	5.33	6.43	9.93
	P5 <sub>U</sub>	64.37	66.15	62.75	2.76	2.52	P5 <sub>S</sub>	69.31	72.15	67.15	4.10	3.11
	P6 <sub>U</sub>	28.90	32.27	31.46	11.66	8.87	P6 <sub>S</sub>	42.27	43.44	42.98	2.77	1.68
	P7 <sub>U</sub>	11.51	12.90	10.95	12.07	4.84	P7 <sub>S</sub>	15.40	15.02	14.15	2.41	8.07
	P8 <sub>U</sub>	6.90	6.65	6.54	3.76	5.29	P8 <sub>S</sub>	8.16	7.86	7.45	3.68	8.70
Average $ E _{\%}$					8.38	5.63					5.20	6.55

Table A3

Comparison of maximum strain on transverse direction computed by two numerical models with experimental data, and the corresponding percentage error ( $|E|_{\%}$ ) at 4.00 [m/s] impact velocity on unstiffened (U) and stiffened (S) bottom plates.

		Unstiffened Plate					Stiffened Plate					
		Maximum Strain (mm/m)			$ E _{\%}$		Maximum Strain (mm/m)			$ E _{\%}$		
$V_i$ (m/s)	Sensor No.	EFD	MMALE	CFD/FEM	MMALE	CFD/FEM	Sensor No.	EFD	MMALE	CFD/FEM	MMALE	CFD/FEM
4.00	S2T <sub>U</sub>	281.21	235.41	253.05	16.29	10.01	S2T <sub>S</sub>	206.41	214.90	200.59	4.11	2.82
	S3T <sub>U</sub>	156.81	139.09	171.55	11.30	9.40	S3T <sub>S</sub>	109.72	94.63	111.21	13.76	1.36
	S5T <sub>U</sub>	248.75	227.66	245.13	8.48	1.46	S5T <sub>S</sub>	75.59	67.06	74.09	11.29	1.99
	S6T <sub>U</sub>	230.09	205.10	217.58	10.86	5.44	S6T <sub>S</sub>	47.19	38.31	45.33	18.82	3.94
	S8T <sub>U</sub>	351.44	325.15	345.08	7.48	1.81	S8T <sub>S</sub>	275.85	268.39	287.87	2.70	4.36
	S9T <sub>U</sub>	107.24	125.10	121.35	16.66	13.16	S9T <sub>S</sub>	84.78	78.89	77.30	6.94	8.82
Average $ E _{\%}$					11.84	6.88					9.60	3.88

Table A4

Comparison of maximum strain on longitudinal direction computed by two numerical models with experimental data, and the corresponding percentage error ( $|E|_{\%}$ ) at 4.00 [m/s] impact velocity on unstiffened (U) and stiffened (S) bottom plates.

		Unstiffened Plate					Stiffened Plate					
		Maximum Strain (mm/m)			$ E _{\%}$		Maximum Strain (mm/m)			$ E _{\%}$		
$V_i$ (m/s)	Sensor No.	EFD	MMALE	CFD/FEM	MMALE	CFD/FEM	Sensor No.	EFD	MMALE	CFD/FEM	MMALE	CFD/FEM
4.00	S1L <sub>U</sub>	160.44	141.43	117.57	11.84	26.72	S1L <sub>S</sub>	33.54	34.29	35.35	2.24	5.41
	S4L <sub>U</sub>	163.23	152.22	126.93	6.75	22.24	S4L <sub>S</sub>	25.60	30.39	29.80	18.71	16.38
	S7L <sub>U</sub>	66.31	78.07	55.16	17.74	16.82	S7L <sub>S</sub>	50.67	59.65	49.22	17.73	2.86
	S10L <sub>U</sub>	191.32	152.92	167.47	20.07	12.47	S10L <sub>S</sub>	84.30	67.33	74.86	20.12	11.20
	Average $ E _{\%}$					14.10	19.56					14.70

References

Abrate, S., 2013. Hull slamming. *Appl. Mech. Rev.* 64 (6) <https://doi.org/10.1115/1.4023571>.

Aquelet, N., Souli, M., 2008. Damping Effect in Fluid-Structure Interaction: Application to Slamming Problem, 460. American Society of Mechanical Engineers, Pressure Vessels and Piping Division (Publication) PVP, pp. 233–242. <https://doi.org/10.1115/PVP2003-1968>.

Aquelet, Nicolas, Souli, M., Olovsson, L., 2006. Euler-Lagrange coupling with damping effects: application to slamming problems. *Comput. Methods Appl. Mech. Eng.* 195 (1–3), 110–132. <https://doi.org/10.1016/J.CMA.2005.01.010>.

Bathe, K.J., 2006. *Finite Element Procedures*. Klaus-Jürgen Bathe.

Benson, D.J., 1992. Computational methods in Lagrangian and Eulerian hydrocodes. *Comput. Methods Appl. Mech. Eng.* 99 (2–3), 235–394. [https://doi.org/10.1016/0045-7825\(92\)90042-1](https://doi.org/10.1016/0045-7825(92)90042-1).

Causin, P., Gerbeau, J.F., Nobile, F., 2005. Added-mass effect in the design of partitioned algorithms for fluid–structure problems. *Comput. Methods Appl. Mech. Eng.* 194 (42–44), 4506–4527. <https://doi.org/10.1016/J.CMA.2004.12.005>.

Cheon, J.S., Jang, B.S., Yim, K.H., Lee, H.S.D., Koo, B.Y., Ju, H., 2016. A study on slamming pressure on a flat stiffened plate considering fluid–structure interaction. *J. Mar. Sci. Technol.* 21 (2), 309–324. <https://doi.org/10.1007/S00773-015-0353-Y/TABLES/2>.

Dassault Systèmes, 2016. *Abaqus Theory Guide*. Providence, RI.

- Donea, J., Huerta, A., Ponthot, J.-P., Rodríguez-Ferran, A., 2004. Arbitrary Lagrangian-Eulerian Methods.
- DNV, 2010. DNV-RP-C205 Environmental Conditions and Environmental Loads. October. Det Norske Veritas.
- Faltinsen, O.M., 1999. Water entry of a wedge by hydroelastic orthotropic plate theory. *J. Ship Res.* 43 (3), 180–193. <https://doi.org/10.5957/JSR.1999.43.3.180>.
- Faltinsen, O.M., 2000. Hydroelastic slamming. *J. Mar. Sci. Technol.* 5 (2), 49–65. <https://doi.org/10.1007/s007730070011>.
- Faltinsen, O.M., 2005. Hydrodynamics of High-Speed Marine Vehicles. Cambridge University Press.
- Heuzé, O., 2012. General form of the Mie-Grüneisen equation of state. *Compt. Rendus Mec.* 340 (10), 679–687.
- Hirdaris, S.E., Bai, W., Dessi, D., Ergin, A., Gu, X., Hermundstad, O.A., et al., 2014. Loads for use in the design of ships and offshore structures. *Ocean. Eng.* <https://doi.org/10.1016/j.oceaneng.2013.09.012>.
- Hosseinzadeh, S., Izadi, M., Tabri, K., 2020. Free fall water entry of a two-dimensional asymmetric wedge in oblique slamming: a numerical study. In: 39th International Conference on Ocean. Offshore & Arctic Engineering.
- Hosseinzadeh, S., Tabri, K., 2021a. Hydroelastic effects of slamming impact loads during free-fall water entry. *Ships Offshore Struct.* 16 (S1), 68–84. <https://doi.org/10.1080/17445302.2021.1954320>.
- Hosseinzadeh, S., Tabri, K., 2021b. Free-fall water entry of a variable deadrise angle aluminium wedge: an experimental study. In: Developments in the Analysis and Design of Marine Structures, 29–37. <https://doi.org/10.1201/9781003230373-4>.
- Hosseinzadeh, S., Tabri, K., Hirdaris, S.E., Sahk, T., 2023. Slamming Loads and Responses on a Non-prismatic Stiffened Aluminium Wedge: Part I. Experimental Study. *Ocean Engineering*.
- Huang, L., Tavakoli, S., Li, M., Dolatshah, A., Pena, B., Ding, B., Dashtimanesh, A., 2021. CFD analyses on the water entry process of a freefall lifeboat. *Ocean. Eng.* 232, 109115. <https://doi.org/10.1016/j.oceaneng.2021.109115>.
- Izadi, M., Ghadimi, P., Fadavi, M., Tavakoli, S., 2018. Numerical modeling of the freefall of two-dimensional wedge bodies into water surface. *J. Braz. Soc. Mech. Sci. Eng.* 40 (1), 1–19. <https://doi.org/10.1007/S40430-017-0941-3/FIGURES/27>.
- ITTC. Uncertainty analysis in CFD Verification and validation methodology and procedures. ITTC - Recommended Procedures and Guidelines 2017. Procedure 7.5-03-01, pp.1–13. <https://www.ittc.info/media/8153/75-03-01-01.pdf>.
- Joint Accident Investigation Commission (JAIC), 1997. Final Report on the Capsizing on 28 September 1994 in the Baltic Sea of the Ro-Ro Passenger Vessel MV Estonia. Edita Books, Helsinki, 1997.
- Kamath, A., Bihs, H., Arntsen, Ø.A., 2017. Study of Water Impact and Entry of a Free Falling Wedge Using Computational Fluid Dynamics Simulations. <https://doi.org/10.1115/1.4035384>.
- Kapsenberg, G.K., 2011. Slamming of ships: where are we now? *Trans. R. Soc. A* 369, 2892–2919. <https://doi.org/10.1098/rsta.2011.0118>.
- Kim, Y., Yang, K.K., Kim, J.H., Zhu, Z., 2017. Study of water-entry impact of wedge and ship-like section using potential theories and CFD. *Int. J. Offshore Polar Eng.* 27 (2), 168–176. <https://doi.org/10.17736/IJOPE.2017.JC670>.
- Ladeira, Í., 2020. Simulation of Slamming on a Fiber Reinforced Composite Structure Using the ALE/Eulerian Numerical Approach. Retrieved from. <https://matheo.uliege.be/handle/2268.2/8499>.
- Lakshmyanarayana, P.A.K., Hirdaris, S., 2020. Comparison of nonlinear one-and two-way FFSI methods for the prediction of the symmetric response of a containership in waves. *Ocean Eng.* 203, 107179.
- LS-DYNA Theory Manual, 2022. Livermore Software Technology (Lst). An Ansys Company.
- Luo, Han-bing, Wang, S., Soares, C.G., 2011. Numerical prediction of slamming loads on a rigid wedge subjected to water entry using an explicit finite element method. Undefined 551–580. <https://doi.org/10.1201/B10771-7>.
- Luo, Hanbing, Hu, J., Soares, C.G., 2010. Numerical simulation of hydroelastic responses of flat stiffened panels under slamming loads, 6. In: Proceedings of the International Conference on Offshore Mechanics and Arctic Engineering - OMAE, pp. 373–381. <https://doi.org/10.1115/OMAE2010-20027>.
- Luo, Hanbing, Wang, H., Guedes Soares, C., 2012. Numerical and experimental study of hydrodynamic impact and elastic response of one free-drop wedge with stiffened panels. *Ocean. Eng.* 40, 1–14. <https://doi.org/10.1016/j.oceaneng.2011.11.004>.
- Mori, K., 1977. Response of the bottom plate of high-speed crafts under impulsive water pressure. *J. Soc. Nav. Archit. Jpn.* 142, 297–305 [Japanese].
- Piro, D.J., Maki, K.J., 2013. Hydroelastic analysis of bodies that enter and exit water. *J. Fluid Struct.* 37, 134–150.
- Savander, B.R., Scorpio, S.M., Taylor, R.K., 2002. Steady hydrodynamic analysis of planing surfaces. *J. Ship Res.* 46 (4), 248–279. <https://doi.org/10.5957/JSR.2002.46.4.248>.
- Souli, M.H., Benson, D.J. (Eds.), 2013. Arbitrary Lagrangian Eulerian and Fluid-Structure Interaction: Numerical Simulation. John Wiley & Sons.
- Southall, N., Choi, S., Lee, Y., Hong, C., Hirdaris, S., White, N., 2015. Impact Analysis Using CFD – A Comparative Study. OnePetro.
- STAR-CCM+, 2020. STAR-CCM+ Version 15.06 Manual, 2020.
- Stenius, I., Rosén, A., Kuttenukeuler, J., 2007. Explicit FE-modelling of fluid – structure interaction in hull – water impacts. *Int. Shipbuild. Prog.* 53, 103–121.
- Stenius, I., Rosén, A., Kuttenukeuler, J., 2011. Hydroelastic interaction in panel-water impacts of high-speed craft. *Ocean. Eng.* 38 (2–3), 371–381. <https://doi.org/10.1016/j.oceaneng.2010.11.010>.
- Truong, D.D., Jang, B.S., Ju, H.B., Woong Han, S., 2020. Prediction of slamming pressure considering fluid-structure interaction. Part I: numerical simulations. <https://doi.org/10.1080/17445302.2020.1816732>.
- Truong, D.D., Jang, B.S., Janson, C.E., Ringsberg, J.W., Yamada, Y., Takamoto, K., et al., 2021. Benchmark study on slamming response of flat-stiffened plates considering fluid-structure interaction. *Mar. Struct.* 79 <https://doi.org/10.1016/J.MARSTRUC.2021.103040>.
- von Karman, T., 1929. The Impact on Seaplane Floats during Landing. National Advisory Committee for Aeronautics.
- Vorus, W.S., 1996. A flat cylinder theory for vessel impact and steady planing resistance. *J. Ship Res.* 40, 89–106.
- Wagner, H., 1932. Über Stoß- und Gleitvorgänge an der Oberfläche von Flüssigkeiten. *Angew Math Mech* 12 (4), 193–215.
- Wang, S., Soares, C.G., 2012. Analysis of the water impact of symmetric wedges with a multi-material eulerian formulation. *Int. J. Marit. Eng.* 154 (A4) <https://doi.org/10.5750/IJME.V154IA4.888>.
- Wang, Shan, Soares, C.G., 2017a. Review of ship slamming loads and responses. *J. Mar. Sci. Appl.* 16, 427–445. <https://doi.org/10.1007/s11804-017-1437-3>.
- Wang, S., Soares, C.G., 2017b. Hydroelastic analysis of a rectangular plate subjected to slamming loads. *J. Mar. Sci. Appl.* 16, 405–416. <https://doi.org/10.1007/s11804-017-1434-6>.
- Wang, S., Guedes Soares, C., 2018. A numerical investigation on water slamming of stiffened panels, 3. In: Proceedings of the International Conference on Offshore Mechanics and Arctic Engineering - OMAE. <https://doi.org/10.1115/OMAE2018-77908>.
- Wang, S., Islam, H., Guedes Soares, C., 2021. Uncertainty due to discretization on the ALE algorithm for predicting water slamming loads. *Mar. Struct.* 80, 103086 <https://doi.org/10.1016/J.MARSTRUC.2021.103086>.
- Yan, D., Mikkola, T., Kujala, P., Hirdaris, S., 2022a. Hydroelastic Analysis of Slamming Induced Impact on Stiff and Flexible Structures by Two-Way CFD-FEA Coupling, pp. 1–13. <https://doi.org/10.1080/17445302.2022.2116231>, 10.1080/17445302.2022.2116231.
- Yan, D., Mikkola, T., Lakshmyanarayana, A., Tödter, S., Schellin, T.E., Neugebauer, J., et al., 2022b. A study into the FSI modelling of flat plate water entry and related uncertainties. *Mar. Struct.* 86, 103296 <https://doi.org/10.1016/J.MARSTRUC.2022.103296>.
- Yu, P., Li, H., Ong, M.C., 2019a. Hydroelastic analysis on water entry of a constant-velocity wedge with stiffened panels. *Mar. Struct.* 63, 215–238. <https://doi.org/10.1016/j.marstruc.2018.09.007>.
- Yu, Z., Amdahl, J., Greco, M., Xu, H., 2019b. Hydro-plastic response of beams and stiffened panels subjected to extreme water slamming at small impact angles, Part I: an analytical solution. *Mar. Struct.* 65, 53–74. <https://doi.org/10.1016/J.MARSTRUC.2019.01.002>.
- Zhao, R., Faltinsen, O.M., 1993. Water entry of two-dimensional bodies. *J. Fluid Mech.* 246, 593–612.
- Zhao, R., Faltinsen, O.M., Aarsnes, J., 1996. Water entry of arbitrary two-dimensional sections with and without flow separation. In: Proceedings of the 21st Symposium on Naval Hydrodynamics. National Academy Press, Washington, DC, USA, pp. 408–423. Trondheim, Norway.

# Curriculum vitae

## 1. Personal data

Name Saeed Hosseinzadeh; [ETIS](#), [ORCID](#), [SCOPUS](#)  
Date and place of birth 08.06.1990, Iran  
Nationality Iranian

## 2. Contact information

Address Tallinn University of Technology, School of Engineering, Department of Civil Engineering and Architecture, Ehitajate tee 5, 19086 Tallinn, Estonia  
Phone (+372) 5820 3434  
E-mail saeed.hosseinzadeh@taltech.ee

## 3. Education

2019–2023 Tallinn University of Technology, School of Engineering, Department of Civil Engineering and Architecture, Coastal and Marine Engineering, PhD  
2013–2015 Sharif University of Technology, Department of Mechanical Engineering, Marine Architectural Engineering, Ship Structure, MSc  
**Thesis:** Mathematical model for longitudinal motions of HYSUCAT vessel with respect to the interaction between hydrofoil and hull

## 4. Language competence

Persian Native  
English Fluent

## 5. Fields of research

ETIS CLASSIFICATION: 4. Natural Sciences and Engineering; 4.13. Mechanical Engineering, Automation Technology and Manufacturing Technology; CERCS CLASSIFICATION: T210 Mechanical engineering, hydraulics, vacuum technology, vibration acoustic engineering; SPECIFICATION: Ship Hydrodynamics, Fluid-Structure Interaction, Marine structures

## 6. Publications

### Journal articles

**Hosseinzadeh, S.**, Tabri, K., Hirdaris, S., & Sakh, T. (2023). Slamming loads and responses on a non-prismatic stiffened aluminium wedge: Part I. Experimental study. *Ocean Engineering*, 279, 114510.

**Hosseinzadeh, S.**, Tabri, K., Topa, A., & Hirdaris, S. (2023). Slamming loads and responses on a non-prismatic stiffened aluminium wedge: Part II. Numerical simulations. *Ocean Engineering*, 279, 114309.

**Hosseinzadeh, S.**, & Tabri, K. (2021). Hydroelastic effects of slamming impact loads during free-fall water entry. *Ships and Offshore Structures*, 16(sup1), 68-84.

**Hosseinzadeh, S.**, Khorasanchi, M., & Seif, M. S. (2019). Investigation of planing vessels motion using nonlinear strip theory—an experimental and numerical study. *Ships and Offshore Structures*, 14(7), 684-697.



## Conference papers

**Hosseinzadeh S.,** Topa, A., Tabri, K., (2023). A Numerical Sensitivity Analysis of Fluid-Structure Interaction Simulations on Slamming Loads and Responses. In The 12th International Workshop on Ship and Marine Hydrodynamics (IWSH). Aalto University, Finland.

**Hosseinzadeh, S.,** & Tabri, K. (2021). Free-fall water entry of a variable deadrise angle aluminium wedge: An experimental study. In Developments in the Analysis and Design of Marine Structures: Proceedings of the 8th International Conference on Marine Structures (MARSTRUCT 2021), Trondheim, Norway.

Yan, D., **Hosseinzadeh, S.,** Lakshmyanarayanan, A., Mikkola, T., & Hirdaris, S. (2021). Comparative study on numerical hydroelastic analysis of impact-induced loads. In Proceedings of the 23rd numerical towing tank symposium. NuTTs (p. 6).

**Hosseinzadeh, S.,** & Tabri, K. (2020). Numerical investigation of hydroelastic response of a three-dimensional deformable hydrofoil. In HSMV 2020 (pp. 77-86). IOS Press.

**Hosseinzadeh, S.,** Izadi, M., & Tabri, K. (2020). Free fall water entry of a two-dimensional asymmetric wedge in oblique slamming: a numerical study. In International Conference on Offshore Mechanics and Arctic Engineering (Vol. 84409, p. V008T08A013). American Society of Mechanical Engineers.

## 7. Professional employment

2018	Marine Hydrodynamic Engineer at Tarh Afarinan Pasargad Co., Tehran, Iran
2015–2018	Junior Naval Architect Behrad Marine Snanaat Arvand Co., Tehran, Iran
2014–2015	Hydrodynamic Engineer at Marine Engineering Research Center (MERC), Sharif University of Technology, Tehran, Iran

## 8. Other activities

### Supervised dissertations:

2021	Tarmo Sakh, Master's degree, (supervisor) Saeed Hosseinzadeh, "Wedge drop tests for studying slamming effects", Tallinn University of Technology, Faculty of Engineering, Institute of Construction and Architecture
2020	Kristen Paalandi, Bachelor's degree, (supervisor) Saeed Hosseinzadeh, "Sonar Box Development for Autonomous Catamaran NYMO", Tallinn University of Technology, Faculty of Engineering, Mechanical Engineering Department

### Visiting activities:

2021–2022	Visiting Researcher at Aalto University, Espoo, Finland
-----------	---

### Teaching experience:

2021	Teaching assistant in Ship Stability and Seaworthiness at Tallinn University of Technology, Estonian Maritime Academy
2014	Teaching assistant in Dynamics of Marine Vehicles at Sharif University of Technology, Department of Mechanical Engineering
2014	Teaching the simulation of marine vessels with Star CCM+ at Sharif University of Technology, Department of Mechanical Engineering
2013	Teaching the design of ship structure and hull at Sharif University of Technology, Department of Mechanical Engineering

# Elulookirjeldus

## 1. Isikuandmed

Nimi Saeed Hosseinzadeh; [ETIS](#), [ORCID](#), [SCOPUS](#)  
Sünniaeg ja 08.06.1990, Iraan  
-koht  
Kodakondsus Iraani

## 2. Kontaktandmed

Adress Tallinna Tehnikaülikool, Ehituse ja arhitektuuri instituut, Ehitajate tee 5,  
19086 Tallinn, Estonia  
Telefon (+372) 5820 3434  
E-post saeed.hosseinzadeh@taltech.ee

## 3. Hariduskäik

2019–2023 Tallinna Tehnikaülikool, Ehituse ja arhitektuuri instituut, ranniku- ja  
meretehnika, doktoriõpe  
2013–2015 Sharif University of Technology, Masinaehituse osakond, mere arhitektuuri  
tehnikalaevaehitus, MSc  
**Lõputöö:** Matemaatiline mudel HYSUCAT aluse pikisuunaliste liikumiste  
jaoks, võttes arvesse hüdrofoili ja kere vahelist vastasmõju

## 4. Keelteoskus

Pärsia keel emakeel  
Inglise keel kõrgetase

## 5. Teadustöö põhisuunad

ETIS KLASSIFIKATSIOON: 4. Loodusteadused ja tehnika; 4.13. Mehhanotehnika, automaatika,  
tööstustehnoloogia; CERCS KLASSIFIKATSIOON: T210 Masinaehitus, hüdraulika,  
vaakumtehnoloogia, vibratsioonakustiline tehnoloogia; TÄPSUSTUS: Laeva hüdrodünaamika,  
vedeliku-struktuuri vastastikmõju, merekonstruktsioonid

## 6. Publikatsioonid

Avaldatud teadusartiklite, muude publikatsioonide ja peetud konverentsiettekannete  
loetelu on toodud ingliskeelse elulookirjelduse juures

## 7. Teenistuskäik

2018 Mere hüdrodünaamiline insener at Tarh Afarinan Pasargad Co., Tehran, Iran  
2015–2018 Noorem mereväe arhitekt Behrad Marine Snanaat Arvand Co., Tehran, Iran  
2014–2015 Hüdrodünaamiline insener at Marine Engineering Research Center (MERC),  
Sharif University of Technology, Tehran, Iran

## 8. Teised tegevused

### Juhendatud väitekirjad:

- 2021 Tarmo Sahl, magistrikraad, 2021, (juh) Saeed Hosseinzadeh, Wedge drop tests for studying slamming effects (Kiilu kukutamise katse lämmingu mõju uurimiseks), Tallinna Tehnikaülikool, Inseneriteaduskond, Ehituse ja arhitektuuri instituut
- 2020 Kristen Paalandi, bakalaureusetööd, (juh) Saeed Hosseinzadeh, "Robotlaev Nymo sonari korpuse tehniline lahendus", Tallinna Tehnikaülikool, Inseneriteaduskond, Mehaanika ja tööstustehnika instituut

### Külastustegevused:

- 2021–2022 Külalisuurija, Aalto ülikool, Espoo, Finland

### Õpetamiskogemus:

- 2021 Laevade stabiilsuse ja merikindluse õppeassistent, Tallinna Tehnikaülikooli, Eesti Mereakadeemias
- 2014 Meresõidukite dünaamika õppeassistent, Sharifi Tehnikaülikool, Masinaehituse osakond
- 2014 Star CCM+ abil merelaevade simuleerimise õpetamine, Sharifi Tehnikaülikool, Masinaehituse osakond
- 2013 Laeva konstruktsiooni ja kere projekteerimise õpetamine, Sharifi Tehnikaülikool, Masinaehituse osakond

ISSN 2585-6901 (PDF)  
ISBN 978-9916-80-060-7 (PDF)